

Thèse de Doctorat

présentée devant

POLITECNICO di TORINO

Scuola di dottorato: SCUDO

L'ÉCOLE CENTRALE DE LYON

École doctorale: Mécanique - Energétique - Génie civil - Acoustique

pour obtenir le titre de DOCTEUR

Spécialité: Mécanique des fluides

Pietro SALIZZONI

MASS AND MOMENTUM TRANSFER IN THE URBAN
BOUNDARY LAYER

Turin, 31 mars 2006

Jury: M. PERKINS R.
M. RICCARDI G.
M. ROBINS A.-G. - *président*
M. PORCELLI F.
M. BOTTARO A.
M. BRITTER R. - *rapporteur*
M. PASCHEREIT O. - *rapporteur*

AUTORISATION DE SOUTENANCE

Vu les dispositions de l'arrêté du 7 août 2006,

Vu la demande des Directeurs de Thèse

Messieurs R. PERKINS et C. CANCELLI

et les rapports de

Monsieur R. BRITTER
Professor - Department of Engineering - University of Cambridge - Trumpington Street
Cambridge CB2 1PZ - Royaume-Uni

Monsieur O. PASCHEREIT
Professor - Hermann-Föttinger Institut - TU Berlin - Strasse des 17. Juni 135 - 10623 BERLIN - Allemagne

et

Monsieur A. ROBINS
Professor - School of Engineering (H5) - University of Surrey - GUILDFORD - Surrey GU2 7XH
Royaume-Uni

Monsieur SALIZZONI Pietro

est autorisé à soutenir une thèse pour l'obtention du grade de **DOCTEUR**

Ecole doctorale MECANIQUE, ENERGETIQUE, GENIE CIVIL ET ACOUSTIQUE (MEGA)

Fait à Ecully, le 30 mars 2006

P/Le Directeur de l'E.C.L.
La Directrice des Etudes





ECOLE CENTRALE DE LYON
DIRECTION DE LA RECHERCHE

Liste des personnes Habilitées à Diriger des Recherches en poste à l'Ecole Centrale de Lyon

Nom-Prénom	Corps grade	Laboratoire ou à défaut département ECL	Etablissement
AURIOL Philippe	professeur	AMPERE	ECL
BEROUAL Abderrahmane	professeur	AMPERE	ECL
BURET François	maître de conférences	AMPERE	ECL
JAFFREZIC-RENAULT Nicole	directeur de recherche	AMPERE	CNRS/ECL
KRÄHENBÜHL Laurent	directeur de recherche	AMPERE	CNRS/ECL
MARTELET Claude	professeur	AMPERE	ECL
NICOLAS Alain	professeur	AMPERE	ECL
NICOLAS Laurent	directeur de recherche	AMPERE	CNRS/ECL
SIMONET Pascal	chargé de recherche	AMPERE	CNRS/ECL
THOMAS Gérard	professeur	AMPERE	ECL
VOLLAIRE Christian	maître de conférences	AMPERE	ECL

Nbre Ampère 11

HELLOUIN Yves	maître de conférences	DER EEA	ECL
LE HELLEY Michel	professeur	DER EEA	ECL

Nbre DER EEA 2

GUIRALDENQ Pierre	professeur émérite	DER STMS	ECL
VINCENT Léo	professeur	DER STMS	ECL

Nbre DER STMS 2

LOHEAC Jean-Pierre	maître de conférences	ICJ	ECL
MAITRE Jean-François	professeur émérite	ICJ	ECL
MARION Martine	professeur	ICJ	ECL
MOUSSAOUI Mohand	professeur	ICJ	ECL
MUSY François	maître de conférences	ICJ	ECL
ROUY MIRONESCU Elisabeth	professeur	ICJ	ECL
ZINE Abdel-Malek	maître de conférences	ICJ	ECL

Nbre ICJ 7

DAVID Bertrand	professeur	ICTT	ECL
----------------	------------	------	-----

Nbre ICTT 1

CALLARD Anne-Ségolène	maître de conférences	INL	ECL
CLOAREC Jean-Pierre	maître de conférences	INL	ECL
GAFFIOT Frédéric	professeur	INL	ECL
GAGNAIRE Alain	maître de conférences	INL	ECL
GARRIGUES Michel	directeur de recherche	INL	CNRS/ECL
GENDRY Michel	directeur de recherche	INL	CNRS/ECL
GRENET Geneviève	directeur de recherche	INL	CNRS/ECL
HOLLINGER Guy	directeur de recherche	INL	CNRS/ECL
JOSEPH Jacques	professeur	INL	ECL
KRAWCZYK Stanislas	directeur de recherche	INL	CNRS/ECL
LETARTRE Xavier	chargé de recherche	INL	CNRS/ECL

MARTIN Jean-René	professeur émérite	INL	ECL
O'CONNOR Ian	maître de conférences	INL	ECL
PHANER-GOUTORBE Magali	professeur	INL	ECL
ROBACH Yves	professeur	INL	ECL
SEASSAL Christian	chargé de recherche	INL	CNRS/ECL
SOUTEYRAND Eliane	directeur de recherche	INL	CNRS/ECL
TARDY Jacques	directeur de recherche	INL	CNRS/ECL
VIKTOROVITCH Pierre	directeur de recherche	INL	CNRS/ECL

Nbre INL 19

CHEN Liming	professeur	LIRIS	ECL
-------------	------------	-------	-----

Nbre LIRIS 1

BAILLY Christophe	professeur	LMFA	ECL
BERTOGLIO Jean-Pierre	directeur de recherche	LMFA	CNRS/ECL
BLANC-BENON Philippe	directeur de recherche	LMFA	CNRS/ECL
BOGEY Christophe	chargé de recherche	LMFA	CNRS/ECL
CAMBON Claude	directeur de recherche	LMFA	CNRS/ECL
CARRIERE Philippe	chargé de recherche	LMFA	CNRS/ECL
CHAMPOUSSIN J-Claude	professeur émérite	LMFA	ECL
COMTE-BELLOT geneviève	professeur émérite	LMFA	ECL
FERRAND Pascal	directeur de recherche	LMFA	CNRS/ECL
GALLAND Marie-Annick	maître de conférences	LMFA	ECL
GODEFERD Fabien	chargé de recherche	LMFA	CNRS/ECL
HENRY Daniel	directeur de recherche	LMFA	CNRS/ECL
JEANDEL Denis	professeur	LMFA	ECL
JUVE Daniel	professeur	LMFA	ECL
LE RIBAUT Catherine	chargée de recherche	LMFA	CNRS/ECL
LEBOEUF Francis	professeur	LMFA	ECL
PERKINS Richard	professeur	LMFA	ECL
ROGER Michel	professeur	LMFA	ECL
SCOTT Julian	professeur	LMFA	ECL
SHAO Liang	chargé de recherche	LMFA	CNRS/ECL
SIMOENS Serge	chargé de recherche	LMFA	CNRS/ECL
TREBINJAC Isabelle	maître de conférences	LMFA	ECL

Nbre LMFA 22

BENAYOUN Stéphane	professeur	LTDS	ECL
CAMBOU Bernard	professeur	LTDS	ECL
COQUILLET Bernard	maître de conférences	LTDS	ECL
DANESCU Alexandre	maître de conférences	LTDS	ECL
FOUVRY Siegfried	chargé de recherche	LTDS	CNRS/ECL
GEORGES Jean-Marie	professeur émérite	LTDS	ECL
GUERRET Chrystelle	chargé de recherche	LTDS	CNRS/ECL
HERTZ Dominique	past	LTDS	ECL
ICHCHOU Mohamed	maître de conférences	LTDS	ECL
JEZEQUEL Louis	professeur	LTDS	ECL
JUVE Denyse	ingénieur de recherche	LTDS	ECL
KAPSA Philippe	directeur de recherche	LTDS	CNRS/ECL
LE BOT Alain	chargé de recherche	LTDS	CNRS/ECL
LOUBET Jean-Luc	directeur de recherche	LTDS	CNRS/ECL
MARTIN Jean-Michel	professeur	LTDS	ECL
MATHIA Thomas	directeur de recherche	LTDS	CNRS/ECL
MAZUYER Denis	professeur	LTDS	ECL
PERRET-LIAUDET Joël	maître de conférences	LTDS	ECL
SALVIA Michelle	maître de conférences	LTDS	ECL
SIDOROFF François	professeur	LTDS	ECL
SINOUE Jean-Jacques	maître de conférences	LTDS	ECL

<i>STREMSDOERFER Guy</i>	<i>professeur</i>	LTDS	ECL
<i>THOUVEREZ Fabrice</i>	<i>professeur</i>	LTDS	ECL
<i>TREHEUX Daniel</i>	<i>professeur</i>	LTDS	ECL
<i>VANNES André-Bernard</i>	<i>professeur émérite</i>	LTDS	ECL

Nbre LTDS 25

<i>Total HdR ECL</i>	90
----------------------	----

Della serie: osserva, sperimenta e impara...

ANDREA PAZIENZA

Acknowledgments

Many people have helped me think about and write this dissertation. Among them are Franck, Julie, Valeria and Raphael, who gave me a solution to all my informatics problems.

I am particularly grateful to P. Mejean and N. Grossjean for their help in my experimental activities: they have been really patient with me.

I would like to gratefully acknowledge my supervisors, prof. C. Cancelli and R. Perkins, for their guidance on my research activity, as well as L. Soulhac, for his encouragement and his clear thinking about my work.

Finally I'd like to thank Golder Associate and Fondazione ISI for the fellowship accorded to me in the final year of my PhD.

Abstract

The dispersion of pollutants in the atmosphere in urban areas is a complex process which depends on several physical phenomena. The present work analyzes the mechanisms of the mass and momentum exchange in the urban atmospheric boundary layer. In particular we focused our attention on the lower part of the atmospheric boundary layer, where the flow dynamics are typically determined by the size and the density of the buildings and by the street geometry.

In order to analyze these processes we have performed a wind tunnel investigation of the flow dynamics and scalar dispersion in the near-ground region of a neutral atmospheric boundary layer. An idealized street geometry was simulated by an array of 2D parallel canyons, made of a set of square section bars placed normal to the wind; the spacing of the bars (i.e. the ratio H/W between building height and canyon width) could be varied. The velocity measurements have been performed by means of hot-wire anemometry and Particle Image velocimetry (PIV) whilst passive scalar concentration measurements have been performed with a Flame Ionization Detector (FID).

In the first part of the work we studied the influence of small scale roughness (roof shape, chimney....) at the top of the buildings on the flow and the dispersion in the turbulent stream above buildings roofs. The influence of the roof roughness was studied by adding small scale 2D roughness elements to the tops of the bars. In order to evaluate the mass and momentum exchange in the boundary layer above the obstacles, different experiments were conducted for each geometrical configuration: the profiles of mean and fluctuating velocities were measured above the obstacle roof; a passive scalar was released from an elevated line source and from a ground level source, and concentration profiles were measured downstream of the source. We verified that the presence of a smaller scale roughness is felt by the overlying flow only if the larger scale obstacles are sufficiently packed together. The smaller scale structures produced by the small scale roughness influence the flow dynamics if their size is the same order of that of the eddies shed by the shear layer developing at the canopy top: that happens if the canyon width is not too large (i.e. for street aspect ratio $H/W \sim 1$).

In the second part of the work we focused on the processes that determine the mass exchange between the recirculating region within the street canyons and the external flow. The goal of the study was to evaluate how different conditions within and outside the cavity determine the velocity and concentration fields within the cavity itself; the aim was to find the appropriate reference velocity and length scales that characterize the mass exchange between the recirculating region and the external flow.

We verified that the exchange processes are dependent on the canyon geometry as well as on the intensity of the external turbulence, but are not sensitive to the external integral length scale. As a general conclusion we may say that the mass and momentum exchange between a recirculating region and the external flow is a process which is driven by the flow instabilities, arising within the shear layer which develops at the interface between the two regions, and it is influenced even by the turbulent kinetic energy fluxes from the external flow toward the cavity.

Introduction

The present work fits in a research project that started about 10 years ago by the environmental research group of the Laboratoire de Mécaniques des Fluides et Acoustique of the Ecole Centrale de Lyon. The research concerns air pollution in urban areas.

Air pollution is related historically to industrialization and urbanization. In the 20th century atmospheric pollution concerned mostly air quality in urban areas, except for some regional or continental pollution events (Chernobyl). In the first half of the century the main pollutant factor have been emissions due to combustion of fossil fuels, that were largely used in all cities for both domestic and industrial requirements up to 1950-60. During the last century, the city of London has been subjected to several peaks of pollution until the well known *big smoke*, between 4-10 December 1952. In those days the low wind and the permanence of a strong thermal inversion were responsible of the formation and the stagnation of so much pollution that even healthy people had breath disturbances. This situation caused about 4000 deaths, among people affected by sickly health and pulmonary diseases. To give a halt to this dangerous phenomenon a new law was required, to induce the use of natural gas instead of coal. Since then (the end of the 50'ies) the London smoke, also known as *smog*, has been largely attenuated. In some other cases emissions from industrial plants have been the main responsible for air pollution episodes, which occurred in several industrial district all over the world, such as Pittsburgh in Pennsylvania or the entire Ruhr Region, among the others (McNEILL, 2001). Today car emissions are the most important air pollutant factors (on the city scale) in a large part of cities where air pollution arises, as a combined effect of particular meteorological factors and intense traffic levels. Urban pollution phenomena are usually divided in two major categories:

- in warm climates and insolated areas, where both ultraviolet radiation and pollutant emission (due to hydrocarbons combustion) are high, there are conditions for the formation of *photochemical smog*;
- where the solar radiation is less intense, and pollutant are emitted in a cold and humid environment, formation of secondary particulate matter takes place, the so called *smog*.

Los Angeles, Santiago del Chile and Athens (SCORER, 1968) are well known case studies for photochemical smog, as well as Mexico City, placed at 2000 m above sea level, in a valley with frequent thermal inversions. Paris, New York and Tokyo, in spite of their favorable meteorological conditions, are subjected to air pollution episodes, due to their extension and to the large amount of emissions. In Italy, Turin and Milan (as well as most of the cities in Po valley) suffer for both phenomena. In winter, as a consequence of the lowering of the boundary layer height due to a persisting anticyclonic condition, pollutant emissions are trapped in a surface layer whose depth is a few hundred meters, and the high relative humidity induces secondary particulate production, or *London smog*. In summer time, high temperature and high solar radiation induce formation of photochemical smog. In both cases, persisting low wind regimes make worse and worse conditions, so that concentration peaks registered in a park are not so different from peaks registered near big streets, as shown in fig. 1.

The enhanced process of industrialization and urbanization, led in the XX century to an exponential increase of atmospheric pollution, whose effects have been intensified on the city scale and extend to regional and global scales (green-house effect, stratospheric ozone hole, etc.). However, on the city scale, starting from the 70'ies, air pollution effect have been mitigated for economical, political and geographical reasons. From an economical point of view, the reduction of fuel and natural gas price, as

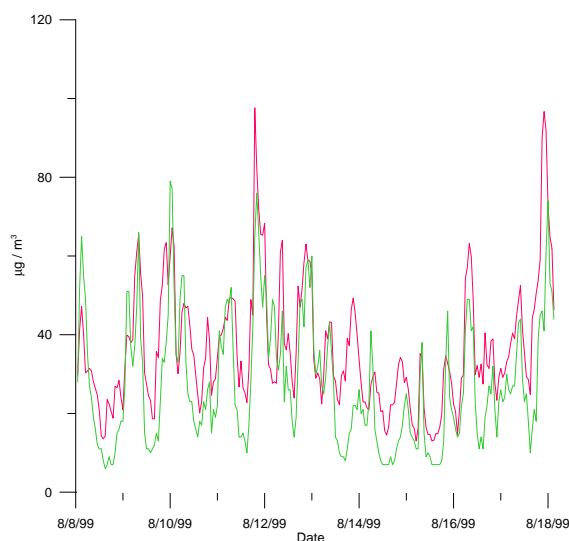


Figure 1: NO_2 concentration in Milan measured in the city centre (red-line) and in Lambro-park (green-line).

a consequence of lower extraction and transportation costs (construction of oil pipelines and huge oil-tanker), induced the substitution of coal as combustible matter for domestic heating and power generation. Less important, however influent, were political effects, due to arising environmental revendication, which induced several governments to adopt legislative restrictions on pollutant emissions¹. Starting from the '60, the distribution of industrial plants began to change. Power and industrial plants, began to be located far away from cities, so that their impact on the surrounding environment and on human health has been progressively reduced. However, even if the pollution level in several cities in Europe and northern America are well below the peak values reached during the XX century, the attention on urban pollution is gradually increased. In the last decades more attention has been devoted to urban pollution, in order to verify monitoring network and to develop computational tools, to simulate pollutant dispersion in urban environment.

The geometry of an urban area can be modelled in different ways in the computational domain, depending on the precision adopted for the description.

On a larger scale, a city can be modelled by means of a limited number of parameters, and can be described as a region with homogeneous properties. When the attention is focused on transport phenomena at smaller scales, as in a city district or in a single street, the geometry of the domain will need a more detailed description. Two types of problems with different spatial and temporal scales are worth mentioning:

- the accidental release of toxic gases within or close to an urban area (Seveso, Tolosa, Bhopal..); the effects of these dispersion processes have to be evaluated on a small time scale, certainly less than

¹In the United States the adoption of unleaded fuel reduced lead concentration in air of about 95 per cent between 1977 and 1994 (MCNEILL, 2001)

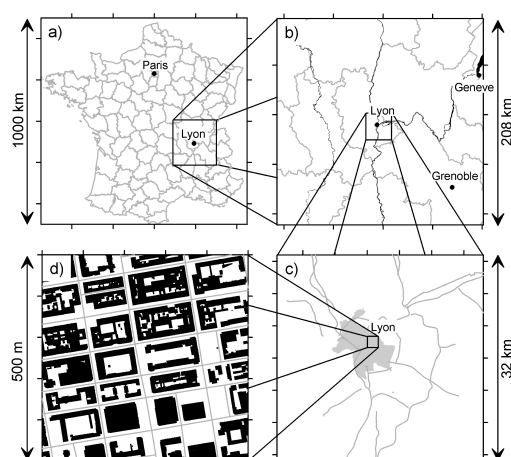


Figure 2: Nested models (SOULHAC *et al.*, 2003).

one hour, and on spatial scales on the range of a hundred to thousand meters. The analysis of the process will require detailed information about urban geometry, while meteorologic conditions can be considered stationary, from a statistical point of view, as long as the pollutant dispersion takes place on a time scale which is smaller than that of weather changes.

- ozone pollution, which is due to photochemical reactions whose time scales are of the order of several hours. During this period the pollutant plume can be advected far away from the emission point, thus involving a bigger region.

The gap between different spatial or temporal scales, which characterize pollutant dispersion in urban area, implies some difficulties in reproducing the pollutant distribution by means of numerical simulations. A technique usually adopted is to use nested models (SOULHAC *et al.*, 2003), refining step by step the detail of the time and spatial resolution on the flow field, using the results of the previous step as boundary condition for the next step (fig. 2). In such a way it is possible to reach a sufficiently detailed description in order to examine pollutant dispersion on a local scale, without excessive computational resources.

The previous examples illustrate that, in order to model flow and dispersion in urban areas, we need to be able to deal with several phenomena. In the present work we study the influence of an urban area on the mass and momentum transfer in a neutral atmospheric boundary layer. In chapter 1 are briefly summarized the basic concepts on the boundary layer dynamics and atmospheric dispersion that we will be using in the present work. In chapter 2 two are exposed the particular aspects of flow and dispersion in urban areas. In chapter 3 are presented the experimental facilities and techniques that we used. In chapter 4 and chapter 5 we focus on some aspects of pollutant dispersion in urban areas that are still not completely understood:

- how to characterize the lower part of the atmospheric boundary layer, where the flow dynamics are typically determined by the size and the density of the buildings and by the street geometry (chapter 4);

- how to parameterize the mass exchange between the recirculating region within the street canyons and the external flow(chapter 5).

In the text we will use x, y, z to denote respectively the longitudinal, transversal and vertical coordinate. u, v, w denote the component of the velocity vector \mathbf{u} (or u_i) along x, y, z . Over bars denote time averages and the variables with a prime sign denote the fluctuations (i.e. $u' = u - \bar{u}$). In the text the mean horizontal velocity component is denoted by a capital letter (i.e. $U = \bar{u}$) as well as the mean concentration of a passive scalar (i.e. $C = \bar{c}$).

ESSENTIALS ON BOUNDARY
LAYER DYNAMICS AND
ATMOSPHERIC DISPERSION

1.1 Introduction

Wall turbulence is a case of inhomogeneous and anisotropic turbulent flow. Much attention has been given on turbulent flow over walls to clarify the role of a rigid boundary on turbulence properties, such as time and length scales of coherent structures, intermittency and anisotropy. A general description of basic properties of wall bounded flow can be found in classical fluid mechanics text books (TENNEKES and LUMLEY, 1972; BATCHELOR, 1967; TRITTON, 1988; HINZE, 1959; TOWNSEND, 1976).

Atmospheric flows obviously deal with flows over rough walls, as it is the earth surface. The research work on flow over rough wall started from the basic knowledge on flows over smooth walls, in order to find differences and analogies between the two, i.e. showing which characteristics of the flow field were altered by the presence of the wall roughness and how some aspect of the flow could be inferred as universal properties of wall flow. The effect of wall roughness has an evident interest for engineering (pipes and channels) as well as for meteorological studies. Monographic works on the atmospheric boundary layer have appeared since 1960 starting from the books of LUMLEY and PANOFSKY (1964), PANOSKY and DUTTON (1984), KAIMAL and FINNIGAN (1994), among the others.

In this chapter we first focus our attention on the basic hypothesis that lead to the similarity theory for a neutral boundary layer (Par. 1.2) for smooth and rough walls. We will then briefly expose the extension of the theory (Par 1.3), in case of non-neutral stratification, and its shortcomings (Par 1.4), that arise from experimental evidences.

The last paragraph (Par 1.5) contains a recall of the fundamental concepts of turbulent dispersion that will be used in this work.

1.2 Similarity theory of a neutral boundary layer

It is generally assumed that the turbulent velocity field in the atmospheric boundary layer can be divided into different regions, and that the flow in each region can be described by some form of similarity solution, if appropriate scales are chosen. It is then possible to compute the flow for any given situation, once measurements of these scales have been made.

In rough wall-bounded flows with negligible thermal fluxes, it is usually assumed that there is a region in the lower part of the boundary layer where the mean flow can be described reasonably well by a logarithmic law:

$$\frac{U}{u_*} = \frac{1}{\kappa} \ln \left(\frac{z}{z_0} \right) \quad (1.1)$$

where $u_* = (-\overline{u'w'})^{1/2}$ is the friction velocity, κ is the *Von Karman constant* and z_0 is the *roughness length*. It is worth noting that in eq.1.1 the mean velocity U depends on the vertical coordinate z only: this implies the assumption of homogeneity of the flow field on the horizontal planes.

The relation 1.1 can be obtained in different ways, considering the region of its validity as:

- a ‘constant stress’ layer;
- a buffer layer between the outer and the inner part of the flow field;
- a ‘local equilibrium’ layer.

The log-law can be therefore reached in different ways, by keeping however two essential hypothesis:

1. that flow is homogeneous in the horizontal planes and that the only relevant length scale in this region is z , the distance from the wall;
2. that the fluctuating velocity field has only one velocity scale, to which all velocity components are proportional, no matter how they are defined.

1.2.1 The log-law region as the ‘constant stress’ layer

Starting from an empirical point of view we can note that vertical profiles of flow variables show different behaviours departing from the wall toward the outer edge of the boundary layer. The mean velocity U varies from zero to values close to U_∞ (the mean velocity outside the boundary layer) over a relatively short distance, whilst the Reynolds stresses varies so slowly over the same distance that it can be considered effectively constant. In other words we can assert that the condition

$$-\rho \overline{u'w'} = \rho u_*^2 = \text{const}$$

is consistent with a rapid variation of U .

In addition to this first step, which is based on an experimental evidence, we need to make a further assumption, that the tangential stresses can be expressed as a function of the gradient of the mean velocity, through the use of the *kinematic eddy viscosity* ν_t

$$-\rho \overline{u'w'} = \rho u_*^2 = \rho \nu_t \frac{dU}{dz}$$

The kinematic eddy viscosity ν_t is a typical diffusion coefficient whose physical dimension is given by the product of a velocity and a length scale:

$$\nu_t \sim \sigma_u l \tag{1.2}$$

where σ_u and l are two parameters describing the fluctuating part of the flow field, and are related to the turbulence intensity and to the linear dimension of the coherent turbulent structures. Once we have chosen u_* and z as reference velocity and length scale, we can write:

$$\sigma_u = k_1 u_*$$

$$l = k_2 z$$

where k_1 and k_2 are two unknown constants. Substituting these relations into 1.2 we obtain:

$$\frac{dU}{dz} = \frac{u_*}{\kappa z} \tag{1.3}$$

where the symbol $\kappa = k_1 k_2$. Integrating 1.3 we obtain the logarithmic law 1.1.

The length z_o , named *roughness length*, is a constant of integration: strictly speaking, the height at which the mean velocity would reach zero, assuming equation 1.1 to be valid down to the wall level. In this description the wall influence is thus reflected in one scalar only - this follows directly from the assumption that the flow can be considered homogeneous in the planes $x - y$.

1.2.2 The log-law region as a ‘buffer’ layer

Several authors obtained the logarithmic law, which can be seen as an application of the Prandtl’s *mixing length theory* - a general theory of turbulent transport in which turbulence is assumed to act in a way similar to molecular diffusion².

The logarithmic law has been shown to agree well with a range of experimental data and has long been considered a successful result of the theory. Anyway the solidity of the log-law is due to more general and abstract reasons. In fact, among the three previous hypothesis, the only essential proposition deal with the existence of a region in the flow field, where the only significative length scale is z , the distance from the wall, and the only significative velocity scale is u_* , the friction velocity. Once accepted this statement, we can reach the log-law in different ways, even through a simple dimensional consideration: based on dimensional reasoning, the right hand side of 1.3 is the only relation, correct from a dimensional point of view, that we can drive assuming that the two relevant scales u_* and z .

The assertion that in the log-law region there are only two relevant length scales has some important implications. The flow field we are considering is determined on the top by a velocity U_∞ , imposed at height δ (the boundary layer height), and is limited at the bottom by the presence of a rigid surface which imposes the no-slip condition: $U = 0$. The solid boundary, in case of rough wall, is characterized by a typical length h_s , known as *effective roughness length*. We will focus later on that, here we just want to mention that whilst h_s (as z_0) have the dimension of length and represent the effect of wall roughness, they can not be interpreted directly as the height of the roughness elements (denoted here with H) because the effect of wall roughness depends also on the spacing, orientation and organization of roughness elements.

The assumption that in a region of the flow the only relevant length scale is the distance z from the wall, is equivalent to assume that, in this region, δ and h_s do not have any influence on the dynamics. The log-law region is therefore an intermediate region whose dynamics are determined by turbulent structures which are big enough not to be influenced by h_s and too small to be influenced by the whole boundary layer height δ . There is an evident analogy between the log-law region for wall bounded turbulent flows and the inertial domain of the homogeneous and isotropic turbulence³. Both domains are obtained from a decomposition of the flow field, the former in the physical space and the latter in the wave-number space; both of them are characterized by typical length scales which are much smaller than the external scale and much bigger than the smallest scale of the flow, hence independent of them both.

When considering flow over a smooth wall, we can replace the effective roughness length by the viscous length scale: $\varepsilon = \nu/u_*$, obtaining an even stricter analogy. The existence of the intermediate region requires that the inner and the outer scales should be separated by several orders of magnitude, i.e. $\delta \gg h_s$.

These considerations provide the basis of the *boundary layer theory*⁴, a description of the boundary layer which relies on universal relations. Briefly, the global parameters that define the flow field are the boundary layer height δ , the effective roughness length h_s , and the velocity U_∞ imposed at the edge of the boundary layer⁵. We assume also that viscous effects are negligible, which means that we are not

²We may remember that this analogy - between the effects of molecular motion and the effects of the fluctuating motion of the fluid particles - reveals its main limit in the momentum transfer description, as far as momentum is not transferred unaltered by advection from a region to another of the flow field.

³This is the reason why the log-law region is usually called the *inertial layer* BLACKADAR and TENNEKES (1968).

⁴First introduced by MILLIKAN (1939), these arguments provided the basis for the mathematical theory of the of multi-scale analysis SCHLICHTING (1968).

⁵Referring to the atmospheric boundary layer and neglecting thermal effects, we can assume that the outer velocity U_∞

interested in describing the dissipative scales in the core of the flow and that the viscous region near the wall is assumed to be much smaller than h_s , as it is for the earth surface. On the basis of these assertions, we can write:

$$\frac{U(z)}{U_\infty} = g\left(\frac{z}{\delta}; \frac{\delta}{h_s}\right)$$

Whilst this is clearly a correct relation from a dimensional point of view but it is not realistic to assume that a single law can describe the whole flow field, given that the local scales in different regions depend on very different phenomena. In the region near the wall - the so called *inner region* - the natural choice for the geometrical scale seems to be h_s , and not δ . On the other hand, a more appropriate scale for the mean velocity gradient seems to be the friction velocity u_* , since the velocity variations with the distance from the wall are directly related to the fluctuating velocities of the fluid particles. The friction velocity is not an independent variable, it can be considered as imposed by U_∞ and by the two geometrical scales of the problem; in normalized form we set:

$$\frac{u_*}{U_\infty} = g_1\left(\frac{\delta}{h_s}\right) \quad (1.4)$$

Proceeding in that way, we can give a description of the whole boundary layer with different relations for different regions of the flow. For the inner region we can set ⁶:

$$\frac{U}{u_*} = g_{in}\left(\frac{z}{h_s}; \frac{\delta}{h_s}\right) \quad (1.5)$$

while, for the outer region, the relation will be:

$$\frac{U}{u_*} = g_{ex}\left(\frac{z}{\delta}; \frac{\delta}{h_s}\right) \quad (1.6)$$

It is evident that, between the inner and the outer layers, a buffer layer is needed where both solutions apply. The mathematical procedure to connect these two solutions is usually called *asymptotic matching*. We consider the problem in the limit⁷ $\delta/h_s \rightarrow \infty$. If this limit exists, 1.4, 1.5 and 1.6 become universal relations. We then obtain:

$$\frac{u_*}{U_\infty} = const \quad (1.7)$$

$$\frac{U}{u_*} = g_{in}(\zeta) \quad (1.8)$$

is determined by the geostrophic wind U_g :

$$U_\infty = U_g$$

and set:

$$\delta = \frac{U_g}{f}$$

where $f = 2\Omega \sin\varphi$ is the Coriolis parameter, Ω is the angular velocity of the earth and φ is the latitude.

⁶The law for the velocity variation for the outer part is usually written as:

$$\frac{U - U_\infty}{u_*} = g_{ex}\left(\frac{z}{\delta}; \frac{\delta}{h_s}\right)$$

and is called *velocity defect law*.

⁷Asymptotic procedures are a useful mathematical tool in the case that real physical phenomena are supposed to evolve sufficiently close to the limit conditions.

$$\frac{U}{u_*} = g_{ex}(\eta) \quad (1.9)$$

where we have introduced $\zeta = z/h_s$ $\eta = z/\delta$, the inner and the outer normalized vertical coordinates. The simplest way to achieve the asymptotic matching between 1.8 and 1.9 is to impose that, in the intermediate region, both expressions have the same slope:

$$u_* \frac{dg_{in}}{d\zeta} \frac{d\zeta}{dz} = u_* \frac{dg_{ex}}{d\eta} \frac{d\eta}{dz} = \frac{dU}{dz}$$

in the double limit $\eta \rightarrow 0$ and $\zeta \rightarrow \infty$. The choice reflects a concept that has been used in several domains since the beginning of the 20th century: the idea that what something very large at a microscopical scale can be seen as a simple spot in a macroscopical scale. Going back to the previous relation:

$$\frac{1}{h_s} \frac{dg_{in}}{d\zeta} = \frac{1}{\delta} \frac{dg_{ex}}{d\eta}$$

and multiplying both sides by z we have:

$$\zeta \frac{dg_{in}}{d\zeta} = \eta \frac{dg_{ex}}{d\eta}$$

In order that the first limit exists for $\zeta \rightarrow \infty$, it is necessary that for large values of ζ we have:

$$\zeta \frac{dg_{in}}{d\zeta} = \text{const}$$

Substituting, we obtain, once again, the log law.

In case of *smooth walls*, we can choose a viscous length scale ν/u_* so that the log law is written as

$$\frac{U(z)}{u_*} = \frac{1}{k} \ln z^+ + A \quad (1.10)$$

where $z^+ = z * u_*/\nu$ is known as wall unit. The integration constant A takes, values between 5,1 (RAUPACH *et al.*, 1991) and 6,2 (WOSNIK *et al.*, 2000; POGGI *et al.*, 2003).

The presence of roughness elements alters the nature of the wall flow, as a function of their dimension and density. The wall may be considered *rough* as soon as there are some geometrical irregularities on it which are of the same order of a few wall units. The knowledge of a dynamical effect of roughness in wall bounded flows arised historically from the evidence of a defect in the mean velocity profile if compared to that of smooth wall flows ⁸(NIKURADSE, 1933; CLAUSER, 1956). Nikuradse described first the effect of wall roughness by changing the A constant (eq. 1.10); he introduced a new inner variable scaled on h_s (NIKURADSE, 1933), which is the already mentioned “*equivalent*” (or “*effective*”) *roughness length*

$$\frac{U(z)}{u_*} = \frac{1}{k} \ln(z/h_s) + 8.5 \quad (1.11)$$

As mentioned before, both z_0 and h_s are not the roughness element height but are function of the geometry and the orientation of roughness elements. As first approximation we can assume that $z_0 \sim 0.033h_s$ (JIMÉNEZ, 2004).

⁸This is not an absolute rule, since some particular rough surfaces allow a drag reduction. The most evident case is the flow over *ribblets* which are narrow grooves aligned with the flow direction (WALSH, 1990).

Otherwise, maintaining the constant A , it is also usual to take account of the defect of the mean velocity profile introducing the *roughness function* ΔU

$$\frac{U(z)}{u_*} = \frac{1}{k} \ln(z_+) + A + \frac{\Delta U}{u_*} \quad (1.12)$$

or by using the roughness length z_0

$$\frac{U(z)}{u_*} = \frac{1}{k} \ln(z/z_0) \quad (1.13)$$

The three quantities h_s , ΔU and z_0 characterize the roughness interchangeably; they are all measures of the wall resistance to the flow stream⁹. The first is common in engineering application (pipes, channels...), the second in wind tunnel research and the third in meteorology.

1.2.3 The log-law region as the ‘local equilibrium’ layer

The arguments we exposed establish the essentials for the so called *wall similarity* proposed by TOWNSEND (1976) in analogy with the well known asymptotic similarity of incompressible flows. The latter states that geometrically similar flow may reach similar dynamical conditions not only if their respective Reynolds number are the same, but also if their respective Reynolds number are large enough, i.e. $Re \rightarrow \infty$. The *wall similarity* states that turbulent motion above the roughness (or viscous) sub-layer, provided a sufficiently large Reynolds number, depends only on u_* , δ and z .

By transposing the previous concepts from a mere scale analysis to a energy balance point of view, we reach the concept of *equilibrium layer* (TOWNSEND, 1976), which has become a consolidated argument in turbulent wall flows research. Townsend started from the same empirical consideration we exposed at the beginning of this paragraph, from the evidence that in a *small* region adjacent to the wall:

- total shear stress are nearly constant
- the large part of the mean velocity variation is concentrated.

⁹A composite relation, valid for the whole boundary layer, is obtained by introducing the so called *wake function* $W(z/\delta)$, that takes account of the effects of the outer structures on the mean velocity profile. For smooth walls we have

$$\frac{U(z)}{u_*} = \frac{1}{k} \ln z^+ + A + k^{-1} \Pi W(z/\delta) \quad (1.14)$$

and for rough wall

$$\frac{U(z)}{u_*} = \frac{u_*}{k} \ln(z^+) + A + k^{-1} \Pi W(z/\delta) - \frac{\Delta U}{u_*} \quad (1.15)$$

where Π is a constant, named *wake strength*; procedures to evaluate the wake function and wake strength could be found in works by HAMA (1954), GRANVILLE (1976) or KROGSTAD et al. (1992) among the others. It is worth noting that 1.14 and 1.15 are empirical relations that violate the similarity condition, as long they are built using different length scales. Those relations are usual in engineering applications (pipes and channels), as well as in wind tunnel research, for self developing boundary layers. However that is not the case in meteorology studies.



Figure 1.1: Shear mixing layer

By writing the turbulent kinetic energy budget for the energy of an incompressible flow, neglecting heat transfer, and with the usual boundary layer approximation, we obtain the following equation:

$$U \frac{\partial \overline{q^2}}{\partial x} + W \frac{\partial \overline{q^2}}{\partial z} = -\overline{u'w'} \frac{\partial U}{\partial z} - \frac{\partial \overline{wq^2}/2}{\partial z} - \frac{\partial \overline{wp}}{\partial z} - \epsilon \quad (1.16)$$

The conclusion we reached already by means of a scale analysis can be deduced by 1.16 as well, if we assume that in the energy equation the production and the dissipation terms are by far more important than flux terms. Neglecting flux terms, we can write 1.16 as:

$$\overline{u'w'} \frac{\partial U}{\partial z} + \epsilon = 0 \quad (1.17)$$

If we consider as usual that the only relevant scales are the friction velocity u_* and the distance from the wall z , we can first evaluate the dissipation term

$$\epsilon = \frac{u_*^3}{\kappa z}$$

and then, by 1.17, obtain once again the equation 1.3, the differential form of the log-law of the wall:

$$\frac{dU}{dz} = \frac{u_*}{\kappa z}$$

Townsend emphasized how these arguments, that he presented for a flow in a two dimensional channel, are valid for whatever flow in which the assumption of *local equilibrium* is satisfied, such as boundary layer flows.

Another important case, relevant to this thesis, is a *shear mixing layer* (fig. 1.1), a region which develops between two parallel flows with different mean velocities (RAJARATNAM, 1976). In these cases, the flows can be considered to have an *autonomous* dynamics.

1.3 Extension of the similarity theory

Even if this work will not deal with thermal fluxes, for the sake of completeness on the description of the boundary layer theory, we give a brief recall on the way the theory is extended, in order to take account of thermal fluxes.

Thermal fluxes between earth and atmosphere alter radically the structure of the planetary boundary layer, whose depth δ varies periodically during the day ¹⁰.

¹⁰The time dependence of δ does not have an effect on the structure of the turbulent flow field, as long as the process can be considered pseudo-stationary, i.e. as a succession of configuration that are in dynamical equilibrium.

The physical parameters that influence the flow field are the already mentioned variables - δ , h_s (or z_o), u_* (or U_∞) - and the convective thermal flux F_c .

To take in account the effect of this term on the boundary layer structure, Monin and Obukhov proposed an extension of the similarity theory (MONIN and ОБУКHOV, 1954), by introducing a new length scale - \mathcal{H} , named Monin-Obukhov height.

The Monin-Obukhov height is defined as the distance from the wall at which the thermal production¹¹ of turbulent kinetic energy equals the mechanical production. That new scale allows to take into account the effect of F_c on the functions that describe the flow field, and to keep an invariant description of it.

a) Below Monin - Obukhov height, for

$$z < | \mathcal{H} |$$

in the *surface layer*, the characteristic scales are:

- as length scale \mathcal{H} ¹²;
- the friction velocity u_* as velocity scale;
- a temperature scale¹³

$$\Theta_* = - \frac{\langle w \Delta \Theta \rangle}{u_*}$$

where $\Delta \Theta$ denotes potential temperature fluctuations from a mean value Θ_0 .

The laws of vertical variation of flow variables can be expressed, within the domain $z < | \mathcal{H} |$, in an invariant form as a function of the normalized variable $\varsigma = \frac{z}{\mathcal{H}}$.

For the vertical variation of the mean velocity we have

$$\frac{\kappa z}{u_*} \frac{dU}{dz} = \Phi(\varsigma)$$

whereas for the potential temperature we have:

$$\frac{\kappa z}{u_*} \frac{d\Theta}{dz} = \Psi(\varsigma)$$

In a neutral atmosphere $| \mathcal{H} | \rightarrow \infty$, the universal functions $\Psi(\varsigma)$ and $\Phi(\varsigma)$ are equal to 1. In a stable or instable atmosphere these function are defined by means of empirical function (BUSINGER *et al.*, 1971), (DYER, 1974):

$$\begin{cases} \Phi(\varsigma) = \sqrt{\Psi} = (1 - 16\varsigma)^{-1/4} & \text{if } | \mathcal{H} | < 0 \text{ instable atmosphere} \\ \Phi(\varsigma) = \Psi = 1 + 5\varsigma & \text{if } | \mathcal{H} | > 0 \text{ stable atmosphere} \end{cases}$$

b) Above Monin - Obukhov height, for

$$| \mathcal{H} | < z < \delta$$

¹¹The so called *thermal production term* is a term which arises from the power of buoyancy forces, due to density variations; as the density variations are linked to temperature variations through the Boussinesq approximation, the thermal flux comes in.

¹² $\mathcal{H} > 0$ when F_c is directed toward the wall (stable condition).

¹³ $\Theta_* > 0$ when F_c is directed toward the wall (stable condition).

we have to distinguish between stable ($F_c < 0$) and unstable ($F_c > 0$) cases. In stable atmosphere the turbulent motion is damped and the boundary layer depth can be considered $\delta \sim \mathcal{H}$. For high values of ς , the universal functions Φ and Ψ tends to be equal to:

$$\Phi \propto \varsigma$$

$$\Psi \propto \varsigma$$

which implies a constant gradient with height of mean variables, as long as $\varsigma = z/\mathcal{H}$,

$$\frac{dU}{dz} \sim \frac{u_*}{\mathcal{H}}$$

$$\frac{d\Theta}{dz} \sim \frac{\Theta_*}{\mathcal{H}}$$

which is a typical behaviour of laminar flows.

In the unstable case, with ($F_c > 0$), the boundary layer develops well above $|\mathcal{H}|$, where a region called *convective layer* (or *well mixed region*) takes place. The dynamics of this region, for $|\mathcal{H}| < z < \delta$, tends to be independent from the typical variables that influence the surface layer, u_* and z_o . If the ratio $\delta/|\mathcal{H}|$ is sufficiently large, experimental data of flow variables of the convective layer collapse in one universal curve, through the adoption of the following scales:

- the boundary layer depth δ , as length scale
- the convective velocity, as velocity scale

$$u_c = \left(\delta g \frac{\langle w \Delta \Theta \rangle}{\Theta} \right)^{\frac{1}{3}}$$

- a temperature scale, defined as:

$$\Theta_c = \frac{\langle w \Delta \Theta \rangle}{u_c}$$

Experimental data on the convective layer are lacking in comparison to those of surface region, and they do not always agree with Monin - Obukhov theory. Results obtained by WILLIS and DEARDORFF (1976) in wind tunnel, and by DEARDORFF (1972) by means of numerical simulations¹⁴, show good agreement with theoretical results, given that

$$\frac{\delta}{|\mathcal{H}|} > 10$$

and that

$$\frac{u_c}{U_\infty} > 0.15 \div 0.2$$

¹⁴For a complete bibliography on this topics see CAUGHEY (1984).

1.4 Short-comings of the similarity theory

The separation of the boundary layer in autonomous regions, whose dynamics follows universal laws, is a simplification of reality which has not always been confirmed by experimental data. Asymptotical conditions, as well as simple geometrical configurations, are required for the theory to apply. This is not always the case. However, even if asymptotical conditions $\delta/h_s \rightarrow \infty$ is approached, a limitation of the similarity theory is shown by the experimental evidence that flows with same u_* and different turbulent intensity $i = \sigma_u/U$ occur (TOWNSEND, 1976).

That can be explained by assuming that some eddies do not contribute to the momentum transfer in the vertical direction. The friction velocity u_* therefore, which was supposed to be the only velocity scale for the whole flow field, is not a scale for the turbulent kinetic energy, i.e. for

$$\frac{\sigma_u^2 + \sigma_w^2}{u_*^2}$$

In order to explain that feature, Townsend stated another assumption, the *attached eddy hypothesis*. He described the turbulent motion in the inner layer as a random superposition of eddies, whose diameter are proportional to the wall distance z , and whose velocity distribution could be expressed as

$$u_i(\mathbf{x}) = u_0 f_i[(\mathbf{x} - \mathbf{x}_a)/z_a]$$

where $\mathbf{x}_a = (x_a, y_a, z_a)$ is the centre of a particular eddy. By imposing a no-slip condition on f_i to account for the presence of the wall, and considering uniform Reynolds stress in the domain, he obtained the following relations:

$$\begin{aligned} \frac{\sigma_u}{u_*} &= C_1 + D_1 \log z_l/z \\ \frac{\sigma_v}{u_*} &= C_2 + D_2 \log z_l/z \\ \frac{\sigma_w}{u_*} &= C_3 \end{aligned}$$

Townsend commented upon his results in the following way (TOWNSEND, 1976, pp 153-154):

“It now appears that similarity of the motion is not possible with attached eddies and, in particular, that the stress-intensity ratio, $-\overline{u'w'}/q^2$, depends to some extent on position in the layer. The variation of the ratio does not invalidate the previous similarity analysis because the ‘non-similar’ logarithmic terms in the expression for σ_u and σ_v represent motions which are large-scale swirling in planes parallel to the wall and do not extract energy from the mean flow or affect the rate of energy transfer to smaller eddies for viscous dissipation. Swirling motions contribute little to Reynolds stress, and their effect on that part of the layer between the point of observation and the wall is one of slow random variations of ‘mean velocity’ which cause corresponding variations of wall stress. It is possible and useful to regard the ‘swirl’ component of local motion as an *inactive* component which may be ignored in any discussion of the local flow, for example when using similarity assumption to interpret the turbulent energy equation as an equation for Reynolds stress”.

Other experimental results invalidate the assumption of *wall similarity*, which states that the turbulence structures should be unchanged in the inertial and in the external regions by roughness effect, if not for modifications of the wall geometry that would alter the mean stream lines. In terms of turbulence

structures, works by ANTONIA and KROGSTAD (2001; 1999) show that roughness effects are not confined in the wall region only, and that normalized statistical moments of the component of the fluctuating flow field differ significantly from smooth to rough walls.

1.5 Lineaments of turbulent dispersion

The transport of a passive scalar within the turbulent flow field is described by the *advection-diffusion* equation

$$\frac{\partial c_t}{\partial t} = -\frac{\partial}{\partial x_j} \left((u_t)_j c_t - D_m \frac{\partial c_t}{\partial x_j} \right) \quad (1.18)$$

where $c_t(x, y, z, t)$ and $u_t(x, y, z, t)$ are instantaneous scalar concentration and wind velocity, and D_m is the molecular diffusion coefficient.

By applying the Reynolds average operator (in this paragraph the over-line and capital letter will denote ensemble averages) and neglecting molecular diffusion, equation 1.18 becomes

$$\frac{\partial C}{\partial t} = -\frac{\partial}{\partial x_j} (\overline{u_j c} + U_j C) \quad (1.19)$$

where $\overline{u_j c}$ is the turbulent flux of the passive scalar and C is the mean scalar concentration.

Equations 1.18 and 4.4 can be written in another way, the former as:

$$\frac{dc_t}{dt} = \frac{\partial}{\partial x_j} \left(D_m \frac{\partial c_t}{\partial x_j} \right) \quad (1.20)$$

through the continuity equation

$$\frac{(\partial u_t)_j}{\partial x_j} = 0$$

and the latter as:

$$\frac{DC}{Dt} = -\frac{\partial}{\partial x_j} (\overline{u_j c}) \quad (1.21)$$

through the averaged continuity equation

$$\frac{\partial U_j}{\partial x_j} = 0$$

In equation 1.20 $\frac{d}{dt}$ indicates the usual material derivative:

$$\frac{d}{dt} = \frac{\partial}{\partial t} + (u_t)_j \frac{\partial}{\partial x_j}$$

while in equation 1.21

$$\frac{D}{Dt} = \frac{\partial}{\partial t} + U_j \frac{\partial}{\partial x_j}$$

indicates the derivative with respect to time of a variable measured by means of an instrument moving within the fluid with the mean velocity U_j .

A comparison between 1.20 and 1.21 allows to grasp an analogy firstly pointed out by Boussinesq (BOUSSINESQ, 1897), between the effect of thermal motion of molecules on the instantaneous concentration c_t of a scalar field, in a single realization of the process, and the effect of the turbulent flux $\overline{u_j c}$ - expressed by the correlation of the fluctuating part of the velocity field and of the fluctuating part of the scalar field - on the averaged concentration C . Averaged concentration changes because of the divergence of turbulent fluxes (HUNT, 1985).

In mathematical terms, as long as the tensor $\overline{u_j c}$ is unknown, equation 1.21 can not be solved, and the whole problem of turbulent dispersion appears underdetermined. The previous analogy suggests to relate the unknown tensor to the other variables, already presented in our problems, by means of a Fick law

$$\overline{u_j c} = -K_{ji} \frac{\partial C}{\partial x_i} \quad (1.22)$$

where K_{ji} , the turbulent diffusion tensor, depends on the lineaments of the fluctuating part of the velocity field, and is generally varying with time and space coordinates. The assumption 4.7 is the simplest way of treating the mathematical problem, posed by equation 1.21, which is often referred to as the *closure problem*; it can be shown that 4.7 establishes too strict a link between the molecular thermal motion and the turbulent fluctuation, but it is commonly used. By assuming Fick's closure the advection-diffusion equation 1.21 becomes

$$\frac{\partial C}{\partial t} = -\frac{\partial}{\partial x_j} \left(-K_{ji} \frac{\partial C}{\partial x_i} - U_j C \right) \quad (1.23)$$

A solution to 1.23 is given by the gaussian distribution

$$C(x, y, z) = \frac{\dot{M}_q}{2\pi\sigma_y\sigma_z U} \exp\left(-\frac{y^2}{2\sigma_y^2}\right) \exp\left(-\frac{z^2}{2\sigma_z^2}\right) \quad (1.24)$$

which describes the spatial evolution of the passive scalar concentration, in the case that the following conditions can be accepted:

- a) the flow is stationary in statistical terms
- b) the mean concentration C is due to a source point of intensity \dot{M}_q (kg/s)
- c) the mean flow field is homogeneous

$$U = \text{const}$$

$$V = W = 0$$

d) the fluctuating field is homogeneous and x, y and z are the principal directions of the tensor K_{ji} , which can be written as

$$\begin{bmatrix} K_{xx} & 0 & 0 \\ 0 & K_{yy} & 0 \\ 0 & 0 & K_{yy} \end{bmatrix}$$

being K_{jj} independent from the time and the spatial coordinates.

e) the turbulent mass flux in the stream-wise direction x is negligible in comparison to the flux of the mean motion, i.e.

$$UC \gg \bar{u}c$$

In that case the standard deviations of the gaussian curves are given by $\sigma_z = \sqrt{2K_{zz}t}$ and $\sigma_y = \sqrt{2K_{yy}t}$.

In order to have a better estimate of the scalar concentration field one can give a finer parametrization of the tensor K , or introduce a higher-order closure hypothesis.

The physical meaning of the zero-order approximation - the Fick law - may be enlightened by a lagrangian approach to the same problem. Actually, equation 1.21 can be thought as directly obtained by averaging an ensemble of realizations, each of them ruled by the pure convective equation:

$$\frac{\partial c_t}{\partial t} = -\frac{\partial}{\partial x_j} ((u_t)_j c_t) \quad (1.25)$$

whose solution is:

$$c_t = \text{const.}$$

along the trajectory

$$d\mathcal{Y}_i = \mathcal{V}_i dt$$

where \mathcal{Y}_i indicates the displacement and \mathcal{V}_i the lagrangian function of velocity of the fluid particles. It appears that the process we name turbulent dispersion is given by a statistical averaging of a class of trajectories of fluid elements, that are wandering in space because of the stochastic nature of the velocity field, each of them keeping an invariant quantity - a sort of quantum of contaminant. The process can therefore be modelled by reproducing a large number of trajectories with the same statistical features of the actual ones, and the concentration can be computed simply by counting the number of end points of the trajectories in every volume cell. TAYLOR (1921) gave a first account of the lineaments of the lagrangian dispersion. We can consider a stochastic homogeneous motion in the \mathcal{Y} direction with statistical structure given by the lagrangian autocorrelation function:

$$\overline{\mathcal{V}(t)\mathcal{V}(t+\tau)} = L(\tau)\sigma_{\mathcal{V}}^2$$

where $L(\tau)$ is the autocorrelation coefficient, and $\sigma_{\mathcal{V}}^2$ is the variance of lagrangian velocities. The coefficient $L(\tau)$ varies only with the time delay τ because of the supposed stationarity of the process, in a statistical sense; it is equal to 1 for $\tau = 0$, as obvious, and goes to zero for a finite value of τ .

Now, if we have an ensemble of particles, emitted at the same point, we can compute the time variation of $\overline{\mathcal{Y}^2}$, the variance of the particle distribution along the \mathcal{Y} axis. We write:

$$\frac{d\overline{\mathcal{Y}^2}}{dt} = 2\sigma_{\mathcal{V}}^2 \int_0^t L(\tau) d\tau$$

Integrating the previous equation we obtain the *Taylor equation* (TAYLOR, 1935):

$$\overline{\mathcal{Y}^2} = \sigma_{\mathcal{Y}}^2(T) = 2\sigma_{\mathcal{V}}^2 \int_0^T \int_0^t L(\tau) d\tau dt \quad (1.26)$$

where T is the flight time of fluid particles since the instant they were emitted. The equation 1.26 allows to relate the time evolution of the size of a pollutant puff to the statistical properties of the turbulent flow field.

To examine the asymptotical behaviour of σ_y , we consider the properties of the function $L(\tau)$:

$$\begin{cases} L(0) = 1 \\ \int_0^\infty L(\tau) d\tau = T_L \end{cases}$$

where T_L is the lagrangian macro scale. It is then possible to show that

$$\begin{cases} T \ll T_L & \Rightarrow \sigma_y^2 \sim \sigma_y^2 T^2 \\ T \gg T_L & \Rightarrow \sigma_y^2 \sim 2\sigma_y^2 T_L T \end{cases}$$

For a short dispersion time, the puff size is proportional to T , whereas for a very long time the puff size tends to be proportional to \sqrt{T} .

Through a comparison of those results with the properties of equations 1.21 and 4.7, it can be guessed that the Fick's approximation gives a faithful description of the process in the limit :

$$\frac{T}{T_L} \rightarrow \infty$$

The dispersion model based on turbulent diffusion coefficient

$$K_y = \sigma_y^2 T_L$$

represent actually asymptotic solutions of the dispersion problem.

FLOW AND DISPERSION IN URBAN AREAS

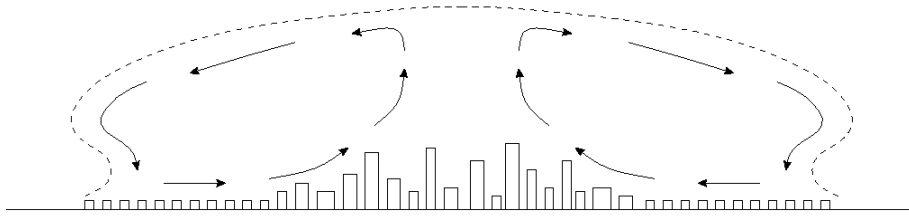


Figure 2.1: Diurnal circulation above a town for low wind speed (OKE,1979).

2.1 Introduction

In a general way pollutant dispersion in the atmosphere can be easily modelled (in a statistical sense) when it takes place in a region where the earth surface can be represented as flat terrain whose geometrical irregularities are supposed to be homogeneously distributed all over the domain. Things become more complicated when the earth surface is occupied by obstacles (due to the orography or to the presence of buildings) and its geometry can not be reduced to the previous simplified representation. The presence of obstacles influence the stream lines orientation of the mean flow as well as the turbulent fluctuations, i.e. the pollutant dispersion. In this chapter we give an overview of the peculiar aspects of air pollution in urban areas, that make it a complex matter, if compared to other air pollution processes.

2.2 Urban climatology

Urbanization alters radically earth surface properties, changing heat, mass and momentum transfer between the soil and the atmosphere. A flow coming from a rural area feels the altered surface boundary conditions; in terms of momentum exchange, the presence of buildings enhances surface roughness; in terms of heat and moisture exchange, an urban area is a region with particular microclimatic characteristics, related to urban geometry and human activities.

The most evident phenomenon is a presence of the so called *heat island* (OKE, 1988a), a limited region above the city with increased air temperature compared to surroundings rural and suburban areas. In most of big cities the temperature excursion can reach, in the early morning, about $4 \div 5 \text{ }^\circ\text{C}$ (LANDSBERG, 1981). There are many processes which induce the heat island effect in cities:

- the solar radiation absorption is increased because of the *albedo* of building materials (cement, plastic materials, asphalt, glasses)¹⁵ which is smaller than the albedo of soil and vegetation in rural areas (DABBERDT and DAVIS, 1978). Furthermore the incident radiation absorption is enhanced by multiple reflection due to the high building density;
- evaporation and transpiration, due to the presence of vegetation, are reduced, as well as evaporation and transpiration of the soil, in reason of the drainage of meteoric water;

¹⁵The *albedo* of a surface is the ratio between radiating energy reflected and incident on it.

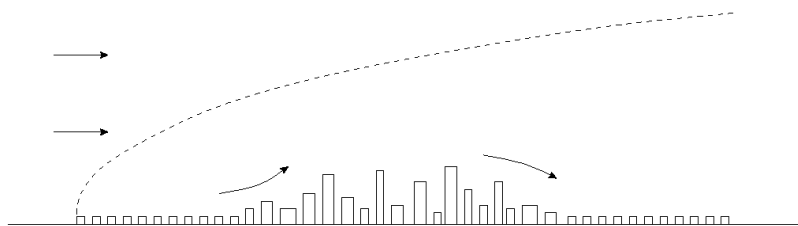


Figure 2.2: Diurnal circulation above a town for higher wind speed (OKE,1979).

- convective fluxes of heat toward the atmosphere are limited for the presence of recirculating regions within the urban canopy, while the wind mean velocities are reduced as a consequence of the increased aerodynamic drag;
- there are several heat sources related to human activities;
- infrared radiation, emitted at ground level, is partially reflected toward the earth surface by the pollutant cloud overlying the urban area (local green-house effect);
- the temperature decrease during night time is delayed by buildings thermic inertia.

Urban islands are particularly evident when wind speed is lower than 3 m/s (OKE, 1979); in that condition, the flow is dominated by thermal effects that produce a double recirculation zone overlying the urban area, as shown in fig. 2.1. This particular flow pattern influences the pollutant transfer and produces an enhanced concentration of pollutant in the city center. When the wind intensity is higher than 3 m/s, this flow pattern disappears and the influence of the urban area on the flow field is revealed by a warm air plume advected downstream(fig. 2.2).

2.3 Spatial Scales

Emission and dispersion phenomena close to or within urban areas are characterized by a variety of time and length scales. Depending on the scale we are interested in, different mathematical models are used. A rough classification - usually adopted - identifies three different spatial scales:

- The regional scale, of the order of 100 km
- the city-district scale, between 1 and 10 km
- the local scale, between 10 and 100 m

As already mentioned, the geometry of an urban area can be modelled in different ways in the computational domain, depending on the precision adopted for the description.

2.3.1 The regional scale

The regional scale is usually defined as the larger region surrounding a town which is influenced by the phenomena produced at city scale. The flow field, on a regional scale, reacts to the presence of a town because of the heat island effect and of the decreased wind speed due to the drag forces exerted by buildings. Considered at this scale, without any will of describing the complex flow close to the ground, a town could be seen as a warm rough section of the overall surface. The atmospheric boundary layer above a town can be divided vertically in the usual way of the similarity theory:

- the logarithmic law profile, or inertial zone, whose typical scales are roughness length z_o and friction velocity u_* ;
- a region where thermal effects begin to appear; the length scale is the Monin-Obukhov height \mathcal{H} and the velocity scale is still u_*
- the region between Monin-Obukhov height and the top of the boundary layer, whose typical scales are the boundary layer depth δ and the convective velocity u_c .

The problem is to find the values of u_* , z_o , \mathcal{H} , u_c , defined in the previous chapter.

It is worth noting that, passing from rural to urban areas, the atmospheric boundary layer is subjected to a transition due to the new surface condition; the influence of buildings extends toward the upper part of the boundary layer: a new region, called *internal boundary layer*, grows within the boundary layer extending downstream the beginning of the surface change. The distance required by the boundary layer to reach a new equilibrium condition is called *fetch*, and can be evaluated in several ways (cfr. Chap.3.2).

In this kind of description, the complexity of urban geometry is synthesized in one parameter only (tab. 2.1), the roughness length z_o (WIERINGA, 1993). This means that a town is considered as a region with uniformly distributed drag forces. The problem is thus to parameterize small scale geometry details in order to give an evaluation of z_o .

z_o (m)	Surface type
0.0002	Sea, loose sand and snow
0.005	Concrete, flat desert
0.03	Short grass and moss
0.04 ~ 0.09	Low mature agricultural crops
0.12 ÷ 0.18	High mature crops
0.35 ~ 0.45	Continuous bushland
0.4 ~ 0.7	Dense low building (“suburb”)
0.7 ~ 1.5	Regularly-built large town

Table 2.1: *Roughness length classification (WIERINGA, 1993).*

In terms of fluctuating flow field, the presence of a town enhances intensity of fluctuating components, due to increased surface roughness as well as enhanced thermal fluxes, especially at night time. In situ observations shows that turbulence intensity above urban areas is, during the day, higher of about 20 ÷ 30%, and at night, twice as much as that of rural areas (CLARKE *et al.*, 1978).

Mathematical modelling of flow on the regional scale requires parameterization of the effects of the urban surface on the flow. For example, there are mesoscale models, with a horizontal resolution of about 10 km and a vertical resolution of 20 m near the surface, and of 200 m in the rest of the boundary layer, in which the surface effect are taken in account by means of few parameters related to land use, soil moisture, albedo, and Bowen ratio (BRITTER and HANNA, 2003). Parameterization for mesoscale models need not to be too complex as long as, for numerical weather prediction models, the surface exchange is a small percentage of the overall computational cost. However, any parameterization need to be able to reproduce general properties of cities that influence the meteorology within the urban environment and downstream of it, first of all the heat island effect.

In order to reproduce the urban heat island effect, BEST (2005) suggested a new parameterization of urban areas for operational numerical prediction models. The urban area is represented as an homogeneous region with a thermal inertia, which is taken into account introducing an ‘effective heat capacity per unit area of the surface’ in a time-dependent balance equation for the temperature over an urban surface.

2.3.2 The city and the district scales

When the scale is reduced, passing from regional to city scale, difficulties arise: the geometrical details of the surface are no longer negligible, and what could be seen as a rough surface becomes a region occupied by densely packed obstacles. Urban geometry reveals all his complexity, due to the structure and orientation of buildings, whose influence on the flow can not be expressed by just one parameter. Obstacles of different dimensions influence mean wind direction and intensity of turbulent fluctuations, hence pollutant dispersion.

The problem now is to investigate the flow and the dispersion within and above a group of obstacles (MACDONALD *et al.*, 2000; DAVIDSON *et al.*, n.d.; ISNARD, 1999; PERKINS and BELCHER, 1997; HANNA *et al.*, 2002). Even neglecting thermal effects, the description of the vertical structure of the atmospheric boundary layer requires two other regions (fig. 2.3) in addition to the inertial and the outer region, in order to describe more precisely the flow field close to the ground:

- the *urban canopy*;
- the *roughness sub-layer*.

In the *urban canopy*, the flow is directly affected by orientation and position of each single building. Related to wind direction and street geometry, semi-permanent recirculating regions arise within the urban canopy. Immediately above this region, there is a region, the *roughness sub-layer*, where the flow is influenced by the wakes of buildings; the flow is there non-homogeneous in the horizontal planes. This region extends up to the so called *blending height* z_* , which is far enough from the canopy so that wakes of buildings merge with each other; above the blending height the flow fields feels the presence of obstacles placed on the earth surface as a unique element of aerodynamic drag, uniformly distributed on the whole surface. Then the inertial region takes place, where the logarithmic law applies. However a new parameter d is made to appear, the *displacement height*, which allows to shift vertically, respect to

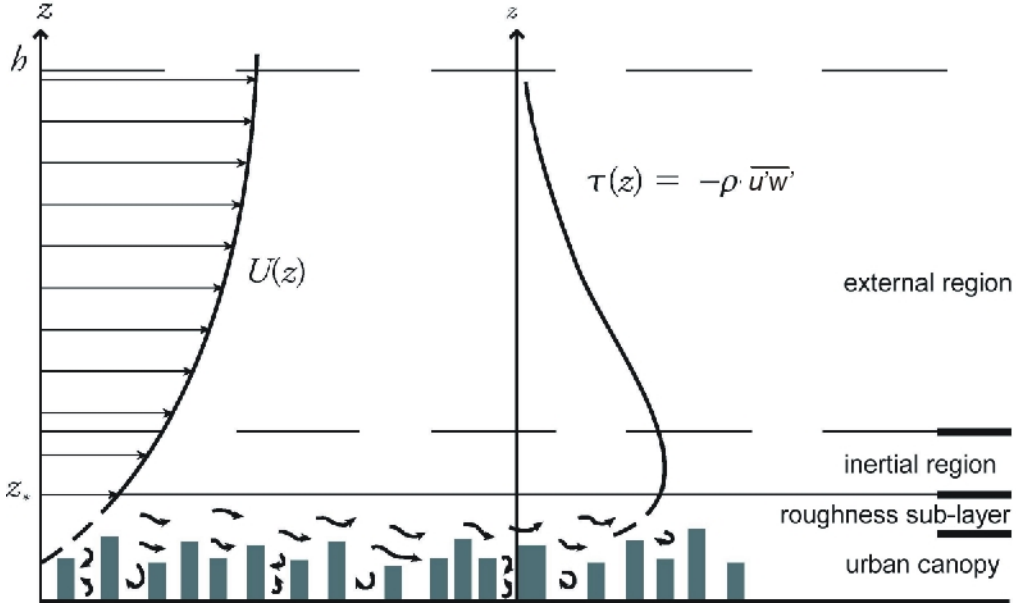


Figure 2.3: Vertical structure of the urban boundary layer in neutral conditions.

the value z_o , the virtual plane where the mean velocity goes to zero:

$$\frac{U}{u_*} = \frac{1}{k} \ln \frac{z-d}{z_o} \quad (2.1)$$

The parameter d is introduced when recirculating regions affect the flow pattern.

Another usual way of expressing the mean velocity profile is to use a power-law:

$$\frac{U}{u_*} = \left(\frac{z-d}{\delta-d} \right)^n \quad (2.2)$$

where the exponent n is a function of wall roughness. The power-law allows good approximation of the mean velocity profile but it does not have any theoretical support.

A phenomenological description usually adopted to describe the flow field in the lowest part of the boundary layer (below the inertial zone) identifies three different flow regimes, as a function of the obstacles aspect ratio H/W between H , the obstacle height and W , the distance between them (OKE, 1987).

In the *isolated roughness* regime (for $H/W < 0.15 \div 0.2$), obstacles are sufficiently far one from the other that, before another obstacle, the flow has time enough to reach the dynamical condition it had before passing the previous. A recirculating region develops downstream of the obstacle, whose length is about 6 – 7 times the obstacle height. Recirculating region occurs even upstream of the obstacle, of a smaller extent, if compared to the downstream “bubble”. In terms of pollutant dispersion the wake behind a bluff body retain pollutants in his recirculating motion, exchanging mass with the surroundings

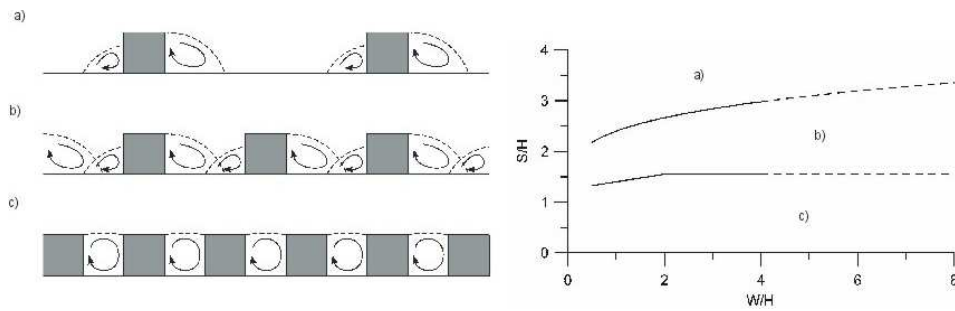


Figure 2.4: Flow regimes above groups of obstacles (OKE, 1987): a) isolated roughness, b) wake interference, c) skimming-flow. S represents the lateral spacing between obstacles.

flow by mean of an intermittent vortex shedding (LOUKA *et al.*, 2000). For values of H/W between 0.2 and 0.65 another regime takes place, known as *wake interference*. Buildings are sufficiently close to each other that the wake generated by each building interacts with the downstream buildings; the resulting flow pattern shows an increasing complexity. In the last of the three regimes, the so called *skimming flow*, the buildings are so densely packed that an about steady recirculating region develops within them¹⁶, as shown in fig. 2.4. Interaction between external flow and recirculating regions is reduced in comparison to the previous regime, and it is controlled by the dynamics of a shallow *shear layer*, which develops at the external boundary of the cavity.

In micro-meteorology studies the Oke's distinction is usually adopted to distinguish different kind of flow regimes, depending on obstacle configurations. However, before that, a similar distinction has been widely used in engineering applications and wind tunnel research. Following this classification two different roughness type are identified (PERRY *et al.*, 1968):

- the d-type roughness (corresponding to skimming flow)
- the k-type roughness (corresponding to wake-interference flow)

This classification raised after the evidence that, for flows in pipes and channels, in case of d-type roughness, the effective roughness h_s was not proportional to the roughness height H ¹⁷.

¹⁶To be more precise, the number of vortex arising in the canyon depends on street aspect ratio (Chap 4). However even in the case of square cavity $H/W = 1$, secondary vortex develops in the corners

¹⁷PERRY *et al.* (1968) argued that h_s seemed to be proportional to the boundary layer thickness δ :

$$h_s \approx 0.02\delta$$

However, experimental support for the previous relation is lacking, especially for boundary layers. TOWNSEND (1976) argued that, for flows in pipes, this could be explained by the action of large scale pressure fluctuations that would lead to "simultaneous ejection of stagnant fluid over areas comparable with the flow width and with normal velocities comparable with the friction velocity".

It is worth noting to remember that this results would be in contrast with almost all assumptions of the boundary layer theory, as far as the only relevant scale in the flow field would be the boundary layer thickness: as recognized by Perry, this would invalidate the basic assumption leading to the need of an asymptotic matching (and thus to the logarithmic profile) between different regions characterized by very different length scales.

PERRY *et al.* (1968) emphasize how, from a phenomenological point of view, it is evident that cavity flow in d-type roughness is separated and therefore “isolated” from the main flow, so that the length scale in determining h_s can not be H . After several experiment with varying obstacle density, interpolating the results with a classical logarithmic law they found that, for a d-type roughness:

$$\frac{\Delta U}{u_*} = \frac{1}{k} \ln \frac{(z-d)u_*}{\nu}$$

where ΔU is the roughness function.

Roughness length and displacement height evaluation

The evaluation of the parameters d , z_o and z_* , is usually done following empirical relation that relate their values to geometrical properties of obstacle shape and orientation. A first approximation (GRIMMOND and OKE, 1999) is given by relations that take only account of the mean obstacle height \hat{H} ¹⁸:

$$z_* = a\hat{H}$$

$$z_o = b\hat{H}$$

$$d = c\hat{H}$$

with $2.5 < a < 4.5$, $b \simeq 0.1$ and $c \simeq 0.7$.

For the blending height, there are other relations in the literature, that are based on the dependence of only one parameter (ROTACH, 1993a):

$$z_* = 50 - 100z_0$$

$$z_* = 3\hat{W}$$

where \hat{W} is the mean distance between buildings.

A second order approximation takes also account of the mean gap between obstacles. For the blending height a usual relation is (RAUPACH *et al.*, 1980):

$$z_* = \hat{H} + 1.5\hat{W}$$

About the two other parameters, in fig. (2.5) are shown two empirical curves, relating the variation of d and z_o , normalized to mean obstacle height, as a function of the ratio H/W ; otherwise, with a three-dimensional analysis, they can be computed as a function of the porosity factor $\lambda_p = A_P/A_T$, the ratio between the surface occupied by obstacles on the horizontal plane to total surface.

In an alternative way, both parameters can be evaluated as a function of the *frontal area index* $\lambda_F = A_F/A_T$, where A_F corresponds to the average frontal area of roughness elements perpendicular to the wind direction.

¹⁸We define the mean obstacle height as

$$\hat{H} = \frac{\sum_{i=1}^N H_i A_{p_i}}{\sum_{i=1}^N A_{p_i}}$$

where N is the obstacles number and A_{p_i} denotes the surface occupied by each obstacle.

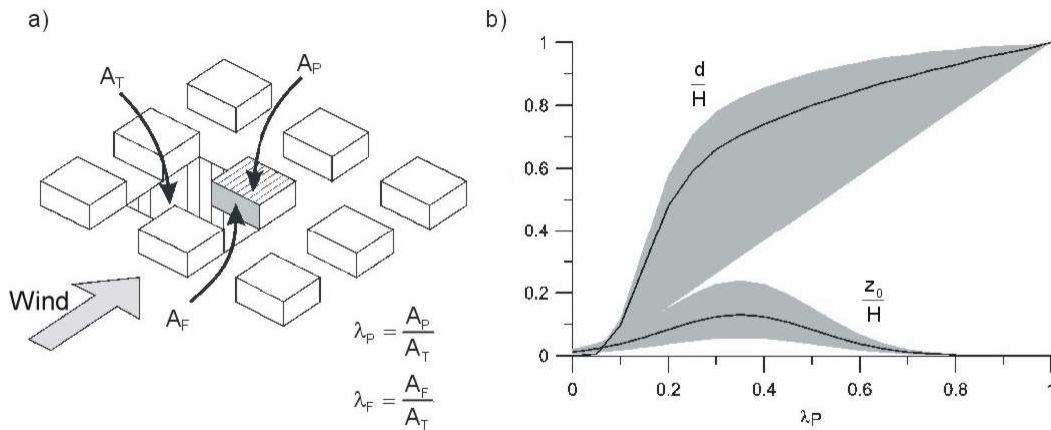


Figure 2.5: Variation of the displacement thickness d and of the roughness height z_o as a function of the porosity factor λ_p of a group of obstacles (GRIMMOND *et* OKE, 1999).

ROTACH (1994) suggested a method to evaluate the displacement height d based on *in situ* turbulence measurements in urban areas. More complex relations are also available in the literature for the determination of d and z_0 (BOTTEMA, 1997), as function of several parameters describing the geometry of building groups. A critical review on the methods used to evaluate surface parameters can be found in GRIMMOND *et al.* (1999).

In Fig. (2.5) it is evident that, the porosity increase has two opposite effects on the drag exerted from the wall to the flow. For low values of $\lambda_p < 0.35$ the roughness length increases linearly with increasing obstacle density. For $\lambda_p > 0.35$, z_0 decreases with increasing λ_p as long as roughness element placed at the wall begin to be enough densely packed to shelter each other.

Similar plots relating the effective roughness length to porosity parameters can be found in review works by JIMÉNEZ (2004) and RAUPACH *et al.* (1991).

Some more considerations about the displacement height

As mentioned before, the effect of roughness elements on the mean velocity profile is not only to change the slope of it, in a part or in the whole boundary layer, but also sometimes to shift it vertically, when the elements are sufficiently height and densely packed. The upward displacement of the entire flow is evaluated by finding a new origin for the vertical coordinate z , introducing the new parameter d , *displacement height*. The dynamical meaning of the displacement height (THOM, 1971; JACKSON, 1981) can be interpreted as ‘the level of the actual momentum sink’ or ‘the mean height at which the mean surface shear τ_0 appears to act’. This means that if the average moment per unit plan area of τ_0 is M , then

$$d = \frac{M}{\tau_0}$$

is the level of action of τ_0 .

Jackson emphasize how “ z_0 expresses the *magnitude* of forces which act on the surface, whereas d is related to the *distribution* of these forces”.

Choosing $(z - d)$ as the length scale, we can rewrite the differential form of the logarithmic law as

$$\frac{dU}{dz} = \frac{u_*}{k} \frac{1}{(z - d)}$$

Expressing the turbulent viscosity as

$$\nu_T = u_* |z - d|$$

according to the mixing-length hypothesis, we can enlighten the physical significance of d . The average horizontal force per unit plan area exerted between wall and fluid can be written as

$$\tau = \rho \nu_T \frac{dU}{dz} = \rho \nu_T \frac{u_*}{k} \frac{1}{z - d}$$

By substituting ν_T , we obtain

$$\tau = \rho u_*^2 |z - d| \frac{1}{z - d}$$

showing that, when $z > d$, the stress assume a positive values, whereas his negative values, when $z < d$, imply the presence of a recirculating region.

Surface roughness changes

As long as the urban geometry is not homogeneous, the description of the flow field has to deal with effects induced by roughness changes.

Flow over changing terrain constitutes itself a research topic in the domain of rough-wall turbulence (KAIMAL and FINNIGAN, 1994; BELCHER *et al.*, 1990; ANTONIA and LUXTON, 1971; CHENG and CASTRO, 2002a; PLATE, 1995). As long as in the present work there is no investigation over this phenomenon we want just review the main properties of these flows:

- the presence of an internal boundary layer develops over the new surface, growing in height with downwind distance
- the fact that all flow variable profiles are no longer in equilibrium with the new surface, as far as the vertical extension of the internal boundary layer is smaller the boundary layer depth.

The downwind distance needed for the new boundary layer to reach a new equilibrium condition is called *fetch*.

The simplest way to classify a surface roughness change is to evaluate its *magnitude*, defined as

$$M = \ln\left(\frac{z_{01}}{z_{02}}\right)$$

where the subscripts 1 and 2 describe upwind and downwind surface conditions.

The internal layer growth rate, and consequently the fetch distance, can be evaluated in different ways. A simple one is an empirical relation proposed by SCHLICHTING (1968)

$$\frac{\delta_i}{z_{02}} = A_r \left(\frac{x}{z_{02}} \right)^n$$

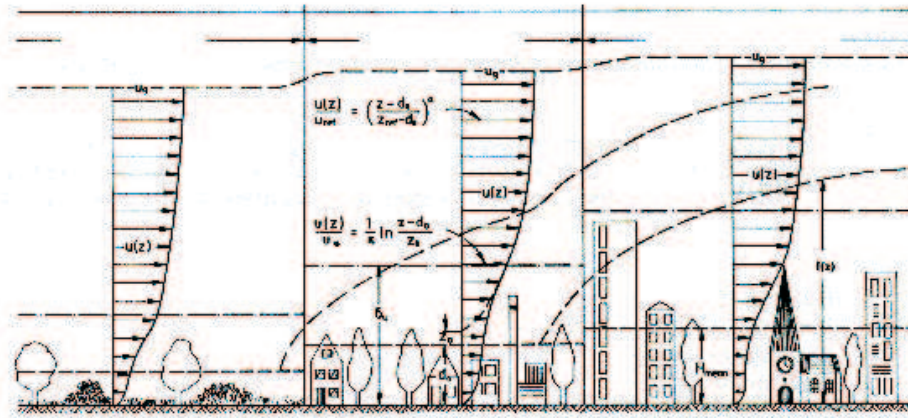


Figure 2.6: Boundary layer flow over changing terrain (PLATE, 1995).

where $n \approx 0.8$, δ_i is the internal layer depth and A_r is a constant of proportionality defined as

$$A_r = 0.75 + 0.03M$$

Considering for example that $z_{02} = 1m$ and $A_r = 0.5$, a downwind distance of $5.6km$ is required by the internal boundary layer to reach a height of $500m$, which can be considered a standard urban boundary depth in neutral conditions. On the other hand, keeping the same surface conditions, after a downwind distance of $100m$ the upper limit of the internal boundary layer would be $\delta_i = 20m$. That means that surface properties have to be homogeneous for significant downwind distance, otherwise their effect would be confined in a small portion of the boundary layer. This is the reason why surface variation of the order of few hundred meters do not usually affect significantly the boundary layer structure.

Therefore, at the city scale, spatial averaged properties of the surface are usually considered (WIERINGA, 1986; FIEDLER and PANOFKY, 1972; GOODE and BELCHER, 1999; BALDAUF and FIEDLER, 2003).

Canopy models - spatial average operators

The lineaments of the flow field above a city following the similarity theory are based on a number of assumption, among which some are consistent enough with experimental data, some others show discrepancies with reality. A statement of the similarity theory requires the flow to be homogeneous over horizontal plane, so that all flow variables vary with the vertical coordinate (z or $(z - d)$) only. The condition lacks near the surface, as the flow below the *blending height* z_* is shaped by the the wakes of single obstacles.

To cancel horizontal variations of the flow, a description of the dynamics of the roughness sub-layer can be given by means of spatially averaged variables. RAUPACH and SHAW (1982) used a spatial operator, which for horizontal averages, is defined as

$$\langle \Phi \rangle (z) = \frac{1}{A} \int_A \int \Phi(x, y, z) dx dy$$

where the angle brackets denote the horizontal average ¹⁹.

The time averaged variable Φ can be expressed as

$$\Phi(x, y, z) = \langle \Phi \rangle (z) + (\Phi)''(x, y, z)$$

where $\langle \Phi'' \rangle = 0$.

It is worth noting that a general criterion for this spatial average to be representative is that the spatial average length, $L \sim \sqrt{A}$ has to be much larger than the typical length scale of roughness elements, for example the gap between individual roughness elements.

Applying both time and spatial average operator to the continuity and Navier-Stokes equation for incompressible flow and neglecting the viscous term, we obtain

$$\frac{\partial \langle U_i \rangle}{\partial x_i} = 0$$

for the continuity equation and

$$\frac{\partial \langle U_i \rangle}{\partial t} + \langle U_j \rangle \frac{\partial \langle U_i \rangle}{\partial x_j} = \frac{1}{\rho} \frac{\partial \langle P \rangle}{\partial x_i} - \frac{\partial \langle \overline{u_i' u_j'} \rangle}{\partial x_j} - \frac{\langle U_i'' U_j'' \rangle}{x_j} + f_{Fi} \quad (2.3)$$

for the momentum equation, where

$$\langle \overline{u_i' u_j'} \rangle$$

is the spatial average of the turbulent stresses and

$$\langle U_i'' U_j'' \rangle$$

are the so called *dispersive stresses* (RAUPACH and SHAW, 1982; FINNIGAN, 1985), due to the transport of momentum by spatial fluctuations of the mean flow (i.e. by the waviness of streamlines), and the term $f_{Fi} = \frac{1}{\rho} \langle \frac{\partial P''}{\partial x_i} \rangle$ represents the distributed aerodynamic drag due to pressure forces exerted on roughness elements. Closure model for spatially averaged Reynolds stresses and distributed drag force are available in theoretical and numerical works (WILSON and SHAW, 1977; YAMADA, 1982; WILSON, 1988; SVENSSON and HÄGGKVIST, 1990; AYOTTE *et al.*, 1999).

By considering the group of obstacles as a porous medium with uniformly distributed drag force within it, several authors found a canopy flow model to describe the mean wind (BELCHER *et al.*, 2003;

¹⁹The operator satisfies all but one properties of Reynolds averaging procedures. The exception concern commutation between spatial averaging and spatial differentiation, in case of waving surfaces at the air-element interfaces; in this case particular it is

$$\langle \frac{\partial \Phi''}{\partial x_i} \rangle \neq 0$$

MACDONALD, 2000; SOULHAC, 2001). Considering the flow stationary and homogeneous over the horizontal planes, and neglecting the dispersive stresses ²⁰, equation 2.3 reduces to

$$0 = -\frac{\partial \langle \overline{u_i' u_j'} \rangle}{\partial x_j} + f_{Fi} \quad (2.4)$$

MACDONALD (2000), as well as BELCHER *et al.* (2003), developed an analysis of flow within and above the canopy by using a Prandtl mixing-length model, and adopting a boundary layer approximation; They modelled the Reynolds stresses as

$$\frac{\partial \langle \overline{u'w'} \rangle}{\partial z} = \frac{\partial}{\partial z} \left\{ l_m^2 \left(\frac{\partial \langle U \rangle}{\partial z} \right)^2 \right\}$$

where l_m is the mixing length within the canopy. To justify the choice ²¹, the mixing length model could be considered as the first term of an expansion.

By mean of simple dimensional considerations f_{Fi} can be expressed as the product of $\langle U \rangle^2$ and a parameter c_f related to a canopy length scale L_c (independent of U),

$$f_F(z) = c_f(z) \langle U^2(z) \rangle$$

Estimates of $c_f \propto (L_c(z))^{-1}$ are available, as function of obstacle height, orientation and density in (SOULHAC, 2001; BELCHER *et al.*, 2003). The horizontally averaged momentum balance is then:

$$c_f(z) \langle U^2(z) \rangle = \frac{d}{dz} \left\{ l_m^2 \left(\frac{d \langle U \rangle}{dz} \right)^2 \right\} \quad (2.5)$$

A first integration of this differential equation has been proposed by CIONCO (1965) for plant canopies, followed with similar arguments by other authors (MACDONALD, 2000; SOULHAC, 2001; BELCHER *et al.*, 2003; BENTHAM and BRITTER, 2003) that considered groups of obstacles. Considering both c_f and l_m constants with height a solution ²² of equation 2.5 is given by

$$\frac{\langle U(z) \rangle}{\langle U(H) \rangle} = \exp[-\alpha(1 - \frac{z}{H})]$$

where $U(H)$ is the mean velocity at the top of the canopy and α is a coefficient depending on H , c_f and l_m (that are all function of canopy density). The solution is supposed to be valid in the canopy.

The region between the canopy and the inertial layer, where the drag exerted by single obstacles still influences the flow because of the wake diffusion and the spreading of turbulent eddies - generated within shear layers at the top of recirculating regions - is named roughness sub-layer.

Up to now, there are still some disagreements in the literature over the form of mean-velocity profile (spatially averaged) within it. This is may be due to the lack of a consolidated procedures in evaluating u_* , z_0 , d .

²⁰Dispersive stresses can be neglected as long as several experimental works evidenced that their role is very small (at least two order of magnitude) compared to Reynolds stresses (FINNIGAN, 1985; CHENG and CASTRO, 2002b) .

²¹To adopt a mixing-length model the integral scale of the eddies has to be much smaller than the length scales over which the mean shear change, which is not the case for mixing layers and wakes developing at the top of obstacles canopy.

²²This solution does not satisfy the no-slip condition at the bottom of the canopy.

Experimental data collected (ROTACH, 1993a; RAUPACH *et al.*, 1991) in the open field and within wind tunnel suggest that

$$\left(\frac{\partial \langle U \rangle}{\partial z}\right)_{RSL} < \left(\frac{\partial \langle U \rangle}{\partial z}\right)_{IR}$$

in reason of the enhanced diffusivity within the RSL respect to the inertial region.

DE BRUIN *et al.* (1985)) results suggest the opposite conclusion, as well as results obtained by MAC DONALD (2000). The former provided a matching between the log-law and the exponential law by imposing mass conservation criteria, the latter by assuming a linear variation of the turbulence mixing length scale l_m within the matching region up to the blending height z_* . In both cases those authors reached the conclusion that

$$\left(\frac{\partial \langle U \rangle}{\partial z}\right)_{RSL} > \left(\frac{\partial \langle U \rangle}{\partial z}\right)_{IR}$$

Finally, CHENG and CASTRO (2002b) suggested that the spatially averaged mean velocity within the RSL can be well approximated by a log-law as well, provided correct estimation of u_* .

Some more aspects on the turbulence structure within the roughness sub-layer

The interest for more detailed studies on the structure and the dynamics of the roughness sub-layer raised from the end of the 70'ies as a consequence of micro-meteorology applications. Most work on this topics has been carried in studies related to flow, heat, moisture and mass transfer within and over vegetation canopies (THOM, 1971; GARRATT, 1978; RAUPACH *et al.*, 1986; KAIMAL and FINNIGAN, 1994).

Beginning from the 80'ies open field studies have been conducted to characterize the dynamics of the roughness sub-layer in urban areas (HÖGSTRÖM *et al.*, 1982; ROTACH, 1993a; ROTACH, 1993b; ROTACH, 1995; OIKAWA and MENG, 1995; KASTNER-KLEIN *et al.*, 2004).

The RSL is recognized as a region with enhanced diffusivity compared to the overlying inertial layer.

The enhanced diffusivity of momentum was associated by RAUPACH *et al.* (1980) and by BANDY-OPADHYAY *et al.* (1988) to a wake diffusion effect, related to 'horse-shoe vortex' dynamic, i.e. to the transfer of vorticity from the mean shear flow to stream-wise directed vorticity concentrated in the two horse-shoe limbs.

In many experimental studies a Reynolds stresses decrease with height has been observed, within the RSL, in contrast with idea of enhanced momentum flux, (RAUPACH *et al.*, 1980; MULHEARN and FINNIGAN, 1978; MULHEARN, 1978). As long as, referring to eq. 2.3, the contribute of dispersive stresses could not explain this decrease (the magnitude of dispersive stresses is less than a few percent of u_* , as estimated by the several authors), hot-wire measurement error due to probe velocity acceptance angle ($\pm 45^\circ$), as documented by PERRY *et al.* (1986) and mentioned in Chapter 3, give a convincing explanation of this phenomenon.

However in field measurement by ROTACH (1993a) an analogous Reynolds stresses decrease was observed. Since it could no longer be inferred to systematic measurement errors (measurement were performed by mean of sonic-anemometer) the only explication for this decrease is due to horizontal average

of stream wise pressure fluctuation $\frac{1}{\rho} < \frac{\partial p''}{\partial x_i} >$. Rotach suggested a high dependence model for the

Reynolds stresses by evaluating the 'local' friction velocity $u_*(z)^{RS} = \sqrt{\overline{u'w'} + \overline{u'v'}}$ from the friction velocity u_* (measured or evaluated in the inertial region). The relation he proposed has an an exponential form:

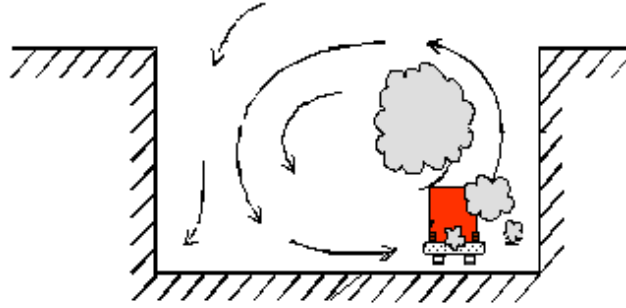


Figure 2.7: Pollutant transport within a street canyon

$$\frac{u_*(z)^{RS}}{u_*} = C_1 \{1 - \exp(-C_2(z - d))\}^{1/3}$$

where C_1 and C_2 are empirical constants.

2.3.3 The local scale: the street canyon

Flow phenomena in the local scale have been studied in the context of pollutant dispersion in urban areas. The main interests arises from the proximity of the receptors to the sources (vehicles exhaust gases), in an environment partially sheltered from the influence of wind blowing above buildings roof. Pollutant dispersion is therefore limited and the characteristics of the flow field can induce high concentration at ground level (Chap 5). A classical case in the study of the flow which develops in a street within two buildings, whose orientation is perpendicular to the mean wind direction, and whose distance W is much smaller than the street length, so that the phenomenon can be considered bidimensional, at least for the mean motion. In the last twenty five years, several studies have been carried out to represent flow field and pollutant dispersion in a street canyon; we will give references and an overview of the main results obtained until today in the first paragraph of Chapter 5. Here we just want to mention that several models (BERKOWICZ *et al.*, 1997) assume the mass exchange rate at roof height as proportional to a reference wind speed of the external flow, adopting a simple analytical relation to evaluate the mean concentration within the canyon of the type:

$$C = \alpha \frac{\dot{M}_q}{U_H D^2} \quad (2.6)$$

In the relation 2.6, α is an empirical constant whose values are between 6 and 13 (Chapter 5), U_H is a reference velocity variation of the external flow, adopted as scale of the velocity field inside the cavity, D is a characteristic length - the cavity height- and \dot{M}_q is the mass flow emitted within the canyon. In the next paragraph it is reviewed the way these models are taken in account in complete urban dispersion models. Here we just want to emphasize that these models provide good estimation of mean concentration values when the street aspect ratio H/W is about 1. Things become more complicated when the aspect ratio increases (narrower canyons) as multiple vortex arise, and when it increases (larger canyons). In

wake interference regime the structure of the shear layer at the interface between the recirculating region and external flow is highly unstable (LOUKA *et al.*, 2000) and the mass exchange between the two regions is characterized by intermittent shedding of vortices whose length scale is proportional to H . Thermal effects are not so relevant in these processes, except for very low wind speed, as long as they take place well below the Monin-Obukhov height. As already mentioned, much studies have been done over this topic. A complete review can be found in VARDOULAKIS *et al.* (2003).

2.4 Numerical modelling of urban pollutant dispersion

Pollutant dispersion modelling has to deal with modification into the atmospheric flow by the presence of a city. The main effects, as summarized by ROTH (2000) are:

- presence of intense shear layer at the top of the canopy;
- wake diffusion induced by buildings which enhances turbulent transport of momentum, heat, moisture and pollutants;
- drag induced by buildings;
- heat and radiation trapping effects.

Transposed to pollutant dispersion modelling, two main difficulties arise concerning:

- how to characterize the lower part of the atmospheric boundary layer, where the flow dynamics are typically determined by the size and the density of the buildings and by the street geometry;
- how to parameterize the mass exchange between the recirculating region within the street canyons and the external flow.

Two choices are available:

- a complete reconstruction of the urban geometry within the computational domain, followed by the solution of the system of differential equations by means of CFD codes, i.e. (MAHÉ *et al.*, 2004);
- a parametrization of momentum and mass exchange processes that take place in the lower part of the boundary layer.

In order to use simple gaussian plume models GIFFORD (1970) suggested that the increased turbulence of an urban area can be approximated by first estimating the standard Pasquill (PASQUILL and SMITH, 1983) stability class, and then shifting the class to the next higher.

A second step is to describe the flow field according to the similarity theory, expressing the turbulent diffusion term as function of the friction velocity (CARRUTHERS *et al.*, 1994).

The main limitation in applying the similarity theory arises as long as the domain we are interested in can no longer be considered homogeneous in the horizontal plane, at least in a non negligible part of it (Roughness sub layer, urban canopy). In order to simplify the representation of an urban area it is therefore usual to take into account spatially averaged variables, as mentioned in the previous paragraph.

This average procedure is always applied for the so called *urban parametrization*: sometimes explicitly some times not.

In order of computing long term mean concentration using a gaussian plume model, DE HAAN *et al.* (2001) proposed to described the vertical dependence of the friction velocity as

$$\left(\frac{u_{*loc}(z)}{u_*}\right)^b = \sin\left(\frac{\pi}{2}Z\right)^a \quad (Z \leq 1)$$

where u_* is the friction velocity measured in the inertial region derived from Reynolds stresses, $u_{*loc}(z)$ is the so called *local friction velocity*, a and b are two empirical constants deduced by fitting data of full-scale observations and $Z = (z-d)/(z_*-d)$. This parametrisation (completed by modified energy balance into the meteorological processor), instead of using a constant value of the friction velocity, permitted better estimation of yearly average surface pollution concentration in the city of Zurich.

In the aim of simulating flow and dispersion in urban areas, MARTILLI *et al.* (2002) proposed a new urban parametrisation to express the term

$$f_{Fi} = \frac{1}{\rho} \left\langle \frac{\partial P''}{\partial x_i} \right\rangle$$

arising from a spatial average of the time mean momentum equation. The goal is to introduce the influence of the roughness sub-layer by parametrization of building effect on the grid-averaged variables without explicitly resolving flow around them.

The city is represented as a series of parallelepiped of concrete of the same width, same distance between each other (which is also equal to the horizontal grid size in the urban area), but with different height. In such a way, the impact of the buildings on the flow (momentum, temperature and turbulent kinetic energy equations) is vertically distributed within the urban canopy, leading to vertical profiles of turbulent variables than ones obtained with Monin-Obukhov theory. The drag distributed force f_i was given at each height z as a function of the obstacle density at each level. Turbulent vertical fluxes of momentum and mass are computed by mean of a gradient law whose diffusion coefficient is expressed as

$$K_z = Cl_k E^{1/2}$$

where $E = 1/2q^2$ is the turbulent kinetic energy, l_k is a typical length scale and C is a model parameter. Of course two more equation are needed to compute both $1/2q^2$ and l_k .

In the next paragraphs we give a quick overview on two codes for air pollution dispersion modelling adapted to urban areas (referred also as *operational models*): ADMS-Urban (CERC, Cambridge) and Sirane (LMFA - Coparly Lyon).

2.4.1 ADMS-Urban

ADMS-Urban (MCHUGH *et al.*, 1997) is a urban-scale dispersion model that includes a street canyon module nested within the core Gaussian code, named ADMS.

ADMS assumes mean and fluctuating velocities as a function of the height z according to Monin - Obukhov similarity within all the domain. In order to compute horizontal inhomogeneities due to surface roughness changes or because of the presence of hills and obstacles, ADMS provides a module (called

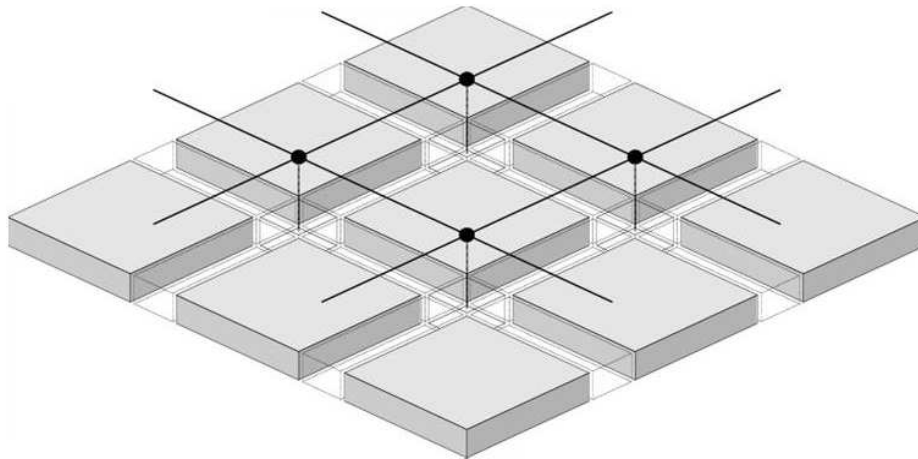


Figure 2.8: SIRANE street network (SOULHAC,2002).

FLOWSTAR) containing a model which calculates the change in mean flow and turbulence based on linearized analytical solutions of the momentum equation (JACKSON and HUNT, 1975; BELCHER *et al.*, 1990; BELCHER and HUNT, 1998). In a similar way ADMS can include the effect of dominant buildings, modelling the re-circulating flow in the lee of the building by mean of analytical relations (COUNIHAN *et al.*, 1974).

ADMS is a so called *second generation* gaussian model. This means that the transverse and the vertical plume spread σ_y and σ_z are height dependent and are calculated as function of the friction velocity u_* and $\eta = z/\delta$, as well as the mean velocity.

A particular module, called ADMS-Urban, is used to compute mean concentration in the regions of the domain where street canyon effect arises. This street canyon module is activated when street aspect ratio H/W is higher than 0.5, otherwise pollutant concentration are compute by mean of simple gaussian plumes.

For each street canyon, concentration are computed as the sum of two component: the background concentration due to street canyon trapping effect and the concentration due to a plume that takes account for the contribution of vehicles emissions within the street.

The street canyon trapping effect is parameterized using the Danish Operational Street Pollution Model (HERTEL and BERKOWICZ, 1989); the background concentration within the canyon are computed by mean of a relation like equation 2.6.

The gaussian plume transversal spreading is computed by mean of relations that evaluate turbulent fluctuations within the canyon.

2.4.2 SIRANE

The SIRANE model is a pollutant dispersion model for urban environment adapted at neighborhood scale (SOULHAC, 2002). The streets in a district are modelled as a simplified network of connected street segments (fig. 2.8).

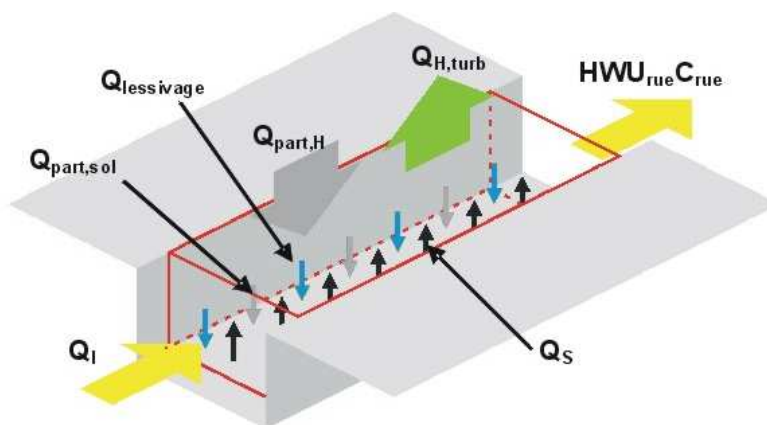


Figure 2.9: SIRANE box model for each street(SOULHAC,2002).

The flow within each street is driven by the component of the external wind parallel to the street, and the pollutant is assumed to be uniformly mixed within the street. The flow above the street network is described, as in ADMS, according to Monin-Obukhov similarity theory.

In order to compute mean concentration within each street, SIRANE takes account of two mechanism for transport in and out of street segment (fig. 2.9):

- diffusion across the interface between the air in the street and overlying air: this is modelled by standard concentration gradient diffusion approach; the transfer velocity is calculated from the external boundary layer properties (friction velocity and Monin-Obukhov height).
- exchanges with other streets, at intersections, due to advection along street: these exchange ratio have been parameterized using experimental and numerical simulations. the model assumes the conservation of mass at each intersection, generating a vertical flux when horizontal advection fluxes into and out the intersection are not equal. The mixing rate of pollutants advected from different upwind streets is related to the fluctuation of the external wind direction.

The dispersion of pollutants advected or diffused into the overlying air is taken into account using a Gaussian plume model, with the standard deviations σ_z and σ_y parameterized by similar theory. The input data for the final model are the external wind velocity and direction, the atmospheric stability, the background concentration and car emissions.

The model has been first validated on a district of the town of Lyon. Today SIRANE is currently used for urban air pollution modelling in several cities, such as Lyon, Paris, Chambéry, Grenoble.

EXPERIMENTAL METHODS AND FACILITIES

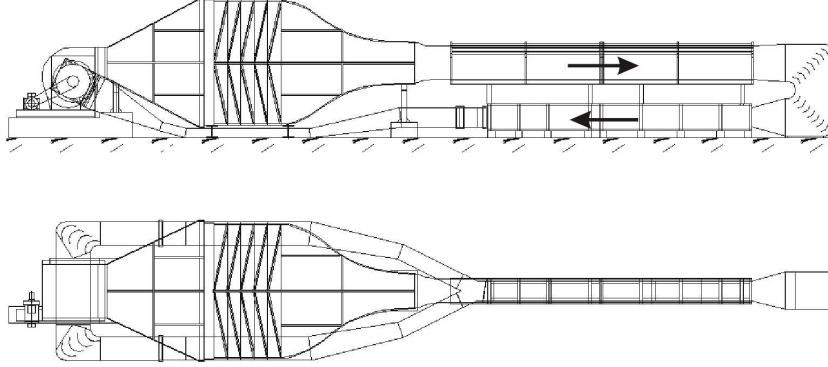


Figure 3.1: LMFA Wind Tunnel.

3.1 Experimental set-up

The study has been carried in a recirculating wind tunnel in the Laboratoire de Mécanique des Fluides et d'Acoustique at the Ecole Centrale de Lyon (see fig. 3.1). The test section of the wind tunnel is $8m$ long, $1m$ high and $0.7m$ wide, with lateral wall glasses. The wind velocity varies between 2 m/s and 12 m/s . Within the test section we reproduced a simplified bidimensional urban geometry, by mean of an array of rectangular bars, placed perpendicularly to the wind direction.

3.1.1 Similarity conditions

Wind tunnel simulation is based on the concept of *similarity*. Given the flow similarity is possible to reproduce the behaviour of a flow field by changing the characteristics scales but without changing the physical processes that take part to the process. In particular, it is useful to change the length scales in order to reproduce atmospheric flow within a wind tunnel. Neglecting thermal effect, i.e. supposing that the boundary layer has neutral stratification, the only similarity parameter is the Reynolds number Re .

As long as the height of the test section is $1m$, the geometrical scales of the experimental simulation have to be at least 100 times smaller than the real scales. The boundary layer thickness at the measurements station was about $\delta \sim 0.6m$.

To keep a constant Reynolds number between reality and wind tunnel, a free stream velocity of about $100m/s$ would be required²³. As long as the free stream velocity is about $U_\infty \sim 6 \div 7\text{ m/s}$, the Reynolds number within the wind tunnel is

$$Re = \frac{U_\infty \delta}{\nu} \sim 10^4 \div 10^5$$

which is approximately 100 times smaller than in real situations.

This implies that in the experimental conditions the ratio between the dissipative Kolmogorov scale and the external scale is larger of about two order of magnitude, compared to real conditions. However, even in experimental conditions, the Kolmogorov scale ($\eta \sim 10^{-5}$) m is two order of magnitude smaller

²³In case of free stream velocity of $100m/s$, the Mach number is larger than 0.3 and the assumption of incompressible flow is no longer justified.

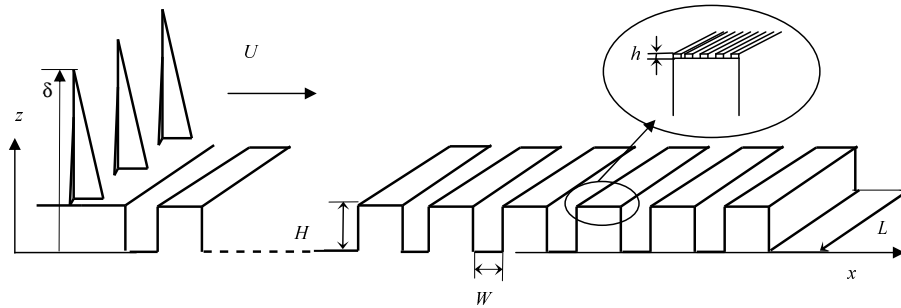


Figure 3.2: Overview of the wind tunnel installation.

than h_s , the ‘effective roughness length’, which is, in our case (see chap.4) of about $\sim 10^{-3}m$; we can thus assume that effects related to molecular diffusion do not affect the dynamic of the turbulent field and that this ‘partial’ similarity condition allows anyway studies on turbulent dispersion phenomena.

3.1.2 On simulating the atmospheric boundary layer

In order to study atmospheric dispersion by mean of wind tunnel experiments, it is necessary to reproduce a flow field which is similar to the atmospheric boundary layer. In particular it is important to:

- maintain the ratio δ/h_s between the boundary layer depth and the ‘effective roughness length’ as big as possible, in order to obtain a ratio $\delta/h_s \rightarrow \infty$ as large as possible;
- reproduce a spectral composition of the velocity field which is similar to the atmospheric flows spectral composition.

The atmospheric boundary layer is usually generated by using a combination of spires located at the entrance to the test section, with a lateral spacing equal to half the spire height (IRWIN, 1981; COUNIHAN, 1969) and roughness blocks on the floor of the tunnel. Spires are necessary to accelerate the boundary layer growth. Several adjustment of this method are available in the literature (CASTRO *et al.*, 1975; COOK, 1977; COOK, 1973) as well as comparisons between atmospheric and wind tunnel data in terms of turbulence intensity profiles and spectral density of the fluctuating velocity field (DE BORTOLI *et al.*, 2002).

To generate a boundary layer with characteristics similar to those of an atmospheric boundary layer, we used four spires of height 0.4 m were installed at the entry of the test section. We have simulated an idealized urban geometry using an array of 2D parallel canyons, formed by a set of square section bars (60 mm \times 60 mm) placed normal to the wind, as shown in Figure 3.2. The influence of roughness at roof level was studied by adding small 2D roughness elements (5 mm \times 5 mm) to the tops of the bars.

Before starting the experiments, special attention was devoted to ensuring that the incident velocity field was two-dimensional. Velocity profiles at different distances from the wall confirmed that the flow field was uniform in the transverse direction, with variations of less than 1% for the mean flow and 5% for the turbulence quantities. The velocity profiles were measured at a distance equal to about 12 times the height of the vortex generators downstream of the entry to the test section. We measured vertical

velocity profiles upstream and downstream of the test section, verifying that there were no significant differences in the flow parameters. This means that the measurement positions are located within an interval for which we can assume that the development of coherent structures in the wake of vortex generators has already reached an equilibrium condition and that the longitudinal scale related to the growth of the boundary layer is much larger than the boundary layer depth. In other words, in that interval, the boundary layer growth $\Delta\delta$ is much smaller than the boundary layer depth δ .

3.2 Measurement technique

3.2.1 Hot-wire anemometry

For the measurement of the velocity field above obstacles a hot-wire anemometer has been used.

The hot-wire anemometer is made up of a thin wire (CORRSIN, 1963), made of platine or tungsten, which is heated by joule effect by an electric stream. The wire, placed within the flow stream, is cooled by forced convection and his electric resistance changes as a function of flow velocity. Although the wire is very thin, it has a thermic inertia, which has to be estimated and compensated in order to have accurate measure of small velocity fluctuation.

In order to correct error induced by thermal inertia, different anemometer system are used; these are known as *constant current anemometer*, *constant voltage anemometer* and *constant temperature anemometer*, that, in reality has a constant electric resistance. We adopted a constant temperature anemometer, which is considered the best for high turbulence intensity flows, and we used a X probe, with a $5\ \mu\text{m}$ diameter wire, and an acceptance angle of $\pm 45^\circ$, in order to measure two velocity components. The response curve, which relates the tension E coming out from the anemometer and the velocity U of the stream has been determined with a series of constant velocity (between 0.5 m/s e 13 m/s), keeping as reference the Pitot tube measurements. The dependence on the inclination on stream direction has been measured for $\pm 20^\circ$ angles. The calibration curves have been interpolated with 4th order polynomes.

When a wall surface is approached, difficulties arise in the measurements process; measurements errors arise mainly because of the enhanced (CASTRO and DIANAT, 1990) turbulence intensity and because relevant differences take place in sharp regions whose length scale are of the same order of the wire length. Perry et al. (PERRY *et al.*, 1986) documented and highlighted the misbehaviour of X-wires probes in measuring Reynolds shear stress above a rough surface. These errors occurs in probe with low acceptance angle ($\pm 45^\circ$) and are induced essentially by high turbulence intensity. To reduce these errors, Perry et al. suggested to use probe with higher acceptance angle ($\sim 120^\circ$).

3.2.2 Flame Ionisation Detector - FID

In order to measure scalar concentration, a tracer gas was used and concentrations were measured using a Flame Ionization Detector (FID). Ethane (C_2H_6) was used as the passive tracer, since its molecular weight is nearly the same as that of air. FID system permits to measure hydrocarbons concentration in air. Air containing hydrocarbons is aspirated continuously in the measure point by mean of a tube, which is as thin as possible, not to perturb the flow (fig. 3.3). The air and hydrocarbons mixing is the injected in a hydrogen flame. The ions produced by the combustion are collected by an electrode. The basic physical principle of this system is that the current induced is proportional to hydrocarbon concentration. The length of the tube determines the frequency response of the system. For a 30cm long

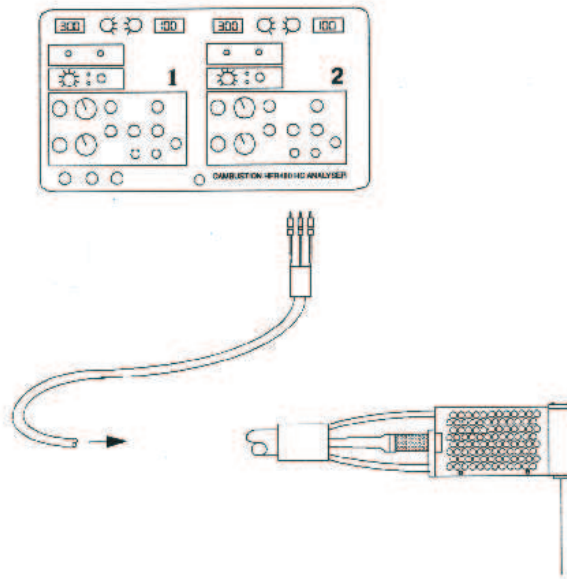


Figure 3.3: FID system.

tube the frequency cut-off is about 300 Hz. The measurement system is very sensible to temperature changes in the surrounding environment. In reason of this sensibility measurement errors can arise up to 10%.

Experiments were carried out with a line source located at ground level $z_s = 0$, and at heights $z_s = 2H$ and $z_s = 3H$ above the ground. The ground level source (fig. 3.4) was constructed from a 4 cm diameter porous tube, located in a slot cut into the floor, so the top of the tube was flush with the floor of the tunnel²⁴. The elevated line source (fig. 3.5) was made from a 5 mm diameter pipe into which regularly spaced holes were drilled²⁵, at an axial separation of 1 cm. Hyperdermic tubes 3 cm long were soldered into each hole, and the source was orientated with the needles pointing downstream.

Both sources were tested in a uniform velocity field to verify that the tracer emission was homogeneous in the transverse direction and that the emitted tracer plume was truly two dimensional²⁶.

²⁴Meroney et al. (1996) provide a summary of devices that can be used to simulate ground level emissions from car exhaust.

²⁵Similar sources have been used by Kitabayashi (1976) and Bultjes (1984).

²⁶Even if the source itself is two-dimensional, the concentration field at ground level exhibits higher values in the central region of the canyon. This inhomogeneity is due to secondary flow within the canyon, in the horizontal plane, which consists of two elongated counter-rotating recirculating cells, with vertical axes; the intensity of the secondary flow increases with increasing aspect ratio. For this reason it is very hard to generate a two-dimensional concentration field in narrow cavities, even if the flow field above roof level is two-dimensional. For the same reason, an accurate evaluation of the mass emission rate per unit length \dot{M}_q is not trivial, even if all experimental parameters are known.



Figure 3.4: Ground level source line source.

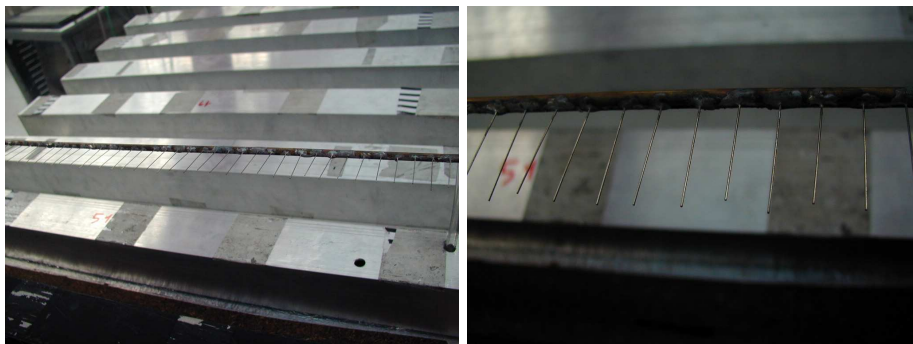


Figure 3.5: Elevated line-source.

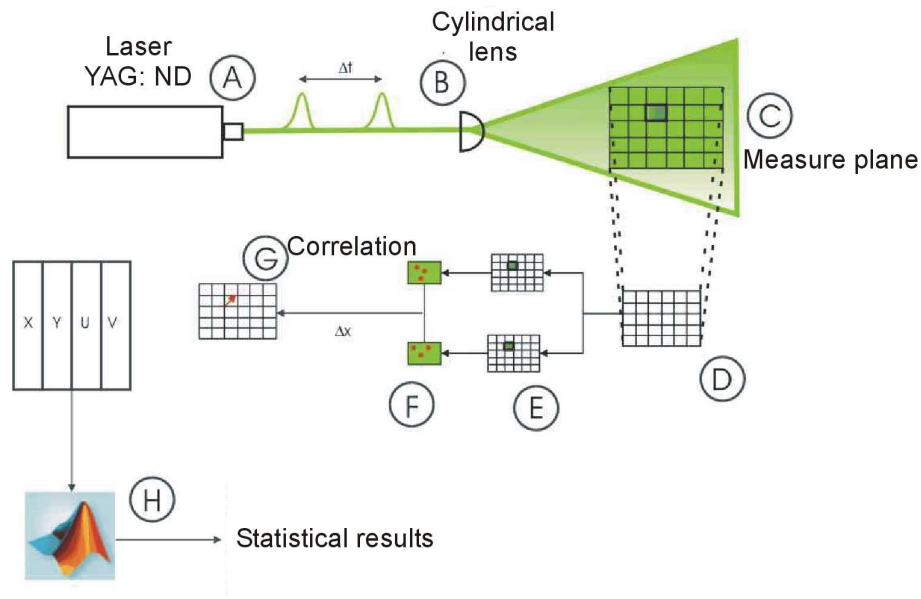


Figure 3.6: PIV system.

3.2.3 Particle Image velocimetry - PIV

For velocity measurements within and above recirculating regions, inside street canyons, a particle image velocimetry (PIV) system has been used. In spite of hot-wire anemometer, that gives single point measurements, PIV permits measure on the whole flow field (BÉRA *et al.*, 2001). Measurement are carried out on a bidimensional domain (referred here as $x - z$). The flow velocity is obtained calculating the displacement on the two directions Δx and Δz of a group of particles, within a short time interval Δt . Two velocity components are thus computed for each time step for the observed plane

$$u = \frac{\Delta x}{\Delta t} \quad w = \frac{\Delta z}{\Delta t}$$

As shown in fig. 3.6 the observation plane is lighted by a laser. The width of this plane is about 1mm .

Measures were carried out with a Dantec system. Two coupled YAG laser sources provide pairs of laser pulses at a synchronisable frequency of about 8 Hz. The visualization light sheet was 1 mm in width. The flow was seeded with micrometer-sized droplets generated by smog generator. The 1280×1024 pixels images were processed using cross-correlation. The interrogation window was fixed to 32×32 pixels, providing a spatial resolution of about $1\text{mm} \times 1\text{mm}$. The observation field was $120 \times 120\text{mm}$. The overlap ratio between adjacent interrogation windows was 50 %, providing instantaneous velocity fields with 63×63 vectors. A total set of 1000 instantaneous samples was available for time-averaged computations. As it is shown in fig. 3.7, the 1000 samples allowed us to compute reliable flow statistics up to the third order moment of the probability density function of the velocity.

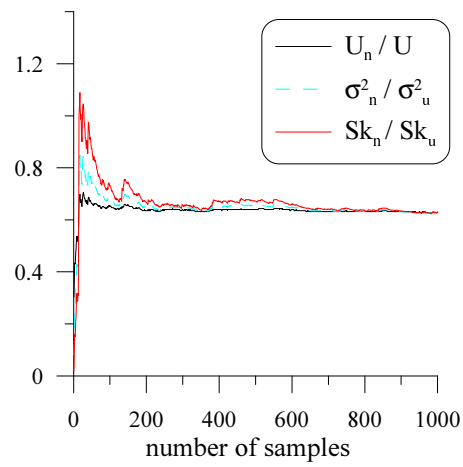


Figure 3.7: Convergence of the PIV statistics. U , σ_u^2 and Sk_u are the mean, the variance and the skewness of the longitudinal velocity calculated over 1000 samples at a fixed point; U_n , σ_n^2 and Sk_n are the same moments calculated over n samples.

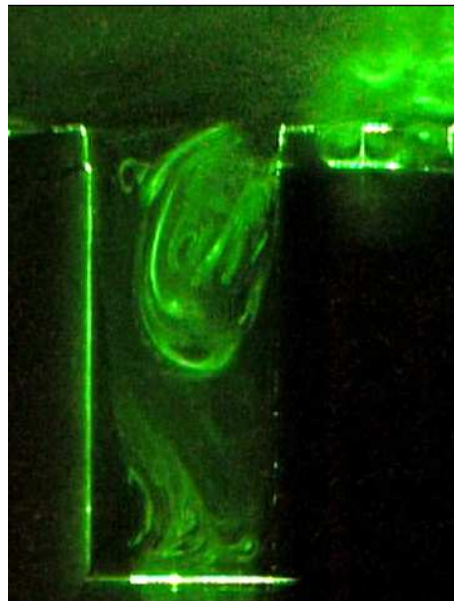


Figure 3.8: Flow visualization.

3.2.4 Flow visualizations

To realize flow visualization we injected nebulized olive oil particles as tracer element. Nebulized oil particles were brightened by means of a sharp laser blade. In such a way we could film the visualizations of turbulent coherent structures within the flow field (fig. 3.8). Flow visualizations are presented in the Annex 1.

INFLUENCE OF A TWO-SCALE
SURFACE ROUGHNESS ON A
NEUTRAL TURBULENT BOUNDARY LAYER



Figure 4.1: Urban geometries

4.1 Introduction

In case of a neutrally stratified flow, the main factors that characterize flow and dispersion over urban areas in the lower part of the atmospheric boundary layer are related to the role of the urban geometry, i.e. the shape, the orientation and the density of buildings. In a general way, it is usually assumed that an urban area acts on the atmospheric boundary layer flows as a rough surface. For that reason large part of the results obtained so far on passive scalar dispersion over rough surface are taken as reference. On that topic, FACKRELL and ROBINS (1982) performed an experimental investigation on the turbulent mass fluxes, as well as on the mean and fluctuating concentrations, of a passive scalar within a turbulent boundary layer. That study, which was carried for punctual ground level and elevated sources, provided a detailed analysis of the statistical properties of the near and the far field of passive scalar concentration. Similar experiments were performed by COPPIN et al. (1986) who estimated the passive scalar fluxes over a model plant canopy, by means of a three wire probe. More recently BRITTER et al. (2003) presented an analysis of the short-range dispersion from ground level sources, collecting experimental results obtained in different wind-tunnel, and emphasized the importance of empirical correction of theoretical models, in order to give better estimations of the plume behaviour. The dispersion from a ground-level line source was also studied by KASTNER-KLEIN and FEDOROVICH (2002), who evaluated the accuracy of mean concentration estimation given by simple mathematical models. In case of elevated sources, RAUPACH et al. (1983) and COPPIN et al. (1986) verified the accuracy of numerical simulation adopting a first order closure model.

In this study we will focus on urban-like roughness: we deal with roughness elements (simulating buildings) whose size H is not negligible compared to the boundary layer height δ . In fact this is one of the most important feature in urban dispersion studies, for two main reasons. Firstly because the scalings given by the similarity theory are based on the assumption that $\delta/h_s \rightarrow \infty$, being h_s the so

called ‘effective roughness length’(NIKURADSE, 1933) and depends on the buildings density (in a two-dimensional geometry on the ratio H/W): this is not always the case in urban areas. Secondly because the presence of large roughness elements over the earth surface imply that, in urban areas, the so called ‘roughness sub-layer’ (RSL) occupies a consistent part of the atmospheric boundary layer.

The increasing availability of detailed data giving building locations and heights means that we have detailed data for characterizing this roughness, but in fact, these data are often more detailed than can be used directly in operational models. The problem of converting such detailed geometrical information into an averaged parameter which represents the influence of the obstacles on the flow is not new; as far back as 1933 NIKURADSE (1933) performed a set of systematic experiments using isolated sand grains that were aimed at characterizing the relationship between the size of individual roughness elements and their influence on the flow. The urban surface is considerably more complicated (fig. 4.1), and different from other ‘natural’ surfaces in that it is generally composed of obstacles with distinctly separate scales - typically, for example, one might think of the scale of individual buildings, and then the scale corresponding to objects ‘chimneys, aerials, balconies etc ’) placed on those objects. This surface is also characterised by the fact that very often the large obstacles are not placed randomly on the surface, but are organised into more or less regular ‘blocks’, which define the streets (also having their own characteristic length scales) between them. The question, therefore, is to what extent a surface characterised by two very different, and separate, length scales, can be characterised by a single roughness length scale, and what value should such a length scale take? Clearly, the answer to this question will be useful in determining suitable values of the roughness length scale, given the data available from GIS databases.

Early studies of rough wall turbulent boundary layers had shown that the roughness length scale depends on both the height of the roughness elements and the spacing between them. If the elements are very closely packed then fluid is ‘trapped’ in the cavities between the elements, and has little influence on the flow above the elements. In this case, the effective roughness length does not depend on the actual height of the individual roughness elements. Correspondingly, the displacement height will be close to the physical height of the elements. This led PERRY et al. (1968) to define two types of roughness - d-type roughness, for closely packed roughness elements, and k-type roughness for more widely separated elements.

In the urban boundary layer the roughness elements consist essentially of individual buildings or groups of buildings, and the surface roughness can therefore be characterized in terms of the height of the obstacles (H) and the spacing between them (W). OKE (1987) provides a phenomenological description of the flow regimes in the lowest part of the boundary layer (below the inertial layer) as a function of the characteristic aspect ratio H/W of the obstacles. For low values of the aspect ratio ($H/W < 0.15$) the obstacles behave as isolated roughness elements, and the flow depends on the wake of the individual obstacles. If the obstacles are packed very close together ($H/W > 0.65$) then the flow tends to skim the tops of them, and so this is known as the skimming flow regime. This is broadly equivalent to the d-type roughness defined by PERRY et al. (1968). In the intermediate regime ($0.15 < H/W < 0.65$) the wakes of individual obstacles impact either on other obstacles or merge with other obstacle wakes, so this is known as the wake-interference regime, and is broadly equivalent to the k-type roughness defined by PERRY et al. (1968).

In reality the urban surface consists of roughness elements with a wide range of length scales, and the length scales H and W used by OKE (1987) essentially characterize the largest roughness elements in the surface. So the first important question that needs to be addressed is whether a single roughness scale can adequately represent the range of length scales typically encountered in an urban boundary layer, and if so, how this length scale should be defined. For example, RAUPACH (1992) proposed characterizing

the surface with a porosity factor λ which characterizes the local density of the obstacles, but this only takes into account the blockage created by the obstacles – it does not represent the influence of the spatial organization of the obstacles, nor the scale separation that is probably present. Specifically, we need to examine how the presence of smaller elements modifies the flow regimes and the similarity profiles that have been measured for single scale roughness. It is likely that the influence of the small scale roughness will vary, depending on the type of flow regime created by the large scale roughness. The aim of this study is therefore to investigate how the presence of small scale roughness elements modifies the flow and the dispersion of a passive or a passive scalar in a rough turbulent boundary layer, and how this depends on the form of the large scale roughness elements.

4.2 Experimental conditions

As explained in §3.1.2, we have simulated an idealized street geometry using an array of 2D parallel canyons, formed by a set of square section bars (0.06m x 0.06m) placed normal to the wind, as shown in fig 3.2. The influence of the roof roughness was studied by adding small scale 2D roughness elements (0.05m x 0.05m) to the tops of the bars. This is a highly simplified version of a real urban geometry, but it enables us to understand some of the basic phenomena, and this understanding can then be used to explain more complicated situations²⁷.

The spacing between the bars could be varied, and measurements have been performed for three values of the height to width ratio ($H/W=1, 2, 1/2$); these will be referred to as Configuration 1, 2 and 3 respectively. According to the classification proposed by OKE (1987), the first two configurations correspond to skimming flow, whilst the third condition corresponds to wake-interference flow. In all three configurations the experiments were carried out first without the small scale roughness (Configurations 1a, 2a and 3a) and then with the roughness (Configuration 1b, 2b, and 3b). Finally, in order to evaluate the effect of the ‘small roughness’ alone, we have studied another configuration consisting of a plane wall covered in the small roughness elements – this is referred to as Configuration 0b. So in each configuration the digit indicates the aspect ratio whilst the letter denotes the presence (‘b’) or absence (‘a’) of small scale roughness. Figure 4.2 provides an overview of the configurations studied.

These configurations have been chosen for two main reasons:

- they are representative of typical street aspect ratios in urban areas (in Fig. 4.3)
- they enable us to compare flow dynamics in the skimming regime and wake-interference regime (or d-type and k-type roughness).

The wall geometry is therefore characterized by the following length scales:

- the 2D obstacle height $H = 0.06\text{m}$
- the distance between the large obstacles W ($0.03\text{m} < W < 0.12\text{m}$)
- the small scale roughness at the top of the obstacles $h = 5\text{mm}$
- the distance between the small scale roughness elements $l = 8.75\text{mm}$.

²⁷Anyway, the simplification is not so drastic from all point of view, as long as most of the European cities have nearly uniform building height distribution in large part of their central areas (Paris, Lyon, Turin, Milan...). Uniformity is no longer present in suburban districts.

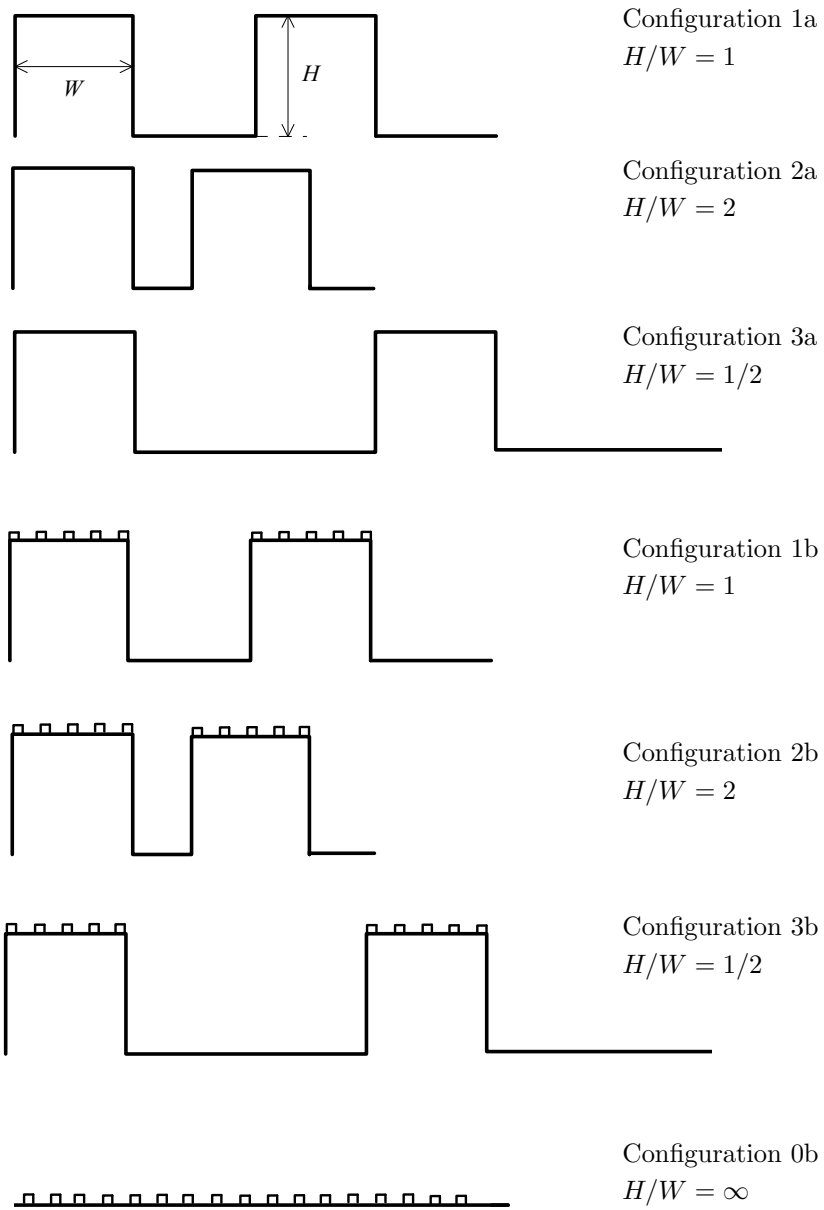


Figure 4.2: Geometrical configurations.

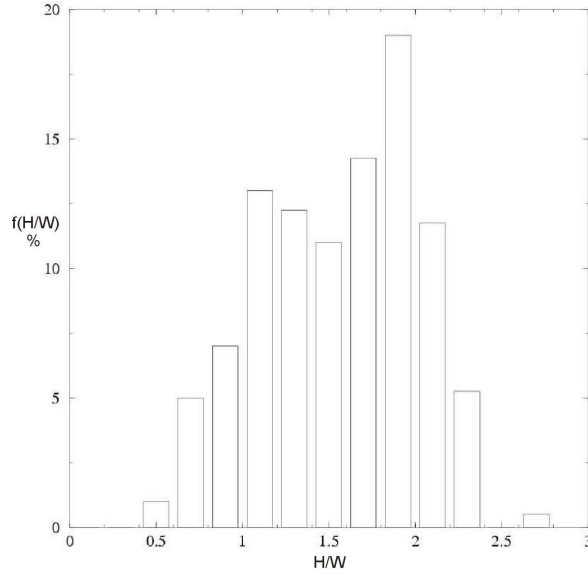


Figure 4.3: Distribution of the street aspect ratio H/W for a district in Lyon (VI Arr.), (Soulhac, 2000).

The dynamics of the flow will depend on both the scales imposed at the wall and another length scale related to the boundary layer thickness. The dimensions of the characteristic length scale of the simulated domain have been chosen to preserve a realistic ratio between the thickness of an adiabatic atmospheric boundary layer (which is of the order of 100m), a typical building height (which is of the order of 10m) and a smaller scale element at the top of the buildings such as a chimney or a roof (which is of the order of 1m).

The typical scale ratio between the wind tunnel model and reality is 1/166.

4.3 Hot wire anemometry velocity measurements

Velocities were measured by hot wire anemometry, using a single probe and an X-probe functioning as a constant temperature anemometer. The diameter of the wire was $5 \mu\text{m}$, and the acceptance angle of the X-probe was $\pm 45^\circ$. For the three configurations ($H/W = 1, 1/2, 2$), vertical profiles were measured at two locations (Figure 4.4):

- above the obstacle mid-point – type A profile
- at the centre of the cavity – type B profile

In all cases the experiments were performed first without the small scale roughness and then repeated with the additional small scale roughness.

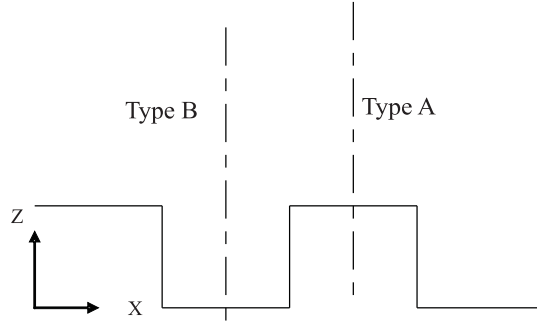


Figure 4.4: Vertical profile locations.

4.3.1 Characteristics boundary layer parameters

Configuration (H/W)	z_0 (mm)		u_* (m s^{-1})		d (mm)		E ($\text{m}^2 \text{s}^{-2}$)		n
	M1	M2	M1	M2	M1	M2	M1	M2	
1a (1)	0.51	0.31	0.37	0.33	55	55	$1.4 \cdot 10^{-2}$	$9.7 \cdot 10^{-1}$	0.21
1_R (1)	0.40		0.3		55		-	0.22	
2a (2)	0.14	0.13	0.31	0.30	59	59	$1.1 \cdot 10^{-2}$	$1.3 \cdot 10^{-2}$	0.18
2_R (2)	0.60		0.31		59		-		0.18
3a (1/2)	2.16	1.70	0.44	0.41	50	50	$8.0 \cdot 10^{-3}$	$2.6 \cdot 10^{-2}$	0.34
1b (1)	0.97	0.64	0.40	0.36	59	60	$3.7 \cdot 10^{-3}$	$1.8 \cdot 10^{-2}$	0.25
2b (2)	0.60	0.38	0.37	0.34	59	60	$1.1 \cdot 10^{-2}$	$1.9 \cdot 10^{-2}$	0.21
3b (1/2)	2.16	1.70	0.44	0.41	50	50	$8.0 \cdot 10^{-3}$	$2.5 \cdot 10^{-2}$	0.34
0b (∞)	0.60	0.38	0.37	0.34	60	60	$4.0 \cdot 10^{-2}$	$3.3 \cdot 10^{-2}$	0.21

Table 4.1: Estimation of u_* , z_0 , d and n by a best fit of the mean velocity profiles. The subscript R refers to the estimate given by RAFAILIDIS (1997) for the same obstacle configurations.

To begin with, we have analyzed the measured velocity profiles to determine the characteristic boundary layer parameters. In all cases the free stream velocity U_∞ at the top of the boundary layer was set equal to 6.7 m s^{-1} . We have assumed that the velocity profile has a logarithmic form (eq. 2.1) and we have computed the values of roughness height z_0 , friction velocity u_* and displacement height d from the measured mean velocity profiles. Several methods can be used to estimate the friction velocity u_* ; RAUPACH et al. (?) provides a review of some of these. We have analyzed our data using two of these methods – referred to here as Method 1 (M1) and Method 2 (M2) – to provide some check on the consistency of the estimates, and their sensitivity to the method, and to the noise in the data. The results are shown in Table I.

In Method 1 the logarithmic velocity profile is fitted to the measured profile by adjusting the values of

u_* and z_0 so as to minimize the sum of the differences between the theoretical and the measured points. The presence of large surface roughness elements has to be accounted for with a displacement height d which is also unknown *a priori*, and becomes a third variable to be estimated. The problem can therefore be defined as follows:

$$E = \sum_{n=N_1}^{n=N_2} \left[u_n - \frac{u_*}{k} \ln \left(\frac{z_n - d}{z_0} \right) \right]^2,$$

with

$$\frac{\partial E}{\partial u_*} = 0, \quad \frac{\partial E}{\partial z_0} = 0, \quad \frac{\partial E}{\partial d} = 0.$$

The inclusion of the displacement height as an unknown makes the problem non-linear, so that it is not possible to obtain an analytical solution for the 3 unknown parameters that will minimize the total error. However, if the displacement height is known, an analytical solution is readily obtained for u_* and z_0 . So the parameters were determined by assuming different values for d , within a predetermined range, solving analytically for u_* and z_0 so as to minimize the total error for that particular value of d , and then finally, selecting the solution set that gave the smallest total error. The dependence of the total error on the assumed displacement height is illustrated in Figure 4.5 for sample two velocity profiles from the two flow regimes – skimming flow (Figure 4.5-a) and wake-interference flow (Figure 4.5-b).

Since the logarithmic profile only applies to a fraction of the full velocity profile, it is necessary to limit the fitting procedure to a subset of the measured profile ($N_1 < n < N_2$), and the results can be sensitive to the range of points that are used in the fitting.

In the case of skimming flow the lower limit was set at the blending height of the two profiles (see §3.3) and the calculations were performed with different values of the upper limit, z_{up} . As the results in Figure 4.5-a show, the total error does vary with z_{up} , but the value of the displacement height which minimizes the total error is surprisingly insensitive to z_{up} .

In case of wake-interference flow the RSL occupies an important fraction of the profile (see §3.4), so we varied the lower level and kept the upper level constant at $z_{up} = 3H$, which can reasonably be considered as the top of the ‘constant-stress’ region (see §3.4). The total error has been plotted in Figure 4.5-b as a function of the displacement height, for different values of the lower level, and although the relationship is not as clear as for skimming flow, it is still possible to identify a displacement height which minimizes the total error and which is relatively independent of the assumed lower limit z_{low} .

The correct estimation of the displacement height d is very important for the analysis of the flow dynamics in boundary layers over surfaces occupied by large obstacles²⁸, because the appropriate length scale of the flow – given by the distance from the wall – is $(z - d)$, rather than z .

In the second method, the friction velocity $u_* = \sqrt{\overline{u'w'}}$ has been estimated by averaging the $\overline{u'w'}$ data in the lower part of the flow field, where the Reynolds stresses vary only slightly with respect to their average value. The two other parameters, z_0 and d , are then estimated through the best fit of the mean velocity profile with a logarithmic law, assuming the computed value of u_* .

For four of the configurations (1a, 1b, 3a, 3b) the two methods give total errors that are different by an order of magnitude, and the corresponding estimates of u_* and z_0 are also quite different. For two configurations (0b and 2b) the two methods give similar total errors, but the values of u_* and z_0 remain

²⁸Here ‘large’ means ‘not negligible’ compared with the boundary layer depth.

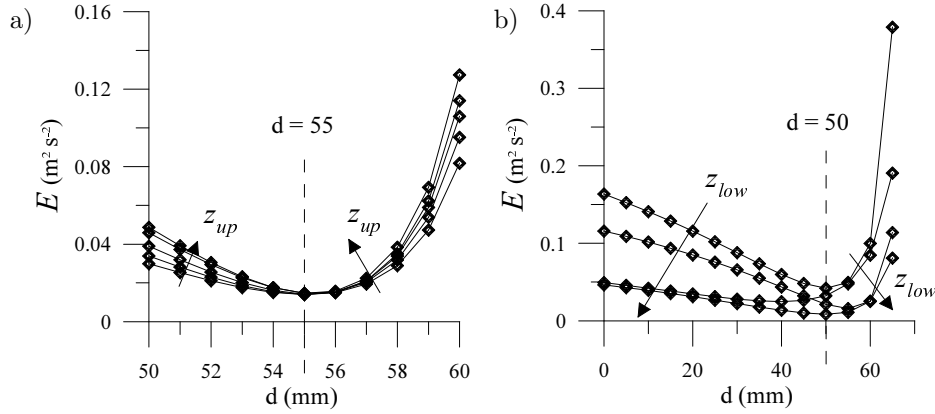


Figure 4.5: Estimation of the error ε given by a best fit of the mean velocity profiles: dependence of E on the displacement height for different vertical extensions of the fitted region.

quite different; this means that in the second method the value of z_0 has been adjusted to compensate for the non-optimal value of u_* , and that the total error is not a linear combination of the errors related to the two variables. For the Configuration 2, both the total errors given by the two methods and the values of the two variables are similar. In fact, by virtue of the minimization used in the second method, if the two methods give similar values for u_* they must inevitably give similar values for z_0 .

Table I also shows the values of the exponent n obtained by modelling the mean velocity profile with a power law of the form:

$$\frac{U(z)}{U_\infty} = \left(\frac{z-d}{\delta-d} \right)^n. \quad (4.1)$$

The measured roughness lengths are shown in Figure 4.6, for all experimental cases. This shows that, as the aspect ratio (H/W) decreases, there is a general tendency for the roughness length to increase, but this is most marked when the flow regime changes from skimming flow to wake-interference flow. Adding small-scale roughness elements increases the roughness length, but their influence diminishes as the aspect ratio decreases. The most plausible physical explanation for this is that when the obstacles are relatively close together (H/W large – skimming flow) the flow in the boundary layer does not have time to penetrate to the bottom of the cavity, so the effect on the boundary layer profiles is independent of cavity depth. The small scale roughness has an effective aspect ratio h/l of about 0.6 and this increases the roughness length, but once again, in skimming flow, this increase in z_0 is independent of H/W . In the wake-interference regime the roughness length is determined by the large scale obstacles, and the small roughness does not change it. This is probably because, in the case of larger cavities, instabilities generated within the shear layer at the interface between the recirculating regions within the cavity and the boundary layer flow have sufficient time to develop; the flow dynamics in the lower part of the boundary layer is then dominated by larger scale structures (of the order of the obstacle height, H) that engulf and dissipate the smaller scale structures generated by the smaller roughness elements.

The conditions used in this study are similar to those in a study performed at the Meteorologisches

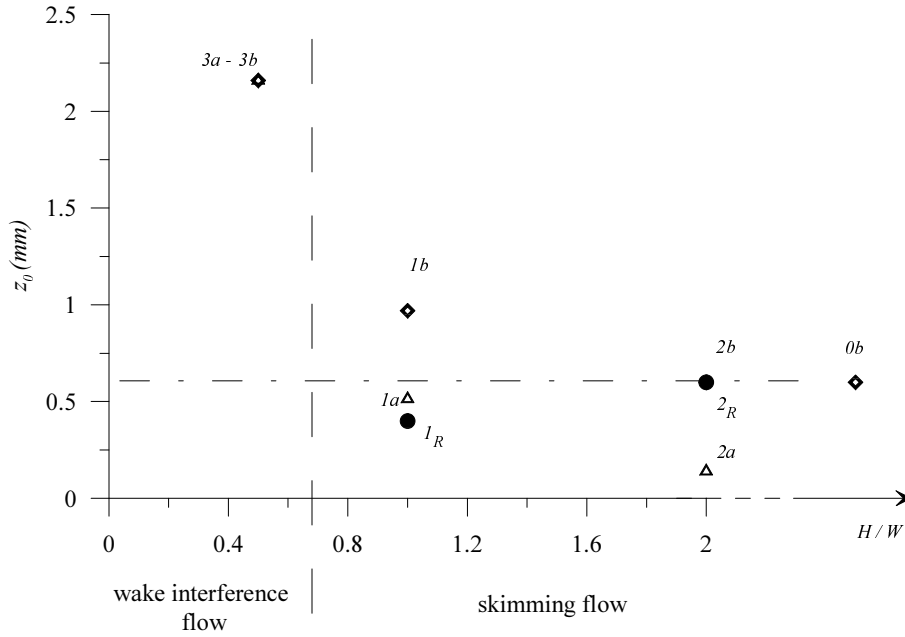


Figure 4.6: Dependence of the roughness length z_0 on the aspect ratio H/W , showing the influence of the smaller scale roughness. Results obtained by RAFAILIDIS (1997) are labelled as 1_R ($H/W = 1$) and 2_R ($H/W = 2$).

Institut of the Hamburg University, and reported in RAFAILIDIS and SCHATZMAN (1995) and Rafailidis (1997). The results from that work are compared with the results from this study in Table I and Figure 4.6. In the case of square cavities (Configuration 1) our results are generally in good agreement with the estimates provided by RAFAILIDIS (1997), for all flow parameters. But for Configuration 2a ($H/W = 2$) our results are significantly different from those reported by RAFAILIDIS (1997). More specifically in our experiments, an increase in aspect ratio (from $H/W = 1/2$ to $H/W = 2$) correspond to a decrease in both u_* and z_0 (from 2.16 mm to 0.14 mm for z_0 and from 0.44 m s^{-1} to 0.31 m s^{-1} for u_*). In the experiments of RAFAILIDIS (1997), however, an increase in H/W leads to increases in z_0 and u_* . The trend observed in the experiments reported here is similar to that reported by other authors (RAUPACH *et al.*, 1991; GRIMMOND and OKE, 1999), and is consistent with the idea that the drag exerted by the surface should be a minimum when the surface is flat, which correspond to the asymptotic cases $H/W \rightarrow 0$ and $H/W \rightarrow \infty$. In fact, in the isolated flow regime ($H/W < 0.15$), the value of z_0 increases for increasing values of H/W . Following the measurements of KOLOSEUS and DAVIDIAN (1966) for a two-dimensional roughness, z_0 reaches a maximum at $H/W \sim 0.25$, in wake-interference flow. For increasing values of H/W , in the wake-interference and in the skimming flow regimes, z_0 decreases and tends to zero for $H/W \rightarrow \infty$. As long as all configurations we are evaluating have $H/W > 0.25$, we expect that increasing aspect ratios have to correspond to decreasing value of z_0 , which is consistent with our measurements.

4.3.2 Wall similarity in the outer and in inertial regions

A further analysis of the results was concerned with their consistency with the assumption of *wall similarity*: the turbulent motion above the depends only on u_* (the friction velocity) δ (the boundary layer thickness) and z (the distance from the wall) provided that the Reynolds number is sufficiently large. If this assumption is valid then the vertical profiles of all the flow variables should collapse onto a single curve in the outer region of the flow if the velocities are scaled on u_* and the vertical distances are scaled on δ . This means

$$\frac{U_\infty - U}{u_*} = G(\eta), \quad \frac{\sigma_u}{u_*} = f_1(\eta), \quad \frac{\sigma_w}{u_*} = f_2(\eta), \quad \frac{\overline{u'w'}}{u_*^2} = f_3(\eta),$$

$$\frac{Sk_u}{u_*^3} = f_4(\eta), \quad \frac{Sk_w}{u_*^3} = f_5(\eta),$$

where $\eta = (z - d)/(\delta - d)$ is the vertical normalized coordinate, $Sk_u = \overline{u'u'u'}$ is the skewness of the longitudinal velocity, $Sk_w = \overline{w'w'w'}$ is the skewness of the vertical velocity and $G, f_1, f_2, f_3, f_4, f_5$ are invariant functions.

For the mean flow, the first relation is usually referred to as the mean defect law. As can be seen in figure 4.7-a, the data agree well with this relation: the mean velocity profiles demonstrate similar dependence on η and they are independent of the obstacle configuration and of the measurement location (type A and type B profiles).

The profiles for the turbulent quantities σ_u, σ_w , and $\overline{u'w'}$, as well as Sk_u and Sk_w show more scatter, particularly close to the ground (Figures 4.7 b-d), but overall the behaviour is similar both in the outer region and in the inertial region $0.1 < \eta < 0.2$ ²⁹.

The scatter close to the ground is partly due to the streamwise variation in wall roughness. In particular, concerning $\sigma_w, \sqrt{\overline{u'w'}}$ and Sk_w , the scatter in the data for low values of η is due mainly to the streamwise variations in the flow, in the wake-interference flow regime; this feature will be discussed §3.4.

The data have been plotted in this normalized form and are shown in Figure 4.7. The values of u_* and d used for the normalization were those obtained by Method 2; if the data are normalized using the estimates for u_* and d given by Method 1 then there is much greater variability between the profiles obtained for different experimental conditions.

On the same graph (Figure 4.7) we have plotted data obtained by RAUPACH et al. (1991) for flows over different kinds of wall roughness and by KROGSTAD and ANTONIA (1999) for rod-mesh roughness. Our measured profiles of σ_u, σ_w and $\overline{u'w'}$ agree well with those presented by RAUPACH et al. (1981), over the whole depth of the boundary layer. The measured profiles also agree well with the data of KROGSTAD and ANTONIA (1999) for the mean velocity defect law (Figure 4.7-a), the second and third order moments of the horizontal fluctuating velocity (Figures 4.7-b and -d) and for the Reynolds stress (Figure 4.7-d). However there are significant differences between the measured profiles of the vertical fluctuating velocities and those reported by KROGSTAD and ANTONIA (1999) for both the second and third order moments (Figures 4.7-c and f).

The differences in the profiles of σ_w are probably related to the differences that are also evident in the profiles of the skewness of the vertical velocity (Figure 4.7-f). KROGSTAD and ANTONIA (1999) suggested

²⁹According to the theory, the inertial region is a buffer layer between the inner and the outer part of the flow field, where both scalings apply – the outer scaling $\eta = (z - d)/\delta$ and the inner scaling $\zeta = (z - d)/z_0$.

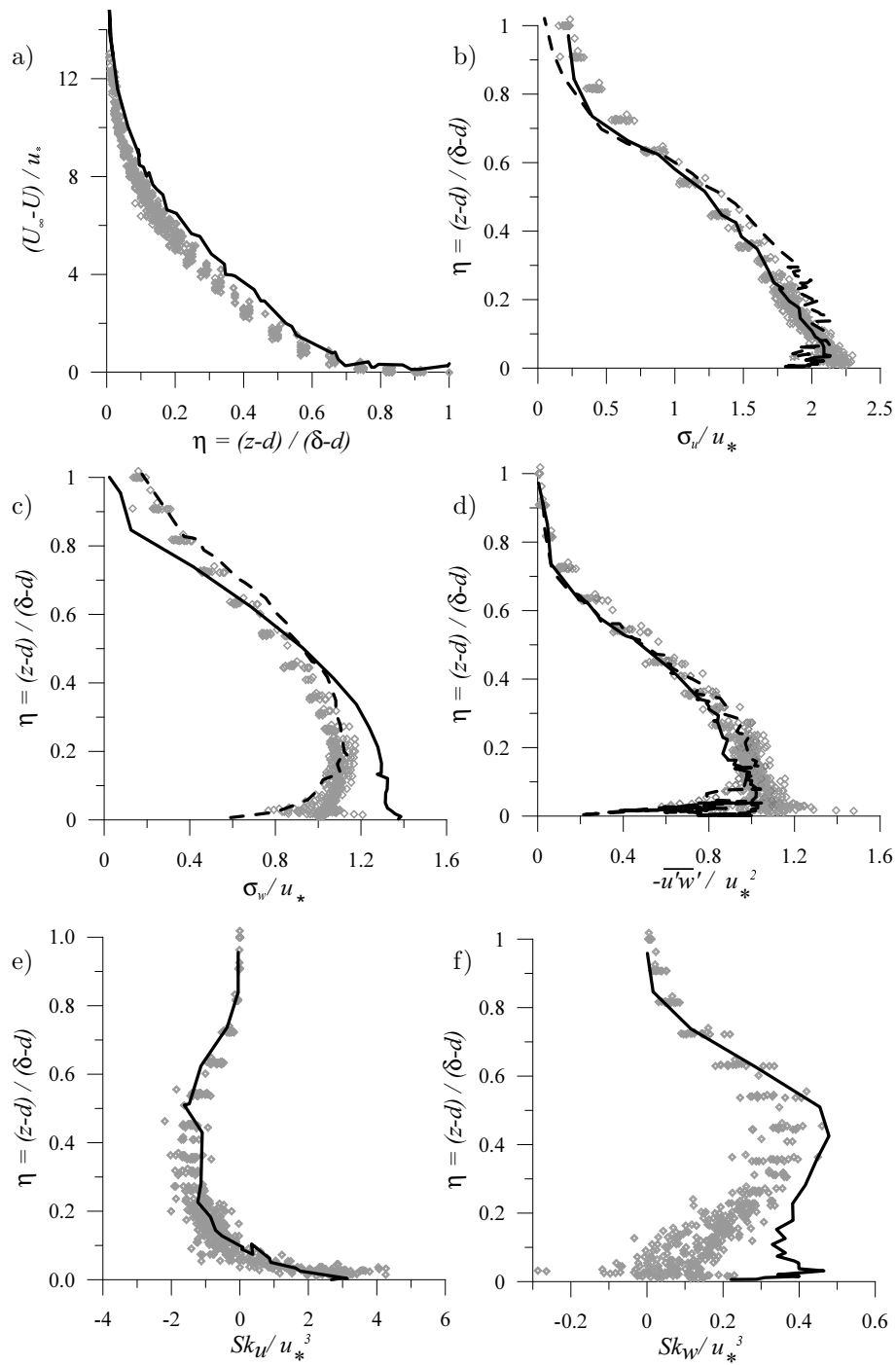


Figure 4.7: Normalized velocity profiles. (a) Mean velocity defect law, (b) σ_u (c), σ_w (d), $\overline{u'w'}$ (e), Sk_u (f), Sk_w . Diamonds: data from this study; solid line: KROGSTAD and ANTONIA (1999); dashed line: RAUPACH et al. (1991).

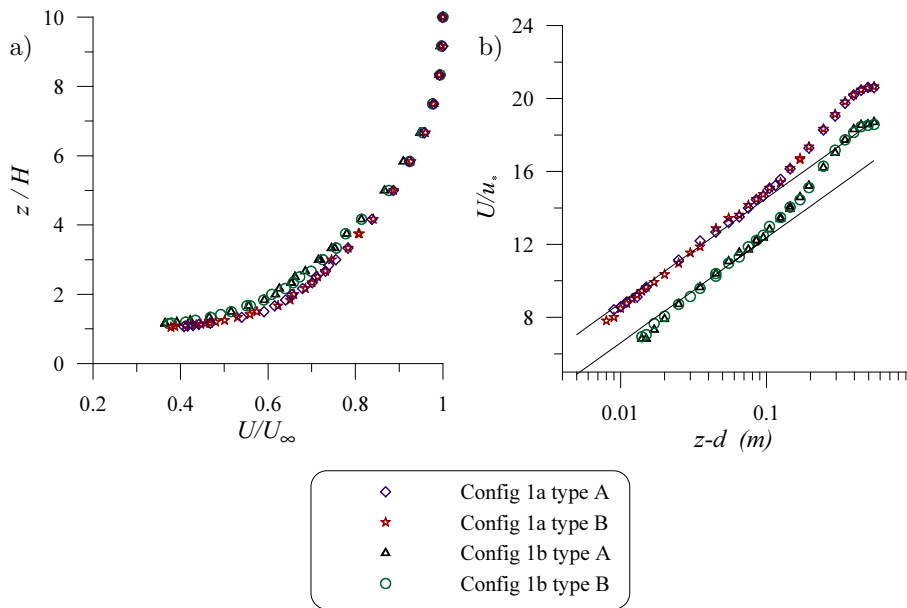


Figure 4.8: Configuration 1; (a,b) dimensionless vertical profiles of horizontal mean velocity.

that the skewness of the vertical velocity represented the dominant diffusion term for the fluctuating vertical velocities σ_w , and the values of Sk_w measured by them in the region close to the wall do indeed correspond to a flatter profile of σ_w , indicating a more rapid diffusion of σ_w . It is interesting to note that both our profile and that measured by KROGSTAD and ANTONIA exhibit a local minimum at a short distance from the wall; this means that there is a counter gradient diffusion of σ_w slightly further out, and this does indeed correspond to negative values of Sk_w in our profile. However the profile of Sk_w measured by KROGSTAD and ANTONIA does not become negative in this region, this may be related to the fact that the local minimum in their profile is very weak. This result illustrates that the second and the third moments of the vertical velocity are very sensitive to the geometry of the wall. They also show that flows with different wall roughness can have the same Reynolds stress and mean velocity profiles, but different r.m.s. velocity fluctuations. As pointed out by ANTONIA and KROGSTAD (2001), this provides experimental evidence of the limits of the similarity theory.

4.3.3 Skimming flow regime

The influence of small-scale roughness

The measurements of roughness length as a function of the aspect ratio (Figure 4.6) show that the small scale roughness has the greatest influence in the skimming flow regime. To investigate this in more detail, we have compared the velocity profiles for the flow regime without small scale roughness (Configurations 1a and 2a) with the corresponding velocity profiles for the case with small scale roughness (Configurations 1b and 2b). We also compare the profiles measured above the obstacles (Type A) with those measured

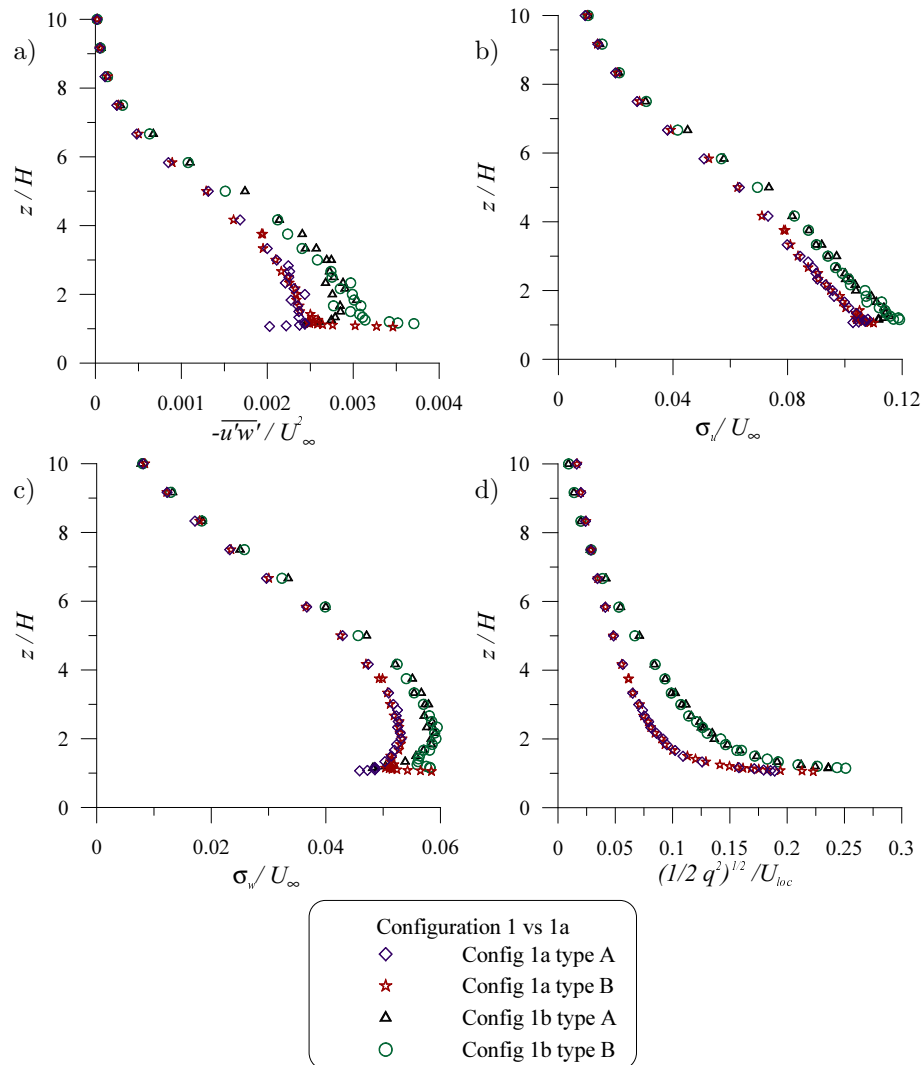


Figure 4.9: Configuration 1; dimensionless vertical profiles of (a) Reynolds stress (b) r.m.s. of horizontal velocity (c) r.m.s. of vertical velocity (d) turbulence intensity.

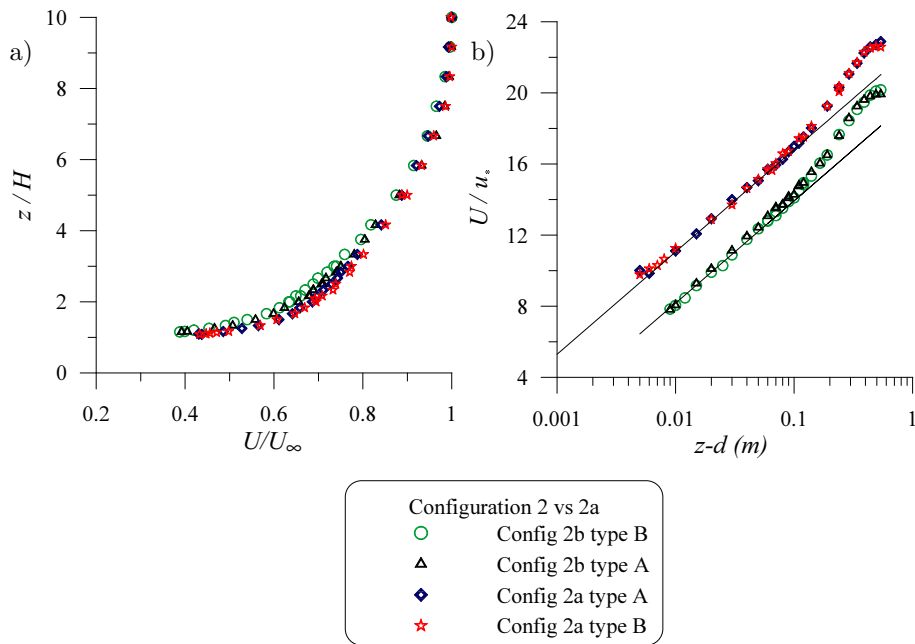


Figure 4.10: Configuration 2; (a,b) dimensionless vertical profiles of horizontal mean velocity.

above the cavity (Type B). The mean velocity profiles for the two configurations are plotted in Figures 4.8 a-b and 4.10 a-b, as functions of different dimensionless variables. The first important conclusion from these profiles is that the mean velocity profile varies very little between the obstacle (Type A) and the cavity (Type B), and the addition of small-scale roughness to the obstacle surfaces has a much greater effect. In fact this feature indicates slight interaction between the cavity and the overlying boundary layer flow, and this is also evident in the profiles of fluctuating velocities; this will be discussed at the end of this section.

For both configurations, the influence of small scale roughness on the mean velocity profile extends into the overlying flow, up to the outer region of the boundary layer. The profiles of turbulent quantities (Figures 4.9 and 4.11) show more variability, both in the streamwise direction (Type A and Type B profiles) and in the influence of small scale roughness. The impact of the small scale roughness is perhaps more evident in the profiles of normalized turbulent kinetic energy – the ratio between the square root of the turbulent kinetic energy $(1/2q^2)^{1/2} = [1/2(\sigma_u^2 + \sigma_w^2)]^{1/2}$ and the local mean velocity value U_{loc} – where it is clear that the presence of the small scale roughness results in much higher turbulence generation at the surface Figures (4.9d and 4.11d). For Configuration 1b the additional kinetic energy persists through the boundary layer, whereas for Configuration 2b it is damped out at about half of the boundary layer thickness.

In general terms, results for Configuration 2a are very similar to those for Configuration 1a. There is very little difference in the mean velocity profiles measured over the obstacle and over the cavity (Figures 4.10 a-c), which is consistent with the idea that the characteristic time scale for the turbulence must

be longer than the typical time to traverse the cavity. It is likely that the characteristic time for the turbulence does not change much between Configuration 1a and 2a, but the advection time decreases by a factor of about 2. So the timescale ratio will increase by a factor of 2. The addition of small scale roughness has a similar effect on the mean velocity profile, although the differences in the mean velocity profiles are confined to the lower half of the boundary layer. This difference is more obvious when the profiles of turbulent quantities are compared – in Configuration 1a the two profiles are noticeably different up to a height of $z/H \sim 8$, whereas in Configuration 2a the differences disappear at $z/H \sim 5$. There seem to be several effects involved here.

To begin with, the turbulence levels close to the surface, and in the absence of small-scale roughness, are slightly higher in Configuration 1a than Configuration 2a. In both cases the small scale roughness generates a big increase in the turbulent quantities close to the surface, but the pre-existing difference in turbulent levels persists – the turbulence is greater in Configuration 1a than in Configuration 2a. In the first case, the increase in turbulence levels penetrates to the top of the boundary layer ($z/H \sim 8$) whereas in the second case it is confined to the lower half ($z/H \sim 5$). It is worth noting that these difference do not agree with the notion of wall similarity. In fact, the fluctuating flow quantities for Configuration 1a and Configuration 2a (Figure 4.8 and Figure 4.10) show that the effect of small roughness is almost the same for the two configurations.

These differences are not entirely compatible with the notion of wall similarity: in both Configuration 1 and Configuration 2 the effect of the small scale roughness is to increase the values of the fluctuating velocities in the lower part of the flow field by about $\sim 20\%$. Now from similarity theory we would expect that, if there is no variation in boundary layer depth and blending height between Configuration 1 and Configuration 2, then the increase in the turbulence levels caused by the small scale roughness should be the same for both configurations. However this is not the case, and we have to conclude that the small scale roughness also affects the rate at which surface generated turbulence is transported away from the surface. This should be visible in differences in the spectral representation of the turbulence for the two configurations.

This diffusion of turbulence will depend principally on the large-scale eddies in the boundary layer and it seems reasonable to conclude that these contain more energy in Configuration 1a compared with Configuration 2a – this is probably part of the reason for the higher turbulence levels in Configuration 1a than Configuration 2, for the case without small scale roughness. Some circumstantial support for this explanation can also be found in the fact that the Reynolds stresses close to the surface are much higher for Configuration 1a (Figure 4.8-a) than for Configuration 2a (Figure 4.10-a) and the variation between the profiles over the cavity and over the obstacle are greater for Configuration 1a than for Configuration 2a.

It should be noted that, in Configuration 2, there is an anomaly in the Reynolds stress profiles close to the surface, where the Reynolds stress appears to decrease. This is certainly unphysical; the high shear in this region should lead to an increase in Reynolds stress, and this has indeed been observed in many experimental studies (MULHEARN and FINNIGAN, 1978; MULHEARN, 1978; RAUPACH *et al.*, 1980). The most likely explanation for this is a measurement error due to the probe velocity acceptance angle ($\pm 45^\circ$), as documented by PERRY *et al.* (1986).

The normalized profiles of Sk_u over the obstacle (Type A) and over the cavity (Type B) have been plotted in Figure 4.12-a, for Configuration 1 (i.e. without the additional small-scale roughness). The profiles are almost identical, as they were for the second order moment σ_u (Figure 4.9-b). On the other hand, the skewness of the vertical velocity (Sk_w , Figure 4.12-b) does exhibit streamwise variations, in the vary lowest part of the profiles, similarly to the second moment σ_w (Figure 4.9-c) and the Reynolds

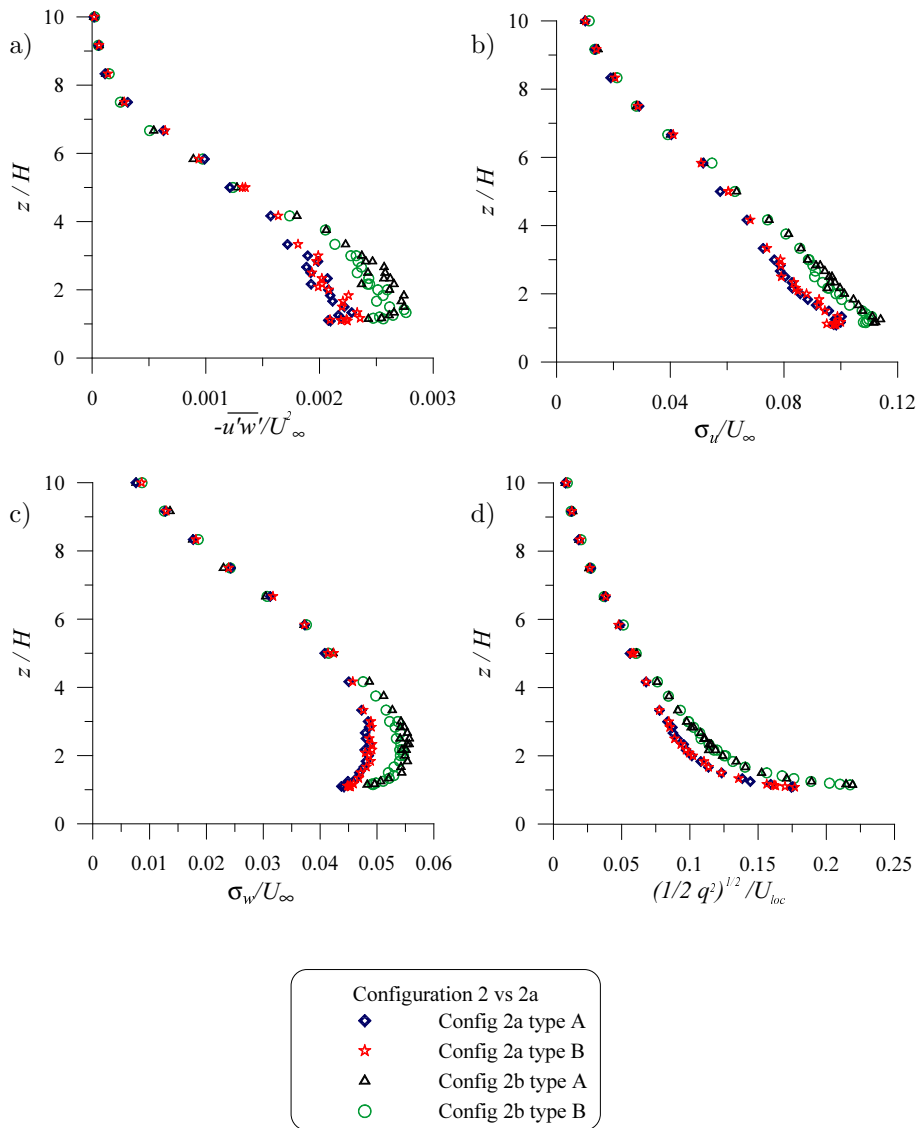


Figure 4.11: Configuration 2; dimensionless vertical profiles of (a) Reynolds stress (b) r.m.s. of horizontal velocity (c) r.m.s. of vertical velocity (d) turbulence intensity.

stress (Figure 4.9-a); the skewness is much greater over the cavity than over the obstacle. Physically, this means that there must be significant peaks in the vertical velocity out of the cavity, possibly related to eddies in the shear layer at the top of the cavity impacting on the upwind face of the next obstacle. The addition of small scale roughness increases the absolute values of Sk_u (Figure 4.12-c) in the whole depth of the boundary layer, even if it has very little effect in the lowest part of the flow field, over the obstacle; there is a small increase in the skewness close to the surface and a larger increase in the absolute value of the negative skewness further away from the surface, but the changes are small compared with the scatter of the data. The profiles for Sk_u over the cavity are almost identical to those over the obstacle, so they have not been plotted here. The effect of the small roughness on the skewness of the vertical velocity Sk_w (Figure 4.12-d) is much more marked; the skewness is reduced – almost to zero – over the obstacle and greatly enhanced in the outer part of the boundary layer. In this sense, lower values of Sk_w in case of Configuration 1a (compared with Configuration 1b) suggest that the presence of small roughness partially ‘shelters’ the cavity from the external flow, reducing the intermittency of the momentum exchange. The small scale roughness also acts to reduce the streamwise variation in skewness, as Figure 4.12-e illustrates: the differences that were evident in the lower part of the boundary layer, in the absence of small scale roughness (Figure 4.12-b) have disappeared completely.

Finally, it is worth noting that, in the skimming flow regime, the roughness sub-layer (the region where horizontal inhomogeneities appear) is very thin, compared with the obstacle height H , and the small roughness elements do not seem to thicken it significantly. In order to give an estimation of the blending height, we can consider that $z_* \sim 7/6H$ in Configuration 1a and $z_* \sim H$ for Configuration 2a (non stream-wise variations could be detected). In fact, the depth of the roughness sub-layer is of the order of $(H - d)$, which can be assumed a rough estimate of the length scale of typical vortical structures shed by the shear layer at the top of the cavity. As already mentioned, this feature suggest weak interaction between the cavity flow and the external boundary layer flow, implying that the characteristic time scale (T_t) for boundary layer flow close to the surface ($z = H$) is much longer than the time scale for the transit across the cavity ($\sim W/U_{loc}$).

Configuration 0b

As the spacing between the obstacles is decreased ($W \rightarrow 0$), the ratio $H/W \rightarrow \infty$, and the flow becomes identical to that over a continuous flat plate, with a displacement height d equal to the obstacle height (the origin of the velocity profile is taken at the base of the obstacles). For the case of small roughness elements on large obstacles the limiting case for $H/W \rightarrow \infty$ is therefore small roughness elements on a flat plate, located at a height H above the base of the obstacles. This corresponds to Configuration 0b, which is therefore the limiting case ($H/W \rightarrow \infty$) for the skimming flow regime studied here in Configurations 1b and 2b. It is instructive to compare the profiles for Configuration 0b with those for Configuration 2b, to isolate the influence of the small scale roughness.

Firstly, the mean velocity profiles for the two configurations are almost identical (Figures 4.13a-b) showing that for skimming flow with $H/W = 2$ the displacement height has become equal to the obstacle height. This confirms the results previously obtained by RAFAILIDIS (1997).

The profiles of horizontal fluctuating velocities σ_u/U_∞ are very similar (Figure 4.13d) – there is very little difference between the profiles over the cavity and the obstacle (2b type A and 2b type B) and the profile for the small-scale roughness (0b).

Differences can be detected for the vertical fluctuating velocities σ_w/U_∞ , as shown in Figure 4.13e. For Configuration 2b, the vertical fluctuating velocities slightly exceed the vertical fluctuating velocities

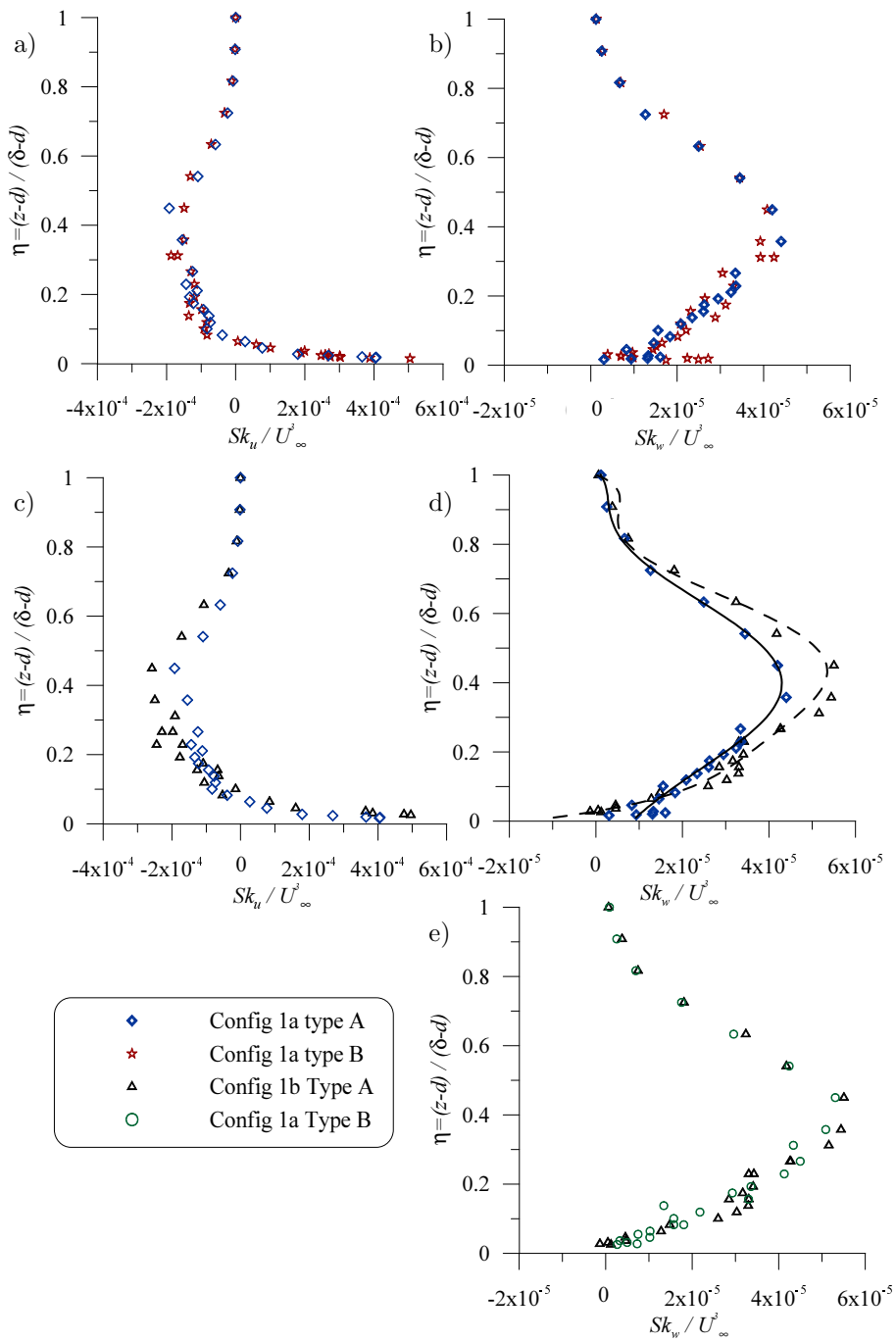


Figure 4.12: Configuration 1. (a) Profiles of Sk_u over the obstacle (Type A) and over the cavity (Type B) without small scale roughness. (b) Profiles of Sk_w over the obstacle (Type A) and over the cavity (Type B) without small scale roughness. (c) Profiles of Sk_u over the obstacle (Type A) with and without small scale roughness. (d) Profiles of Sk_w over the obstacle (Type A) with and without small scale roughness, the experimental curves are fitted by means of a 4th order polynomial – solid line for Configuration 1, dashed line for Configuration 1b. (e) Profiles of Sk_w over the obstacle (Type A) and over the cavity (Type B) with small scale roughness.

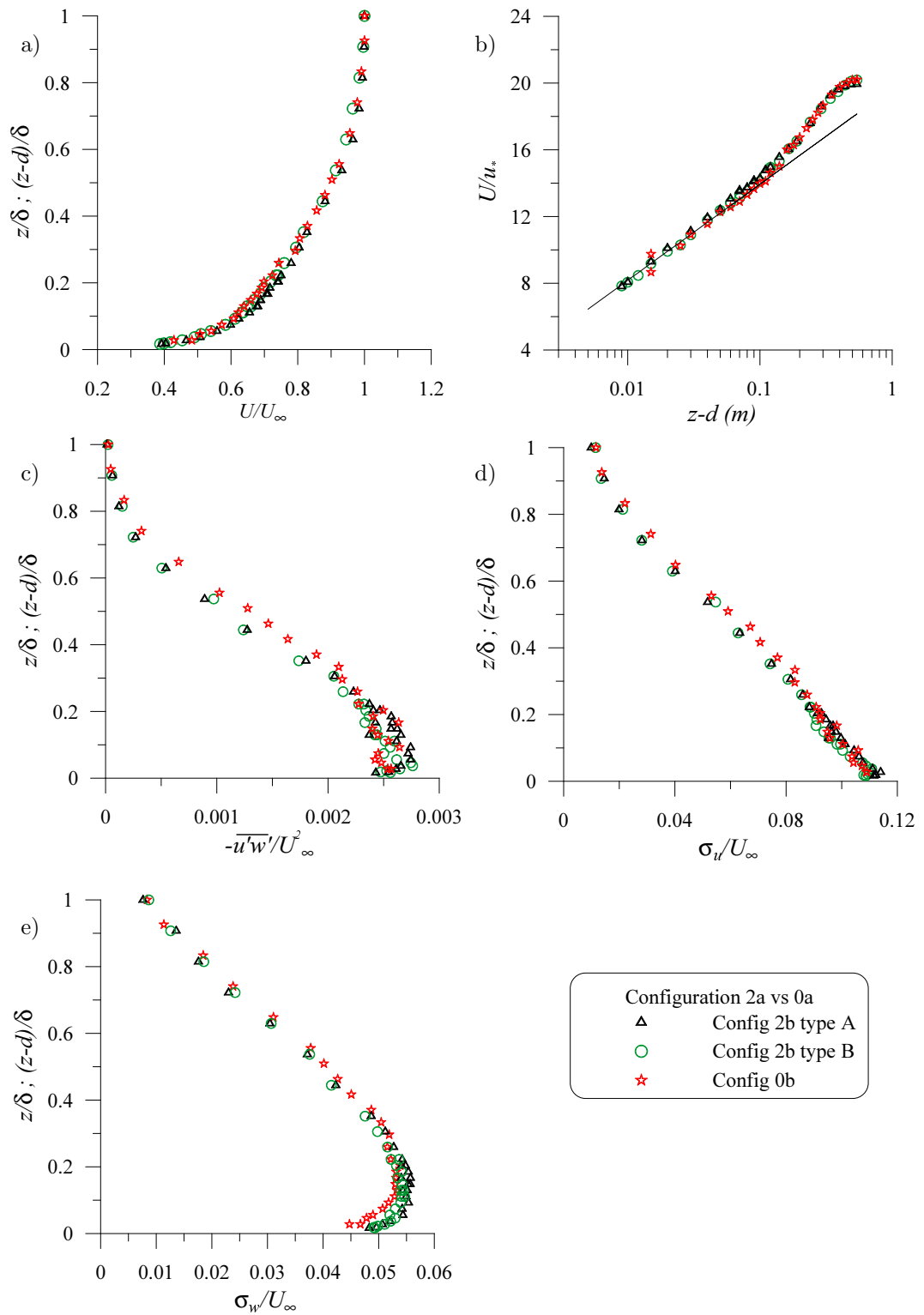


Figure 4.13: Configuration 0b and Configuration 2b; (a) mean horizontal velocity; (b) mean horizontal velocity plotted on a log scale – the solid line is the estimated logarithmic profile; (c) Reynolds stress (d) r.m.s. of the horizontal velocity; (e) r.m.s. of the vertical velocity.

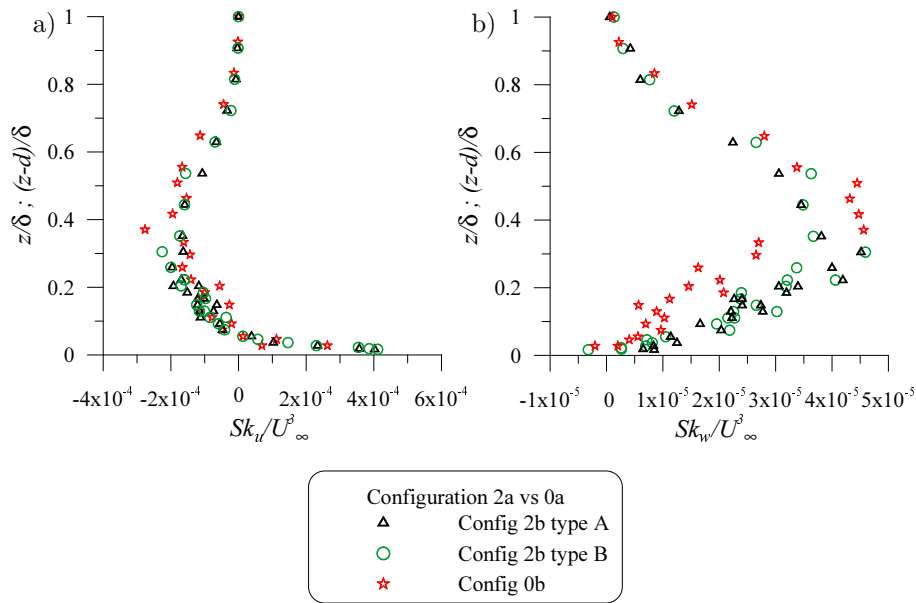


Figure 4.14: Vertical profiles of Sk_u (a) and Sk_w (b) for Configurations 2b and 0b.

measured in Configuration 0b, and this difference extends up to half the height of the boundary layer. There are much greater differences in the profiles of the skewness of the vertical velocity (Figure 4.14b), which shows that the skewness close to the wall is much lower in Configuration 0b than in configuration 2b. Further from the boundary ($z/\delta \sim 0.4$) this effect is reversed.

It is more difficult to distinguish any consistent difference between the Reynolds stress profiles for Configuration 2b (Types A and B) and Configuration 0b, because of the scatter of the data (Figure 4.13c). If we accept that the average Reynolds stress in this lower part of the boundary layer does not differ much between the three profiles, then it follows that the drag exerted by the boundary on the flow does not vary much either, and therefore that the cavity does not have any influence on the drag. This agrees with the idea proposed by PERRY (1968) that in the skimming flow regime all flow variables (blending height, effective roughness length, friction velocity...) should be independent of the ratio H/δ . It might appear somewhat paradoxical that the presence of the cavity appears to increase slightly the vertical fluctuating velocities, but to have almost no effect on the horizontal fluctuating velocity and the Reynolds stress. But in fact this is consistent with results of other researchers, e.g. KROGSTAD (1999) and ANTONIA (2001) and can be directly related to limits of the similarity theory discussed in §3.2.

4.3.4 Wake-interference flow

Configuration 3a vs 3b

The velocity profiles for the wide cavity (Configuration 3a, $H/W = 1/2$) are very different from those for the narrower cavities (Configurations 1a and 2, with $H/W = 1$ and $H/W = 2$ respectively) and this

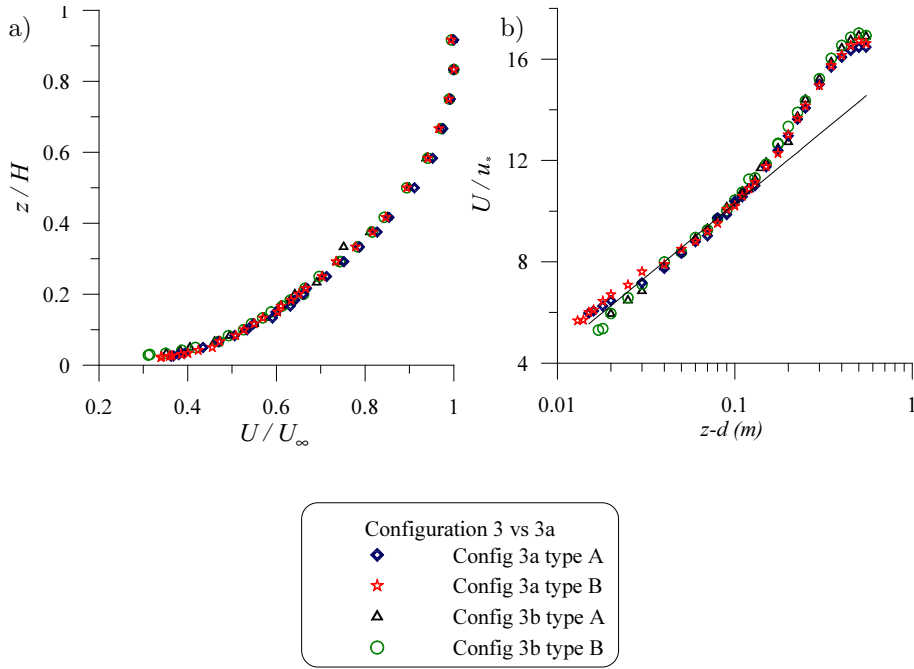


Figure 4.15: Configuration 3; (a,b) dimensionless vertical profiles of horizontal mean velocity.

is indicative of a major change in the flow regime. Instead of just ‘skimming’ the top of the obstacles and the cavity, the external boundary flow interacts with the flow in the cavity, and as a result the velocity profiles (Figure 4.15 and Figure 4.16) are very different from those for the other configurations.

The small scale roughness appears to have hardly any influence on the characteristic velocity profiles; only the profile of average horizontal velocity shows any discernible and consistent difference, and even then this can only really be detected in the logarithmic plot (Figure 4.15-b). The additional small scale roughness reduces the vertical gradient of the horizontal velocity in a region very close to the wall, compared with the standard logarithmic profile, and the depth of this region is of the same order as the height of the roughness element (h). This may be due to an enhanced diffusion of momentum, confined to a very thin layer immediately above the obstacles.

This is the only discernible effect of the small scale roughness; all the other profiles (Reynolds stress, σ_u , σ_w , turbulence intensity – Figures 4.16 a-d) seem to be insensitive to the presence of small scale roughness. It is possible that instabilities generated within the shear-layer at the interface between the cavity and the external flow have sufficient space to evolve and grow to envelope and dissipate the smaller scale structures that are generated by the small roughness elements. In this case the boundary layer is dominated by the dynamics of the larger eddies, with typical length scales which are large in comparison with the small roughness dimension.

The profiles of Reynolds stress (Figure 4.16-a) and r.m.s. of vertical velocity (Figure 4.16-c) show significant streamwise variations, but no such variation can be detected in the profiles of horizontal

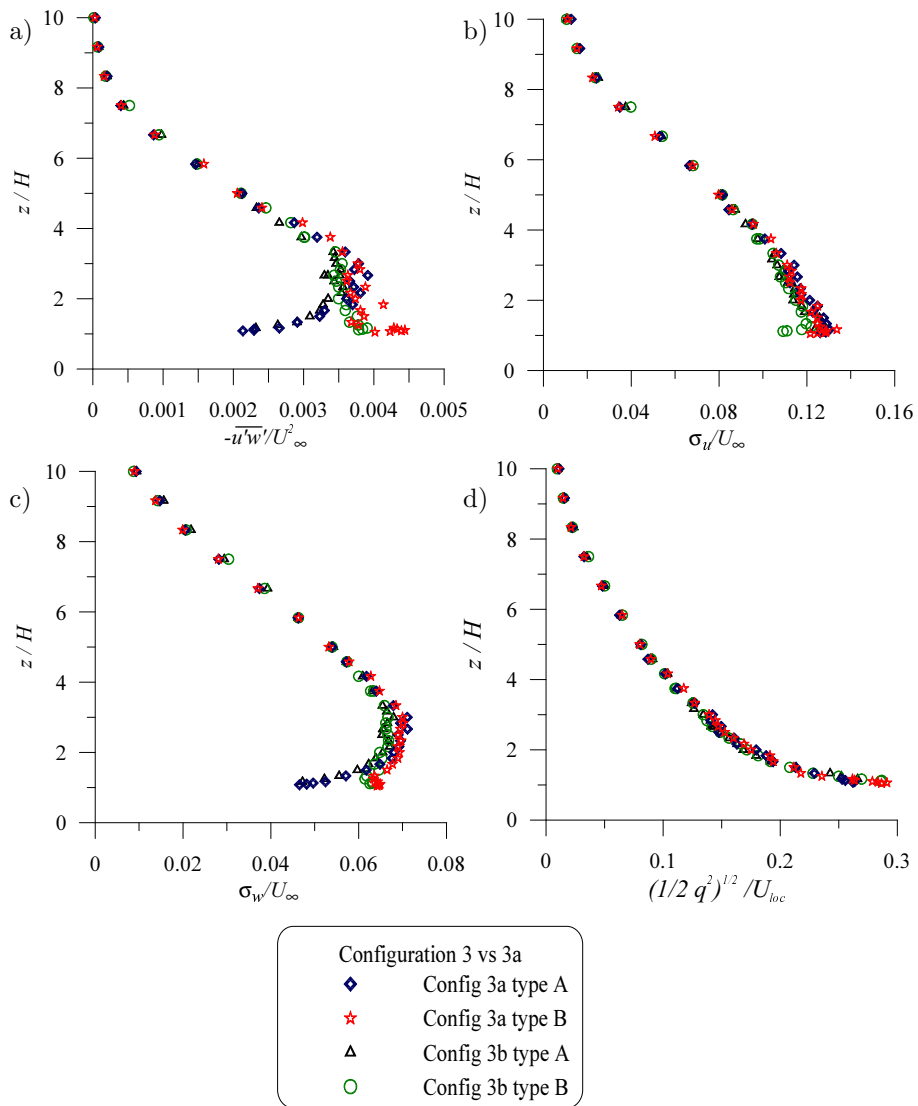


Figure 4.16: Configuration 3; dimensionless vertical profiles of (a) Reynolds stress (b) r.m.s. of horizontal velocity (c) r.m.s. of vertical velocity (d) turbulence intensity.

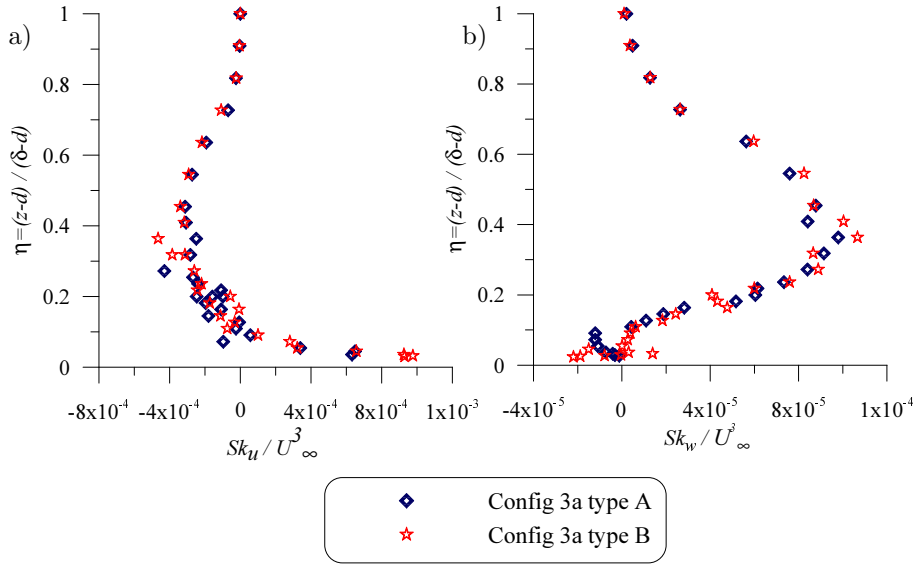


Figure 4.17: Configuration 3. Third order moments of horizontal Sk_u and vertical Sk_w fluctuating velocities in Configuration 3a. Effects of different horizontal location of the measured profiles on Sk_u (a) and Sk_w (b).

mean velocity (Figure 4.15-a and Figure 4.15-b). The profiles of horizontal mean velocity were also measured using a single probe to check that the absence of streamwise variations was not an artifact of the measurements. Since there are no streamwise variations in the mean and fluctuating horizontal velocities, we can write the streamwise component of the Navier-Stokes equation as:

$$\overline{w} \frac{\partial \overline{u}}{\partial z} = -\frac{1}{\rho} \frac{\partial \overline{p}}{\partial x} - \frac{\partial}{\partial z} \overline{u'w'}, \quad (4.2)$$

where \overline{u} and \overline{w} are the mean longitudinal and vertical velocity, \overline{p} the mean pressure and we have neglected viscous terms.

Now in the lower part of the boundary, over the obstacle, $\frac{\partial \overline{p}}{\partial x}$ and $\frac{\partial}{\partial z} \overline{u'w'}$ will be positive; since $\frac{\partial \overline{u}}{\partial z}$ is also positive, there must be a small mean vertical velocity away from the surface toward the interior of the flow field. Conversely, over the cavity $\frac{\partial \overline{p}}{\partial x}$ and $\frac{\partial}{\partial z} \overline{u'w'}$ will both be negative, and there will be a small mean vertical velocity towards the interior of the cavity. This will therefore generate a undulation of the streamlines close to the boundary. A rough estimation of the order of magnitude shows that the vertical velocity will be very small; in our experiments it could well be masked by the blockage effect of the gantry that supports the instrumentation.

The second and third order moments of the horizontal velocity (Figures 4.16-b and 4.18-a) do not seem to vary in the streamwise direction, but this is not true for the second and third order moments of the vertical velocity (Figure 4.16-c and Figure 4.18-b) and the Reynolds stress (Figure 4.16-a). For $\overline{u'w'}$

and σ_w the biggest streamwise variation in the profiles occurs close to the wall, in the region $0 < z/H < 4$, whereas for Sk_w the major variations occur at $\eta \sim 0.4$.

The streamwise variation demonstrates that the RSL in the wake-interference regime occupies a much larger fraction of the boundary layer than in the skimming flow. In the wake-interference configuration the RSL extends up to a height of about H – the obstacle height – so the blending height z_* is about equal to $2H$. It is also worth noting that within the RSL the skewness the vertical velocity profiles Sk_w (Figure 4.18 b) assumes both positive and negative values. This is the case for the other configurations presented here, and it suggests that the dynamics of the RSL are significantly different from those of the rest of the boundary layer.

4.4 Particle image velocimetry measurements

In order to investigate the flow structure of the lower part of the boundary layer, we used a PIV system to measure the velocity field in a domain that included the cavity and the overlying region. The PIV measurements domain is a square, with a lateral dimension of $2H$. We shall analyze the flow within the cavity in chapter 5. We focus here on the flow field developing just above it, i.e. for $H < z < 2H$.

The adopted reference frame work assumes $z = 0$ at the bottom of the cavity (as usual) and $x = 0$ at the cavity center, for whatever cavity geometry.

4.4.1 Horizontal inhomogeneities in the lower part of flow field

In fig. 4.18-4.21 are compared PIV and hot-wire anemometry measurements.

In terms of mean velocity values, PIV measurements detects horizontal inhomogeneities that we could not find by means of hot-wire anemometry³⁰. In configuration 1a and configuration 3a, for example, the mean velocity vertical gradient observed at the obstacle mid-height is greater than that observed at the centre of the cavity.

The best agreement between PIV and hot-wire anemometer results is achieved in configuration 2a ($H/W = 2$), when the flow has the lowest level of turbulence. On the other hand, the agreement is least satisfactory for configuration 3a³¹.

The PIV Reynolds stress profiles show a higher dispersion of data compared to those of the hot-wire anemometer (especially for configuration 3a).

In agreement with previous hot-wire anemometer results, even in this case, we can assert that:

- in skimming flow regime the roughness sub-layer depth is smaller than obstacle height, $\sim 0.1H$ in configuration 2a, and $\sim 0.2H$ in configuration 1a;
- the presence of small roughness increases slightly the roughness sub layer depth (on the order of the small roughness size $\sim h$) ;

³⁰As mentioned in Chapter 3, while approaching obstacle roof level, hot wire anemometry measurement errors arise, as long as the X-probe we have been using has an acceptance angle of 45° , which does not allow much precision close to the surface.

³¹As a general consideration we can assert that our PIV measurements tend to overestimate the velocity fluctuation and underestimate the mean velocity, if compared to hot-wire anemometry results; this not in agreement with the usual behaviour of PIV measures, which tend to underestimate velocity measurements, if compared with hot anemometer measurements (ADRIAN, 1991).

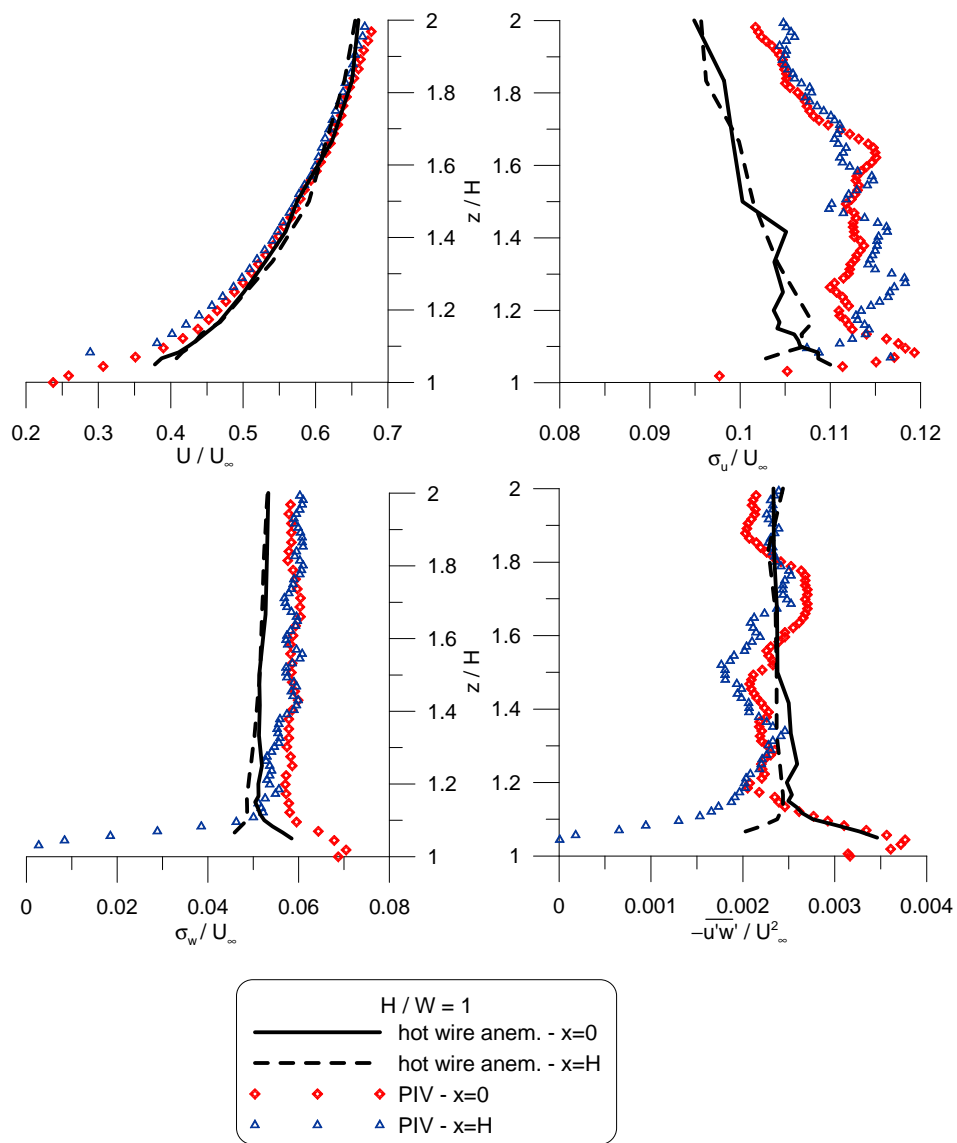


Figure 4.18: Comparison between hot-wire anemometry and PIV measurements, configuration 1a.

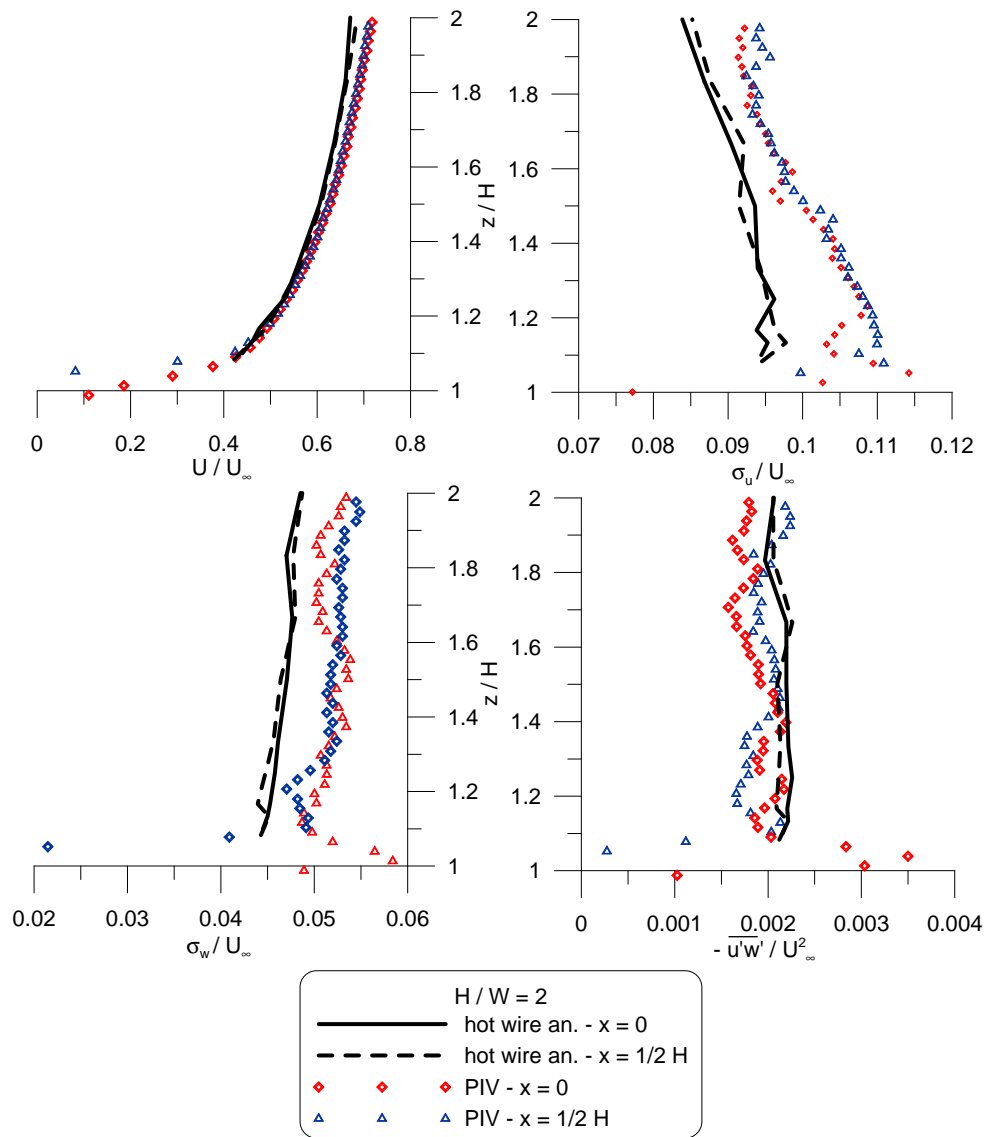


Figure 4.19: Comparison between hot-wire anemometry and PIV measurements, configuration 2a.

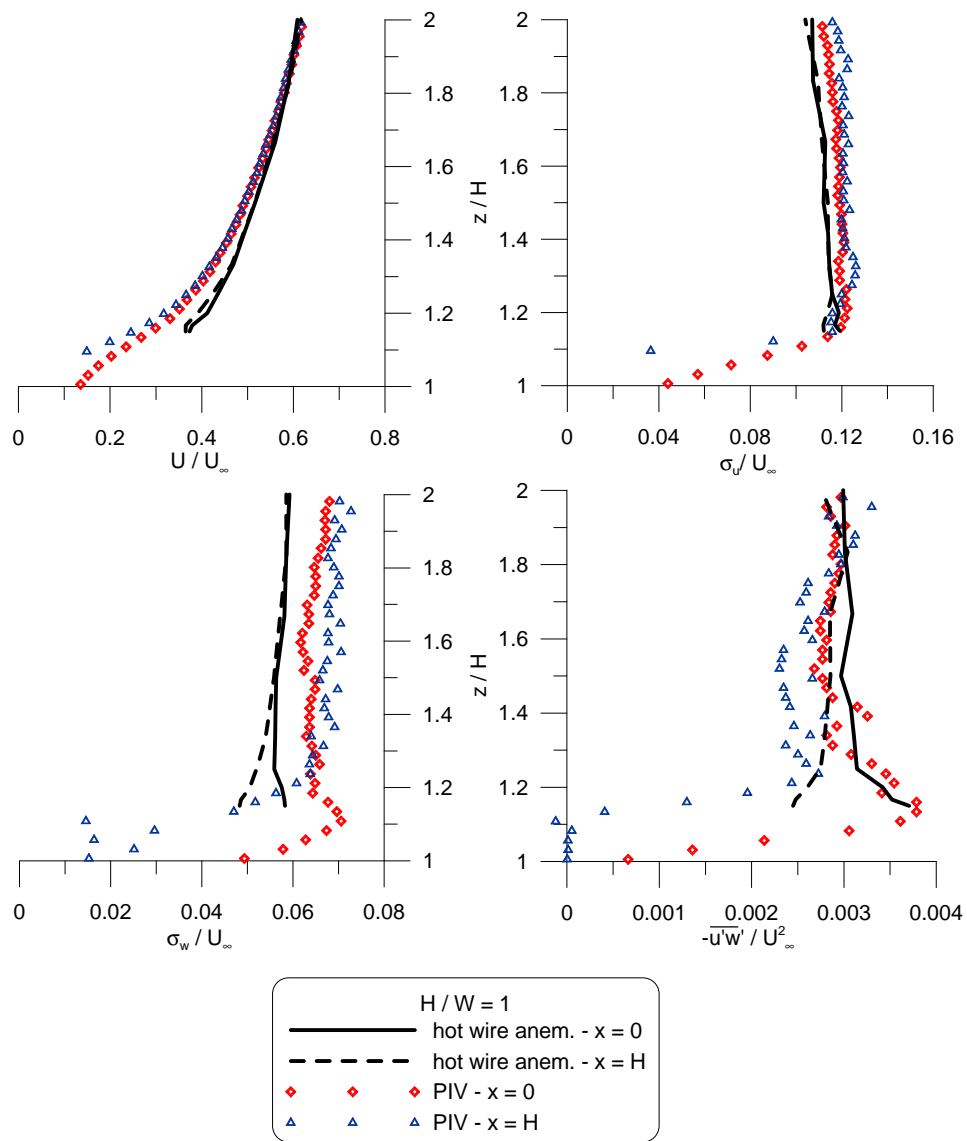


Figure 4.20: Comparison between hot-wire anemometry and PIV measurements, configuration 1b.

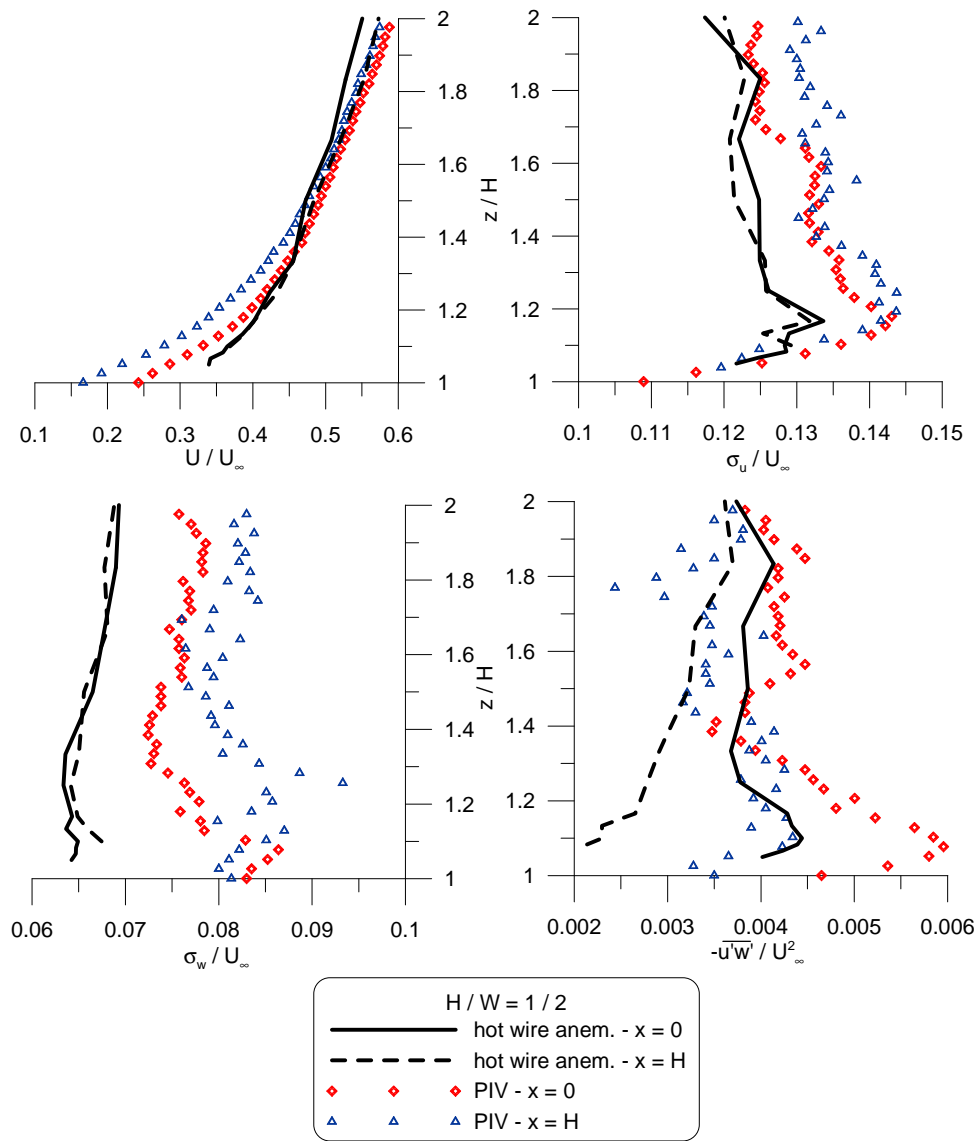


Figure 4.21: Comparison between hot-wire anemometry and PIV measurements results, configuration 3a.

- in wake interference flow the RSL depth is $\sim H$.

In configuration 1a and 2a, an analysis of horizontal inhomogeneities is however difficult even with PIV data, as far as the RSL depth is too thin and, close to the wall, the collected PIV measures are not accurate.

4.4.2 Spatial correlations

The turbulence spatial structure is usually analyzed by means of a *two-point spatial correlation*

$$\overline{u(\mathbf{x}_0)u(\mathbf{x}_0 + \mathbf{r})} = L_{uu}(\mathbf{x}_0, \mathbf{r}) [\sigma_u(\mathbf{x}_0)\sigma_u(\mathbf{x}_0 + \mathbf{r})]$$

for the stream-wise component of the fluctuating velocity, and

$$\overline{w(\mathbf{x}_0)w(\mathbf{x}_0 + \mathbf{r})} = L_{ww}(\mathbf{x}_0, \mathbf{r}) [\sigma_w(\mathbf{x}_0)\sigma_w(\mathbf{x}_0 + \mathbf{r})]$$

for the vertical component. L_{uu} and L_{ww} are the correlation coefficients. The eulerian macroscales are given by

$$\mathcal{L}_{uu}(x, z) = \int_0^\infty L_{uu}(x, z, \mathbf{r}) d\mathbf{r}$$

for the correlation in the stream wise direction, and by

$$\mathcal{L}_{ww}(x, z) = \int_0^\infty L_{ww}(x, z, \mathbf{r}) d\mathbf{r}$$

for the correlation in the vertical direction.

In a general way we may suppose a dependence of any correlation coefficient from all the length scales imposed by the geometry, and the dynamics of the problem (RAUPACH *et al.*, 1991), as

$$\frac{\overline{u_i(z)u_j(z + \mathbf{r})}}{u_*^2} = L_{ij}(z, \mathbf{r}; \delta, H, W, \nu/u_*)$$

where H and W are the linear dimensions of the roughness elements and the distance between them, while ν/u_* is a viscous inner scale.

However, according to the wall similarity hypothesis, the flow field above the roughness sub-layer has to be independent from length scales related to the roughness geometry, as well as from the viscous scale, so that we can write

$$\frac{\overline{u_i(z)u_i(z + \mathbf{r})}}{u_*^2} = L_{ij}(z, \mathbf{r}, \delta)$$

which is a general relation valid for the whole extent of the boundary layer, above the blending height, i.e. except for the roughness sub-layer.

In a more detailed way, making a distinction between inner and outer region we may write

$$L_{ij} = f(\delta, \mathbf{r})$$

for the outer layer, and

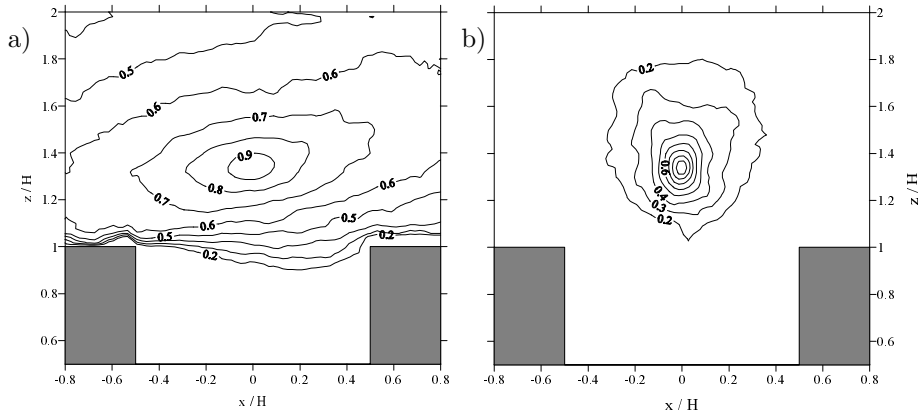


Figure 4.22: Spatial correlation at $x = 0$ and $z = 4/3H$ for configuration 1a ($H/W=1$). a) L_{uu} ; b) L_{ww} .

$$L_{ij} = f(z, \mathbf{r})$$

for the inner layer.

Within a roughness sub-layer, we can assume that the integral length scale in a roughness sub-layer should scale with H (if the obstacles are far enough one from the other, i.e. in the isolated roughness or in the wake interference regime) or with $(H - d)$ when the obstacles are sufficiently densely packed: the dependence of correlation scales within the RSL can be expressed, in the following relation

$$L_{ij} = f((H - d), H, \mathbf{r})$$

ROTTA (1962) suggested that near the wall, within the roughness sub-layer, the momentum flux was increased because of an enhanced length scale of the flow structures, i.e. of the Prandtl mixing length. More recently, the evidence of organized motion just above a vegetation canopy was given by observations of coherent waving (known as ‘honami’) above the vegetation corps surface (FINNIGAN, 1979). These structures seem to scale vertically with canopy height.

In fig 4.22 - ?? are shown the coefficients L_{uu} and L_{ww} calculated at $z = 4/3H$, i.e. at $z = 4/3H$, and at the cavity centre ($x = 0$). As expected the results show a high anisotropy in the flow field: horizontal correlations are more intense than vertical correlations.

In terms of horizontal spatial correlation there is no significant difference in the magnitude of L_{uu} between the three configurations 1a, 2a and 3a. However for configuration 1a and 2a the presence of small roughness reduces slightly the magnitude of L_{uu} .

In the vertical direction, the presence of a large cavity (configuration 3a, i.e. $H/W = 1/2$), seems to affect the magnitude of the spatial correlation, which is higher than those measured in the other two cases, with narrower cavity (configuration 1a and 2a).

The pictures shown in fig. 4.23 - 4.26 give a first over view on the structure of coherent motion in the region close to obstacle top. In a general way according with previous authors (KROGSTAD and ANTONIA, 1995), we can observe that the main effects of roughness on turbulence structure are:

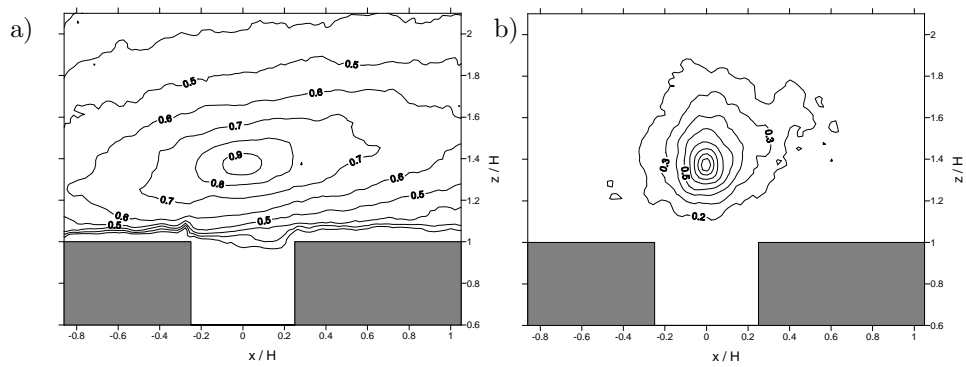


Figure 4.23: Spatial correlation at $x = 0$ and $z = 4/3H$ for configuration 2a ($H/W=2$). a) L_{uu} ; b) L_{ww} .

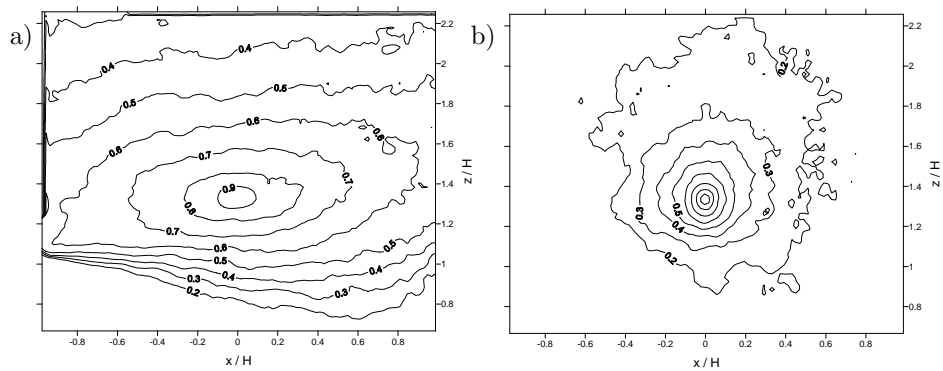


Figure 4.24: Spatial correlation at $x = 0$ and $z = 4/3H$ for configuration 3a ($H/W=1/2$). a) L_{uu} ; b) L_{ww} .

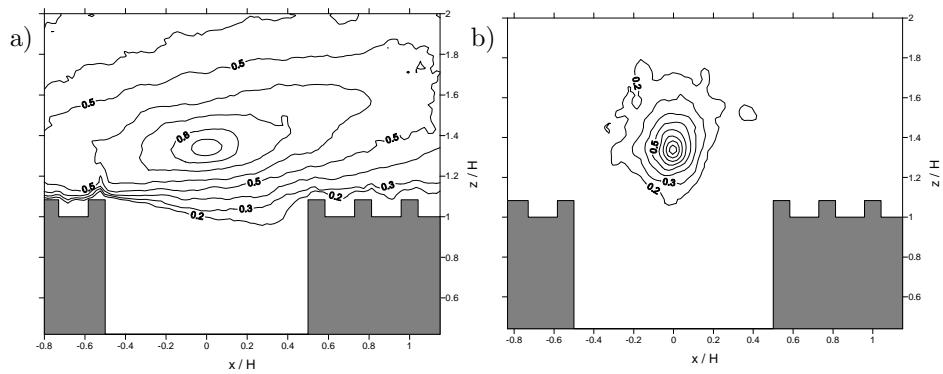


Figure 4.25: Spatial correlation at $x = 0$ and $z = 4/3H$ for configuration 1b ($H/W=1$). a) L_{uu} ; b) L_{ww} .

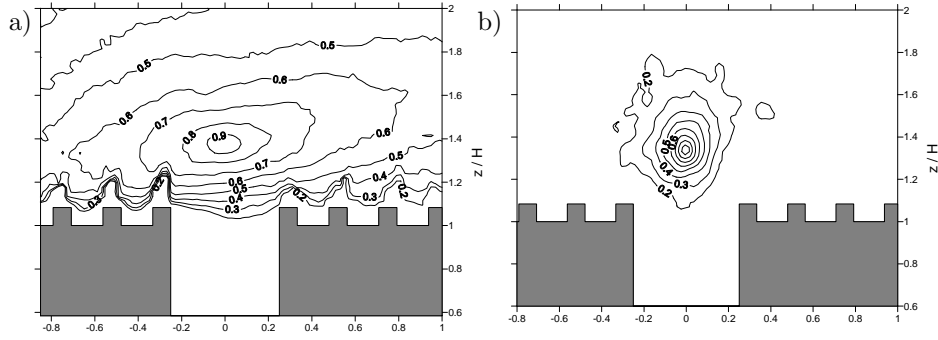


Figure 4.26: Spatial correlation at $x = 0$ and $z = 4/3H$ for configuration 2b ($H/W=2$). a) L_{uu} ; b) L_{wv} .

- to tilt coherent structures toward the stream-wise direction
- to reduce the damping of wall-normal velocity fluctuations
- to reduce the length scales of structure in the stream-wise direction
- to increase the isotropy of the flow field.

To give a more detailed analysis of the phenomenon, we computed spatial correlations in the whole domain, in order to clarify their dependence on:

- the vertical and horizontal coordinates;
- the cavity aspect ratio;
- the presence of the small roughness.

Instead of calculating the integrals $\mathcal{L}_{uu}(x, z)$ and $\mathcal{L}_{wv}(x, z)$, a simpler way of computing a typical length scale of spatial correlation is to interpolate the correlation coefficients by means of an exponential law, such as

$$f(r) = e^{-\frac{r}{\Lambda}} \quad (4.3)$$

and evaluate the length Λ , which gives a measure of the integral length scale.

In order to analyse the dependence of the integral length scale on the vertical coordinate z , we considered the evolution of the correlation coefficient L_{wv} along the stream-wise direction.

In fig. 4.27 is plotted the horizontal cut of the coefficient L_{wv} , in case of configuration 2a and 3a, computed for increasing distance from obstacle level. It is worth noting that all curves show a sharp peak for $r = 0$: this shows that molecular diffusion has a negligible role on the flow dynamics. The curves in fig. 4.27 clearly show that for increasing distances from the amplitude of the correlated region increases. To quantify the integral length scale on the vertical coordinate z we have therefore interpolate the correlation coefficients by means of the exponential law given in eq. 4.3. The results are plotted in fig. 4.4.2 and show the vertical profiles of the $\Lambda(z)$, computed at different stream-wise positions for

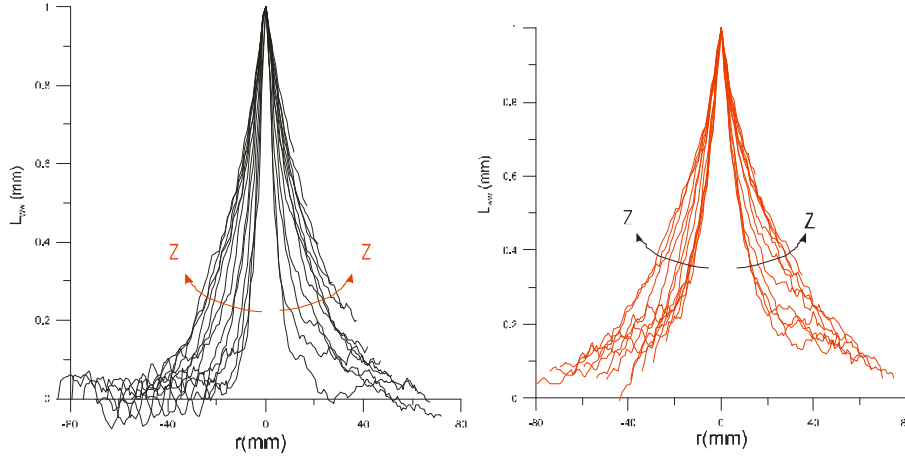


Figure 4.27: Evaluation of L_{ww} for different distances from the wall. Configuration 2a ($H/W = 2$) on the left; configuration 3a ($H/W = 2$) on the right.

configuration 2a and configuration 3a. The profiles for the two configuration appear different on two aspects: the spatial variability in the streamwise direction and the magnitude of the values in the lower part of the flow field. To quantify these differences we have compute the spatial average of $\Lambda(x, z)$. these were computed as

$$\langle \Lambda(z) \rangle = \frac{1}{2H} \int_{-H}^H \Lambda(x, z) dx \quad \text{for configuration 2a}$$

$$\langle \Lambda(z) \rangle = \frac{1}{3H} \int_{-3/2H}^{3/2H} \Lambda(x, z) dx \quad \text{for configuration 3a}$$

The vertical profiles of $\langle \Lambda(z) \rangle$ are shown in fig. 4.29, tighter with an estimation of the r.m.s. of $\Lambda(x, z)$ around the average. The results show that:

- the values of $\Lambda(x, z)$ in configuration 3a are characterised by a greater variability, especially in the lower part of the flow filed;
- the values of $\Lambda(x, z)$ in configuration 3a are characterised by a higher values;

Both feature are due to the presence of an enhanced RSL in case of configuration 3a. As the distance between the obstacles increase the integral length scale increases too and tends to reach the obstacle dimension H . We can think at the flow dynamics in wake interference regime as an intermediate regime between skimming flow and isolated roughness regime, the latter being similar to the case of a back-ward facing step. In the latter case H is the typical length scale of large-scale vortices shed downwind (HUNT and CASTRO, 1984; PICCOLO *et al.*, 2001). Actually the instabilities generated within the shear-layer (that

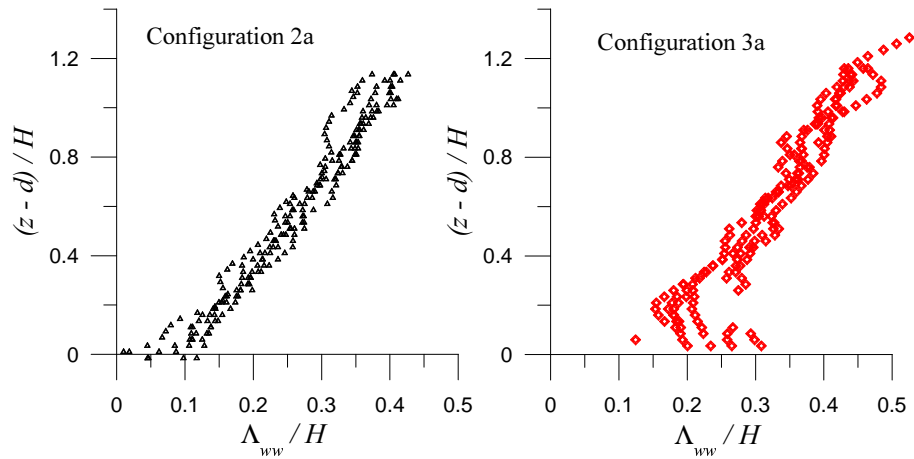


Figure 4.28: $\Lambda(z)$ for different distances from the wall. Configuration 2a ($H/W = 2$) - left; Configuration 3a ($H/W = 1/2$) - right.

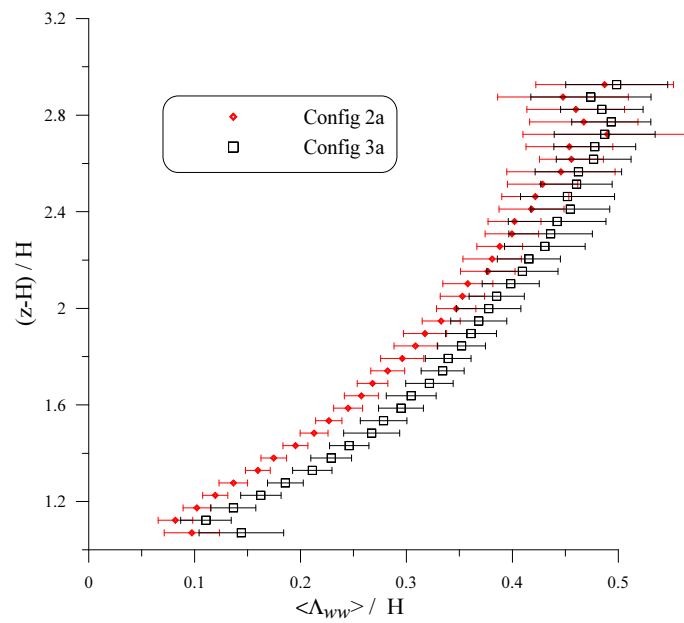


Figure 4.29: $\Lambda(z)$ for different distances from the upwind corner in case of configuration 3a ($H/W = 1/2$) and configuration 2a ($H/W = 1/2$); error bars give a measure the variability of $\Lambda(z)$ along the streamwise axis x .

takes place at the interface between recirculating region and external flow) grow travelling downwind, until they reach a linear dimension $\sim H$. At that time the blocking effect exerted by the wall does not allow those coherent structures to grow any more.

4.5 Passive scalar dispersion

In this section we study the influence of different urban-like roughness on the dispersion of a passive scalar in the overlying turbulent boundary layer. The passive scalar experiments were thus performed for different obstacle configurations at the wall, i.e. for varying wall roughness. Experiments were carried out with a line source located at ground level $z_s = 0$, and at heights $z_s = 2H$ and $z_s = 3H$ above the ground, as shown in Figure 4.30. Vertical mean concentration profiles were measured for increasing downstream distances from the sources. As already mentioned in §3.1.2, the most upstream measurement profile was located at a distance of about 5 m downstream of the vortex generators. This corresponds to about 12 times the height of the spires, and is sufficient to ensure that the turbulent structures generated by the spires have reached a quasi-equilibrium state. As a result the change in the boundary layer depth $\Delta\delta$ is small compared with the boundary layer thickness δ . This means that for the dispersion of a passive scalar, the only relevant length scale in the streamwise direction is the downwind distance from the source, which is assumed to be $x = 0$ (Figure 4.30).

Experimental results are analyzed by means of analytical and numerical solutions of the advection diffusion equation, in order to evaluate how the dispersion of a passive scalar is influenced by:

- the distance of the source from the wall;
- the geometrical configuration of the large scale obstacles of the wall, i.e. the street aspect ratio H/W ;
- the presence of the small scale roughness at the top of the obstacles;
- the vertical extent of the roughness sub-layer.

In order to detect any drift in the calibration of the FID, we computed the total streamwise mass flux per unit length for each profile, defined as

$$\dot{M}_q = \int_0^\delta \bar{u}(z)\bar{c}(z)dz$$

where $\bar{u}(z)$ is provided by the measured mean velocity profiles (see §2.2) and $\bar{c}(z)$ is provided by the FID measurements. In those cases in which the evolution of the mass flux with distance downstream varied by more than $\pm 5\%$ (due to drift in probe calibration) the vertical concentration profiles were adjusted with a correction factor in order to conserve the mass flux.

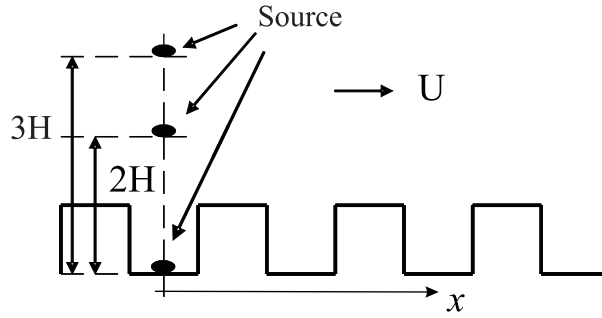


Figure 4.30: Source positions.

4.5.1 Mathematical model and numerical methods

Neglecting molecular diffusion and assuming stationary conditions, the spatial evolution of the mean concentration of a passive scalar in a turbulent flow is given by the Reynolds-averaged advection-diffusion equation:

$$-\nabla \cdot (\overline{\mathbf{u}'c'} + \overline{\mathbf{u}} \cdot \overline{c}) = 0 \quad (4.4)$$

where $\overline{\mathbf{u}'c'}$ is the turbulent flux of the passive scalar and \overline{c} is the mean scalar concentration, the three component of the velocity vector \mathbf{u} in the x, y and z direction are denoted u, v and w respectively.

We assume that turbulent dispersion in the stream-wise direction is negligible, compared with the advection of pollutant by the mean flow, i.e. that

$$\overline{u'c'} \ll \overline{u} \cdot \overline{c} \quad (4.5)$$

and that advection in the vertical direction is negligible compared with turbulent dispersion:

$$\overline{w'c'} \gg \overline{w} \cdot \overline{c} \quad (4.6)$$

We assume that the turbulent fluxes can be modelled by a gradient-diffusion term (the Boussinesq hypothesis):

$$\overline{\mathbf{u}'c'} = -\mathbf{K} \nabla C \quad (4.7)$$

where \mathbf{K} is the turbulent diffusivity tensor. It is well known that this model provides a reasonable description of the process in the limit $T/T_L \rightarrow \infty$, where T_L is the lagrangian timescale and T is the dispersion time (§1.5).

Then if the gradient-diffusion model is substituted into the advection-diffusion Equation 4.4, the resulting equation can be regarded as a long-time asymptotic version of the original equation. If we also include the other assumptions concerning the relative importance of diffusion in the different directions (Equations 4.5 and 4.6), and if we consider a two-dimensional case, the advection-diffusion equation becomes:

$$\overline{u} \frac{\partial \overline{c}}{\partial x} + \frac{\partial}{\partial z} K \frac{\partial \overline{c}}{\partial z} = 0 \quad (4.8)$$

We have assumed that this equation can be applied to the experiments that we have performed, with the velocity profile $\bar{u}(z)$ obtained by fitting a power law (Equation ??) to the measured velocity profiles. The resulting equation can be solved analytically or numerically. For both solutions, the lower boundary was taken to be $z = H$ and the upper boundary $z = \delta$.

To solve Equation 4.8 numerically, we first write the equation in dimensionless form, using normalized vertical (η) and horizontal (ξ) co-ordinates, where:

$$\eta = \left(\frac{z - H}{\delta - H} \right) \quad \xi = \left(\frac{x}{\delta - H} \right)$$

Equation (4.8) becomes then:

$$U^+(\eta) \frac{\partial}{\partial \xi} \bar{c}(\xi, \eta) + \frac{\partial}{\partial \eta} K^+(\eta) \frac{\partial \bar{c}}{\partial \eta} = 0 \quad (4.9)$$

where $K^+(\eta) = K(\eta)/[U_\infty(\delta - H)]$ and $U^+(\eta) = \bar{u}/U_\infty$.

Equation 4.9 was solved by a pseudo-temporal finite volume method, iterating until the solution converged to a stationary value. The advection term was integrated with an explicit forward-in-time scheme (BOTT, 1989a; BOTT, 1989b; THUBURN, 1997), and the diffusion term was computed by the semi-implicit Crank-Nicholson scheme (solved by the Thomas algorithm). The boundary conditions were defined as follows:

- at the outlet, a Neumann condition was imposed:

$$\frac{\partial \bar{c}}{\partial \xi} = 0$$

- at the lower and upper boundaries of the domain, a Neumann condition was also used:

$$\frac{\partial \bar{c}}{\partial \eta} = 0$$

- at the inlet boundary, a Dirichlet boundary condition was set

$$\bar{c} = \bar{c}(\eta)$$

where the function $\bar{c} = \bar{c}(\eta)$ was obtained by interpolating the measured profile of the mean concentration with a double gaussian curve (in the case of an elevated source) or with a cubic spline (in the case of a ground level source).

To test the convergence of the numerical simulation and to verify that the converged results are independent of the grid resolution, we carried out some initial simulations using two different discretisations – a coarse grid with 10626 cells and a finer grid with 1067220 cells. As it is shown in fig. 4.31, the converged results from the two simulations were identical, so we can conclude that our numerical results are grid independent.

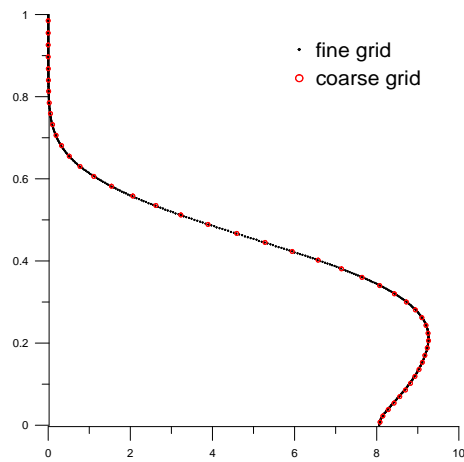


Figure 4.31: Spatial convergence test for the numerical simulations.

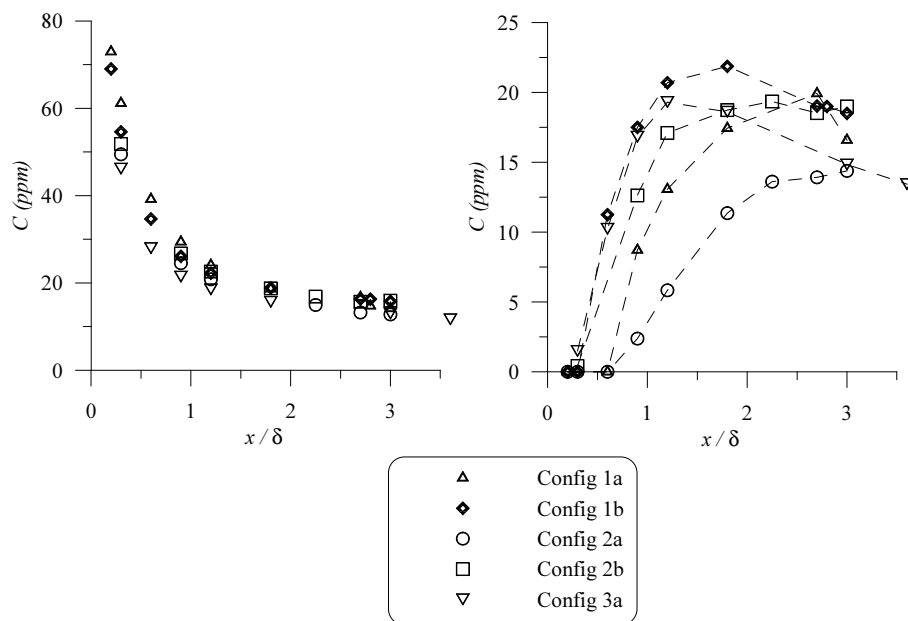


Figure 4.32: Spatial evolution of the mean concentration for an elevated line source ($z_s = 2H$) in the streamwise direction; a) mean concentration at the source height $z = z_s$; b) mean concentration at the obstacle top $z = H$.

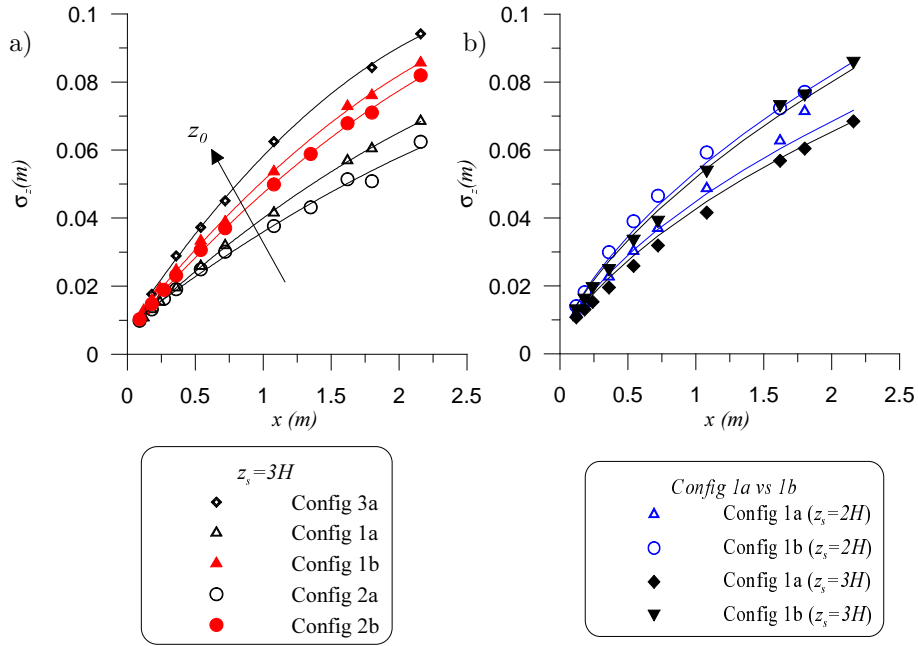


Figure 4.33: a) Plume spreading for increasing distances from the source in case of $z_s = 3H$. b) Effect of the source height on the plume spreading: Configuration 1a and Configuration 1b. The experimental points are fitted by means of a 2nd order polynome.

4.5.2 Experimental and numerical results

Dispersion from an elevated line source

Vertical mean concentration profiles have been measured at different distances downwind of the source. As can be seen in Figure 4.32a, the mean concentration field at the source height z_s does not vary significantly with the wall roughness³². However, for the same configurations, very different mean concentration values can be observed at ground level (Figure 4.32b) for increasing distances from the source: this clearly shows that different physical processes are involved in the dispersion of the plume as it travels downstream, depending on the roughness configuration.

A first analysis of the spatial evolution of the mean concentration field has been done using a simple gaussian model, taking account of the presence of the wall through the usual image source technique

$$\bar{c}(x, z) = \frac{\dot{M}_q}{\sqrt{2\pi}\sigma_z U} \left[\exp \left\{ -\frac{(z - z_s)^2}{2\sigma_z^2} \right\} + \exp \left\{ -\frac{(z + z_s)^2}{2\sigma_z^2} \right\} \right] \quad (4.10)$$

where \dot{M}_q is the mass rate per unit length, z_s is the source height and σ_z is the vertical spread. The gaussian curve represents the mean concentration profile for a passive scalar dispersing from a point source

³²The measurements obtained for configuration 3b do not differ from those of configuration 3a and so are not plotted here.

in a homogeneous flow, but the assumption of a homogeneous flow (for both the mean and fluctuating velocities) is clearly invalid in the configurations studied here.

Nevertheless, by fitting the gaussian curve to the data, we can obtain a relatively robust estimate of the vertical spread of the plume – σ_z – and this enables us to quantify the vertical dispersion of the pollutant as it is transported downwind by the flow.

The values of $\sigma_z(x)$ for each configuration have been estimated by fitting the gaussian curve to the data, using the method of least squares, and assuming σ_z is unknown. The value of U adopted in Equation 4.10 corresponds to the mean velocity at the source level, i.e. $U = \bar{u}(z_s)$.

We have used this to compute the vertical spread of the plume, as a function of downstream distance, for all the experimental configurations, and the results are shown in Figure 4.33.

The profiles of plume spread for the different configurations (Figure 4.33-a) show that the spread increases as the cavity aspect ratio H/W decreases; this corresponds to an increase in the spacing between the obstacles (since H is kept constant) and therefore to an increase in effective wall roughness, as can be seen from Table I. Physically, an increase in the obstacle spacing enhances turbulent mixing in the boundary layer, and thus increases the turbulent diffusivity, leading to larger values of σ_z . The same argument also explains the effect of adding small scale roughness, which also increases turbulent mixing, and results in larger values of σ_z . There is an important limit to this effect, though. Velocity measurements presented in §4.3 showed that the addition of small scale roughness increases turbulent intensities for cavity aspect ratios greater than 1 (Configuration 1 and Configuration 2) but once the aspect ratio falls below 1 (Configuration 3), the cavities become so wide that the influence of the small scale roughness is greatly reduced. This is reflected in the fact that the roughness lengths for Configuration 3a and 3b are the same (Table I). A further consequence of this is that the plume spread for the two configurations (3a and 3b) is identical.

The influence of the diffusivity on the plume spread can also be seen in the way in which σ_z depends on source height (Figure 4.33b). The vertical spread is greater than if the source height is closer to the surface, and this is true for configurations with (1b) and without (1a) the small-scale roughness. However it should be remembered that as the source height decreases, the plume is dispersing in a flow with an increasingly strong mean shear, and that the velocity gradient itself will contribute to spreading the plume, and will increase the effectiveness of the small-scale turbulence in the flow.

For practical purposes, the estimation of the plume spreading is often linked to the theory of diffusion developed by TAYLOR (1921), based on the statistical properties of an ensemble of fluid particle transported in turbulent flow. The statistical theory of turbulent dispersion provided by Taylor is based on a Lagrangian description of the velocity field. However it is impossible to obtain of Lagrangian statistical quantities in the atmosphere (PHILLIPS and PANOFSKY, 1982). For this reason several authors – see, for example, PASQUILL (?) – have adopted a generalized version of Taylor’s analysis, in order to provide an estimation of the plume spreading as a function of eulerian properties of the velocity field. This assumes that the lagrangian time scale is proportional to the eulerian macroscale, which implies that forms of the lagrangian and eulerian autocorrelation functions are similar; this in turn implies the similarity of their corresponding spectral functions. As was pointed out by ARYA (1999), amongst others, there are good theoretical reasons for believing that the two curves cannot be similar. Nevertheless, following PASQUILL (?), the spatial evolution of the plume spreading σ_z is usually expressed by means of a relation such as

$$\frac{\sigma_z}{\sigma'_w T_L} = \frac{T}{T_L} f_u \left(\frac{T}{T_L} \right) \quad (4.11)$$

where T_L is the lagrangian time-scale, σ'_w is a velocity scale and T is the dispersion time.

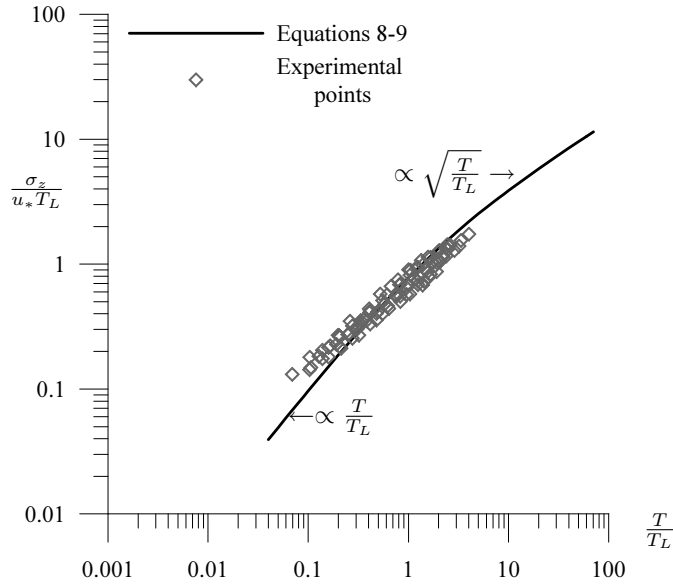


Figure 4.34: Temporal evolution of the plume spreading σ_z : comparison between experimental results and the model of PHILIPS and PANOWSKY (1982).

Several authors have tried to determine the function f_u from experimental data (PASQUILL, 1976; DRAXLER, 1976; DORAN *et al.*, 1978; IRWIN, 1979); here we consider the relation proposed by PHILIPS and PANOWSKY (1982):

$$f_u \left(\frac{T}{T_L} \right) = \sqrt{2} \left[\frac{T_L}{T} - \left(\frac{T_L}{T} \right)^2 \ln \left\{ 1 + \frac{T}{T_L} \right\} \right]^{1/2} \quad (4.12)$$

The form of Equation 4.12 emphasizes the different asymptotic behaviour of σ_z ; for short dispersion times, the puff size is proportional to T , whereas long times the puff size tends to be proportional to \sqrt{T} .

The dispersion time can be evaluated as

$$T = \frac{x}{\bar{u}(z_s)}$$

where x is the distance from the source and $\bar{u}(z_s)$ the mean velocity at the source height, i.e. $z = z_s$. To estimate the lagrangian time-scale, we follow CARRUTHERS *et al.* (2003) and express it as a function of fixed-point eulerian statistics:

$$T_L \simeq \frac{\Lambda_w(z)}{1.3\sigma_w(z)} \quad (4.13)$$

where $\Lambda_w(z)$ is a vertical length scale, given by the following relationship (HUNT *et al.*, 1988):

$$\Lambda_w(z) = \left(\frac{0.6}{z} + \frac{\partial \bar{u} / \partial z}{\sigma_w} + \frac{2}{\delta} + \frac{1}{z_u} \right)^{-1} \quad (4.14)$$

with $z_u = \max(0, (\delta - z))$.

To test the validity of these relationships for the flows studied here, we have plotted the normalized vertical spread $\sigma_z^+ = \sigma_z / u_* T_L$ as a function of the normalized dispersion time T/T_L for all experiments, together with the theoretical relationship (Equations 4.34, 4.12, 4.13, 4.14). In the original formulation – Equation 4.34 – the vertical spread is normalized on the product of a fluctuating velocity σ'_w and the lagrangian time scale; for the purpose of this comparison we have assumed that $\sigma'_w \sim u_*$ so we have actually plotted σ_z^+ as a function of T/T_L . All the experimental data lie in the range $0.05 < T/T_L < 5$, which corresponds approximately to the region of the transition between the two asymptotic regimes ($\sigma_z^+ \propto T/T_L$ and $\sigma_z^+ \propto \sqrt{T/T_L}$).

The experimental data show partial agreement with the analytical expression, confirming that the scaling relationship used to estimate the turbulent diffusivity (Equations 4.12 and 4.13) gives a result with the right order of magnitude. However the data do not really show the two regimes ($\sigma_z^+ \propto T/T_L$ and $\sigma_z^+ \propto \sqrt{T/T_L}$) that are apparent in the theoretical relationship, and it would be perfectly possible to fit a simple straight line to the entire data set, and obtain better agreement than with the analytical model. The differences between the theoretical curve and the experimental results are greatest for small T , and this is due to the influence of the wake of the source.

Although the data for the different configurations cluster around some general profile, there is still considerable scatter in the points. So the scaling used in the model is not strictly universal. The difference between theoretical and measured profiles is related to the inhomogeneity of the fluctuating flow and the shear in the mean flow. However, it is difficult to determine the influence of these two effects on the dispersion process just by analysing the plot in Figure 4.34. In addition to these effects, the scatter in the data is also significantly affected by the incertitude introduced by the different scales adopted; the scaling used in the theoretical model require lagrangian variables referred to a homogenous turbulent field, whilst the scaling used to plot the experimental data in Figure 4.34 adopts eulerian variables referred to an inhomogeneous turbulent flow. In order to analyze the the effect of the inhomogeneity of the mean and fluctuating flow on the dispersion process, we have therefore solved the advection-dispersion Equation 4.9 numerically.

Numerical simulations

The simple analytical model for the vertical spread (Equation 4.11) assumes that the mean flow and the turbulence are homogeneous, and neither of these assumptions is actually valid. In the analysis presented in the previous paragraph, the only parameter in the scaling which takes account of the turbulence in the boundary layer (and hence the effect of changing from one configuration from another) is the friction velocity u_* . This means that the changes in characteristic length scales caused by changing the aspect ratio of the cavity are not represented explicitly. To investigate the influence of the flow inhomogeneity on the dispersion process we have solved the advection-dispersion Equation 4.9 numerically, using the measured mean velocity profiles, and different assumed forms for the dispersion coefficient. In general, the dispersion coefficient can be expressed as the product of a velocity and a length scale

$$K(z) = v(z)\ell(z)$$

so the problem consists of finding the most suitable velocity and length scale for diffusion in a rough boundary layer, and investigating how those scales depend on surface roughness.

The measured and computed concentration profiles are shown in Figures 4.35 – 4.40. In all plots the concentration profile are given in normalized form $C_* = \bar{c}U_\infty(\delta - H)/\dot{M}_q$. We have investigated various formulations for the dispersion coefficient $K(z)$. Physical reasoning suggest that, close to the wall, it should scale on the friction velocity u_* and on a length scale ℓ , which will be related either to the distance from the wall ($z - d$) or to the size of the roughness elements. Further away from the wall, it should approach a constant value, scaling on the friction velocity and the boundary layer depth ($\delta - H$). There are some measurements in the atmospheric boundary layer (CLARKE, 1970) that support this scaling. Based on these arguments we have divided the boundary layer into two regions – a lower region which extends from the wall to the upper limit of the inertial region ($0 < \eta < 0.15$) and an outer region ($0.15 < \eta < 1$), with the following form for $K(z)$:

$$0 < \eta < 0.15 \quad K(z) = \kappa u_*(z - H)$$

$$0.15 < \eta < 1 \quad K(z) = \alpha u_*(\delta - H)$$

where κ is the von Kármán constant and α is another constant.

The simulations show that the model for a two-layer diffusivity profile reproduces the observed concentration profiles satisfactorily in case of skimming flow regime (Figures 4.35-4.38). This agreement is not influenced by the presence of small scale roughness elements. In the case of wake-interference flow (Configuration 3), the two-layer diffusivity profile leads to an underestimate of the concentrations in the lower part of the boundary layer (Figures 4.39, K_{IR}). Other experiments have already demonstrated that the momentum diffusivity in the roughness sub-layer exceeds that in the inertial layer, and this was attributed by RAUPACH et al. (1980) and by BANDYOPADHYAY et al. (1988) to a wake diffusion effect, related to the dynamics of ‘horse-shoe’ vortices.

In the case we are analysing, this difference must be due to the extra diffusion induced by the obstacle wakes, since a comparison of the data for Configuration 3a and 3b shows that the small scale roughness has no effect on the concentrations.

Following RAUPACH and SHAW (1982), we define a horizontally averaged diffusion coefficient $\langle K \rangle$ which we assume scales on the height of the obstacles, and the friction velocity:

$$\langle K \rangle = \kappa H u_*$$

This is analogous to the flow behind a backward facing step; HUNT and CASTRO (1984) observed that the instabilities in the shear layer grow as they travel downstream until they reach a size of the order of H , at which point further growth is blocked by the presence of the wall. The concentrations computed with this form for $K(z)$ are plotted in Figures 4.39 and 4.40, as a continuous line (K_{RSL}). The computed profiles clearly show the influence of the enhanced diffusivity close to the ground, and for most of the profiles there is good agreement between the computations and the experimental data.

According to wall similarity, α should be constant for all boundary layer flows, in the limit $\delta/h_s \rightarrow \infty$, or $\delta/z_0 \rightarrow \infty$ which is the same provided that $h_s \propto z_0$ (JIMÉNEZ, 2004). In our case, we obtained the best results with a value of $\alpha = 0.07$ for Configuration 3 (wake-interference flow), and $\alpha = 0.05$ for all other configurations (skimming flow regime)³³. A different value of α in the two flow regimes is not in

³³The values of α have been chosen in order to guarantee the continuity of the dispersion coefficient too.

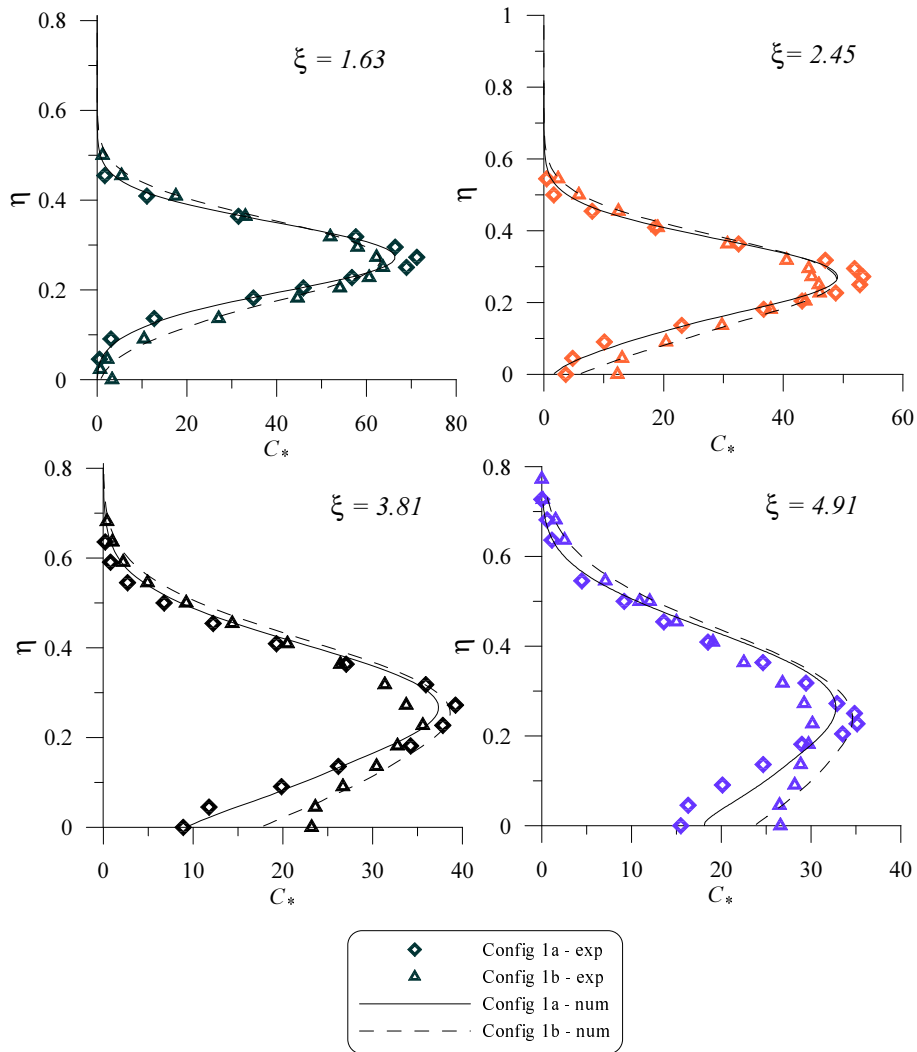


Figure 4.35: Comparison between experimental and numerical results. Configurations 1a vs 1b; source position $z_s = 3H$.

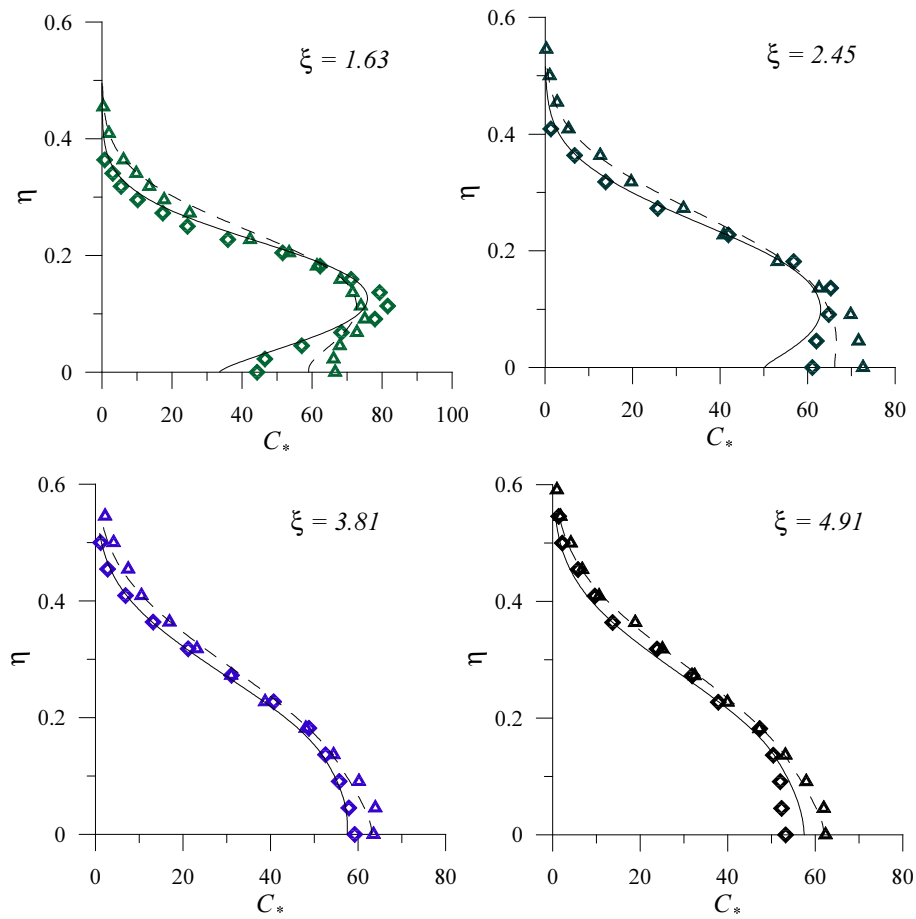


Figure 4.36: Comparison between experimental and numerical results. Configurations 1a vs 1b; source position $z_s = 2H$. Same symbols as Figure 4.35.

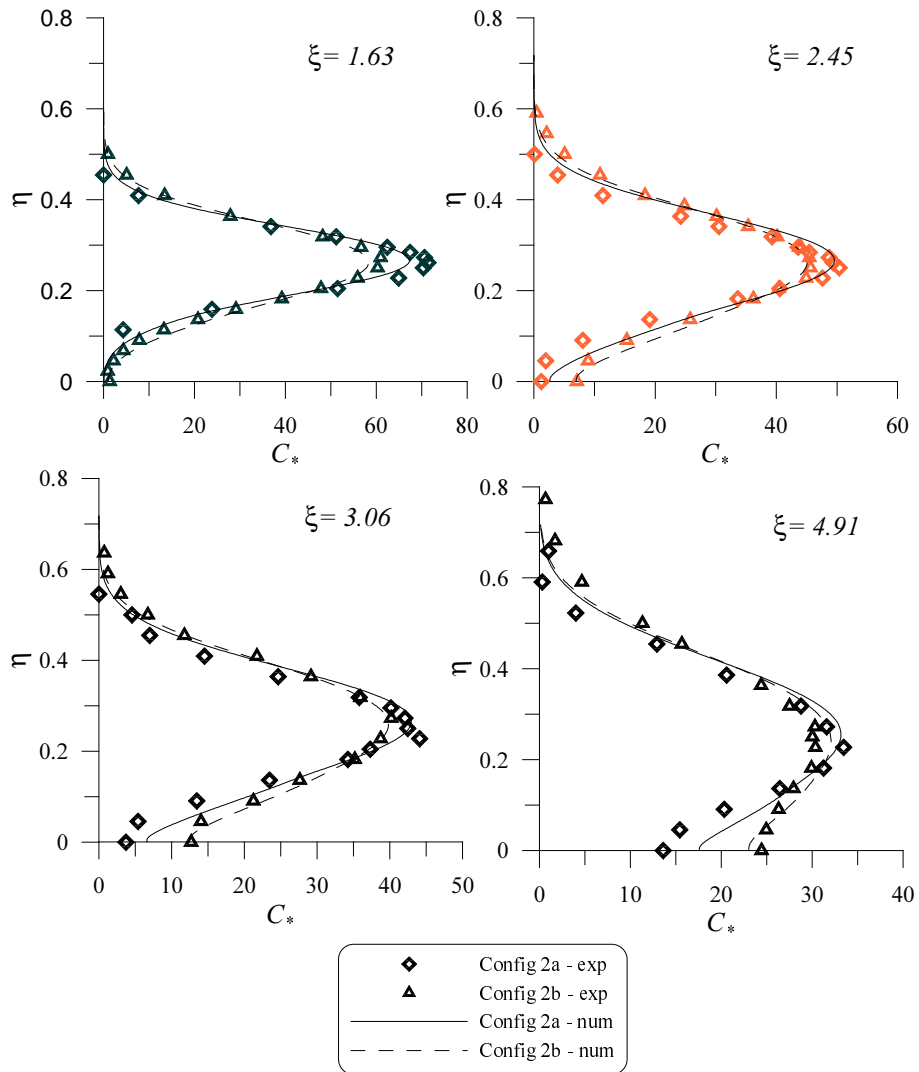


Figure 4.37: Comparison between experimental and numerical results. Configurations 2a vs 2b; source position $z_s = 3H$.

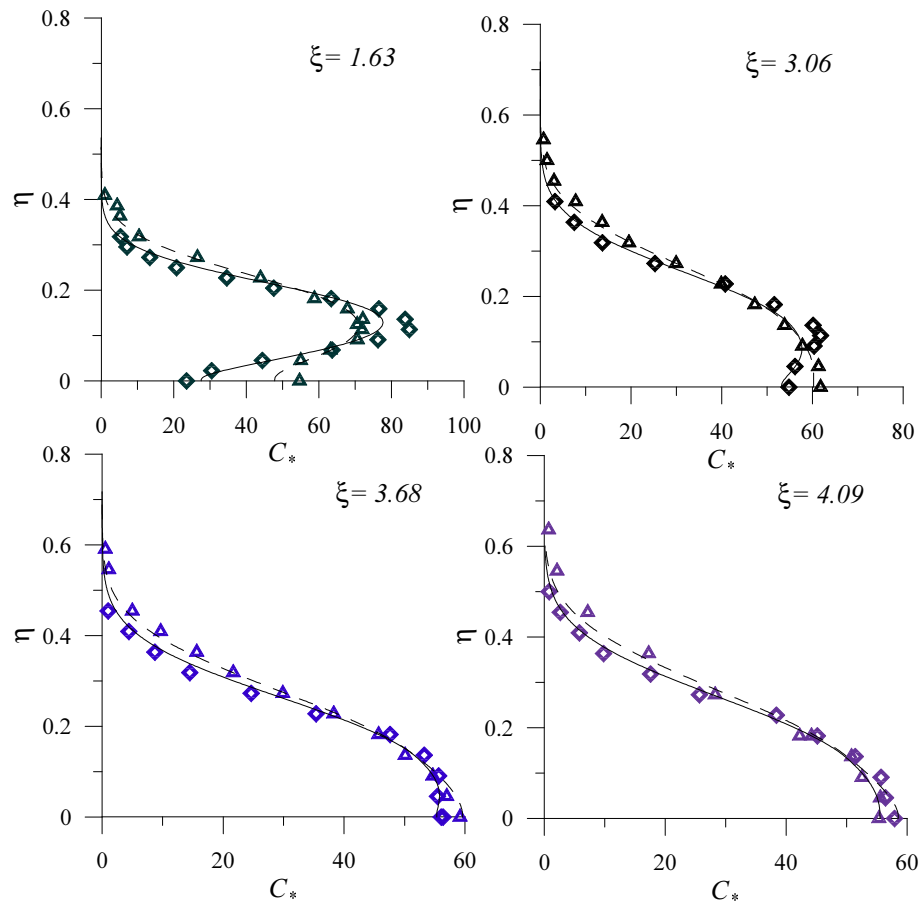


Figure 4.38: Comparison between experimental and numerical results. Configurations 2a vs 2b; source position $z_s = 2H$. Same symbols as Figure 4.37.

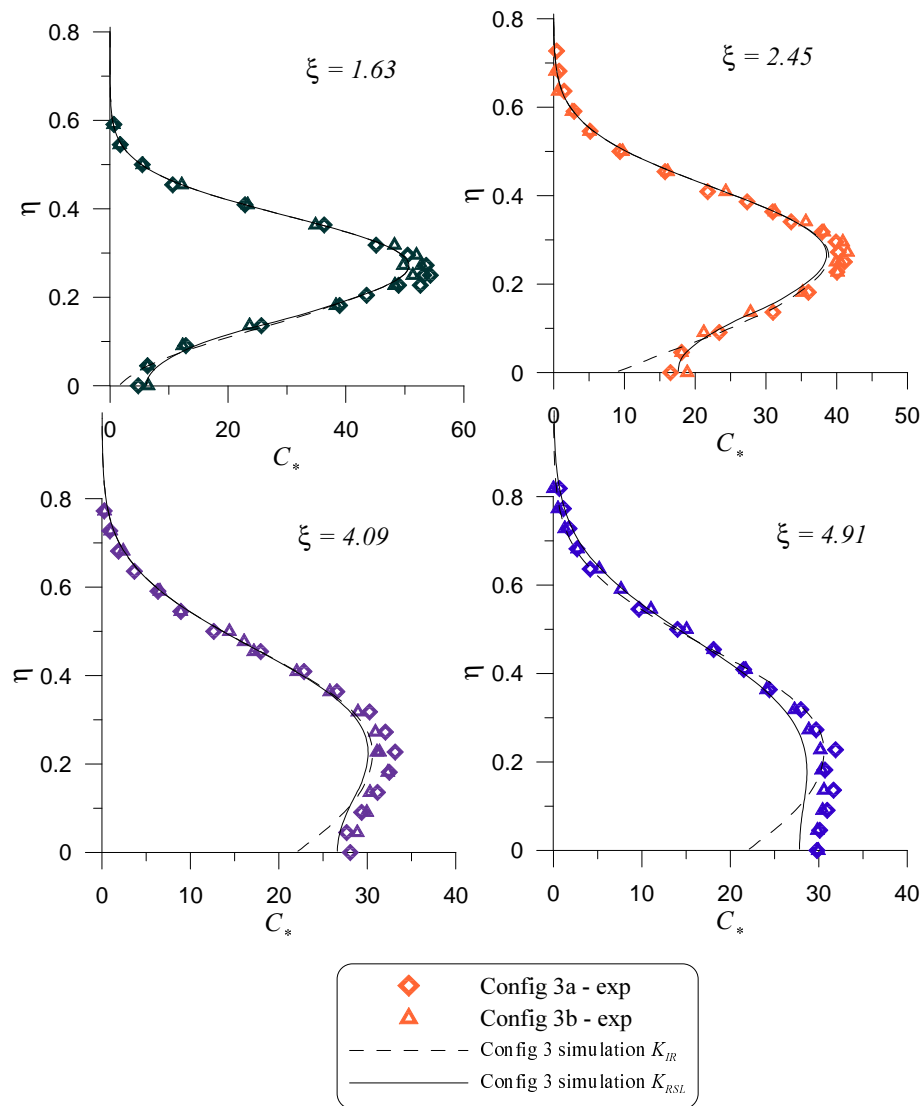


Figure 4.39: Comparison between experimental and numerical results. Configurations 3a vs 3b; source position $z_s = 3H$.

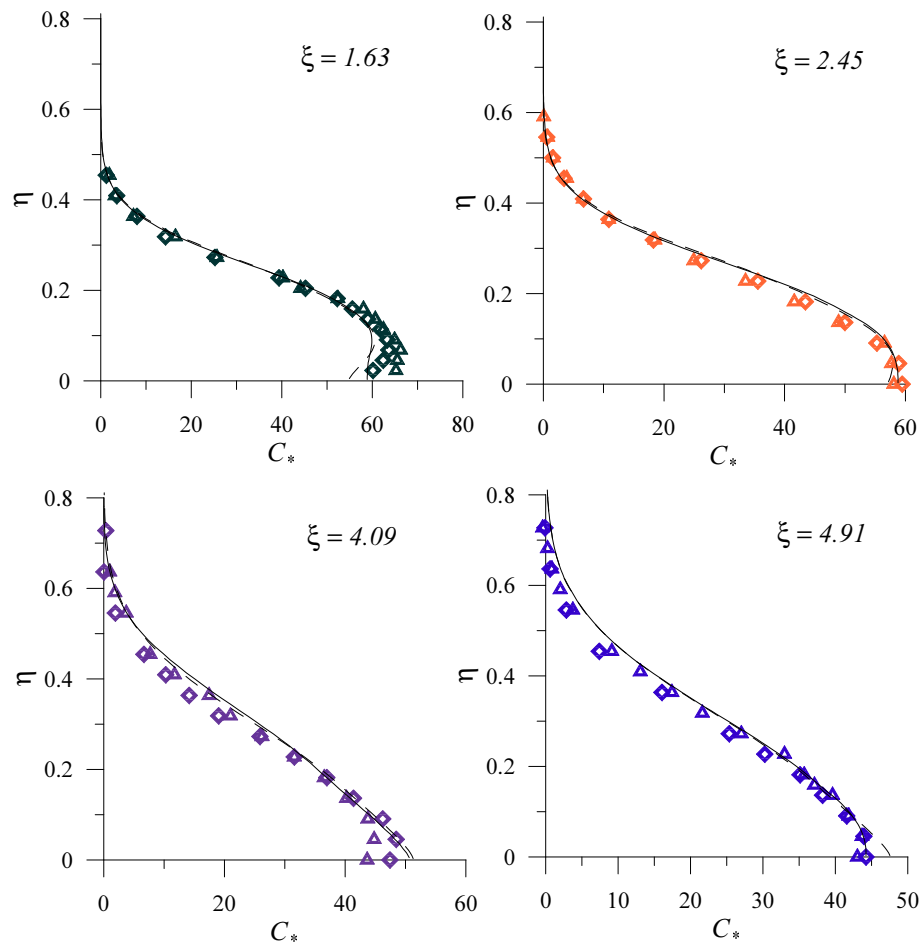


Figure 4.40: Comparison between experimental and numerical results. Configurations 3a vs 3b; source position $z_s = 2H$. Same symbols as Figure 4.39.

agreement statements of the similarity theory. The increased value of α in wake-interference flow may be due to the fact that, in this case, the ratio δ/h_s (Tab. I) is smaller than in skimming flow regime by an order of magnitude. We recall that the theory assumes that the inner and the external scales should be separated by several orders of magnitude, i.e. $\delta \gg h_s$; if this assumption is not satisfied, the dynamical behaviour of the flow may not correspond to the theoretical predictions.

In the numerical simulations we assumed a constant dispersion coefficient in the external region of the boundary layer without imposing that it should go to zero at the upper limit of the velocity field, where the turbulence intensity goes to zero. However for these calculations we verified that the results were not sensitive to the value of the dispersion coefficient in the upper part of the boundary layer (i.e. $\eta > 0.8$) provided that the plume spreading takes place mainly in the lower part of the velocity field.

Dispersion from a line source at ground level

The results presented in §4.1 for dispersion from an elevated line source showed that the effect of the small-scale roughness in enhancing the turbulent diffusivity in the case of skimming flow can be entirely modelled by enhanced values of the friction velocity, without considering any variation in the mixing length scalings. Furthermore it has negligible influence on the depth of the roughness sub-layer.

For those reasons, in this section, we will focus mainly on the influence of the cavity aspect ratio H/W , rather than on the influence of the smaller scale roughness.

The profiles for the skimming flow regime (Configuration 1a and 2a) are very similar at all distances downstream of the source (Figure 4.41). The only difference between them occurs very close to the ground, where the concentrations for Configuration 1a are slightly lower than those for Configuration 2a; the vertical distance over which this difference is noticeable increases with downstream distance.

The concentration profiles for the wake-interference (Configuration 3a) are significantly different from those for the skimming flow regime (Configuration 1a and 2a). The vertical diffusion of pollutant is much more rapid, particularly close to the source and consequently the concentrations in the near wall region are much lower (Figure 4.41).

In both Configurations 1a and 2a, the depth of the roughness sub-layer is very small compared with the depth of the boundary layer (Table I) and the integral length scales of the turbulence vary with height in the same way. The turbulence intensities are also very similar, with $u_* = 0.33 \text{ ms}^{-1}$ in Configuration 1a and $u_* = 0.305 \text{ ms}^{-1}$ in Configuration 2a, so the similarity of the turbulence statistics explains the similarity of the concentration profiles. The slight difference between the two profiles far downwind of the source can be explained by the slightly higher values of u_* and roughness sub-layer depth for Configuration 1a, resulting in a greater dispersion of the pollutant, with lower concentrations near the ground and higher concentration further out.

The concentration profiles in the wake-interference regime show much greater dispersion away from the boundary, and a region of almost constant concentration in the near-boundary region (for which $\frac{\partial \bar{c}}{\partial z} \sim 0$). These results suggest that dispersion from a ground level source is determined mainly by the boundary layer structure in the RSL, rather than increased intensities of the fluctuating flow.

Comparison with analytical solutions

Several analytical solutions of Equation 4.8 are available, for the case of a line source at ground level, depending on the assumptions that are made for the vertical velocity $\bar{u}(z)$ and diffusivity $K(z)$.

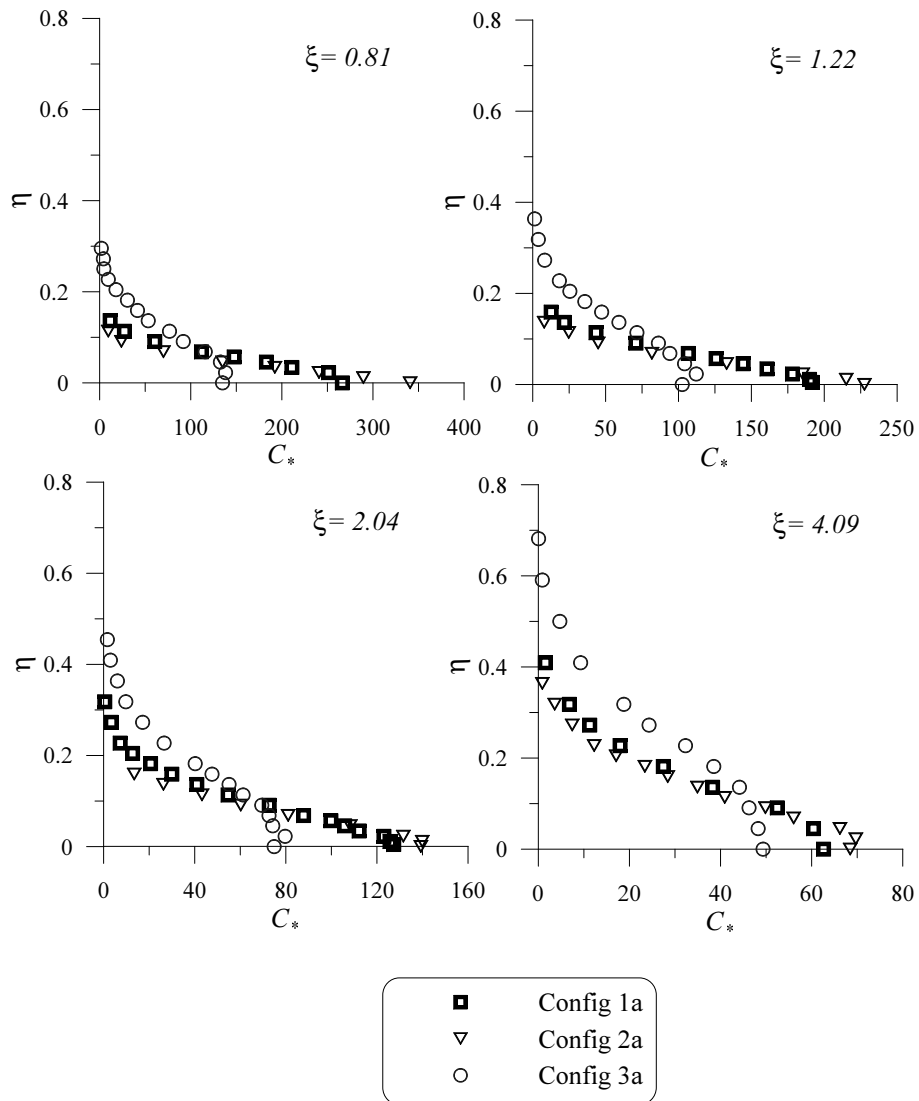


Figure 4.41: Dispersion from a ground level source; Configurations 1a vs 2a vs 3a.

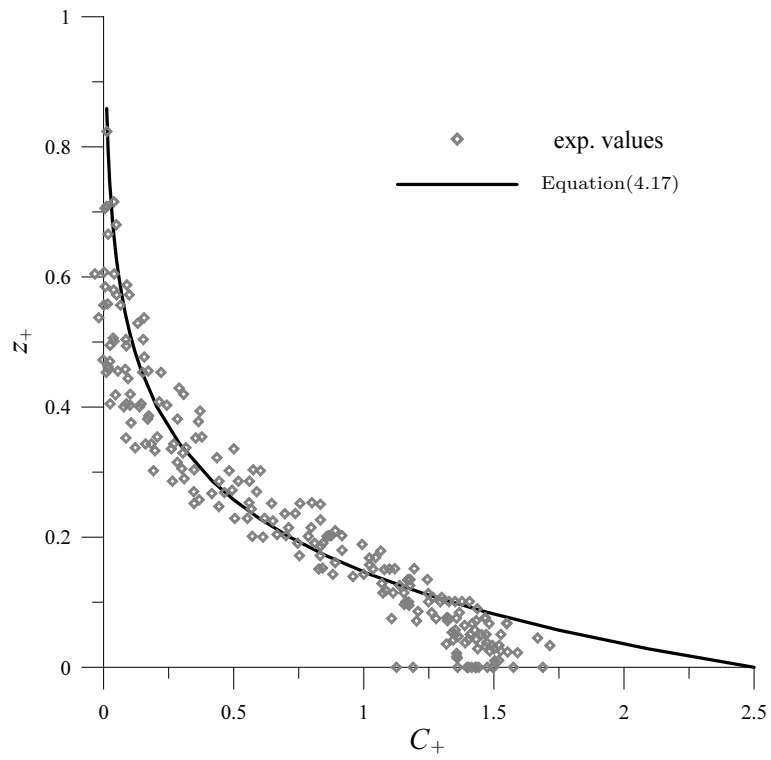


Figure 4.42: Comparison between experimental results and Equation (4.17).

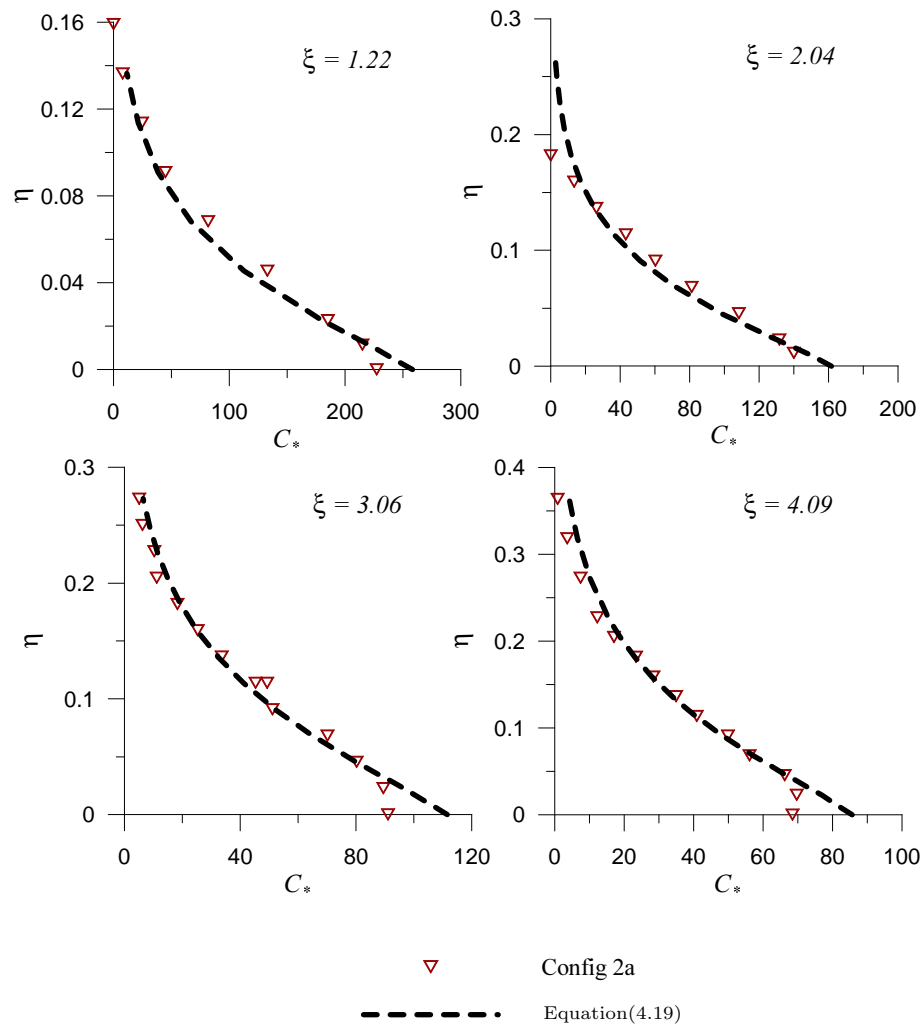


Figure 4.43: Comparison between experiments and Equation 4.19 for Configuration 2a.

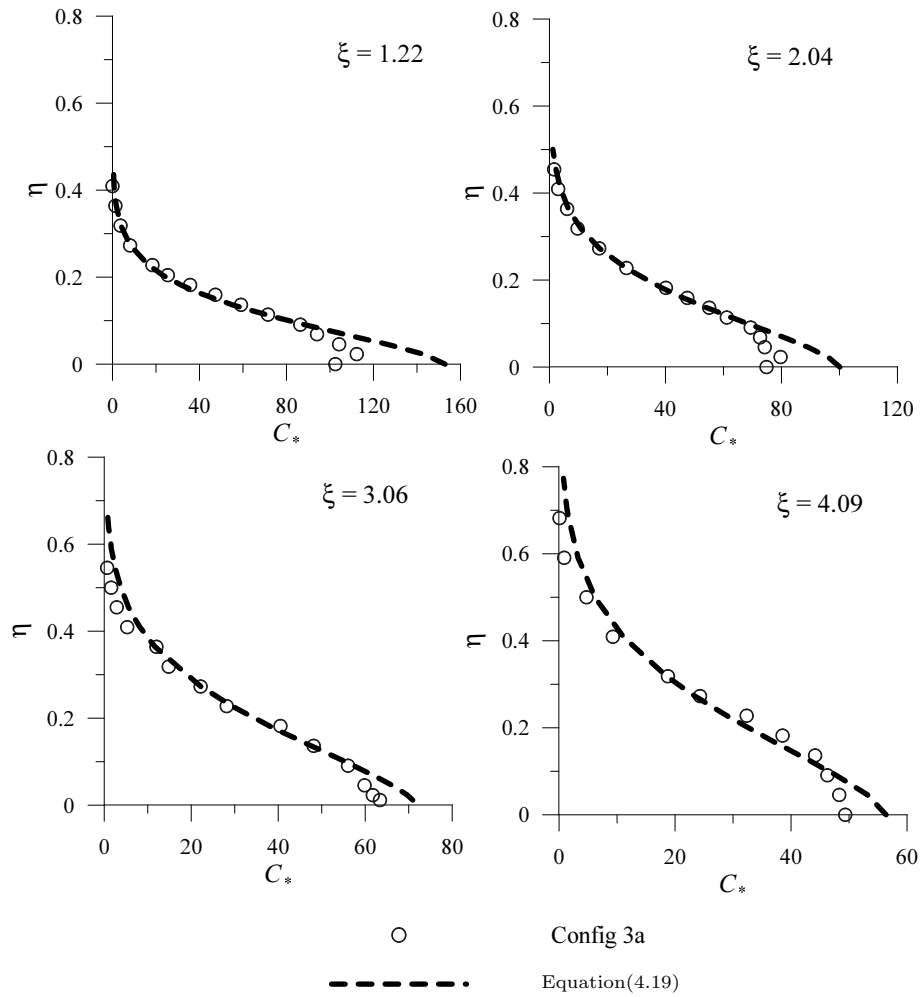


Figure 4.44: Comparison between experimental and theoretical results for Configuration 3a.

If both are assumed to be constant with height then the solution to Equation 4.8 for a line source at ground level, is given by

$$\bar{c} = \frac{\dot{M}_q}{\pi K} \mathcal{K}_0 \left\{ \frac{U\sqrt{x^2 + z^2}}{2K} \right\} \exp \left\{ \frac{Ux}{2K} \right\} \quad (4.15)$$

where \mathcal{K}_0 is the modified Bessel function of order zero. If $x \gg z$ and $\frac{Ux}{2K} \gg 1$ this can be simplified to give:

$$\bar{c} = \frac{\dot{M}_q}{\sqrt{\pi} K x U} \exp \left\{ \frac{-z^2}{4KxU} \right\} \quad (4.16)$$

which yields the conventional Gaussian form for the vertical concentration profile.

CALDER (1952) considered a variation of this solution, for which the advection velocity is still assumed constant, but the diffusion coefficient is assumed to be proportional to distance from the ground:

$$K(z) = \kappa u_* z$$

The Equation 4.8 can be solved exactly to give:

$$\bar{c} = \frac{\dot{M}_q}{\kappa u_* x} \exp \left(-\frac{Uz}{\kappa u_* x} \right) \quad (4.17)$$

Other assumptions concerning the forms of $\bar{u}(z)$ and $K(z)$ yield different solution for \bar{c} (SUTTON, 1953; BRITTER *et al.*, 2003). SUTTON (1953) considered the case in which both the streamwise velocity and the diffusivity varied with height, following the similar power laws:

$$\begin{aligned} \bar{u}(z) &= U_1 \left(\frac{z}{z_1} \right)^n \\ K(z) &= K_1 \left(\frac{z}{z_1} \right)^m \end{aligned} \quad (4.18)$$

where U_1 and K_1 are the values of U and K respectively at a reference height z_1 . He then solved Equation 4.8, with the boundary conditions:

$$\begin{aligned} \bar{c} &\rightarrow 0 && \text{as } x, z \rightarrow \infty \\ K_z \frac{\partial \bar{c}}{\partial z} &\rightarrow 0 && \text{as } z \rightarrow 0, \quad x > 0 \\ \bar{c} &\rightarrow \infty && \text{along } x = z = 0 \end{aligned}$$

$$\int_0^\infty \bar{u}(z) \cdot \bar{c}(x, z) dz = \dot{M}_q \quad \text{for all } x > 0$$

The analytical solution is given by

$$\bar{c} = \frac{\dot{M}_q(2n+1)}{z_1 U_1 \Gamma\{(n+1)/(2n+1)\}} \left[\frac{U_1 z_1^2}{(2n+1)^2 K_1 x} \right]^{(n+1)/(2n+1)} \exp \left\{ -\frac{U_1 z^{2n+1}}{z_1^{2n-1} (2n+1)^2 K_1 x} \right\} \quad (4.19)$$

where Γ is the Gamma function. SUTTON assumes that, as long as the diffusion takes place mainly in the inertial region³⁴, the values of m and n are related by³⁵

$$m = 1 - n \quad (0 \leq n \leq 1)$$

The values of n are obtained from the measured velocity profiles presented in §2.2 (Table I); for example, in case of Configuration 2a, we estimate $n = 0.18$ from which $m = 0.82$.

Here, we compare the experimental data with the solutions derived by CALDER (1952) and SUTTON (1953).

In the case of the Calder's solution we need to define a suitable advection velocity U . The simplest physical solution is to take U as the average velocity over the lower part of the boundary layer

$$U = \frac{1}{z_r - d} \int_d^{z_r} \bar{u}(z) dz \quad (4.20)$$

where z_r is a reference height which we have set equal to the upper limit of the inertial region. The measurements presented in §2.2 show that the velocity profile in this part of the boundary layer is logarithmic, at least for the skimming flow regime, so

$$\bar{u}(z) = \frac{u_*}{\kappa} \ln \frac{z}{z_0} \quad (4.21)$$

and

$$U = \frac{u_*}{\kappa} \left[\ln \left(\frac{z_r - d}{z_0} \right) - 1 \right] \quad (4.22)$$

The concentration profile given by Equation 4.17 is plotted in dimensionless form in Figure 4.42, together with the data from all the configurations. The dimensionless concentration C_+ is defined as follows:

$$C_+ = \bar{c} \frac{u_* x}{\dot{M}_q}$$

and the dimensionless vertical coordinate z_+ is given by:

$$z_+ = \frac{U z}{u_* x}$$

from which

³⁴Sutton points out that, in neutral conditions, the height of a cloud generated at ground level is of the order of 5 to 10 percent of the distance travelled.

³⁵This condition is known as *Schmidt's conjugate power-law*.

$$C_+ = \frac{1}{\kappa} \exp \left\{ \frac{-z_+}{\kappa} \right\}$$

This has been used to scale the data of all the configurations, and the results shown in Figure 4.42 confirm the validity of this scaling since the data collapse onto a universal profile. In the outer part of the boundary layer experimental data also agree well with the theoretical profile derived by CALDER (Equation 4.17) but in the inner region the model overestimates the data by about 60%. This is probably due to the fact that the model assumes a uniform velocity profile, whereas in the experiments there is a significant velocity gradient in the region close to the wall. To test this explanation we have also compared the data with the theoretical profile derived by SUTTON (1953) – Equation 4.19 – which takes into account vertical variations in both velocity and diffusivity.

The analytical solution given by Equation 4.19 has been fitted to the experimental data using K_1 as a free parameter, which was set equal to 0.05 m s^{-2} at the top of the boundary layer, i.e. $K_1^+ = K_1/[(\delta - H) \cdot U_\infty] = 0.00167$. The results for the different configurations are shown in Figures 4.43 and 4.44. These figures show that the measured concentrations for the outer part of the boundary layer agree well with the theoretical profile – Equation 4.19. There are some differences close to the wall, where the theoretical profile overestimates the measured concentrations (KASTNER-KLEIN and FEDOROVICH, 2002); however the error is significantly smaller for Equation 4.19 (about 20%, for all configurations) compared with that for the previous model – Equation 4.17 – for which the error in the ground level concentration was about 60%. The errors are similar for both the skimming flow regime (Configuration 2a, Figure 4.43) and the wake interference flow (Configuration 3a, Figure 4.44).

Numerical simulations

The previous results suggest that in order to compute ground level concentrations correctly, it is necessary to include reasonable vertical profiles of both velocity and diffusivity. Furthermore, for certain configurations neither a simple linear profile of diffusivity, nor a power law profile, is sufficient to reproduce the measured concentrations in the lower part of the boundary layer. To investigate the relative importance of the velocity and diffusivity profiles, and the influence of the form of the diffusivity profile, we have again solved the advection-diffusion Equation 4.9 numerically, using a velocity profile given by a power law fitted to the measured velocities. We have computed concentration profiles for different forms of the diffusivity profile.

The two layer diffusivity profiles adopted for an elevated line source also work reasonably well for a ground level release in skimming flow regime (Configuration 1 and 2), as can be seen from the concentration profiles plotted in Figures 4.45 and 4.46. There are also some interesting differences between the two sets of profiles. In Configuration 1 ($H/W = 1$) the numerical profile over-estimates the measured concentrations close to the ground, and this effect increases – both in magnitude and in vertical extent – with distance from the source. At the furthest position downstream ($\xi = 4.09$) the ground level concentration is over-estimated by about 20%, which does not improve the accuracy compared with the ground level values given by the Sutton’s model. In fact, the reason for this over estimate is the same as for Sutton’s model – the extra-diffusion is the RSL is not take into account.

In contrast, the results for Configuration 2a (Figure 4.46) show that the model reproduces the ground level concentration much more accurately, with, if anything, a slight under-estimate of the concentration at the ground. However Sutton’s model appears to reproduce the overall shape of the measured concentration

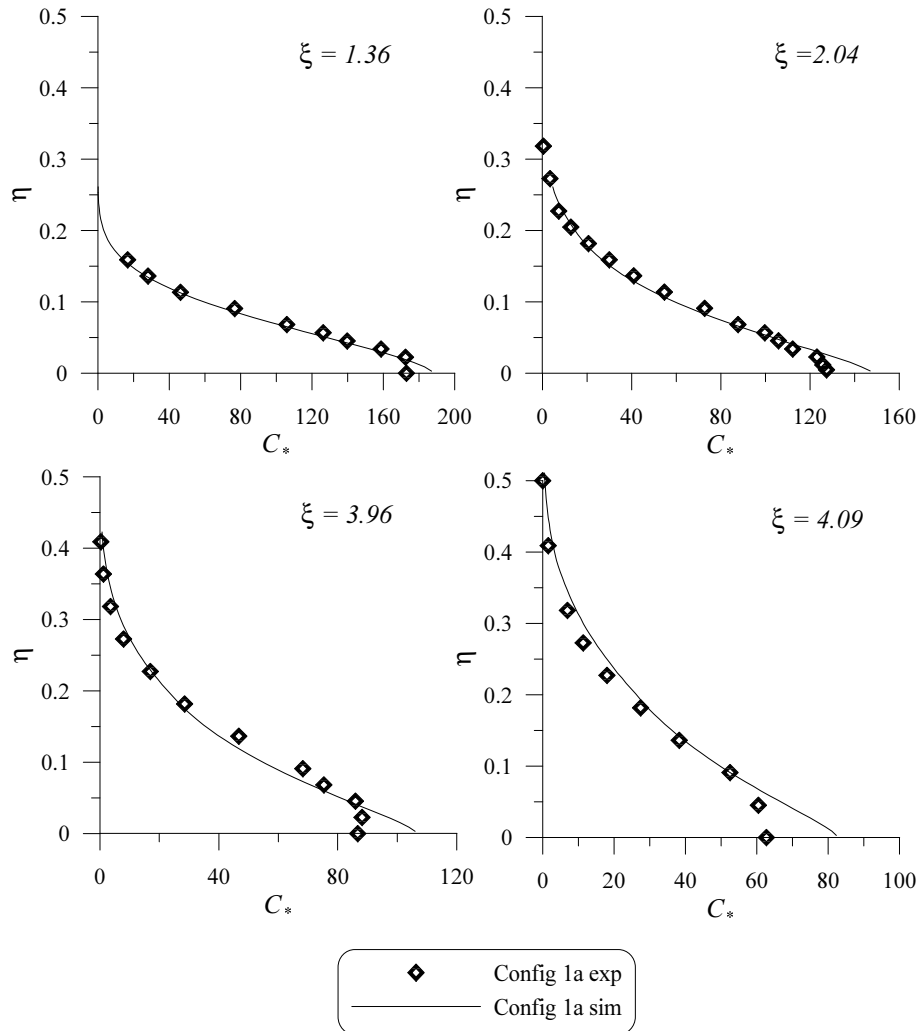


Figure 4.45: Dispersion from a ground level source; comparison between experimental data and numerical simulation: Configuration 1a.

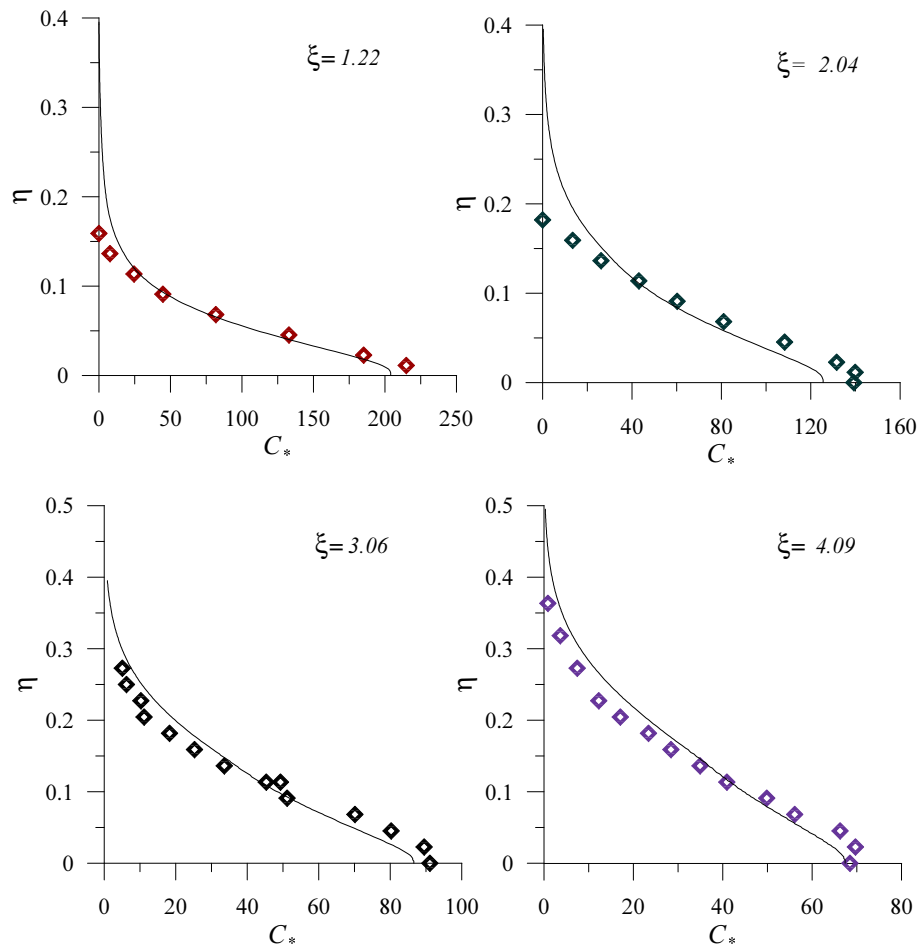


Figure 4.46: Dispersion from a ground level source; comparison between experimental data and numerical simulation for Configuration 2a.

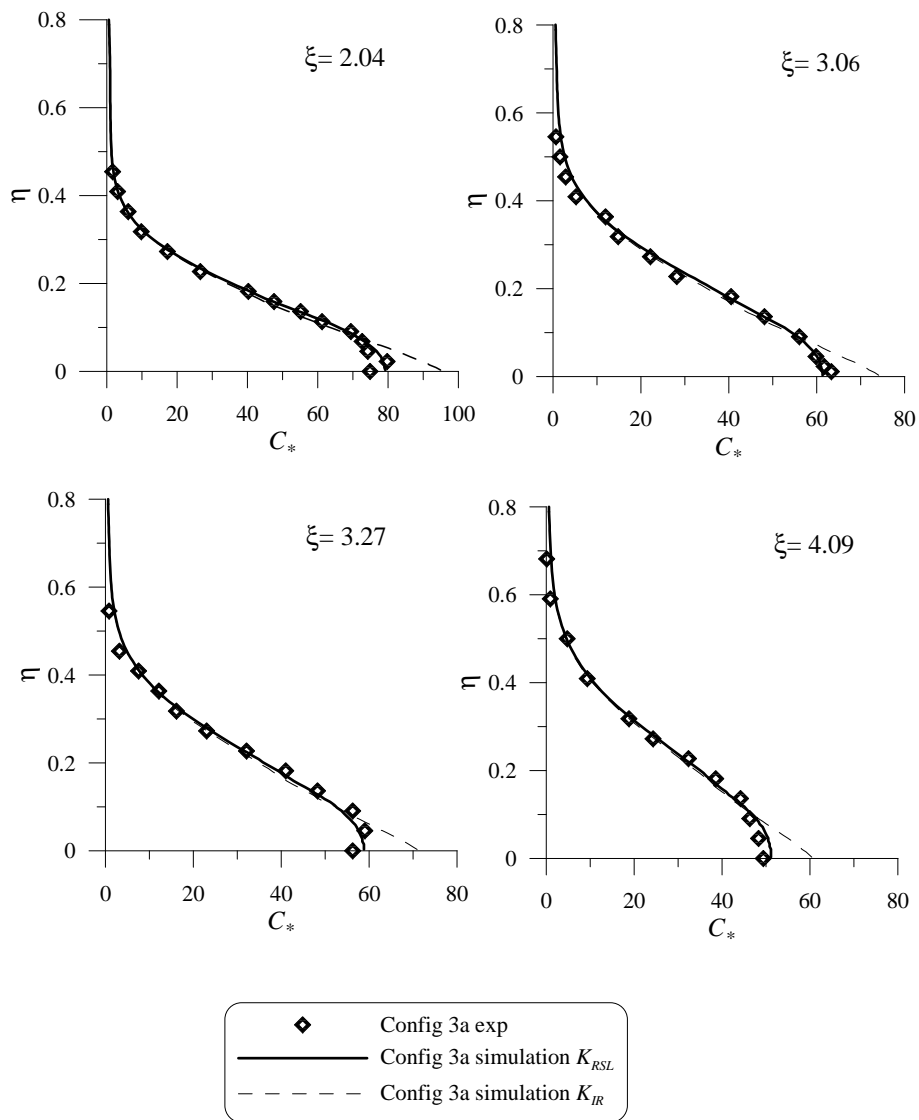


Figure 4.47: Dispersion from a ground level source; comparison between experimental data and numerical simulations for Configuration 3a. K_{IR} : simulations without the RSL; K_{RSL} : simulations with the RSL.

profile more closely (Figure 4.43). A comparison of the forms of the measured and computed profiles suggest that the model diffusivity in the outer region is a little bit higher than in the experiments, and that the model diffusivity close to the boundary is lower than the experimental value. The difference between these two sets of profiles is probably linked to the effect of obstacle spacing on the diffusivity. In Configuration 1 the obstacle separation is twice that in Configuration 2, and we can expect that the diffusivity close to the wall will increase as the obstacle spacing increases, and a linear profile will underestimate the real value.

This effect should be even more noticeable in Configuration 3 ($H/W = 1/2$) for which the spacing between the obstacles is even greater. The concentration profiles for Configuration 3 are shown in Figure 4.46 together with the profiles from two numerical simulations. The first, shown dotted, is the profile obtained using the previous two layer model for the diffusion coefficient (K_{IR}). As expected, this overestimates the measured concentrations in the lower part of the boundary layer, and the difference increases with the distance downstream. In fact the results given by this model seems to be even less accurate than those provided the Sutton's model (Figure 4.44). However the concentration profiles obtained using the RSL model show a good agreement with the experimental profiles even in the lower part of the domain.

4.6 Conclusions

The influence of roughness on flow and dispersion above a series of cavities has been studied using wind tunnel experiments and numerical simulations. Different wall roughnesses were obtained by varying the cavity aspect ratios H/W and by adding smaller scale roughness at the top of the bars.

The velocity measurements were analyzed in order to define the validity and short comings of the similarity theory. If the velocity profiles are scaled on δ – the boundary layer depth – and u_* – the friction velocity – then the velocity profiles for the different wall geometries seem to have a similar behaviour, as stated by the theory.

This is true for almost the entire depth of the boundary layer, except for the lowest part – roughness sub layer – where inhomogeneities arise. However, the different turbulent quantities behave differently for different wall geometries. This is the case for the second and third order moments of the vertical velocity, whose profiles show more scatter compared with those for the longitudinal velocity. The variability in the measured profiles of σ_w/u_* and Sk_w/u_*^3 demonstrates the short-comings of the similarity theory, as already proposed by previous researchers (ANTONIA and KROGSTAD, 2001).

Close to the wall, the flow dynamics depend on both the obstacle height H and the small scale roughness h , and the relative importance of these two scales depends on the cavity aspect ratio H/W .

In case of high aspect ratio cavities ($H/W > 1$), in the skimming flow regime (d-type roughness), the small scale roughness increases the turbulence intensity and the turbulent momentum transfer. In these conditions, the smaller scale structures produced by the small scale roughness influence the flow dynamics as long as their size is of the same order as that of the eddies shed by the shear layer developing at the canopy top.

In the case of wider cavities (for $H/W < 1$), in wake-interference flow (k-type roughness), the effect of the smaller scale roughness is not evident any more. This is probably because the shear layer at the interface has more time to develop, and the flow is then dominated by the larger scale shear-induced eddies, which are generated at the top of the cavities.

The extent of the region influenced by the small scale roughness depends on the cavity aspect ratio H/W .

The extent of the RSL varies significantly from one regime to the other. In case of d-type roughness (skimming flow) the vertical extension of the RSL is much smaller than H and could be considered almost negligible when compared with the boundary layer height. The experiments confirm the observation of PERRY et al (PERRY *et al.*, 1968), who verified that the roughness element height H is not a relevant length in determining the characteristic roughness length z_0 of the wall. On the other hand, in the case of k-type (wake-interference) the extent of the RSL is much larger and appears to be proportional to the obstacle height, i.e. $z_* \sim 2H$.

Concerning the dispersion of a passive scalar, as expected, decreasing the cavity aspect ratio induces higher turbulent mass fluxes. The addition of small roughnesses enhances the turbulent fluxes, but only in the skimming flow regime, where the large scale obstacles are packed sufficiently closely together. This is similar to what has been observed in velocity measurements.

Empirical relations based on eulerian statistics for plume spread have been shown to give satisfactory estimate of measured concentrations, provided that the ratio T/T_L is sufficiently large.

Numerical simulations have been performed, assuming a turbulent diffusivity $K(z) = \ell(z)v(z)$. Based on similarity theory, the domain was decomposed into three regions (outer layer, inertial layer and roughness sub-layer) and appropriate scalings for $v(z)$ and $\ell(z)$ were defined for each layer. Comparisons with data show that a first order model for the dispersion coefficient can provide reasonable estimates for dispersion from both ground level and elevated sources even at short-range, i.e. for $0.5 < T/T_L < 5$. In the numerical simulations, as well as in the estimates for σ_z , the role of the wall roughness was taken into account only by varying the friction velocity. This suggests that the dispersion process within the boundary layer flow is not directly related to the spatial scale imposed at the wall but mainly to the characteristic scaling of the boundary layer flow. The results show that outside the RSL the dispersion coefficient only scales on δ , z and u_* , as predicted by similarity theory. This does not hold in the RSL, where the inhomogeneities in the flow become important. The RSL has a much greater influence on dispersion in the wake-interference regime than in the skimming flow regime, and this is reflected in the different values for the constant of proportionality used to define the integral length scale in the outer region of the boundary layer – $\alpha = 0.05$ for the skimming flow regime and $\alpha = 0.07$ for the wake interference regime. A simple model for a spatially-averaged dispersion coefficient in the RSL has been proposed, which provides a good prediction of ground level concentrations. The results from simulations of scalar dispersion suggest that the enhanced diffusivity within the RSL is due to an increase in the integral length scale. In the wake interference regime, this seems to scale with the obstacle height, H . The proposed model for dispersion in the RSL has only been tested for a few very simple geometries, and it needs to be tested for more complex configurations.

As a general conclusion, we can assert that the dynamics within a turbulent boundary layer bounding a two-scale rough surface are mainly related to only one roughness length:

- when the obstacles are packed sufficiently closely together (skimming flow regime), the flow dynamics are dominated by the influence of the small scale roughness elements;
- when the distance between large scale obstacles increases, the flow is dominated by the larger scale turbulent structures (with linear dimension $\sim H$), that engulf and dissipate the smaller scale structures produced by the small scale roughness elements.

MASS AND MOMENTUM EXCHANGE
BETWEEN A STREET CANYON
AND THE EXTERNAL FLOW

5.1 Introduction

In the last three decades, in order to model pollutant dispersion inside a street canyon, several models have been proposed to describe mean concentration distribution and retention time of pollutant inside the canyon, as a function of the flow dynamics of the external flow and of the canyon geometry (HOTCHKISS and HARLOW, 1973; YAMARTINO and WIEGAND, 1987; BERKOWICZ *et al.*, 1997; SOULHAC, 2000). The purpose of these models is to find simple relations to describe a phenomenon that is highly non-stationary and intermittent: the mass and momentum exchange between a recirculating region and the external flow.

The study of the flow within a cavity started with the experiment performed by ALBRECHT (1933) and has become so far a typical case-study in fluid mechanics. Among all the studies on this topic we cite the studies by MILLS (1965) and BURGGRAF (1966) for viscous flow, by PAN et ACRIVOS (1967) and by MEHTA et LAVAN (1969) on the formation of the counter-rotating vortex on the bottom of the cavity. Other authors focused on their attention on the geometry of the canyon, by studying the effect of the street aspect ratio H/W (HUSSAIN and LEE, 1980; OKE, 1987; OKE, 1988b) and asymmetrical canyon geometries (HOYDYSH and DABBERDT, 1988; HASSAN and CROWTHER, 1998; JOHNSON *et al.*, 1990)

The goal of this study is to evaluate how different conditions within and outside the cavity determine the velocity and concentration fields within the cavity itself; more than that, the aim is to find the appropriate reference velocity and length scales that characterize the mass exchange between the recirculating region and the external flow. So far some experimental study focused on the turbulence structure of the flow above a street canyon (ROTACH, 1993a; ROTACH, 1993b; ROTACH, 1995; LOUKA *et al.*, 1998), in order to give its influence on the turbulent transport at the interface between the canyon and the external flow.

Our approach is to consider the recirculating region within the cavity and the external flow as two systems which are somehow ‘separated’ one from the other. With this assumption, we have performed two kind of experiments:

1. conditions inside the cavity were modified, either by changing the cavity geometry (the aspect ratio H/W) or by adding roughness elements to the sidewalls of the canyon (Par 5.2); the external conditions were held constant;
2. the dynamics of the external flow (Par 5.3) were modified, whilst maintaining conditions inside the cavity unchanged.

The external velocity field was measured using a hot-wire anemometer (Chap. 4) and PIV was used to measure flow within the cavity. Concentrations were measured using a FID system (Chap. 3).

Finally, velocity and concentrations measurements of all experiments have been combined, in order to determine how mass exchange across the upper interface depends on these different parameters.

The adopted reference frame work assumes, as usual, $z = 0$ at the bottom of the cavity and $x = 0$ at the cavity center, for all cavity geometries.

5.2 Varying the boundary conditions within the canyon

5.2.1 On the influence of canyon geometry

In order to evaluate the influence of canyon geometry on the flow and the mixing within it, we varied street aspect ratio (H/W), without modifying the canyons up-wind of the test canyon (this corresponds to configuration 1, see chapter 4). In principle, then the incident flow should be the same in all cases. We

have evaluated the influence of the street cavity aspect ratio on mean velocity, turbulent kinetic energy and mean concentration of a passive scalar field within the canyon. Here the data are plotted using U_∞ as reference velocity. As a general rule, when the boundary layer depth δ is much larger than the canyon size, U_∞ is not the appropriate reference velocity of the flow within the cavity, and here $\delta \sim 10H$. However, in this particular case, this choice is justified, so long as not only U_∞ but all variables of the external flow (mean velocities, turbulence intensity, boundary layer depth...) do not change from one case to another.

Mean flow

It is well known (HUSSAIN and LEE, 1980; OKE, 1987; OKE, 1988b) that the topology of the mean velocity streamlines within the cavity varies as the street aspect ratio is altered. As can be seen in fig. 5.1, in the square and in the wide canyon there is one ‘main’ recirculating cell, with smaller counter-rotating vortices in the corners. As can be observed by means of flow visualization (Annexe 1), in the case of a square canyon, the ‘main’ vortex seems to be quite stable, whereas for a larger cavity the main vortex seems to be more and more intermittent.

As the street aspect ratio increases, a second counter-rotating cell appears at the bottom of the cavity; we will focus on that transition in §5.3.2. The velocities in the upper cell are much greater than those in the lower cell (fig. 5.1). Flow visualization images (Annexe 1) suggest that the flow is almost stagnant, but a time averaged analysis reveals a mean recirculating motion (fig. 5.2).

Fluctuating flow

The turbulent kinetic energy (t.k.e) and the r.m.s. of the fluctuating velocities (σ_w and σ_u) are plotted in figures 5.3- 5.5, for $H/W = 1$, $H/W = 1/2$ and $H/W = 2$. These results show that the aspect ratio has an important influence on turbulence levels in the cavity; it is particularly evident the difference between the two first cases, i.e. for $H/W \geq 1$ (square and narrow cavity), and the third case, i.e. $H/W = 1/2$.

Square and narrow cavity ($H/W \geq 1$) - As shown in fig. 5.3, the fluctuating flow within the canyon seems to be ‘decoupled’ from the external flow, as long as the turbulent kinetic energy level in the cavity is approximately one order of magnitude smaller than that of the external flow. In both cases, as it is evident by looking at fig. 5.4, a mixing layer takes place at the top of the cavity, where the r.m.s. of the vertical fluctuating velocity is intensified, compared to the surrounding flow field. The linear dimension of the mixing layer increases linearly from the upwind corner, but remains by far smaller than the canyon height.

The presence of the thin shear layer seems to shelter the flow within the cavity from the external turbulence. However (fig. 5.4) a turbulent kinetic energy ‘plume’ spreads down in the cavity from the upper edge of the down-wind wall, all along the canyon wall. This is clearly due to an advection of kinetic energy transport along mean velocity stream-lines. In the case of a narrow cavity the t.k.e. plume does not reach the canyon bottom, i.e. the lower recirculating cells, but is confined in the upper cell.

Large cavity ($H/W \leq 1$) - As the street aspect ratio decreases, i.e. for larger cavities, the mixing layer has more space to grow and becomes larger, compared to that observed in the previous cases. The t.k.e. field within the canyon does not seem to be ‘decoupled’ from the external flow any more.

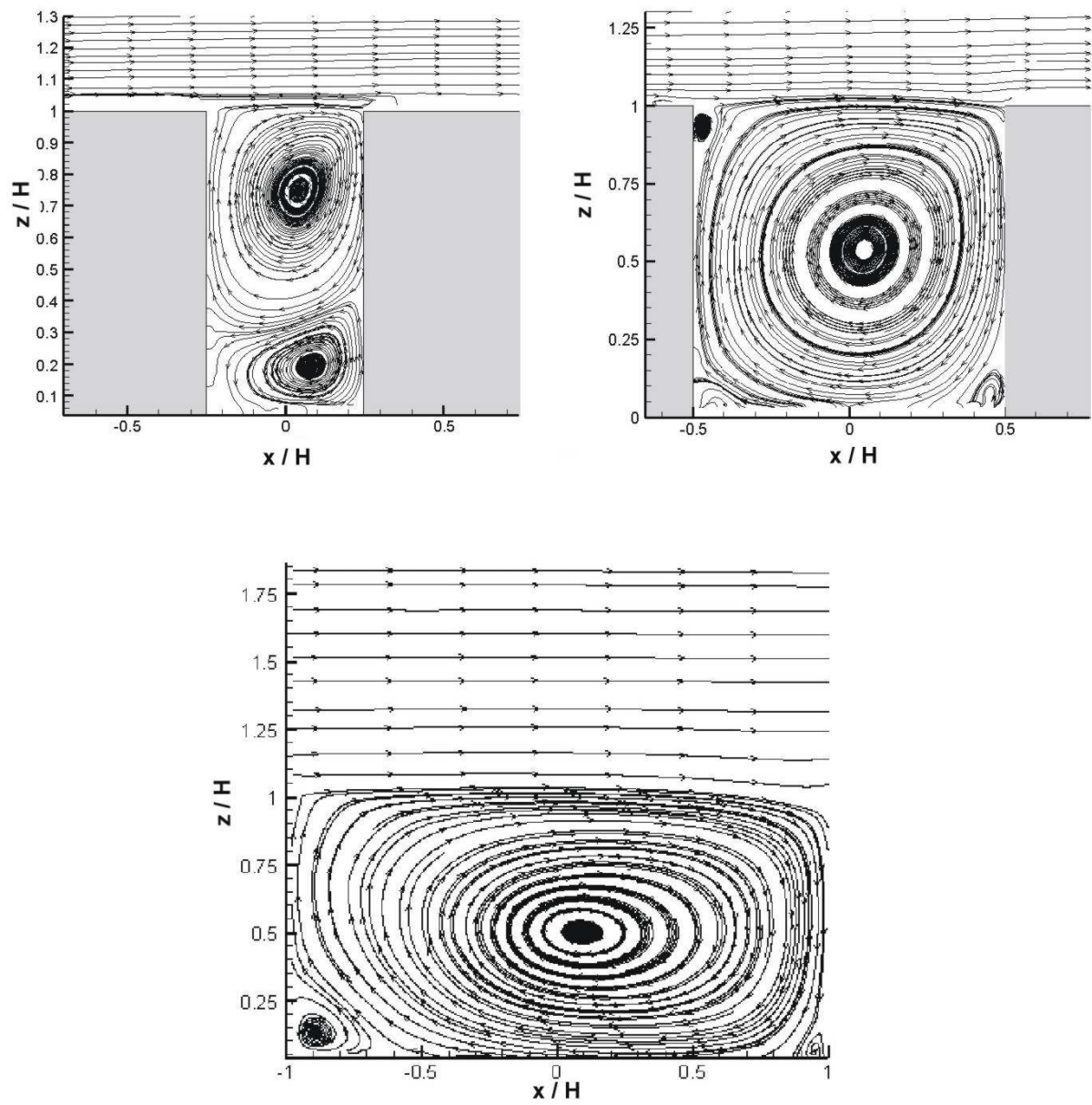


Figure 5.1: Streamlines for different canyon geometries - PIV measurements.

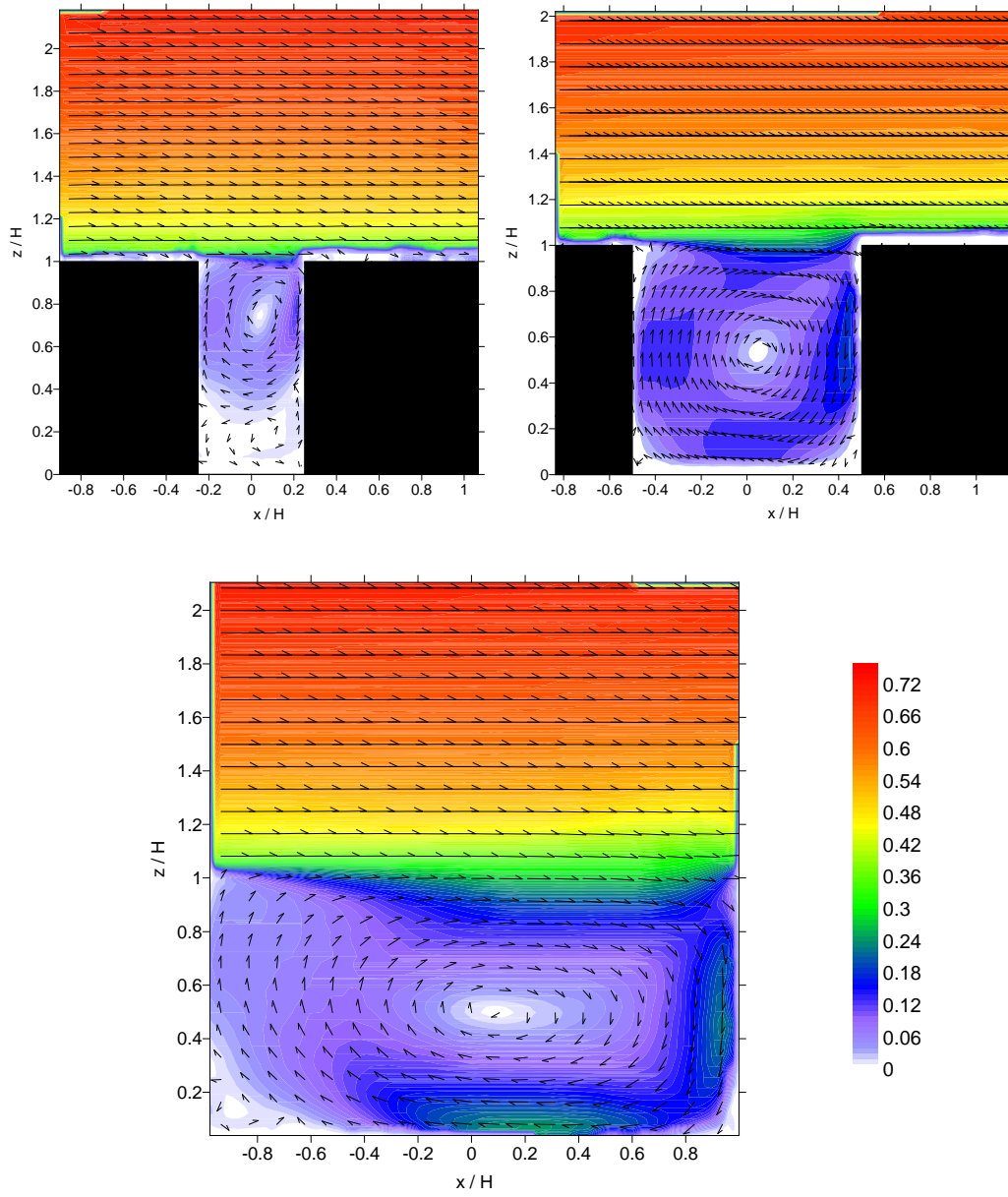


Figure 5.2: Normalized velocity \mathbf{U}/U_∞ within the canyon. Arrows give direction, color magnitude of mean velocity. Strange values at the boundary of the domain are due to measurement errors. Measurements close to the wall failed because of wall reflections.

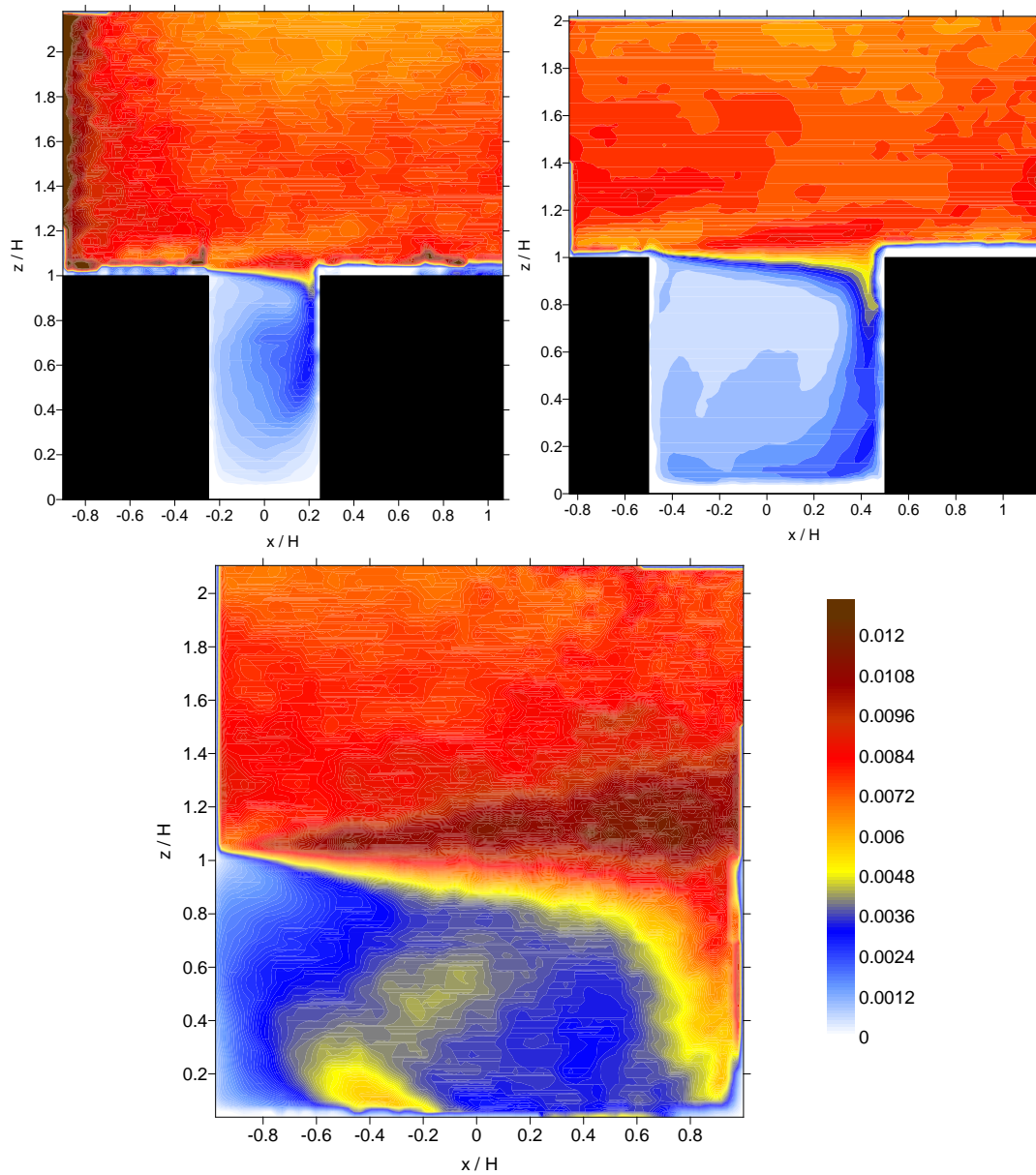


Figure 5.3: Normalized turbulent kinetic energy $1/2q^2/U_\infty^2$ within the canyon. Strange values at the boundary of the domain are due to measurement errors. Measurements close to the wall failed because of wall reflections.

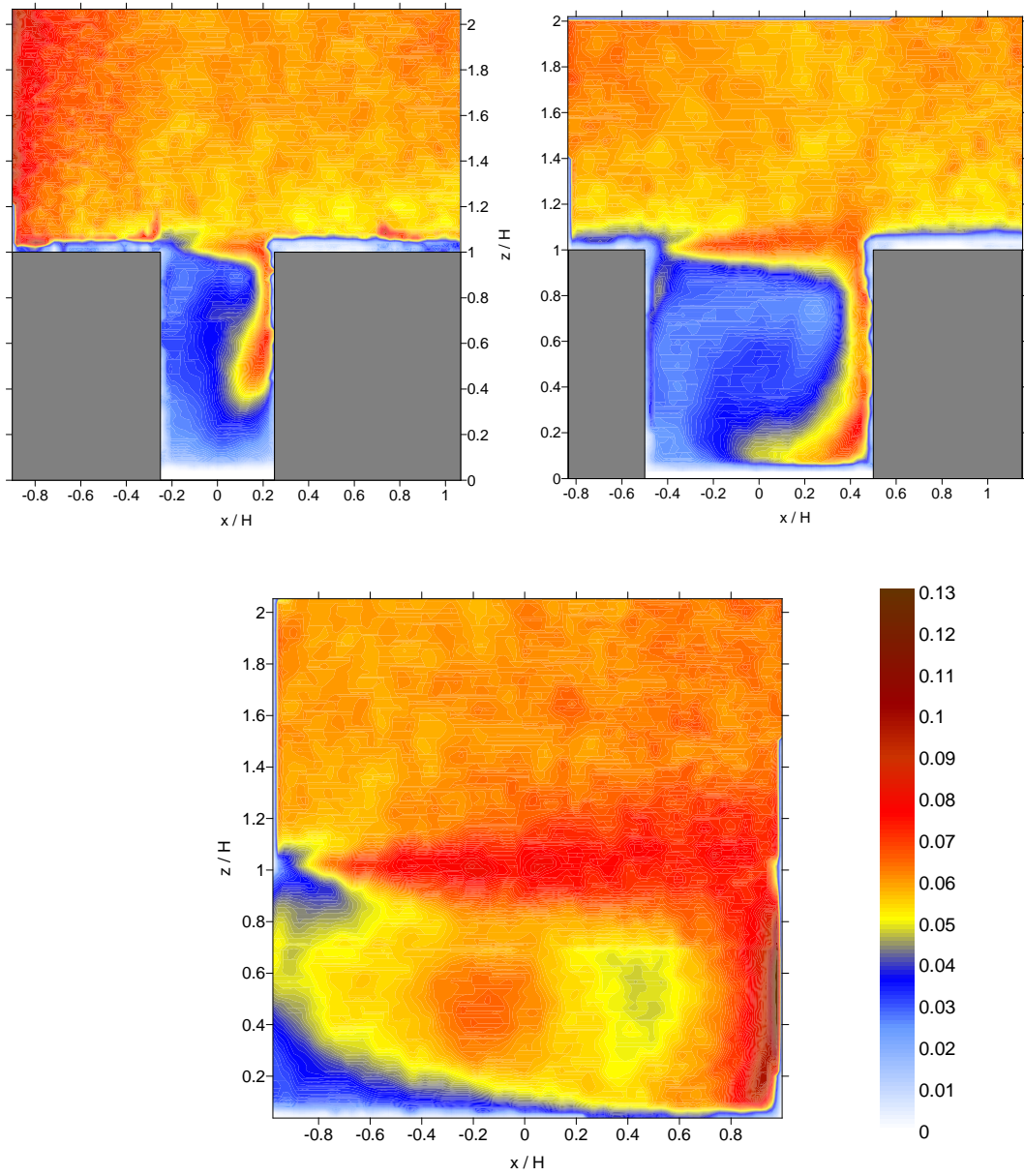


Figure 5.4: Normalized r.m.s. of the vertical velocity fluctuation σ_w/U_∞ . Increased values on the upwind side of the domain in case of configuration 2 ($H/W=2$) are due to inaccurate measurements.

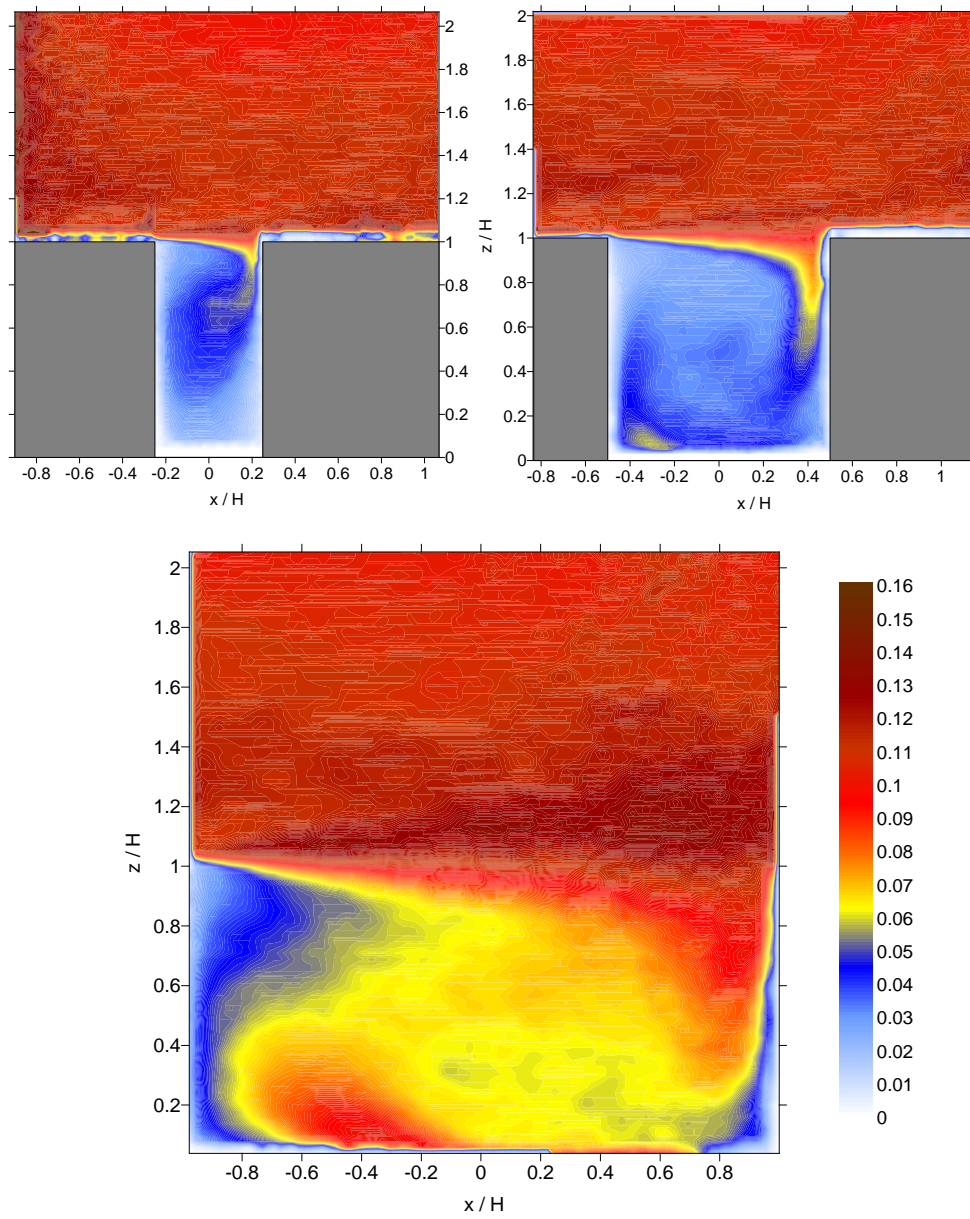


Figure 5.5: Normalized r.m.s. of the horizontal velocity fluctuation σ_u/U_∞ . Inaccurate values at the boundary of the domain, as well as close to the walls, are due to measurements errors.

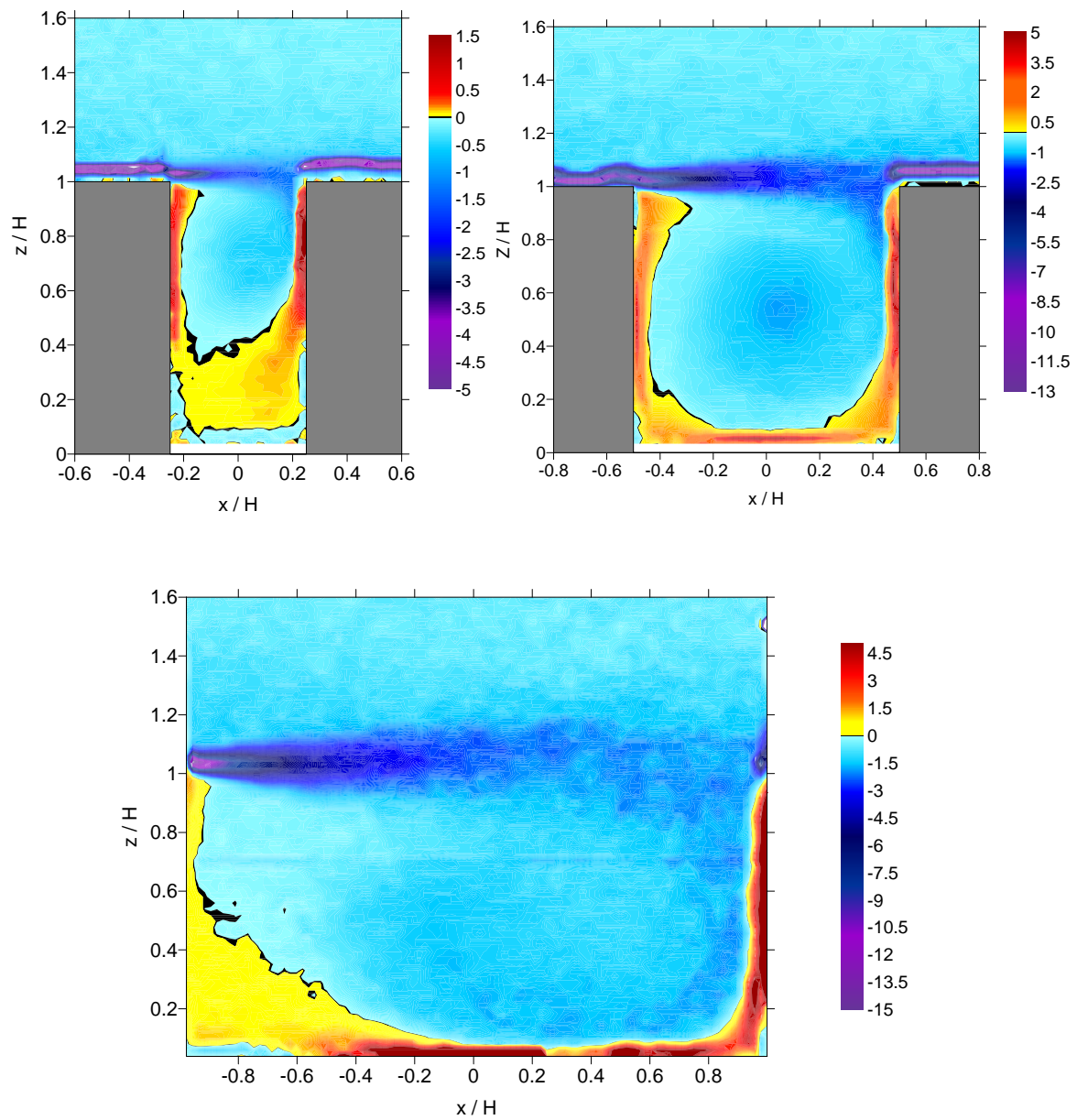


Figure 5.6: Normalized vorticity field ($\frac{\omega W}{U_\infty}$) within the canyon for different cavity aspect ratio ($H/W=2, 1, 1/2$). Wall reflections did not allow accurate measurements in the lower part of the domain close to the cavity bottom and close to the walls.

The plot of σ_w (fig. 5.3) enlightens the presence of the plume all along the down-wind wall, where the vertical velocity fluctuations σ_w are more intense than in the rest of whole flow field. This could be observed also in the two previous cases, but it is particularly evident for the wider cavity.

Clearly, the higher values of σ_w are not only due to the advection of turbulent structure (produced within the shear layer or ‘grasped’ by it from the overlying external flow) and they have to be explained considering the vorticity dynamics within the canyon (fig. 5.6). The vorticity balance equation for an incompressible flow, known as *Helmutz* equation, is

$$\frac{D\omega}{Dt} = (\omega \cdot \nabla)\mathbf{u} + \nu \nabla^2 \omega \quad (5.1)$$

The second term of the right hand side of eq. 5.1 is related to the effect of viscosity, the diffusion of vorticity down a vorticity gradient. The first term represents the action of velocity gradients on vorticity. As can be seen in fig. 5.2, the mean velocity gradients are particularly intense close to the downwind wall and to the bottom of the cavity as well³⁶. The high mean velocity gradients induce the stretching of vortex lines and induce the gain of vorticity, which produces the enhanced velocity fluctuations. This mechanism is known as *vortex stretching* and acts to the fluctuating component of the vorticity field which **lay on the plane of the figure**. It is worth noting that this process implies a three-dimensional flow, as long as, if the flow is bidimensional

$$(\omega \cdot \nabla)\mathbf{u} = \mathbf{0}$$

This mechanism explains the peaks of σ_w in proximity of the downwind wall (fig. 5.4), as well as the peaks of σ_u close to the bottom of the cavity (fig. 5.5).

Passive scalar mean concentration field

A concentration field of a passive scalar has been obtained by placing a linear ground level source at the centre of the canyon (see par. 4.6.2), with a constant source strength per unit length \dot{M}_q .

The resulting mean concentration fields are plotted in fig. 5.7. As expected, the diagrams reveal the presence of a ‘fresh air’ plume entering to the cavity at the upper corner of the downwind wall. The concentration peak reveals the recirculation sense of the mean flow in the lower part of the cavity: clockwise sense for the larger and the square cavity, counter-clockwise for the narrow cavity.

However, from an environmental point of view the most important effect of the presence of two recirculating cells is to slow down the removal of pollutant from the cavity. Adopting an electrical analogy (HARMAN *et al.*, 2004), we can say that the mean flow topology induces a resistance to the passive scalar transport from the inside to the outside of the canyon. The presence of two recirculating cells is analogous to a series of two resistance as long as, before reaching the external flow, a pollutant particle has to be transported from one cell to the other. The results of this process is to induce a much higher peak of mean concentration at the street level, which is approximately two times the concentration reached in case of one cell only.

5.2.2 Influence of roughness on canyon walls

Previous studies determined a typical value of the street aspect ratio H/W at which the transition from one to two recirculating cells takes place. By means of numerical simulations LEE and PARK (1994)

³⁶Mean velocity profiles are showed in the next paragraph, fig 5.12, fig. 5.18 and fig 5.24.

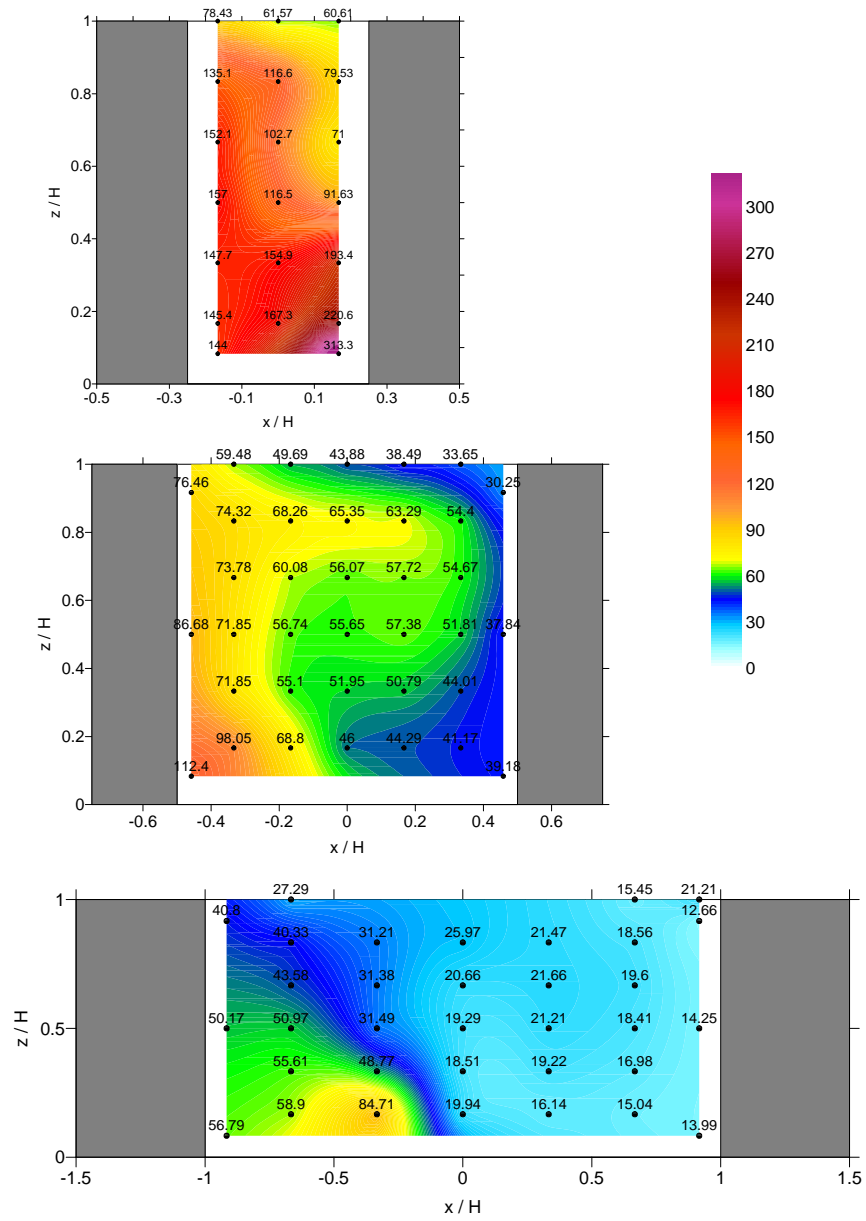


Figure 5.7: Normalized mean concentration $C^* = \frac{CU_\infty H}{\dot{M}_q}$ within the canyon.

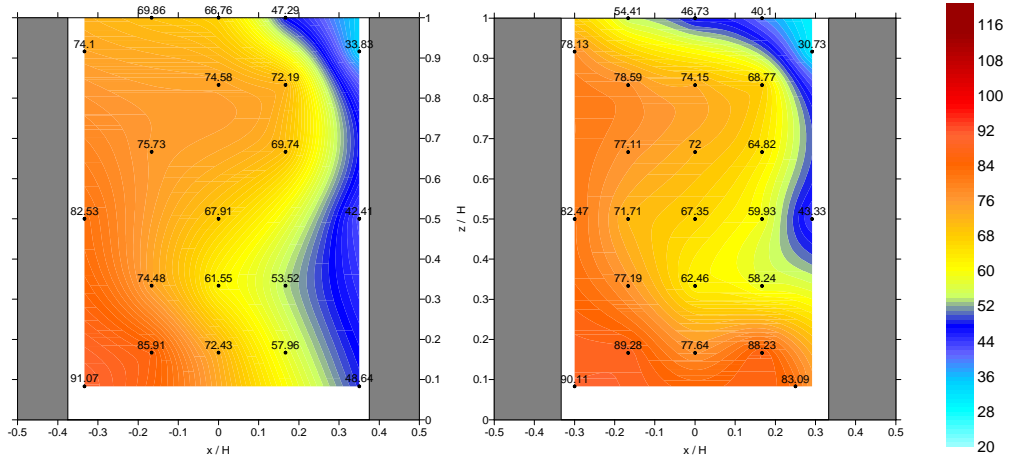


Figure 5.8: Transition from one ($H/W = 4/3$) to two ($H/W = 3/2$) recirculating cells. Normalized mean concentration $C^* = \frac{CU_\infty H}{M_q}$ within the canyon.

determined a value of $H/W \sim 2.1$ whilst SINI *et al.* (1996) obtained a value $H/W \sim 1.7$. In our case we could observe the transition to take place for an aspect ratio H/W between $4/3$ and $3/2$. The mean concentration field in the canyon is shown in fig. 5.8, for the two cases $H/W = 4/3$ and $H/W = 3/2$. In the first case the plume of fresh air reaches the ground but in the second it does not.

The transition from one to two cells occurs because of counter clockwise vorticity diffusing from the cavity walls. The clockwise vorticity is advected into the cavity from the external flow through the mixing layer. In an equilibrium state the two vorticity production terms must balance (otherwise there would be an accumulation of vorticity of one sign or another). When the cavity is reduced, the clockwise vorticity advected inside the canyon is also reduced. The production of anticlockwise vorticity is determined by the total length of the cavity boundary ($2H + W$) and this also decreases as W decreases, but less rapidly, so there is a net surplus of anticlockwise vorticity, which accumulates and generates a second counter-rotating cell at the bottom of the cavity.

Once generated at the wall, the vorticity is brought within the core of flow field by turbulent fluctuations and then advected within it. This process is thus driven by vorticity production on the canyon walls.

As we saw in chapter 4, the main effect of an increased wall roughness is to increase the friction velocity u_* , which leads to an increase in the mean velocity gradient and thus an increase of vorticity production. We have tested the effect of the roughness of the canyon wall by adding small scale roughness elements to one or other of the canyon side walls, for a fixed aspect ratio $H/W = 4/3$, close to the critical ratio for transition.

The effect of wall roughness depends on which wall it is placed on. The results in fig.(fig. 5.9) show that adding roughness to the downwind wall induces transition, whereas adding it to the upwind wall delays it.

In the latter case, the additional anticlockwise vorticity is carried up to the interface and evacuated

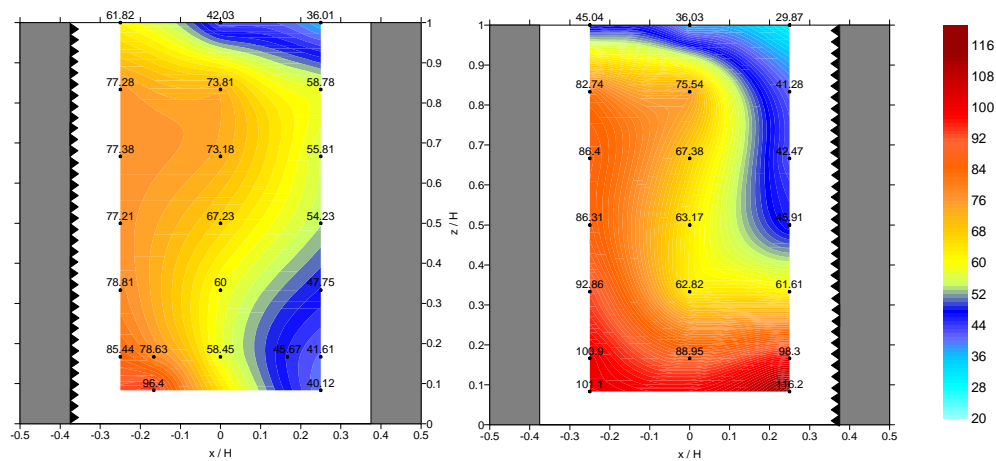


Figure 5.9: Effect of wall roughness on the concentration field within the canyon ($H/W = 4/3$) - normalized mean concentration $C^* = \frac{CU_\infty H}{M_q}$.

from the cavity, so that it does not modify the vorticity balance on the downwind side of the cavity. On the other hand the surplus vorticity generated at the downwind wall, before reaching the mixing layer at the top of the cavity, has to be advected along the stream lines at the bottom of it, where it induces the formation of the anti-clockwise recirculating cell.

5.3 On the influence of varying conditions of the external flow

The goal of this study is to investigate the structure of the mean and the fluctuating velocity field inside a street canyon with different dynamical conditions of the external flow (KIM and BAIK, 2003). Changing the upwind boundary conditions, different oncoming wind profiles have been reproduced, with different mean velocity and turbulent intensities. The different on-coming boundary layers have been obtained by combining the effect of three spires located at the entrance to the test section and the effect of wall roughness, due to an array of 2D parallel bars and of a smaller scale roughness placed on the top of them (Chap. 4). The experiments have been performed for a constant external velocity $U_\infty \sim 6.75m/s$.

5.3.1 Problem setting

As we observed in paragraph 5.2.1, at first glance, for sufficiently high cavity aspect ratio ($H/W > 1$), the flow within the cavity seems to be decoupled from the external flow. The resulting flow field appears to be driven by the dynamics of the shear layer, which takes place at the interface between the two regions.

As mentioned in paragraph 1.2.3, a *shear mixing layer*, arising between two parallel flow with different mean velocity, has an important property: its dynamics can be considered *autonomous* from the rest of the flow field. The production, dissipation and transport of kinetic energy inside the shear layer depend

on the conditions on the boundaries of the shear layer only. In other words, the kinetic energy fluxes do not have any influence on its dynamics. Consequently the only relevant velocity scale is $\Delta U = U_1 - U_2$, the difference between the mean velocities of the two flows (denoted here by U_1 and U_2).

The flow field here is similar to a classical shear mixing layer, but it also has some important differences:

- the flow in the cavity is not always parallel to the external flow;
- the external flow is not uniform (the mean velocities vary with the vertical coordinate);
- the turbulence intensity $i = \frac{q^2/2}{U_{loc}(z)}$ of the external flow is not negligible $0.1 < i < 0.4$.

In order to analyze this flow, we can consider various possible assumptions.

1. The velocity field within the cavity (and the mass exchange at the interface) depends only on the shear layer dynamics; in this case all mean velocities, within the cavity and within the shear layer, should scale with ΔU , only, i.e.:

$$\frac{U}{\Delta U} = const \quad ; \quad \frac{\sigma_u}{\Delta U} = const \quad ; \quad \frac{q^2/2}{\Delta U^2} = const \quad ; \quad etc...$$

2. If this assumption is not satisfied, it means that the shear layer does not act as a filter any more: within it, the kinetic energy flux terms are no longer negligible, compared with the production terms. In this case, the dynamics of the flow within the canyon depend not only on the turbulent structures arising and developing within shear layer, but also on the turbulent eddies of the external flow that the shear layer entrains and injects into the cavity.

In this case three parameters have to be taken into account:

- the mean velocity difference across the shear layer ΔU
- the ratio between the turbulent kinetic energy of the external flow and the mean velocity difference across the shear layer,

$$i_{ext} = \sqrt{\frac{q_{ext}^2/2}{\Delta U^2}}$$

- the turbulent integral length scale of the external flow

$$\frac{\mathcal{L}_{ext}}{W}$$

In this case the mean velocities inside the canyon depend on those parameters, i.e.

$$\frac{U}{\Delta U} = f(i_{ext}; \frac{\mathcal{L}_{ext}}{H}) \quad ; \quad \frac{\sigma_u}{\Delta U} = f(i_{ext}; \frac{\mathcal{L}_{ext}}{H}) \quad ; \quad \frac{q^2/2}{\Delta U^2} = f(i_{ext}; \frac{\mathcal{L}_{ext}}{H}) \quad ; \quad etc...$$

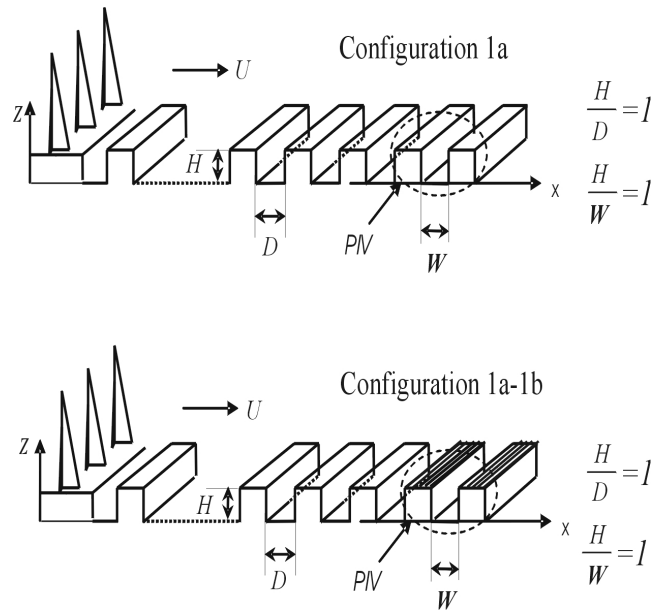


Figure 5.10: Experimental set-up.

One more problem has to be discussed: how to evaluate the spatial extension of the shear layer. In a ‘canonical’ case, the shear mixing layer boundary can be easily evaluated as the points were $U(z) = 0.98U_1$, for the upper limit, and $U(z) = 0.98U_2$ for the lower limit.

In the case we are interested in the external flow is not uniform and the boundary layer height of the external flow is much greater than the canyon size ($\delta \sim 10H$). This means that the external velocity U_1 is not even approximately equal to U_∞ and the mean horizontal internal velocity U_2 varies with horizontal distance x , so the definition of an equivalent shear layer is rather difficult.

The criterion we suggest is to analyze the Reynolds stress profiles to determine the boundary between the region where it varies relatively rapidly, and the region where it is nearly constant. In such a way we can evaluate the vertical extension of the shear layer at different distances from the upwind corner. In order to evaluate the difference ΔU we use the profile at the cavity centre ($z = 0$) assuming that, at that position, the mean flow within the cavity can be considered parallel to the mean flow in the external region.

5.3.2 Square cavity

Perturbation of the shear layer - the role of roughness on roof top

Since the flow field within the cavity seems to be driven by the dynamics of the shear layer we have tried to perturb it, by placing the small scale roughness (we remember that the size of the small elements is $h \sim H/12$) on the tops of the two obstacles that fix the boundaries of the cavity only. The other elements upstream and downstream of the cavity were not modified, so the structure of the incident wind should

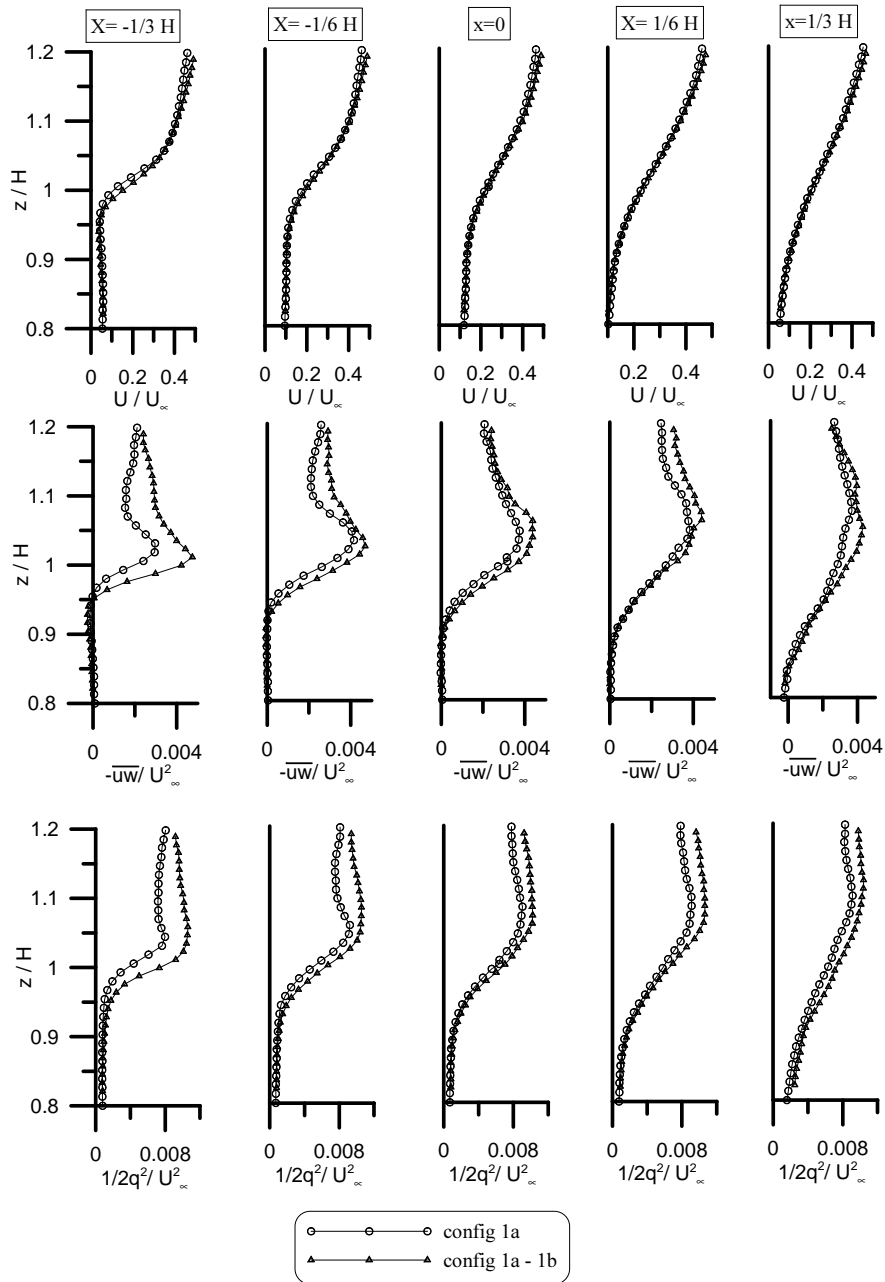


Figure 5.11: Velocity profiles within the shear layer in a square cavity with (configuration 1a-1b) and without (configuration 1) roughness on the roof top.

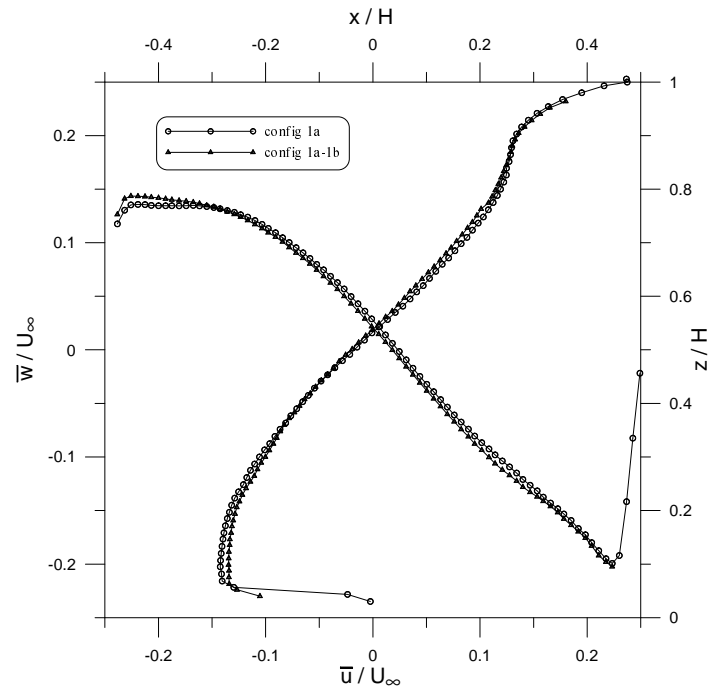


Figure 5.12: Mean horizontal velocity profile (\bar{u}) at the cavity centre and mean vertical velocity profile (\bar{w}) at the cavity mid-height in a square cavity with (configuration 1a-1b) and without (configuration 1a) roughness on the roof top.

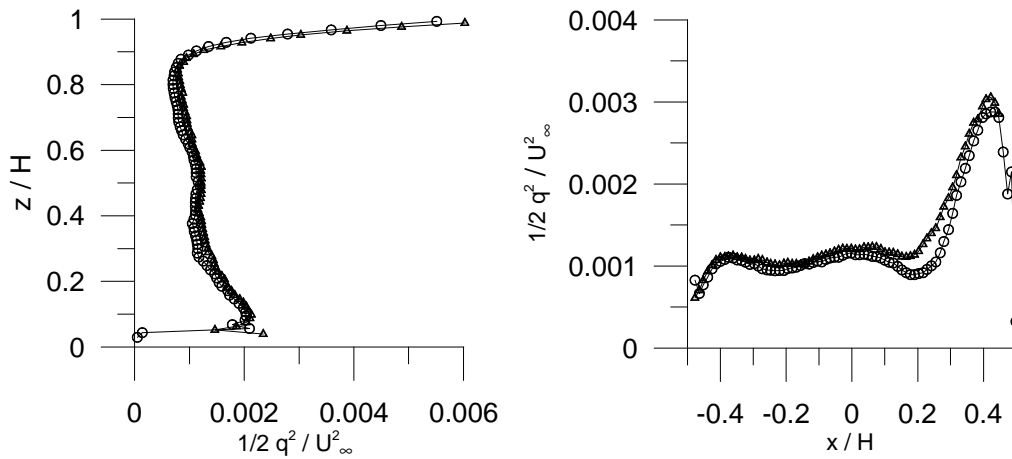


Figure 5.13: Turbulent kinetic energy profiles. Vertical profile (on the left) at the canyon centre ($x = 0$) and horizontal profile (on the right) at the canyon mid-height ($z = 1/2H$); same symbols as for fig. 5.12.

not be affected by this. We compared the flow fields of two configurations: the first one is obtained by an array of square cavities (configuration 1a), the second one (configuration 1a-1b) is identical to the first, except for the presence of the small roughness on the roof-top of the two obstacles bounding the canyon (see fig. 5.10). Fig. 5.11 shows the vertical profiles of the horizontal mean velocities, Reynolds stresses and turbulent kinetic energy at different stream-wise positions along the mixing layer (the frame work reference is presented in fig. ??). Since the configuration and the external flow conditions are identical in the two cases, we have plotted the velocity results using U_∞ as the reference velocity. The roughness at the roof top does not have any effect on the mean velocity profile, but it does produce a slight increase in the velocity fluctuations (turbulent kinetic energy) and the turbulent momentum exchange (Reynolds stress) in a region immediately downwind of the upwind corner. But this enhanced fluctuating motion appears to be rapidly enveloped by the turbulent structures generated in the shear layer and dissipated within it.

Consequently the flow field within the cavity is insensitive to the presence of small scale roughness on the roof top ³⁷: this is evident (see fig. 5.12- 5.13) for the vertical (at the canyon centre $x = 0$) and horizontal profiles (at the cavity mid-height $z = H/2$) of the mean motion and of the turbulent kinetic energy within the canyon.

The influence of the structure of the turbulence in the external flow

In order to verify the ‘autonomy’ of the dynamics of the shear layer and of flow field within the canyon from the external flow dynamics, we varied the turbulence structure of the on-coming wind profiles, whilst maintaining the same geometry of the cavity within which we performed the velocity measurements. The experimental set-up is shown in fig. 5.14. The base configuration is, as usual, obtained by a series of square canyons (configuration 1a). In order to vary the small scale turbulence intensity, we placed the smaller scale roughness on all the obstacle roofs (configuration 1b). In order to vary the large scale turbulence in the flow we have performed experiments with two different values of the aspect ratio of the 2D parallel canyons - $H/D=1$ and $H/D=1/2$ (configuration 3a-1a).

Vertical profiles of mean velocity, turbulent kinetic energy, Reynolds stress and turbulence intensity for three different configurations are shown in fig. 5.15. Similar profiles on the vertical centreline are shown in fig. 5.16. Data within the cavity were obtained using PIV and above the cavity using hot-wire anemometry. These are superposed to produce the full profiles shown in the figures. The mean velocity profiles, as well as the Reynolds stress profiles, show a good agreement, when measured with different systems, but as already mentioned in chapter 4, the PIV system tends to overestimate the velocity fluctuations, when compared with hot wire anemometer.

Shear layer analysis - In fig. 5.17 are shown the vertical velocity profiles at the cavity top, within the shear layer. As already mentioned, the velocity profiles have been normalized using the velocity difference ΔU at the shear layer boundary, taken at the cavity centre ($x = 0$). The mean velocity profiles collapse on one single curve, for each downstream position. On the other hand, the turbulent kinetic energy profiles, as well as the Reynolds stress profiles, show different behaviour in the three different cases. This means that the velocity difference ΔU is not the only relevant scale within the shear layer, even if it seems to be the case for the mean motion. The shear layer developing at the canyon top is not an autonomous region: its dynamics are influenced by the flux of kinetic energy from the external flow.

³⁷Actually very slight difference are detectable in the mean velocity profiles (fig. 5.12); surprisingly, the biggest difference occur farthest from the shear layer.

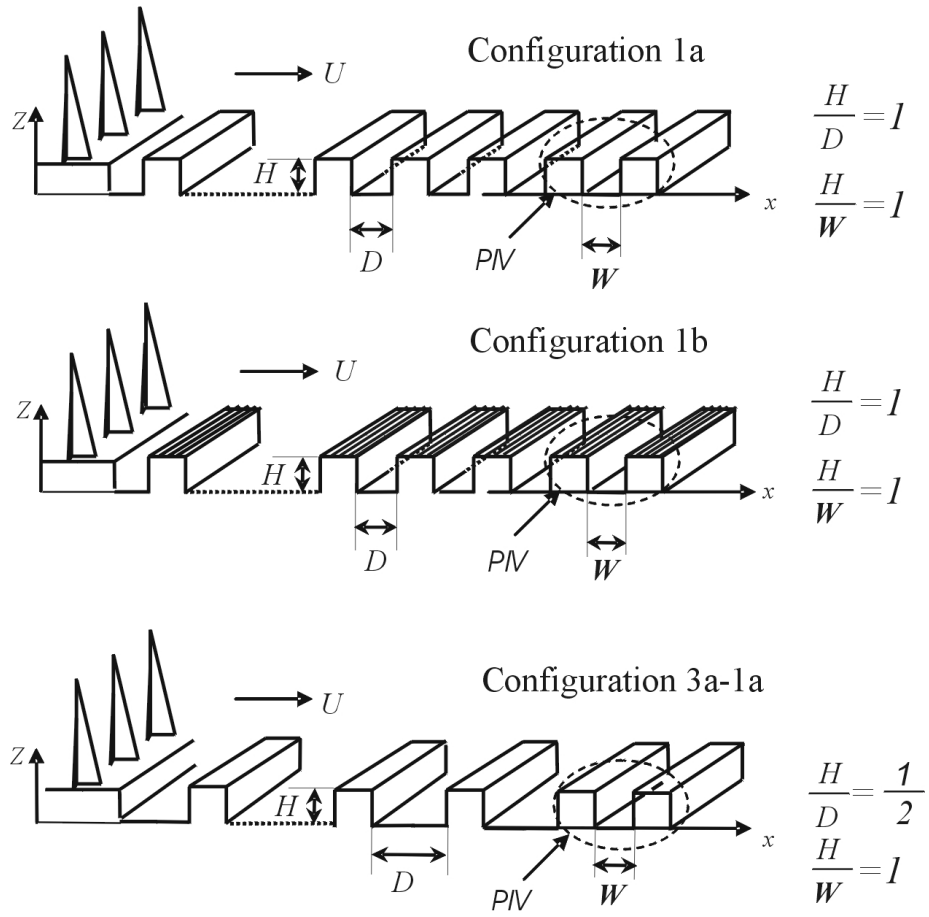


Figure 5.14: Experimental set-up.

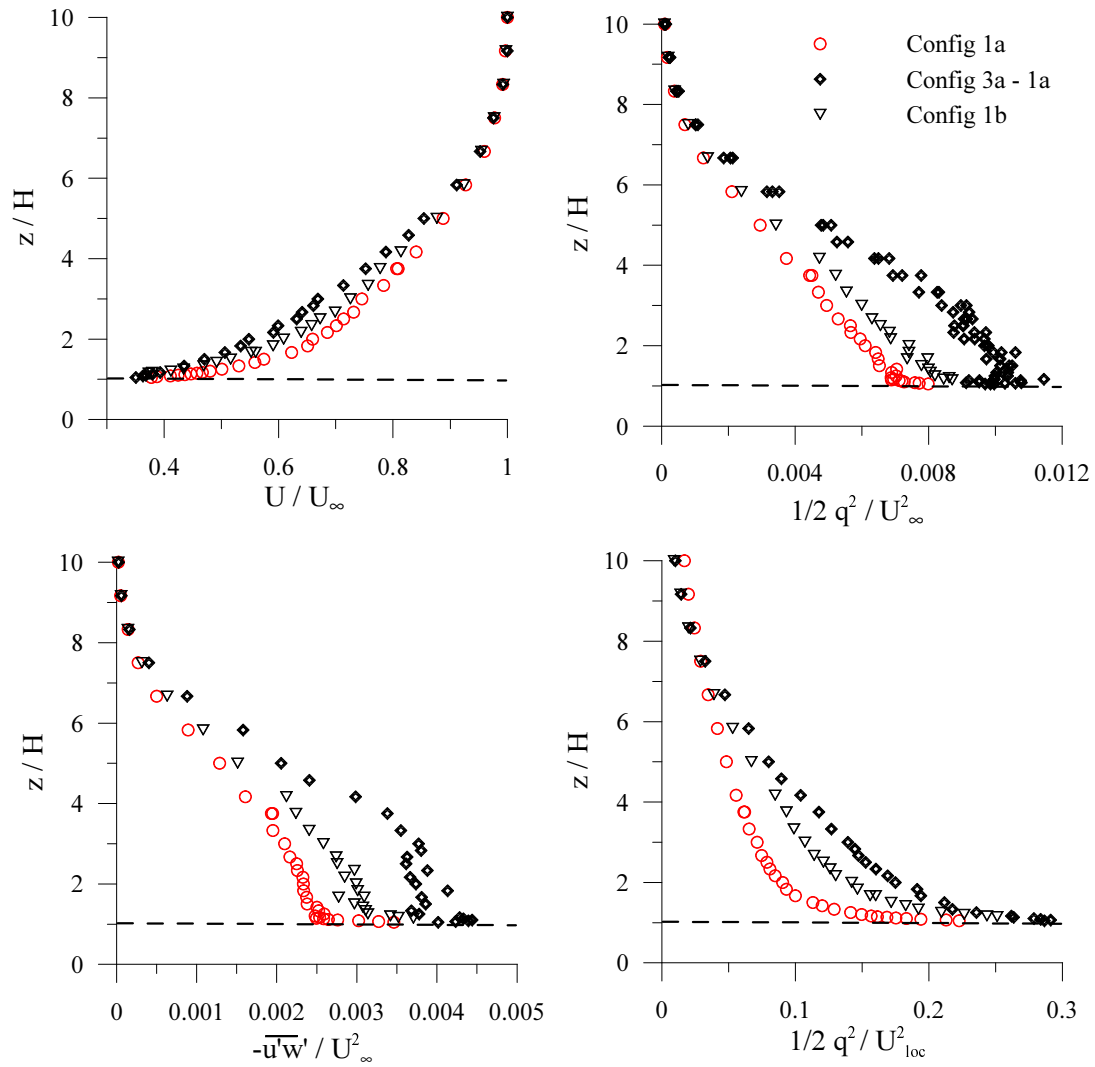


Figure 5.15: External flow conditions.

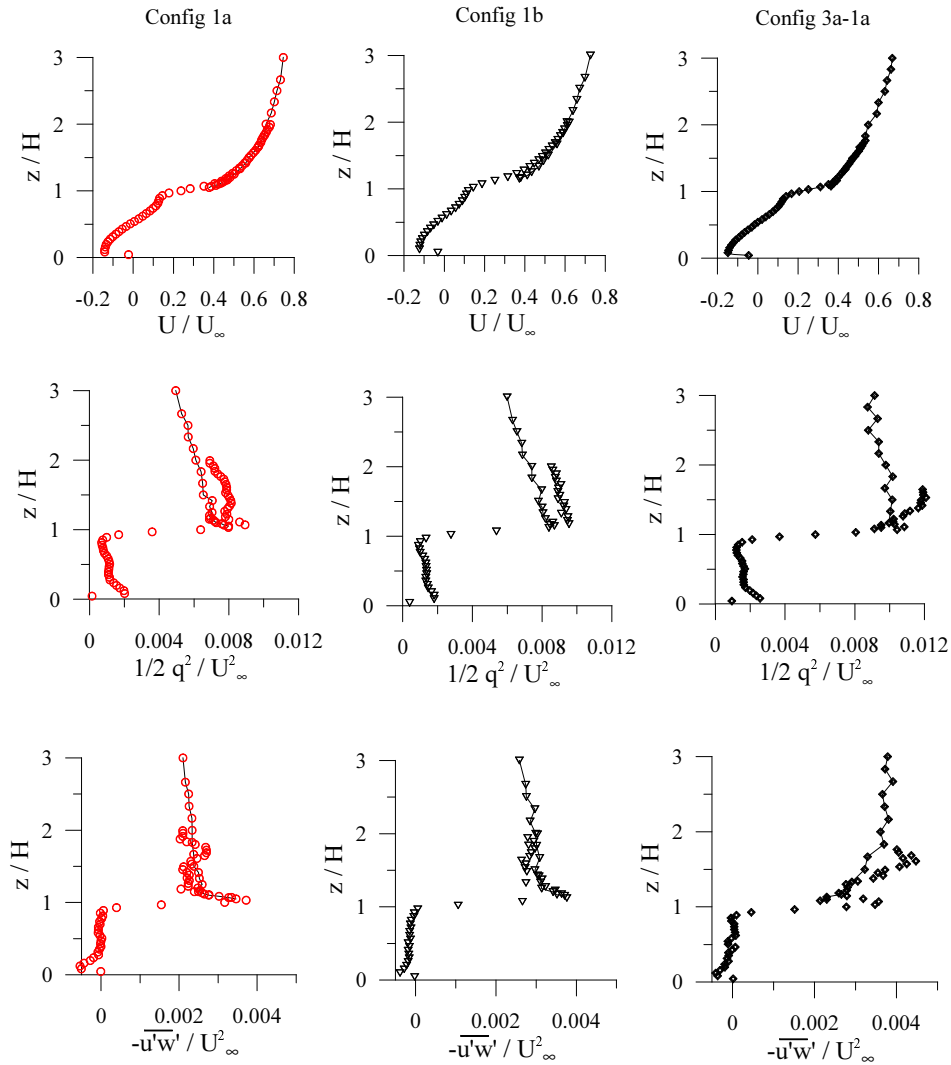


Figure 5.16: Comparison between PIV data ($0 < z < 2H$) and hot-wire anemometry data ($H < z < 3H$). The hot-wire anemometry data concern the external flow, i.e. $1 < z/H < 3$ whereas the PIV data concern the lower part of the external flow and the cavity, i.e. for $0 < z/H < 2$

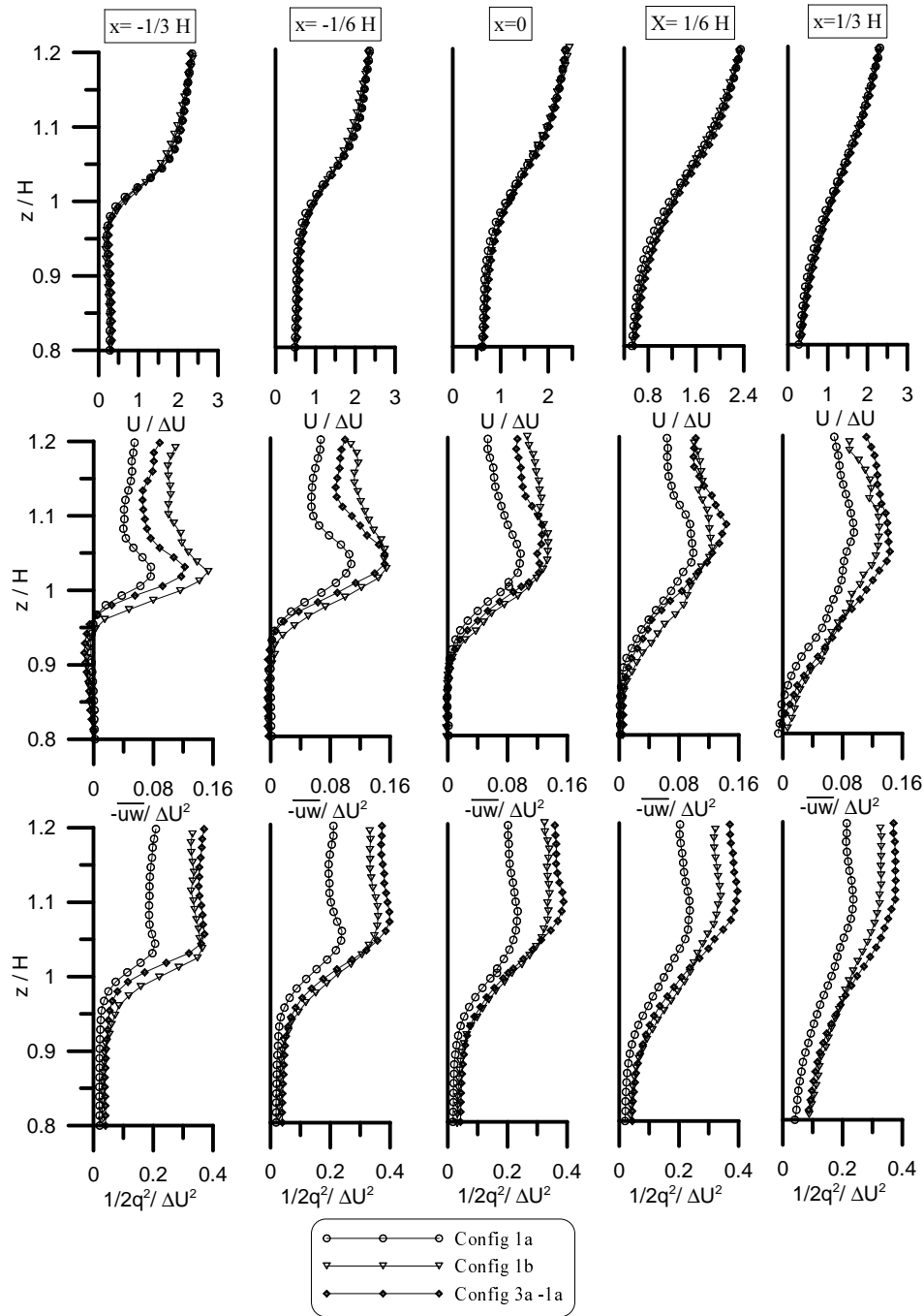


Figure 5.17: Velocity profiles normalized with the mean velocity difference ΔU between the shear layer boundaries.

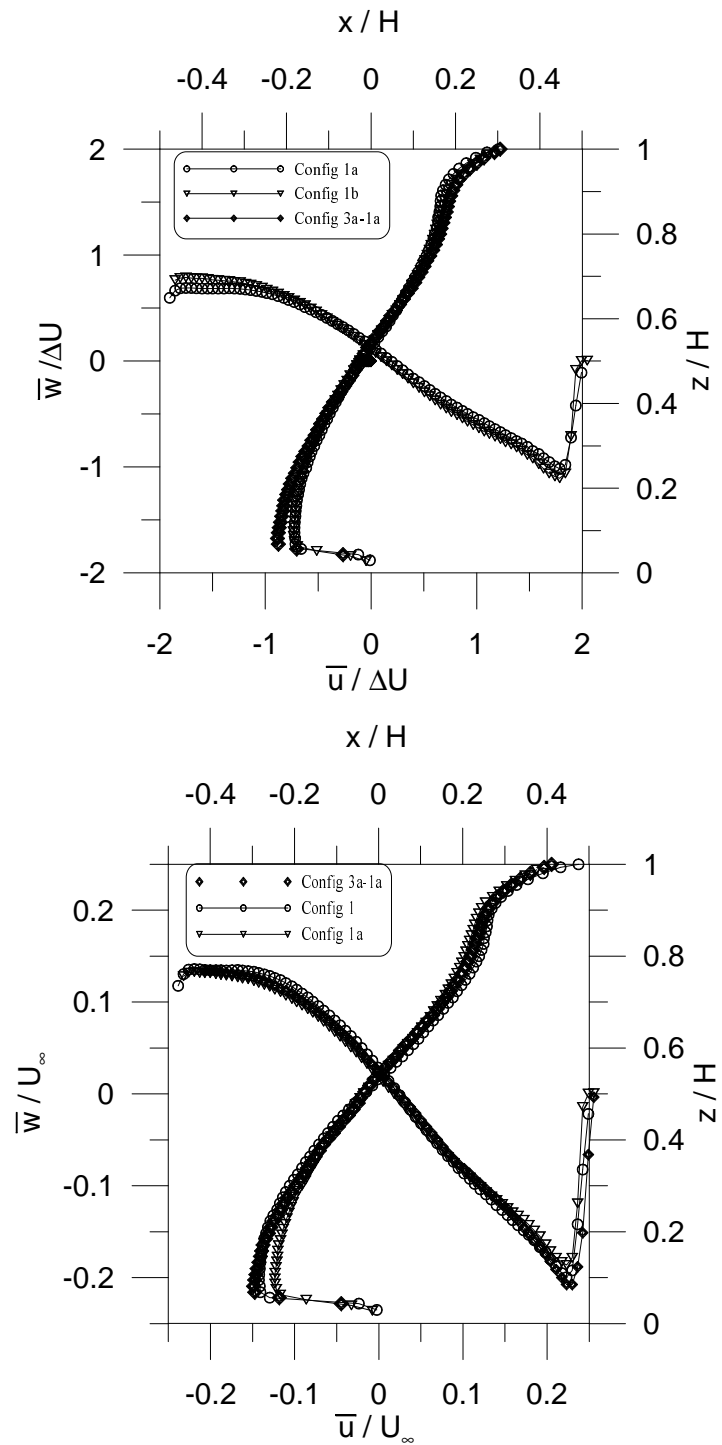


Figure 5.18: Mean velocity profiles within the cavity normalized with the mean velocity difference between the shear layer boundaries ΔU and with the mean velocity at the top of the simulated atmospheric boundary layer U_∞ .

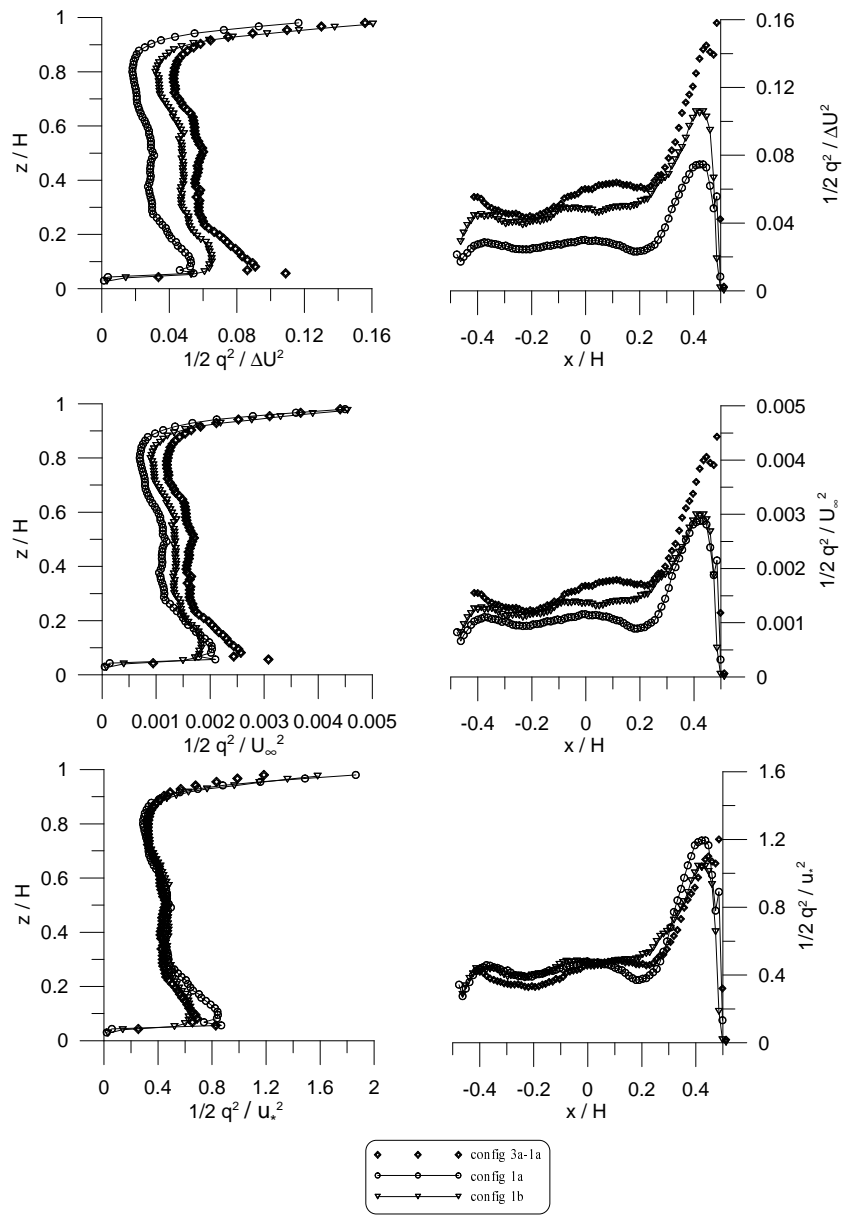


Figure 5.19: Turbulent kinetic energy profiles within the cavity normalized with the mean velocity difference ΔU , the mean velocity at the top of the simulated atmospheric boundary layer U_∞ and with the friction velocity of the external flow u_* .

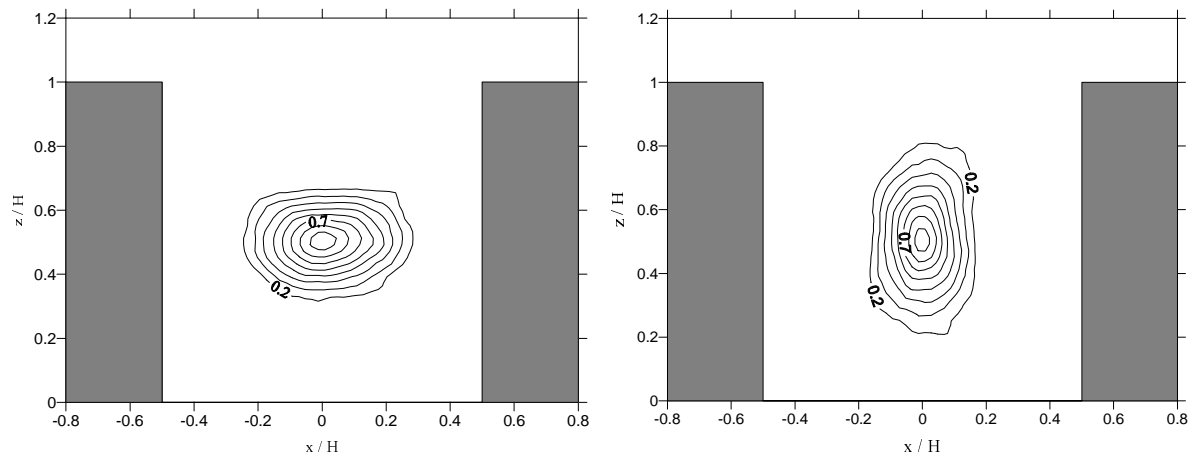


Figure 5.20: Spatial auto correlation within a square cavity computed at the cavity centre ($x=0$, $z=1/2$ H); L_{uu} on the left and L_{ww} on the right.

Flow within the cavity - As long as the shear layer dynamics are not independent of the turbulent kinetic energy fluxes coming from the external flow toward the cavity, the shear layer itself does not shelter the flow field within the canyon from the dynamics of the external flow. The mean velocity profiles (fig. 5.18) do not differ significantly each other, when normalized with ΔU . Using ΔU as reference velocity, however, turbulent kinetic energy profiles (fig. 5.19) are far to collapse on one single curve: as it was expected, ΔU is not the appropriate velocity scale for flow within the canyon. The horizontal profile of t.k.e. indicates the presence of a turbulent plume close to the down-stream wall. In the rest of the flow field however, the turbulence intensity seems to be ‘well mixed’ within the cavity itself, in agreement with previous observations (KASTNER-KLEIN *et al.*, 2001). The level of turbulent kinetic energy within the cavity reflects the turbulence intensity of the external flow, even if the t.k.e. level decreases in the cavity, compared with the level in the external flow. It is worth noting that the best match between the different curves is achieved by normalizing the t.k.e. profiles with u_* , the friction velocity, as measured in the inertial region of the external flow (Tab. 4.1). This demonstrates that the dynamics of the turbulent structures coming from the external flow determines the fluctuating flow within the cavity.

We can conclude that the flow field within the cavity is not driven by the shear layer dynamics only. The presence of the downstream corner induces an oscillation of the shear layer, which ‘grasps’ turbulence structures from the external flow and ‘throws’ them within the cavity. This assertion agrees with the results obtained by LOUKA *et al.* (2000) in an open field study, showing that the coupling between the recirculating motion and the wind aloft plays an essential role of the canyon ventilation.

Integral length scales- Following the analysis presented in par. 5.3.1, we have verified the influence of the turbulent integral length scales of the external flow on the turbulent integral length scales within the cavity, which are given by

$$\mathcal{L}_{uu}(x, z) = \int_0^\infty L_{uu}(x, z, \mathbf{r}) d\mathbf{r}$$

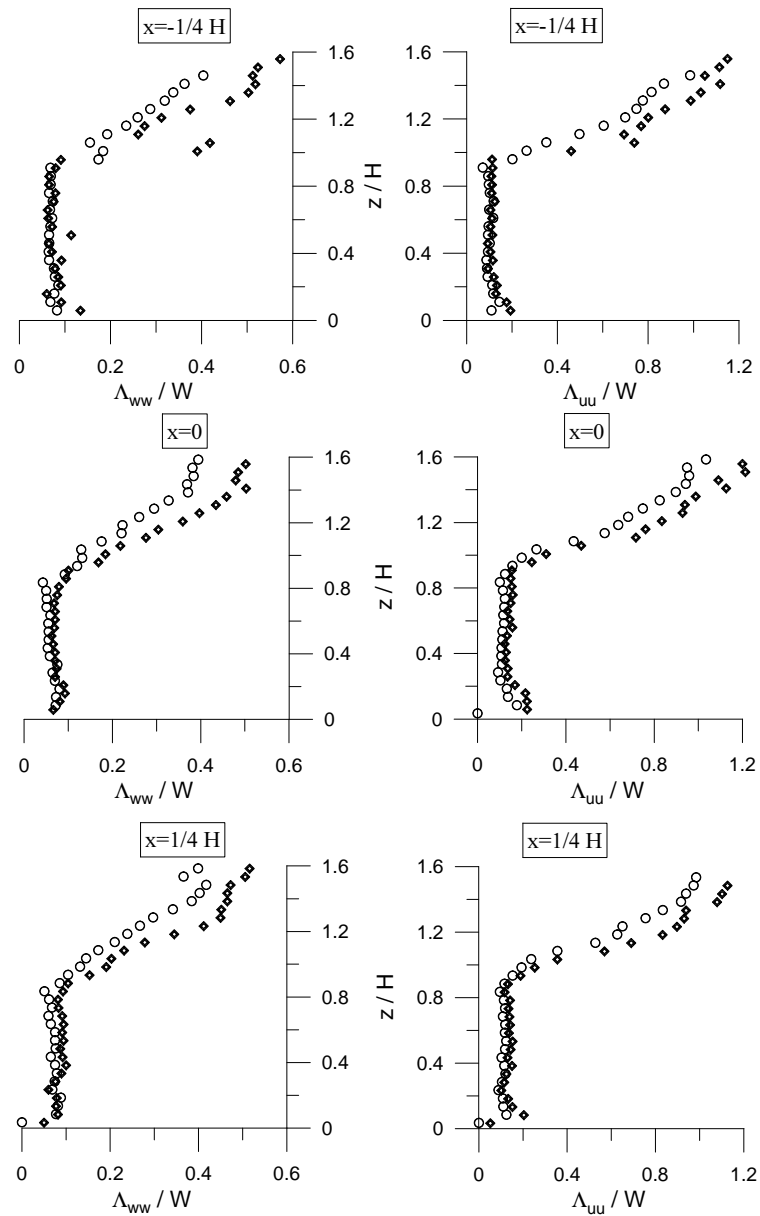


Figure 5.21: $\Lambda(z)$ profiles within and outside the cavity; configuration 3a-1a (diamonds) vs configuration 1a (circles).

and

$$\mathcal{L}_{ww}(x, z) = \int_0^\infty L_{ww}(x, z, \mathbf{r}) dr$$

where \mathbf{r} is the spatial separation, and L_{uu} and L_{ww} are the spatial autocorrelation functions

$$L_{uu}(\mathbf{x}_0, \mathbf{r}) = \frac{\overline{u(\mathbf{x}_0)u(\mathbf{x}_0 + \mathbf{r})}}{[\sigma_u(\mathbf{x}_0)\sigma_u(\mathbf{x}_0 + \mathbf{r})]}$$

$$L_{ww}(\mathbf{x}_0, \mathbf{r}) = \frac{\overline{w(\mathbf{x}_0)w(\mathbf{x}_0 + \mathbf{r})}}{[\sigma_w(\mathbf{x}_0)\sigma_w(\mathbf{x}_0 + \mathbf{r})]}$$

As done in par. 4.4.2, instead of computing the integrals $\mathcal{L}_{uu}(x, z)$ and $\mathcal{L}_{ww}(x, z)$, we evaluated a typical length scale from the spatial correlation functions $L_{ww}(r)$ and $L_{uu}(r)$, by fitting them by means of an exponential law, such as

$$f(r) = e^{-r/\Lambda}$$

In this way we evaluate the length Λ , which gives an estimate of the integral length scale \mathcal{L}_{ww} .

We compared two different cases: the base configuration (configuration 1a) and the configuration with enhanced large scale turbulence in the external flow (configuration 3a-1a). In the two cases we computed the autocorrelation functions over all the observed domain, and then fitted an exponential function $f(r)$ to the data, from which we could evaluate Λ as a function of the spatial coordinate x and z are shown in fig. 5.20.

The autocorrelation functions (L_{uu} and L_{ww}) computed at the centre of the cavity ($x = 0, z = 1/2H$) and the vertical profiles of Λ_{uu} and Λ_{ww} at different positions ($x=-1/4 H, x=0, x=1/4 H$) are plotted in fig. 5.21. From these we see that:

- the integral length scale within the canyon is $\sim 0.1 \div 0.2H$: the turbulent structures within the cavity are of the same order of magnitude as the ‘main’ recirculating cell;
- the turbulence structure within the canyon is anisotropic;
- the integral scale varies very little over the interior of the canyon;
- the integral length scale within the canyon seems to be independent of the turbulence structure of the external flow.

As it could be seen from flow visualizations (DVD, Annexe 1), the entrainment of vortex from the external flow is due to a coupling with the vortices produced in the shear layer. The vortex coupling takes place between turbulent structures whose dimensions are quite the same, otherwise the smaller vortex would be ‘advected’ by the larger one. We can roughly estimate the vortical structures produced within the shear layer as $\Lambda \sim 0.2W$. In case of a square cavity, the canyon width is not large enough to allow the vortices produced within the shear layer to grow enough and to intercept the larger scale size eddies in the roughness sub-layer in the external flow, whose size is $\Lambda \sim H$ (§4.4.2 and §6.6.2). From that point of view, we can assert that the shear layer acts as a filter on the eddies size getting into the cavity.

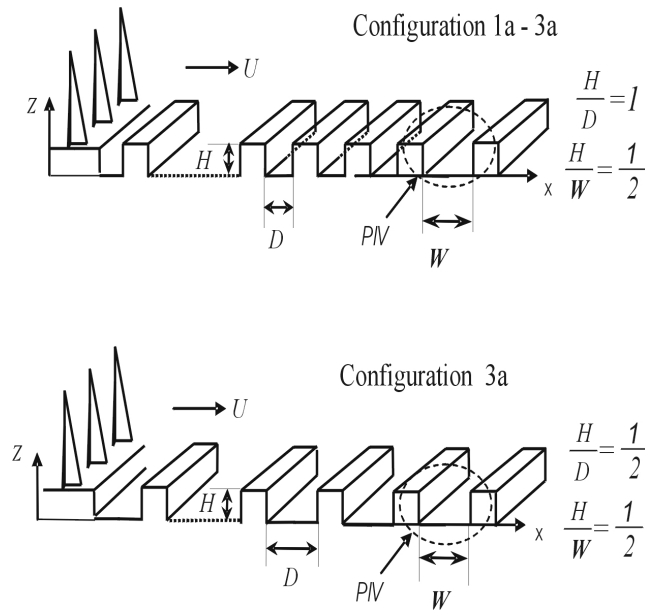


Figure 5.22: Experimental set-up.

5.3.3 Large cavity

As we did for a square cavity, we analyzed the influence of the structure of the external turbulence on the flow within a large cavity ($H/W = 1/2$). As before, the structure of the external flow was varied by modifying the configuration of the obstacle array upwind of the cavity (fig. 5.22). In the same way as for a square cavity, we can observe that the dynamics of the shear layer are not driven by the velocity difference ΔU (fig. 5.23) which seems to be an appropriate scale for the mean velocities but not for the fluctuating ones.

Within the cavity ΔU is not the appropriate scale for either the mean (fig. 5.24) or the fluctuating (5.26) flow field. However, as in the case of a square cavity, the t.k.e. values collapse onto a single curve when normalized with u_* , the friction velocity of the external flow: this demonstrates the influence within the cavity of the turbulent kinetic energy fluxes coming from the external flow.

If we compare the measured autocorrelation function L_{uu} (fig. 5.26) with that obtained for a square cavity (fig. 5.20) we observe that it seems to scale on the width of the canyon; the integral length scale of the horizontal fluctuations is about the canyon width $\sim W$, whereas for the vertical fluctuations it reaches the dimension of the canyon height $\sim H$. Another important difference from the previous results is that the integral length scale in the larger cavity appears to depend on the characteristics of the external flow field. The vertical profiles of $\Lambda_{uu}(z)$ and $\Lambda_{ww}(z)$ (fig. 5.27) show that the Eulerian macro scale within the canyon increases slightly for an increase in the integral length scale of the external flow: in this case the shear layer instabilities have more space to grow and are then able to capture the larger scale structures in the external flow.

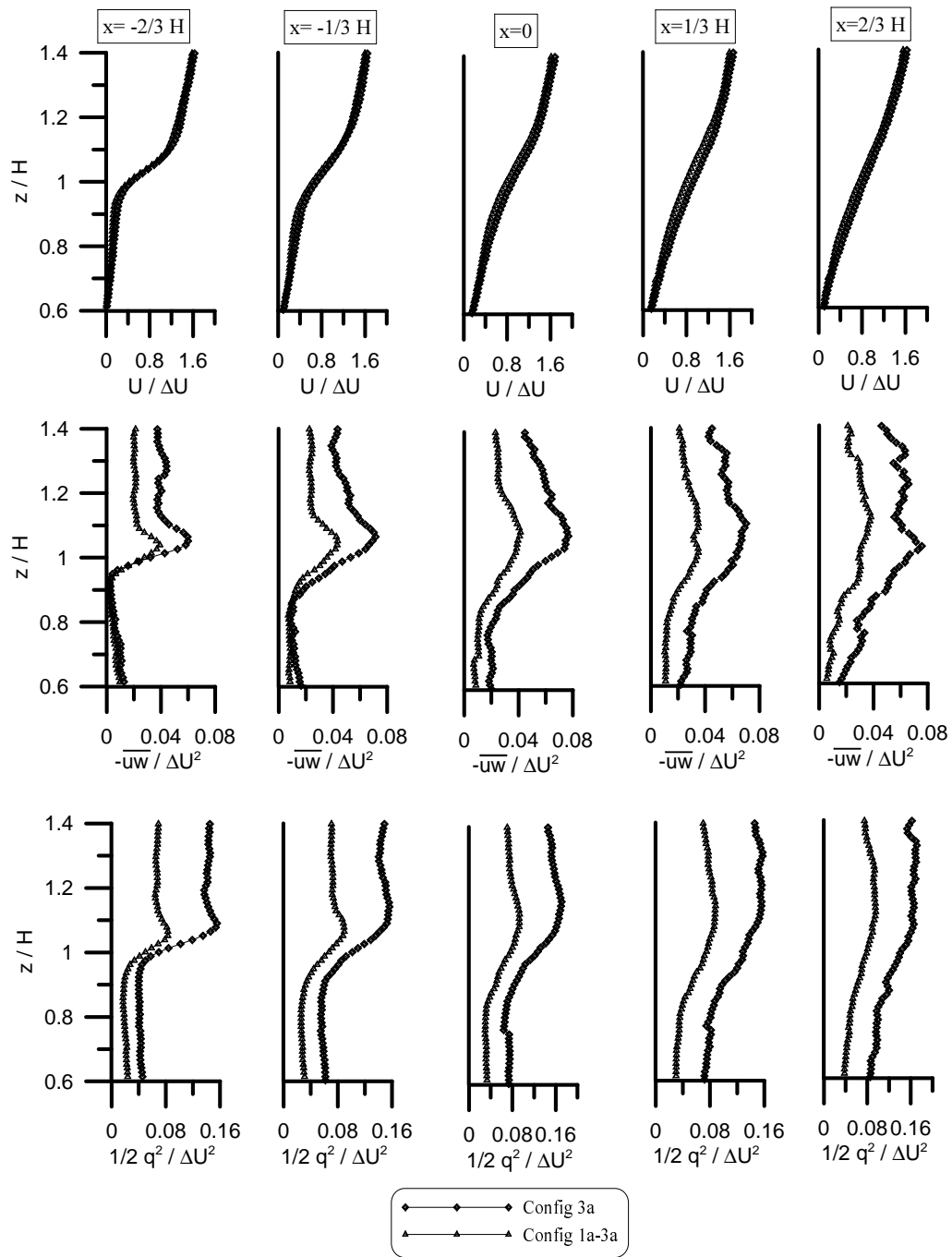


Figure 5.23: Velocity profiles at the cavity top for increasing distance from the upwind corner, normalized with ΔU .

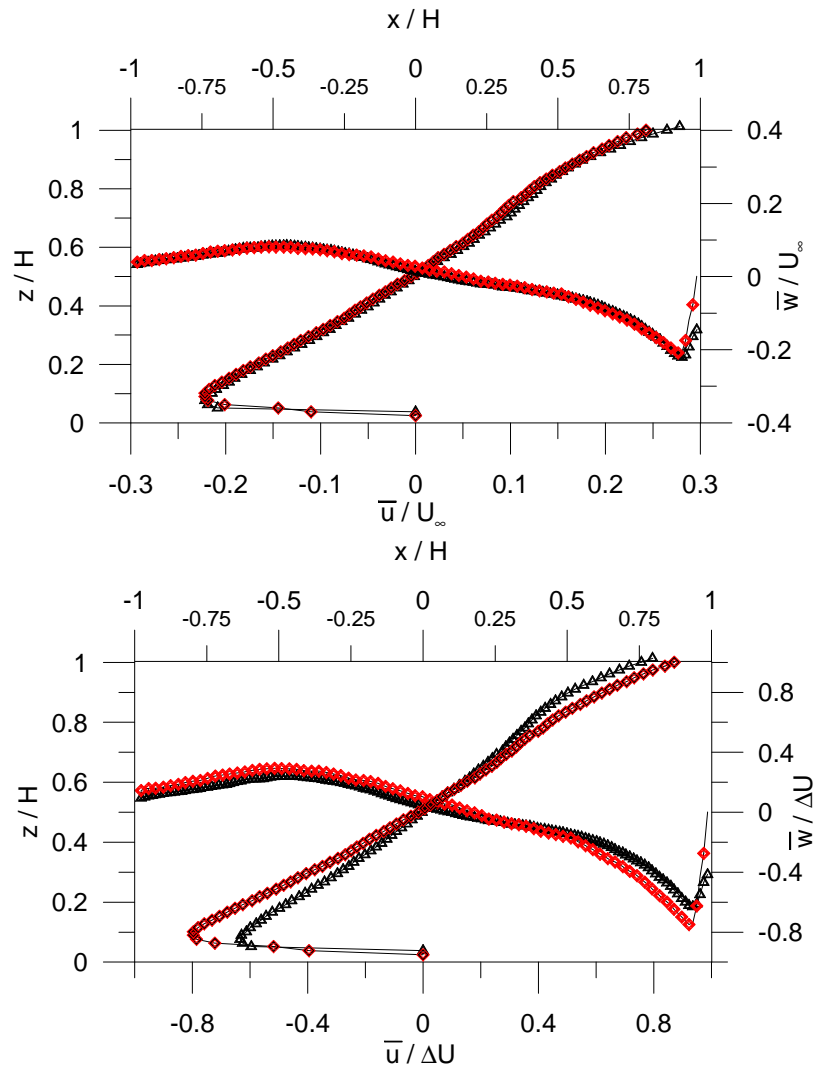


Figure 5.24: Velocity profiles within the cavity normalized with the mean velocity difference between the shear layer boundaries ΔU and with the mean velocity at the top of the simulated atmospheric boundary layer U_∞ . Comparison between configuration 1a-3a (black triangles) with configuration 3 (red diamonds).

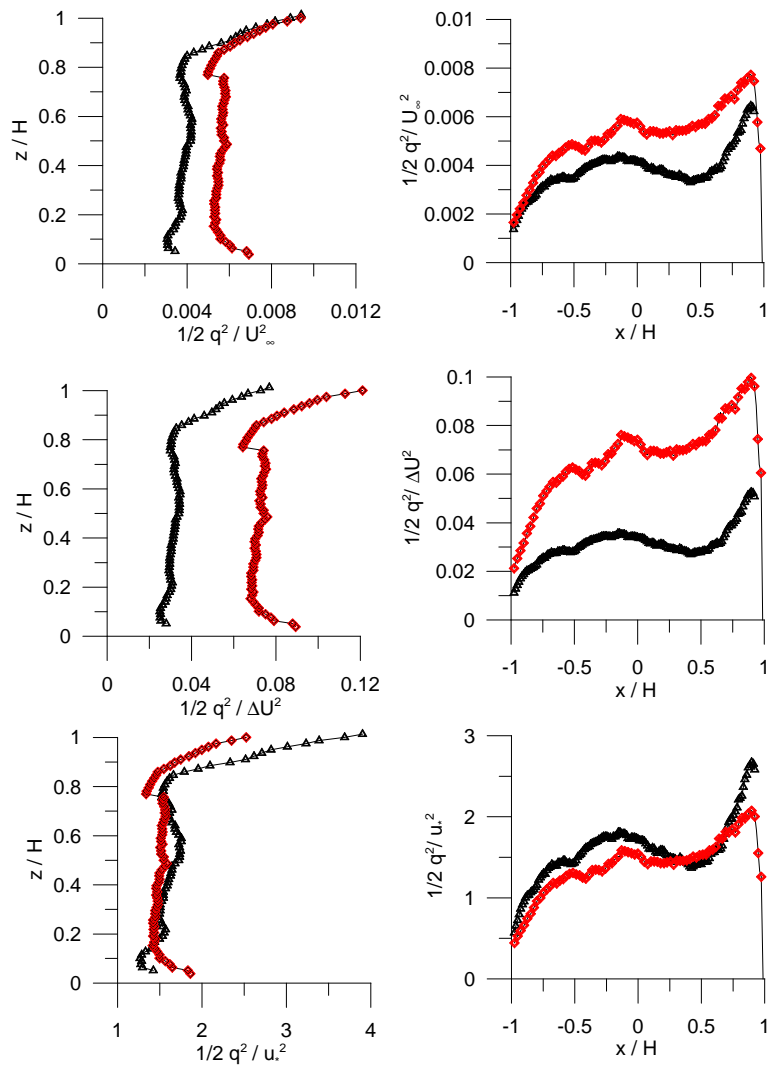


Figure 5.25: Turbulent kinetic energy profiles within the cavity normalized with the mean velocity difference between the shear layer boundaries ΔU , with the mean velocity at the top of the simulated atmospheric boundary layer U_∞ and with the friction velocity of the external flow u_* . Comparison between configuration 1a-3a (black triangles) with configuration 3 (red diamonds).

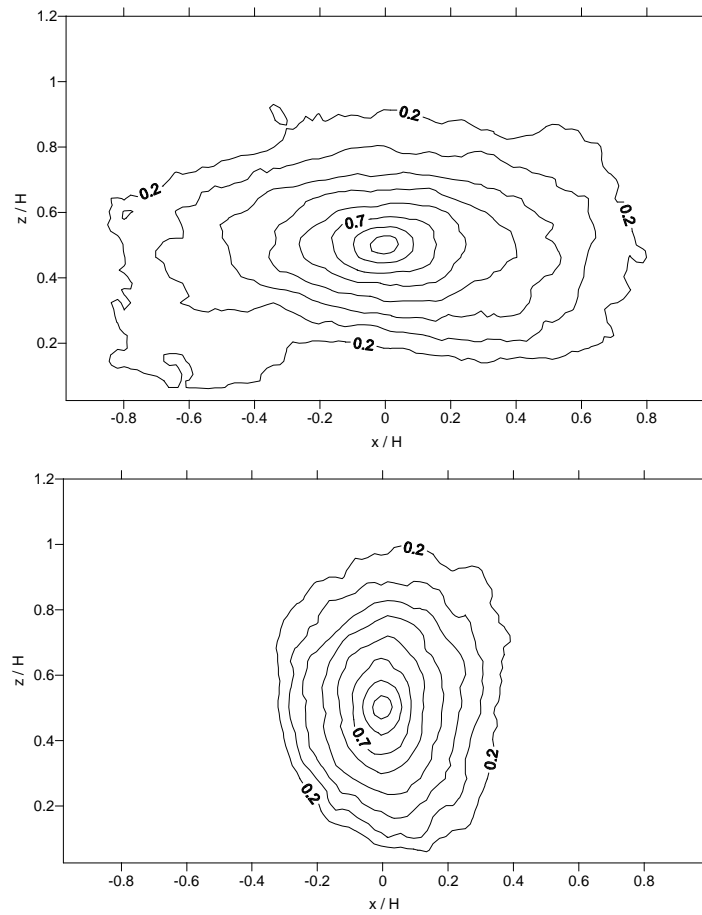


Figure 5.26: Spatial auto correlation within a large cavity computed at the cavity centre ($x=0$, $z=1/2$ H); L_{uu} on the top and L_{ww} on the bottom - configuration 1a-3a.

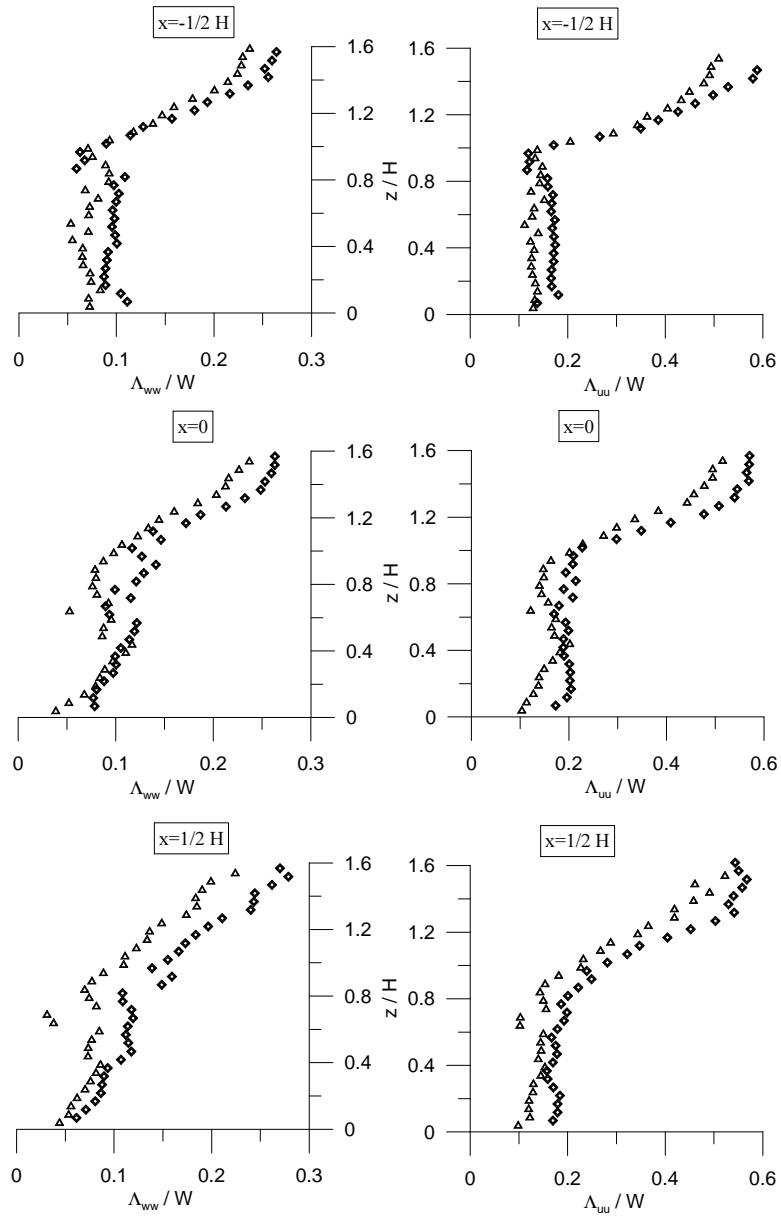


Figure 5.27: $\Lambda(z)$ profiles within and outside the cavity; configuration 1a-3a (triangles) vs configuration 3a (squares).

5.4 Discussion of velocity measurements results

We studied the dependence of the flow within the cavity from the cavity geometry and from the external flow structure, by means of PIV measurements.

The cavity geometry affects the flow field within it in a number of ways. The main effects are due to the changes in the streamline topology and the vorticity dynamics, which induces the transition between one to two recirculating cells for a value of the street aspect ratio between $3/2$ and $4/3$. Related to that topic, we found that the presence of roughness on canyon walls can accelerate the transition, which takes place at a smaller cavity aspect ratio H/W .

The study of the influence of the external flow structure suggests that the shear layer developing at the canyon top is not an autonomous region: its dynamics are influenced by the turbulent kinetic energy fluxes coming from the external flow. This conclusion is in agreement with GRACE et al. (2004) and CASTRO et al. (1987), who argued that the turbulence structure of the shear layer bounding a recirculation region differs from that of a plane mixing layer between two stream in a number of ways, even if some aspects of their behaviour are similar. Inside the canyon the turbulent intensity and the turbulence length scales are approximately constant over the canyon, except for a region near the downwind wall.

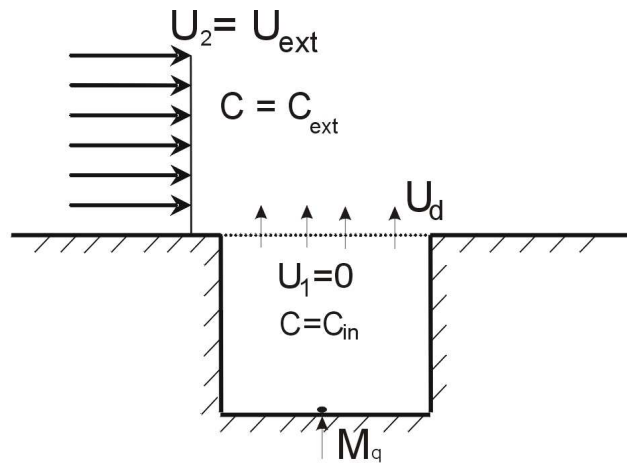


Figure 5.28: Street canyon box model.

5.5 Evaluation of the wash-out time of the cavity

In order to define a typical wash-out time of the cavity, several approach can be adopted. Some authors (CATON *et al.*, 2003; DEZSO-WEIDINGER *et al.*, 2003) measured the spatially averaged concentration within the cavity as it empties, by mean of a Particle Tracking Velocimetry technique. Some others (BARLOW and BELCHER, 2002; BARLOW *et al.*, 2004) evaluated the sublimation-time of naphthalene from the canyon walls.

In our case, the mass exchange between the canyon and the external flow has been estimated by measuring the time for the pollutant to be washed out of the cavity. Using a FID system, we measured the temporal evolution of ethane concentration at different position within the cavity as it empties. For each point of measure, the experiment was repeated between 30 and 50 times to allow an ‘ensemble’ average for the signals.

5.5.1 State of the art: the existing box models

The so called *operational models* (par. 2.4) of pollutant dispersion in urban areas describe the mass exchange between the recirculating region within the urban canopy and the atmosphere aloft by means of a few parameters in order to provide simple relations.

These are box models with one degree of freedom, i.e. they assume that the recirculating flow within each street is driven by the component of the external wind perpendicular to the street. In this simple model, the canyon is described as a box with uniform pollutant concentration and a discontinuity surface at the top, where the mass exchange takes place. In the same way, the velocity and the concentration field of the external flow are assumed to be uniform too. In this representation (fig. 5.28), we can write a mass balance within the canyon as

$$HWL \frac{\partial C_{in}}{\partial t} = WLu_d(C_{ext} - C_{in}) + \dot{M}_q \quad (5.2)$$

where H , W and L are the canyon linear dimensions (height, width and length), u_d is the mass transfer velocity at the interface, C_{in} and C_{ext} are the mean concentrations within and outside the canyon and \dot{M}_q is the source strength of pollutants inside the canyon. Assuming that the system is stationary and that $C_{ext} = 0$, we obtain from eq. 5.2:

$$C_{in} = \frac{\dot{M}_q}{WL} \frac{1}{u_d}$$

If pollutant concentration inside the cavity is $C_{in} = C_0$, at $t = 0$, and $\dot{M}_q = 0$, the time evolution of the mean cavity concentration as it empties is given by

$$C = C_0 e^{-t/\tau} \quad (5.3)$$

where

$$\tau = \frac{H}{u_d}$$

is a typical time constant that gives an estimate of the wash-out time of the cavity.

There are therefore three relevant scales

- u_d as velocity scale;
- τ as time scale;
- H as length scale.

The velocity mass exchange u_d is related to the turbulent fluctuations at the interface between the two regions. Following the arguments of §5.3.1, u_d has to scale with the mean velocity difference across the shear mixing layer at the interface, so we can write

$$\frac{u_d}{\Delta U} = \frac{1}{\alpha}$$

If we give describe this using a simple box model (fig.5.28), we can assume that:

- the mean velocity within the cavity is equal to zero, i.e. $U_2 = 0$;
- the mean velocity in the external flow is uniform, i.e. $U_1 = U_{ext}$.

As long as $U_2 = 0$, $\Delta U = U_{ext}$, we have

$$U_{ext} = \alpha u_d$$

Following the hypothesis exposed in the previous paragraph, we may have two cases:

1. the flow field within the cavity is effectively driven by the shear layer dynamics only, so that:

$$\alpha = const$$

This implies:

$$\frac{\tau\Delta U}{H} = \text{const}$$

where τ is the wash-out time of the cavity. If this hypothesis is satisfied, the normalized mean concentration within the canyon as it empties is not influenced by the turbulence structure of the external flow; we can then write

$$C' \equiv \frac{C}{C_0}(t')$$

where $t' = t\Delta U/H$ is the normalized time and C_0 is the mean concentration within the canyon at the time $t = 0$.

2. Otherwise, if we assume that the fluxes of turbulent kinetic energy (from the outside to the inside of the canyon) are relevant in the dynamics of the flow field within the shear layer and within the cavity, we have to consider that

$$\alpha = f\left(i_{ext}; \frac{\mathcal{L}_{ext}}{H}\right)$$

In the same way, the mass exchange rate, and the wash-out time of the cavity, will also depend on those parameters:

$$\frac{\tau\Delta U}{H} = f(i_{ext}; \frac{\mathcal{L}_{ext}}{H})$$

$$q' = f(i_{ext}; \frac{\mathcal{L}_{ext}}{H})$$

The model STREET (JOHNSON *et al.*, 1973) implicitly assumes the first hypothesis, calculating the mean concentration within the canyon as

$$C \simeq \alpha \frac{\dot{M}_q}{U_{ext}WL}$$

where α has a fixed value³⁸: $\alpha = 7$.

In some other cases α is related to the turbulence intensity of the external flow. This is the case, for example, of the model OSPM (BERKOWICZ *et al.*, 1997) where

$$\alpha = \frac{1}{i_{ext}}$$

³⁸This value of α is in good agreement with the experimental evaluation in a street of Chicago by DE PAUL and SHEIH (1985), who estimated that

$$\alpha \simeq 6, 25$$

However, in the OSPM model, i_{ext} is taken as a fixed value equal to 0.1, which is considered as a representative value of the turbulence intensity in the atmosphere in an urban environment; consequently it is $\alpha = 10$.

Other authors follow the second hypothesis, by considering

$$\alpha = f\left(i_{ext}; \frac{\mathcal{L}_{ext}}{H}\right)$$

HOTCHKISS (1973) assumes that

$$\alpha = \sqrt{\frac{U_{ext}W}{K_m}}$$

where W is the canyon width and $K_m = \mathcal{L}_{ext}\sigma_{q_{ext}}$ is a turbulent diffusion coefficient expressed, following with the Prandtl's mixing length theory, as the product of a typical turbulent length scale \mathcal{L}_{ext} and a velocity scale $\sigma_{q_{ext}}$, i.e. the r.m.s. of the vertical fluctuating velocity or the square root of the turbulent kinetic energy (HUNT and CASTRO, 1984).

In a similar way, in the model SIRANE, SOULHAC (2000) assumes that

$$\alpha = \pi \sqrt{\frac{U_{ext}W}{K_m}}$$

i_H	$\alpha = \sqrt{\frac{1}{\Lambda}}$ Hotchkiss	$\alpha = \sqrt{\frac{\pi}{\Lambda}}$ Soulhac
0.1	10	17.7
0.15	6.66	14.5
0.2	5	12.5
0.25	4	11.2
0.3	3.3	10.23
0.35	2.8	9.47
0.4	2.5	8.86

Table 5.1: Variation of α as a function of the turbulence intensity of the external flow.

We will not go further into detail of each model; in fact, relations given by some authors are complicated by empirical corrective parameters (JOHNSON *et al.*, 1973) to take account for the mechanically induced turbulence caused by traffic or to evaluate an 'effective' exchange surface in case of more complicated canyon geometry, i.e. with non homogeneous building height, or by a shape function (HOTCHKISS and HARLOW, 1973), in order to calculate the concentration inhomogeneities within the canyon.

In all these models it is assumed that U_{ext} is equal to U_H , the mean velocity at roof height.

5.5.2 A simple analytical model with two degrees of freedom

Initially, the aim of this study was to try to describe the mass exchange between the canyon and the external flow by mean of a box-model with one degree of freedom, as done by the authors mentioned in the previous paragraph.

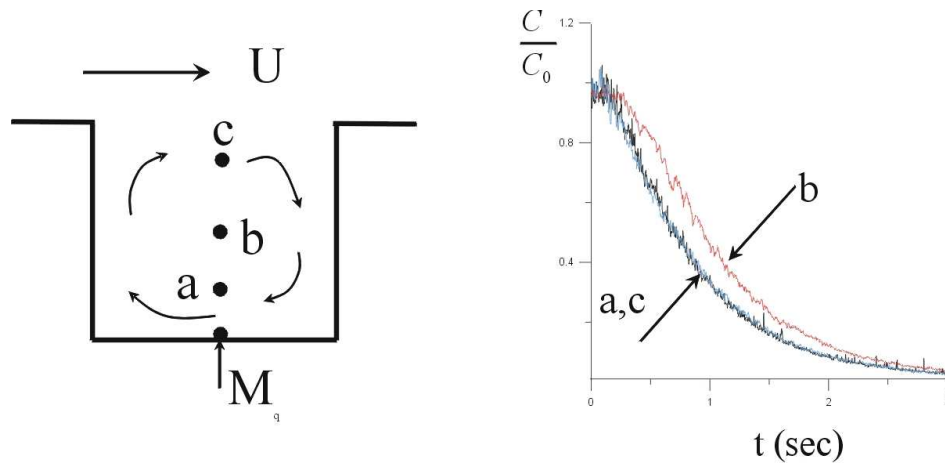


Figure 5.29: Wash-out curves measured at different position within the cavity.

In fig. 5.29 are shown the wash-out curves that we measured at different position within the canyon, in the case of a square cavity (configuration 1a); it is evident that:

- the curves measured at different positions differ significantly one from the other;
- all curves have a horizontal tangent for $t \rightarrow 0$; in the case of a square cavity, this is particularly evident for the curves at the centre ($z = 1/2H$ and $x = 0$).

This behaviour cannot be modelled by mean of a box model with one degree of freedom only, which would lead to an exponential curve with a negative tangent for $t \rightarrow 0$. In order to describe the pollutant transfer between the canyon and the external flow, we have therefore adopted a model with two degrees of freedom; the flow in the cavity consists of two regions and a mass transport is described in terms of a sequence of transfers between three regions, each with a different mean concentration. One region represents the external flow, the two other boxes give a rough description of the pollutant distribution inside the canyon.

We could consider two different cases:

- in a square and in a large cavity the first box represents the core of the flow inside the cavity, while the second box represents the recirculating part of the flow, which leads pollutant in touch with the shear layer at the top of the cavity;
- in a narrow cavity with two recirculating cells, the first box represents the cell at the bottom of the cavity whereas the second box represents the cell at the top of the cavity, exchanging mass with the first cell at the bottom and with the external flow at the top.

Square cavity and large cavity

By looking at the fig. 5.30 we can write a mass balance for the two boxes within the cavity as

and

$$\frac{1}{T_2} = \frac{S_{21}\tilde{u}_d}{(1-\beta)V_0} \quad (5.6)$$

Substituting in eq. 5.4 we obtain:

$$\begin{cases} \frac{dC_1}{dt} = -\frac{C_1}{T_1} + \frac{(1-\beta)}{\beta T_2}(C_2 - C_1) + \frac{\dot{M}_q}{\beta V_0} \\ \frac{dC_2}{dt} = \frac{1}{T_2}(C_1 - C_2) \end{cases} \quad (5.7)$$

Stationary case - Considering that the system has reached a stationary state and that the pollutant concentration in the external flow is equal to zero, i.e. $C_{ext} = 0$ we can write

$$\begin{cases} -\frac{C_1}{T_1} + \frac{(1-\beta)}{\beta T_2}(C_2 - C_1) + \frac{\dot{M}_q}{\beta V_0} = 0 \\ \frac{1}{T_2}(C_1 - C_2) = 0 \end{cases} \quad (5.8)$$

thus obtaining

$$C_1 = C_2 = \frac{T_1 \dot{M}_q}{\beta V_0} \quad (5.9)$$

Instationary case - In order to evaluate the typical time scale for mass transfer between the recirculating region and the external flow, we can evaluate the temporal evolution of a passive scalar concentration in the cavity as it empties, after having stopped the injection. This means that $\dot{M}_q = 0$; as before, we also set the external concentration equal to zero, $C_{ext} = 0$. We write eq. 5.4, with a change in the variables

$$C_1 \rightarrow C'_1 C_{10}$$

$$C_2 \rightarrow C'_2 C_{20}$$

with the initial condition $C_{10} = C_1(0)$ and $C_{20} = C_2(0)$. Eq. 5.7 become

$$\begin{cases} C_{10} \frac{dC'_1}{dt} = -\frac{C_{10} C'_1}{T_1} + \frac{(1-\beta)}{\beta T_2}(C_{20} C'_2 - C_{10} C'_1) \\ C_{20} \frac{dC'_2}{dt} = \frac{1}{T_2}(C_{10} C'_1 - C_{20} C'_2) \end{cases}$$

Setting $\gamma = \frac{C_{20}}{C_{10}}$, we obtain the following initial value system

$$\begin{cases} \frac{dC'_1}{dt} = -\frac{1}{T_1} C'_1 + \frac{(1-\beta)}{\beta} \frac{1}{T_2} (\gamma C'_2 - C'_1) \\ \frac{dC'_2}{dt} = \frac{1}{T_2} (\frac{1}{\gamma} C'_1 - C'_2) \\ C'_1(0) = 1 \\ C'_2(0) = 1 \end{cases} \quad (5.10)$$

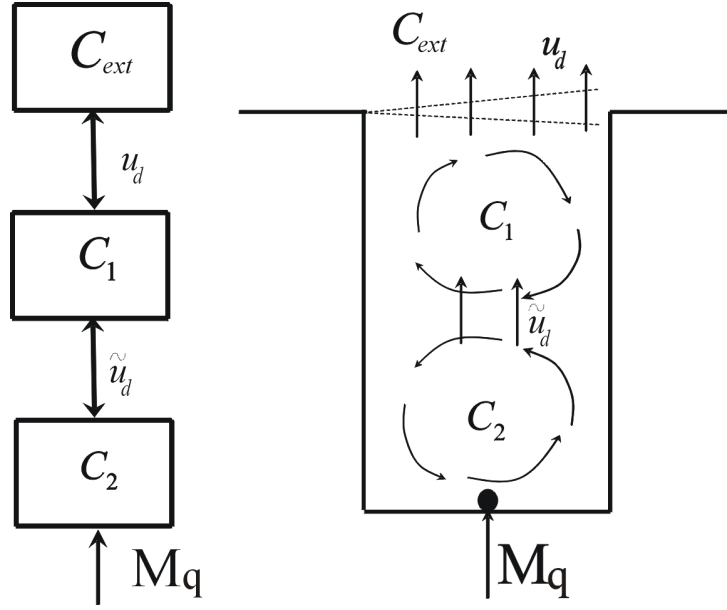


Figure 5.31: Narrow cavity model.

Narrow cavity

In the case of a narrow cavity (fig. 5.31) we have that

$$S_{10} = S_{12} = W$$

where W is, as usual, the canyon width.

$$\begin{cases} V_1 \frac{dC_1}{dt} = W u_d (C_{ext} - C_1) + W \tilde{u}_d (C_2 - C_1) \\ V_2 \frac{dC_2}{dt} = W \tilde{u}_d (C_1 - C_2) + \dot{M}_q \end{cases}$$

$$\begin{cases} \beta \frac{dC_1}{dt} = \frac{W}{V_0} u_d (C_{ext} - C_1) + \frac{W}{V_0} \tilde{u}_d (C_2 - C_1) \\ (1 - \beta) \frac{dC_2}{dt} = \frac{W}{V_0} \tilde{u}_d (C_1 - C_2) + \frac{\dot{M}_q}{V_0} \end{cases}$$

Stationary case - Considering a stationary state and that the pollutant concentration in the external flow is equal to zero, i.e. $C_{ext} = 0$, we obtain

$$\begin{cases} -\frac{W}{V_0}u_d C_1 + \frac{W}{V_0}\tilde{u}_d(C_2 - C_1) = 0 \\ \frac{W}{V_0}\tilde{u}_d(C_1 - C_2) + \frac{\dot{M}_q}{V_0} = 0 \end{cases} \quad (5.11)$$

if we sum the two equations we obtain

$$\frac{W}{V_0}u_d C_1 + \frac{\dot{M}_q}{V_0} = 0$$

substituting

$$\begin{aligned} \frac{W}{V_0} &= \frac{1}{H} \quad ; \quad \frac{u_d}{\beta H} = \frac{1}{T_1} \\ \frac{\tilde{u}_d}{H(1-\beta)} &= \frac{1}{T_2} \end{aligned}$$

we finally have an estimation of T_1 and C_1

$$C_1 = T_1 \frac{\dot{M}_q}{\beta V_0} \quad (5.12)$$

$$T_1 = \beta C_1 \frac{V_0}{\dot{M}_q} \quad (5.13)$$

to have an estimation of T_2 we go back to eq. 5.11

$$\frac{W}{V_0} \frac{H(1-\beta)}{T_2} (T_1 \frac{\dot{M}_q}{\beta V_0} - C_2) + \frac{\dot{M}_q}{V_0} = 0$$

$$V_0(1-\beta)(C_2 - T_1 \frac{\dot{M}_q}{\beta V_0}) - \dot{M}_q T_2 = 0$$

$$T_2 = C_2 \frac{(1-\beta)V_0}{\dot{M}_q} - T_1 \frac{(1-\beta)}{\beta} \quad (5.14)$$

Instationary case - As done before, if we consider that $\dot{M}_q = 0$ and that $C_0 = 0$, we reach the same conditions obtained for the square cavity, i.e. eq. 5.10.

5.5.3 Experimental Results

As for the velocity measurements results, we have studied the dependence of the wash-out times on:

- the canyon geometry, i.e. the aspect ratio H/W ;
- the external flow conditions.

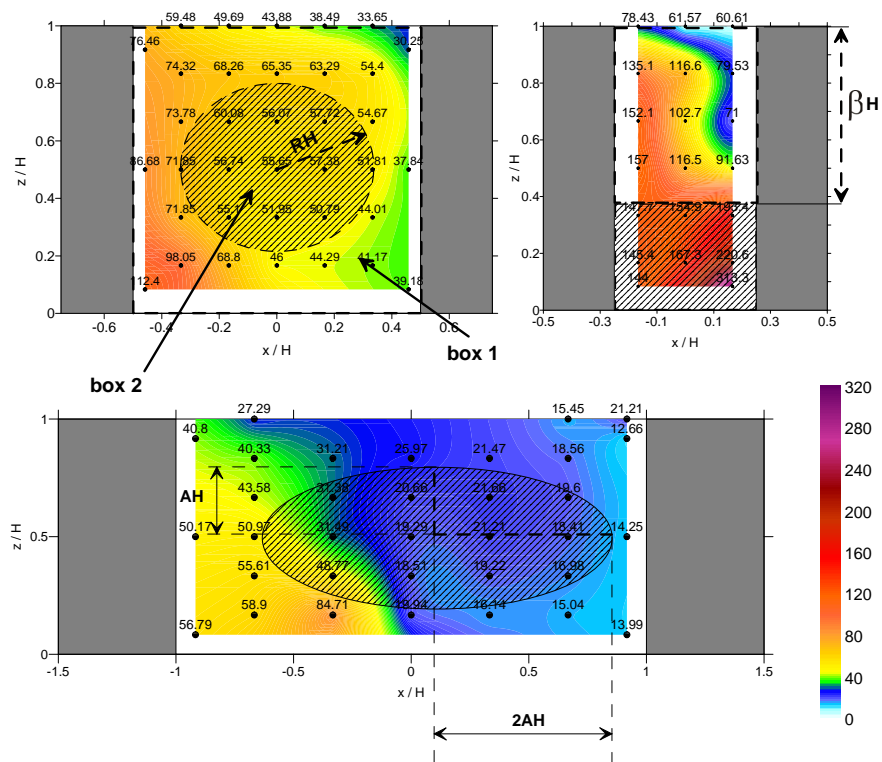


Figure 5.32: Normalized mean concentration $C^* = \frac{CU_\infty H}{\dot{M}_q}$ field within cavities with different aspect ratio. Evaluation of the surface of the two boxes (scratched areas represent box 2).

In case of a narrow cavity, the two wash-out times could be determined by means of stationary measurements (eq. 5.13 and eq. 5.14), if the ratio $\beta = V_1/V_0$ and the mean concentration of the two boxes are known. We measured the mean concentration field within the cavity for all the configuration we studied; however a sufficiently precise measurement of C_1 and C_2 is quite hard as long as the concentration in the cavity is highly inhomogeneous and because lot of measurements point would be needed to define a good averaged concentration (PAVAGEAU and SCHATZMANN, 1999). In case of a square cavity, T_1 can be determined by means of eq. 5.9, whereas the evaluation of T_2 by means of eq. 5.6 requires an additional assumption (for example that $u_d = \tilde{u}_d$) and an estimation of the volume of the two boxes V_1 and V_0 . We evaluated the wash out times interpolating the experimental curves, by using the analytical solution of eq.5.10, which gives the temporal evolution of the spatially averaged concentration in the two regions within the canyon (box 1 and box 2). In order to interpolate the experimental curves we have to define four parameters: T_1 , T_2 , $\gamma = C_{20}/C_{10}$, $\beta = V_1/V_0$. The ratio $\beta = V_1/V_0$, at first roughly determined by means of geometrical considerations, has been corrected, in order to obtain the best fit of the experimental curves.

In case of a narrow cavity (fig. 5.32) we can estimate that $0.6 < \beta < 0.66$, from the topology of the the stream lines (fig. 5.1). The value of γ depends on the ratio between the two exchange velocities \tilde{u}_d and u_d ; combining eq. 5.12 and eq. 5.14 we obtain

$$\gamma = \frac{C_2}{C_1} = 1 + \frac{\beta T_2 H}{(1 - \beta) T_1 H} = 1 + \frac{u_d}{\tilde{u}_d}$$

In case of a square and of a large cavity, we have that $\gamma = 1$ (eq. 5.8), whereas the evaluation of β appears quite difficult. In a square cavity (fig. 5.32) we can represent the internal region (box 2) as a circle placed in the cavity centre with a radius $\mathcal{R} = RH$ (R is a scalar, $0 < R < 1$). We have

$$\begin{aligned} V_2 &= (1 - \beta)V_0 = \pi R^2 H^2 \\ V_0 &= H^2 \\ \beta &= 1 - \pi R^2 \\ S_{10} &= H \quad S_{12} = 2\pi RH \\ u_d &= \frac{\beta H}{T_1} \quad \tilde{u}_d = \frac{(1 - \beta)V_0}{S_{12}T_2} = \frac{RH}{2T_2} = \frac{\sqrt{\frac{1-\beta}{\pi}} H}{2T_2} \end{aligned}$$

In a large cavity (fig. 5.32) we represent the inner box as an ellipse whose semi axes are $\mathcal{A} = AH$ and $\mathcal{B} = AW = 2AH$, so that:

$$\begin{aligned} V_2 &= 2\pi\mathcal{A}\mathcal{B} = 4\pi A^2 H^2 \\ S_{12} &\simeq 2\pi\sqrt{\frac{1}{2}(\mathcal{A}^2 + \mathcal{B}^2)} = 2\pi\sqrt{\frac{1}{2}(5A^2 H^2)} = \pi aH\sqrt{10} \sim \pi^2 aH \\ V_0 &= 2H^2 \quad S_{01} = 2H \\ \beta &= \frac{V_1}{V_0} = \frac{2H^2 - 4\pi A^2 H^2}{2H^2} = 1 - \pi A^2 \end{aligned}$$

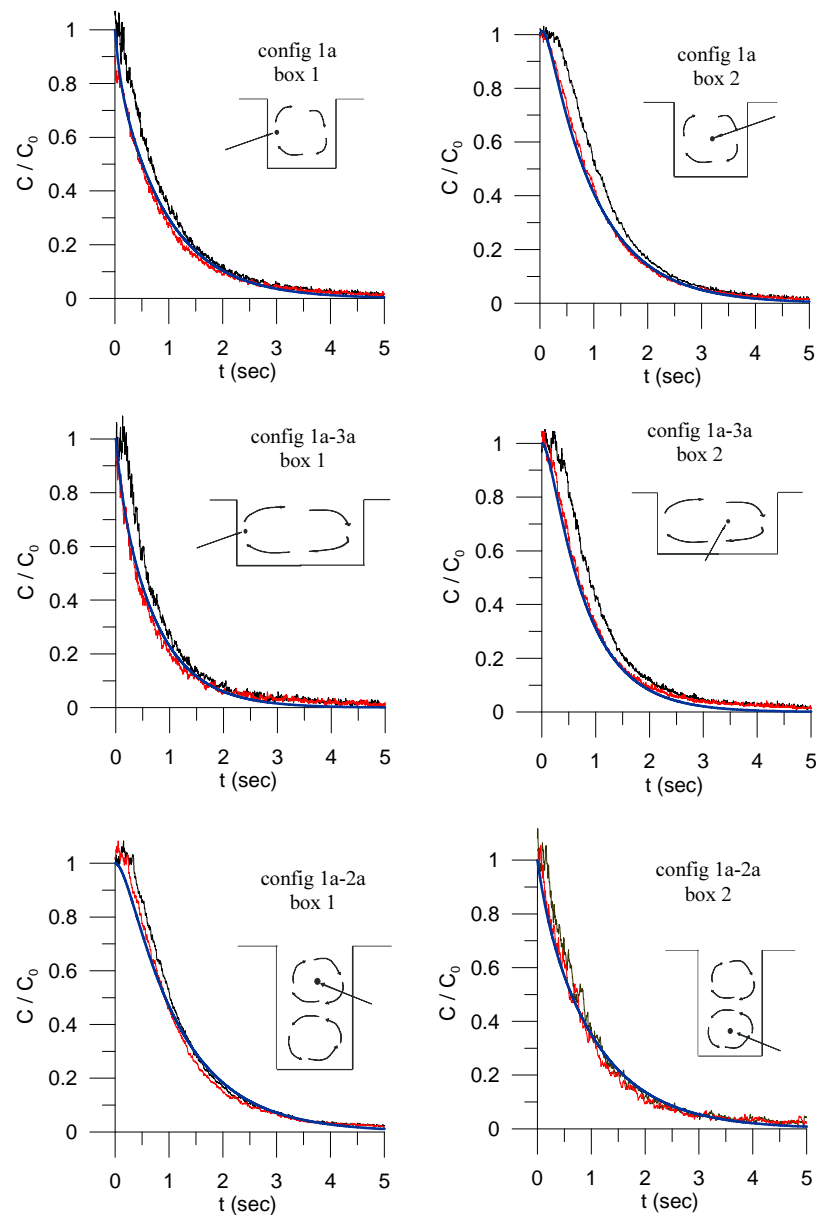


Figure 5.33: Experimental data and results of the analytical model with two degree of freedom; comparison of different canyon geometries and with the same aspect ratio of the upwind canyon array (corresponding to configuration 1, $H/W = 1$); the black-lines are the measured curves, the blue-lines are the model results and the red-line are the measured curves that have been translated on the time axis of a time interval Δt .

$$u_d = \frac{\beta H}{T_1} \quad \tilde{u}_d = \frac{V_2}{S_{12}T_2} = \frac{4\pi A^2 H^2}{\pi^2 AHT_2} = \frac{4\sqrt{\frac{1-\beta}{2\pi}} H}{\pi T_2}$$

Influence of the canyon geometry - We measured the wash-out curves at different position within the cavity, for varying street aspect ratio, and by keeping the same external flow condition, i.e. the configuration of the upwind canyons array (configuration 1a); the configuration taken into account are named configuration 1a (square cavity), configuration 1a-3a (larger cavity) and configuration 1a-2a (narrow cavity). The experimental curves and the model results are shown in fig. 5.33: the black-lines are the measured curves, the blue lines the model results and the red-line are the measured curves that has been translated on the time axis of a time interval Δt . Actually the model predicts well the time evolution of the wash-out curve, except for an initial delay, especially for the square and the larger cavity. This may be due to the fact that the system needs an initial time interval to reach the initial conditions that the model implicitly takes into account. For example, for a square (and a large) cavity, the condition $\gamma = C_{02}/C_{01} = 1$ is related to the assumption that there is no direct exchange between the outer region and the core of the cavity (box2), which may be not true. The limitations of this representation of the phenomenon became apparent as the canyon the canyon aspect ratio decreases (for larger cavities): the ratio between the vertical extent of the shear layer and the canyon height increases and the core of recirculation region within the cavity is more and more perturbed by the ‘flapping’ of the shear layer.

In the case of a narrow cavity the initial delay needed to reach the modelled initial condition is almost negligible, and the agreement between the model and the experimental results, unlike the other two configurations, is much better.

configuration	1a	1a-3a	1a-2a
u_*/U_∞	0.0491	0.0491	0.0491
ΔU (m/s)	1.38	2.35	2.5
β	0.7	0.7	0.6
T_1 (s)	0.5	0.46	0.5
T_2 (s)	0.18	0.2	0.35
u_d (m/s)	0.069	0.086	0.072
\tilde{u}_d	0.06	0.082	0.068
u_d/U_∞	0.01	0.0128	0.01
\tilde{u}_d/U_∞ (s)	0.013	0.0122	0.01
$u_d/\Delta U$	0.051	0.036	0.028
$\tilde{u}_d/\Delta U$	0.044	0.034	0.027
$\alpha = \Delta U/u_d$	19.9	27.2	34.7

Table 5.2: *Variation of the wash-out time of the cavity as a function of the canyon geometry.*

The results, evaluated by means of a best fit of the experimental curves using the two-degree of freedom model (taking into account the initial shift Δt) are summarized in tab. 5.2 and show two main

features.

1. The exchange velocities for a large cavity are greater than these for the other two cases. This feature agrees with the results presented by BARLOW and BELCHER (2002) who found that the transfer velocity u_d/U_∞ reaches a maximum in the wake interference regime.
2. The ratio $\alpha = \frac{\Delta U}{u_d}$ depends on the canyon geometry. The non-similarity of the flow fields we have been comparing implies that the mass exchange between the canyon and the external flow cannot be represented in an invariant form independent of the canyon geometry. This makes quite it quite difficult to parameterize the phenomenon in terms of gradient laws (such as those generally assumed by the operational models as OSPM or SIRANE), where the estimation of flow rate at the interface F_q

$$F_q = u_d W \Delta C$$

implicitly assumes that u_d , the velocity exchange at the interface depends on the mean and fluctuating external flow, but is independent of H/W . Actually the mass transfer from the canyon to the external flow is driven by the dynamics of the shear layer and by the entrainment of vortices from the external flow: both process are highly dependent on the canyon geometry (par. 5.2.1); this feature implies that the mass exchange velocities (\tilde{u}_d depend $\simeq u_d$) on the canyon aspect ratio.

configuration	1a	1b	3a-1a
u_*/U_∞	0.0491	0.053	0.061
ΔU (m/s)	1.38	1.1	1.1
β	0.7	0.7	0.7
T_1 (s)	0.5	0.58	0.41
T_2 (s)	0.18	0.18	0.15
u_d (m/s)	0.069	0.069	0.087
\tilde{u}_d	0.06	0.06	0.073
u_d/U_∞	0.01	0.01	0.013
\tilde{u}_d/U_∞ (s)	0.009	0.009	0.011
$u_d/\Delta U$	0.051	0.063	0.08
$\tilde{u}_d/\Delta U$	0.044	0.055	0.06
$\alpha = \Delta U/u_d$	19.9	15.8	12.2

Table 5.3: Variation of the wash-out time and of the exchange velocities as a function of the turbulence intensity of the external flow.

Influence of the external flow structure- In order to study the dependence of the exchange velocities (\tilde{u}_d and $\simeq u_d$) on the external flow structure, we measured the wash-out curves within a square cavity varying the smaller and the larger scale turbulence intensity of the external flow. The

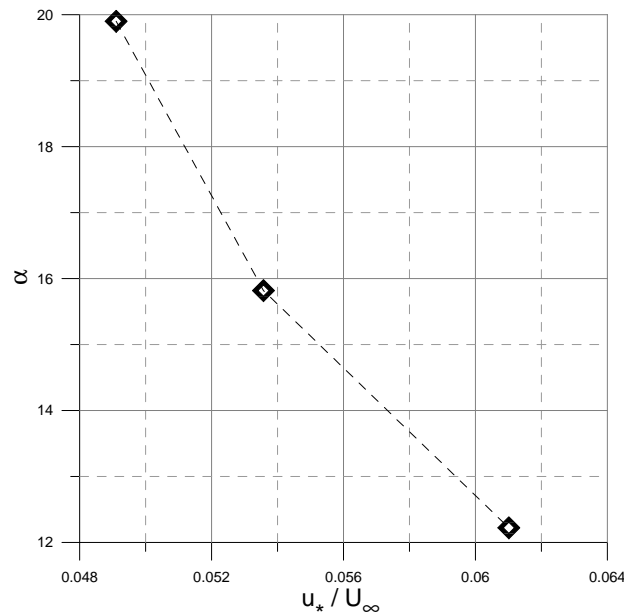


Figure 5.34: Dependence of α of the turbulence intensity of the external flow (square cavity, $H/W=1$).

configurations we have used are the same as those presented in paragraph 5.3.2.: configuration 1 (base configuration), configuration 1b (enhanced smaller scale turbulence), and configuration 3a-1a (enhanced larger scale turbulence). The results are summarized in tab. 5.3. The PIV data showed that the momentum exchange between the cavity and the external flow does not depend only on the shear layer dynamics, but also on the external flow structure. We can reasonably expect that the mass exchange depends on the same parameters as the momentum exchange. By assuming that the fluxes of turbulent kinetic energy (from the outside to the inside of the canyon) are relevant to the dynamics of the flow field within the shear layer and within the cavity, we have to consider that

$$u_d = \frac{\Delta U}{\alpha}$$

where

$$\alpha = f\left(i_{ext}; \frac{\mathcal{L}_{ext}}{H}\right)$$

We verified that the Eulerian macroscale within the cavity is not sensitive to the variation of the turbulence length scale in the external flow. In fact, in the case of a high turbulence, the turbulence structure exhibit a slight dependence on the external flow structure, but we will neglect that feature in what follows. We can thus rewrite the previous equation without taking into account the dependence on \mathcal{L}_{ext} , obtaining

$$\alpha = f(i_{ext})$$

In fig. 5.34 and in tab. 5.3 we show the dependence of α on u_* / U_∞ , which can be considered a representative normalized parameter of the external turbulence, as long as u_* is the only relevant scale

of the external flow field (see par. 4.3.1). As we can see α depends on the external turbulence level: by increasing the external turbulence level the wash-out times are reduced. That confirms the conclusion we reached in par 4.5: the mass exchange (as well as the momentum exchange) between the canyon and the external flow is produced by the intermittent entrainment of vortical structures due to the flapping of the shear layer which ‘grasps’ vortices from the external flow and ‘throws’ them within the canyon.

Influence of the external flow structure and of canyon geometry- Finally we analyzed the influence of the external flow condition on the wash-out time for different canyon geometries ($H/W = 1, 2, 1/2$). The external flow conditions have been varied to increase the larger scale turbulence. The corresponding configuration are configurations 1a , 1a-3a, 1a-2a (square, large and narrow cavity with external conditions given by configuration 1 - $H/W=1$) and configurations 3a-1a, 3a, 3a-2a (square, large and narrow cavity with enhanced larger scale turbulence in the external flow - configuration 3, $H/W=1/2$). For each configuration we determined the exchange velocities u_d and \tilde{u}_d , as well as the wash-out times, by means of a best fit of the experimental curves with the two-degree of freedom model.

configuration	1a	1b	3a-1a	3a	1a-3a	1a-2a	3a-2a
u_*/U_∞	0.0491	0.053	0.061	0.061	0.0491	0.0491	0.061
ΔU (m/s)	1.38	1.1	1.1	1.87	2.35	2.5	-
β	0.7	0.7	0.7	0.7	0.7	0.6	0.6
T_1 (s)	0.5	0.58	0.41	0.38	0.46	0.5	0.41
T_2 (s)	0.18	0.18	0.15	0.16	0.2	0.35	0.29
u_d (m/s)	0.069	0.069	0.087	0.1	0.086	0.072	0.086
\tilde{u}_d (s)	0.06	0.06	0.073	0.094	0.082	0.068	0.082
u_d/U_∞	0.01	0.01	0.013	0.015	0.0128	0.01	0.0128
\tilde{u}_d/U_∞	0.01	0.009	0.01	0.014	0.0122	0.01	0.012
$u_d/\Delta U$	0.051	0.063	0.08	0.055	0.036	0.028	-
$\tilde{u}_d/\Delta U$	0.044	0.055	0.06	0.052	0.034	0.027	-
$\alpha = \Delta U/u_d$	19.9	15.8	12.2	18.5	27.2	34.7	-

Table 5.4: Overview of the results of all configuration studied.

Results are presented on tabb. 5.4. We observe that, for each configuration, the exchange velocities between the inner box and the outer box (\tilde{u}_d) and between the outer box and the external flow (u_d) are nearly the same, i.e. $\tilde{u}_d \simeq u_d$. This result is in agreement with the velocity measurements presented in the previous paragraph: the fact that the level of turbulent kinetic energy within the canyon could be considered fairly constant (except close to the downwind wall), as well as the eulerian integral length scale (which can be roughly estimated $\sim 0.4W$), implies that the turbulent structures, that are responsible of the mass exchange from one region to the other within the core of the cavity, are the same that produce the mass transfer from the outer region to the external flow.

In fig. 5.35 and in fig. 5.36 the experimental curves have been plotted on the normalized time $\tilde{t} = \frac{tu_d}{W}$ and $\tilde{t} = \frac{t\tilde{u}_d}{W}$. The diagrams show that the experimental curves collapse on one single curve,

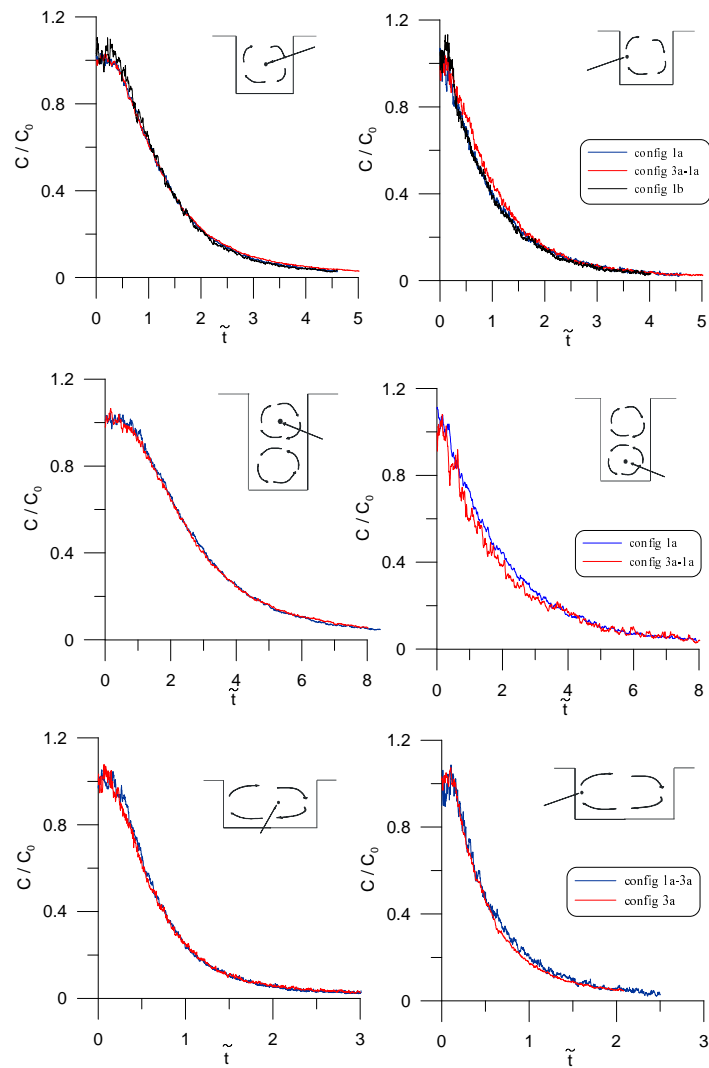


Figure 5.35: Dependence of the wash-out curves from the external flow conditions for different canyon geometries. The normalized time is $\tilde{t} = \frac{tu_d}{W}$. Using u_d as reference velocity the wash-out curves collapse on one single curve (for each canyon geometry and for each position within the canyon).

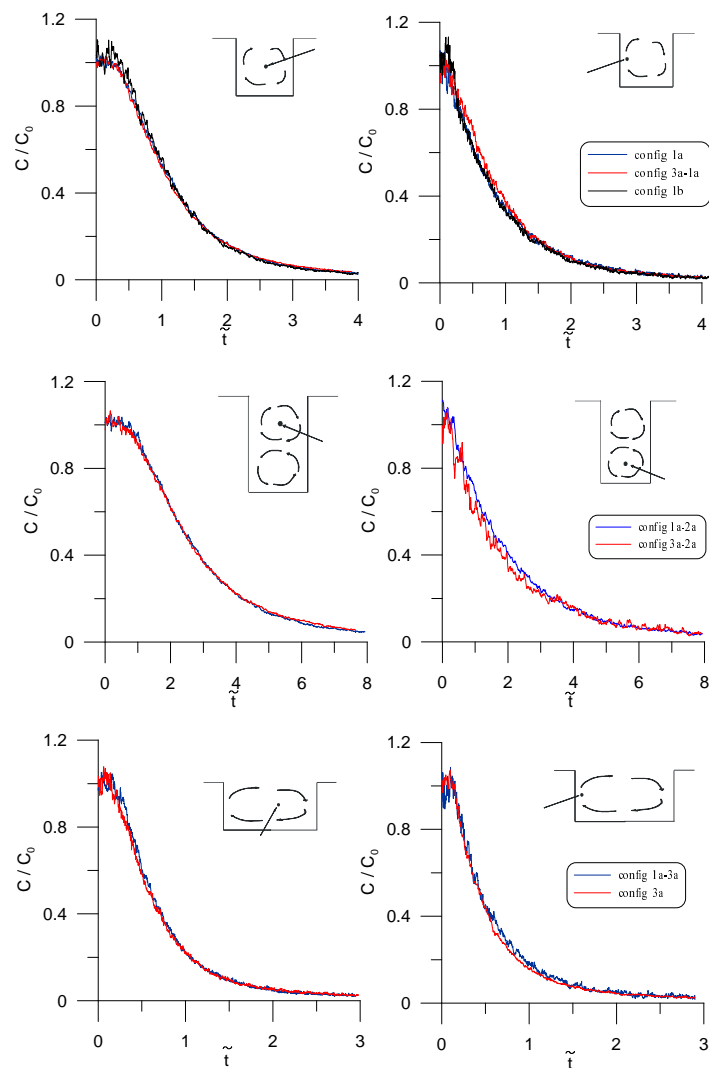


Figure 5.36: Dependence of the wash-out curves from the external flow conditions for different canyon geometries. The normalized time is $\tilde{t} = \frac{t\tilde{u}_d}{W}$. Using \tilde{u}_d as reference velocity the wash-out curves collapse on one single curve (for each canyon geometry and for each position within the canyon).

for each configuration and for each position within the canyon. That demonstrate that u_d and \tilde{u}_d are both appropriate reference velocities to describe the mass exchange process between the canyon and the external flow.

5.6 Conclusions

We studied the mass and momentum exchange between a street canyon and the external flow in order to define its dependence on the canyon geometry and on the structure of the external flow. The influence of canyon geometry mainly concerns the topology of the streamlines within the canyon.

The flow dynamics within the cavity appear to be driven by very complicated mechanisms, which are related to the turbulent transport of momentum within the canyon. The turbulent transport is characterized on one side by a momentum ‘diffusion’ within the shear layer, that depends on the velocity difference ΔU within the shear layer itself, and on the other side by the turbulent kinetic energy fluxes coming from the external flow toward the cavity. The vertical ‘flapping’ of the shear layer produce a transport of coherent structures that are brought within the cavity. Those two mechanism, which are not independent of each other, determine the flow dynamics within the cavity.

The mass-exchange transport between the cavity and the external flows depends on the canyon geometry as well as on the external turbulence intensity. That makes quite difficult to evaluate an exchange velocity, which is needed to describe the phenomenon by means of gradient laws, as is usually done in the so-called operational models.

CONCLUSIONS
and FURTHER WORKS

6.1 Conclusions

The goal of the present work was to investigate the mechanisms that control the complex process of the mass and momentum exchange in the lower part of the atmospheric boundary layer, in the so called *internal region* (the urban canopy, the roughness sub-layer and the inertial region). In particular, we focused on two aspects:

- how does the presence of small scale roughness (roof shape, chimney....) at the top of the buildings affect flow and dispersion in the turbulent stream above buildings roofs;
- what are the relevant processes in determining the mass exchange between the recirculating region and the external flow: what is the influence of the canyon geometry and of the structure of atmospheric turbulence on the shear layer dynamics and on the flow within the cavity.

The first topic deals with the dynamics of the roughness sub-layer, the region of the atmospheric boundary layer located between the urban canopy and the inertial region and characterized by the inhomogeneity of the flow in the horizontal planes. Our results show that for skimming flow, the vertical extent of the roughness sub-layer is ‘squeezed’ into a very thin region, just above the tops of the obstacles. In this case, the presence of horizontal inhomogeneities in the flow can be neglected for pollutant dispersion purposes. On the other hand, in the wake interference flow regime, pollutant dispersion modelling has to take into account the alteration of the dynamics of the flow induced by the presence of the roughness sub-layer, as long as its vertical extent above the roof is of the same order as the obstacle height H : the main change, with respect to the skimming flow case, is given by the increase of the integral length scale, and therefore of the dispersion coefficients.

The presence of a smaller scale roughness is ‘felt’ by the overlying flow only if the larger scale obstacles are sufficiently packed together (skimming flow), so that the larger scale obstacle dimension H is not a characteristic length of the flow field. The smaller scale structures produced by the small scale roughness influence the flow dynamics if their size is the same order as that of the eddies shed by the shear layer developing at the canopy top: this happens if the canyon width is not too large, i.e. for street aspect ratios $H/W > 1$. Otherwise, in case of wake interference flow, when the instabilities arising in the core of the shear layer have sufficient space to grow, the flow is dominated by the dynamics of larger scale vortices which englobe and dissipate the smaller scale ones. The presence of a two-scale roughness does not alter the normalized spectral density of the velocity field, which is mainly determined by the intermittent shedding of vortices by the shear layer at the canopy top. These conclusions all apply to a flow developing over two-dimensional obstacles with similar dimensions; things are surely more complicated for wall geometries with very different obstacle heights.

Concerning the second topic, we have identified some important features. We can say that the mass and momentum exchange between a recirculating region and the external flow is a process which is driven by the flow instabilities, arising within the shear layer which develops at the interface between the two regions, and it is influenced by the flux of turbulent kinetic energy from the external flow toward the cavity. The two mechanisms are not independent: the t.k.e. fluxes in the cavity are due to the entrainment of external vortical structures intercepted by the shear layer during its flapping vertical motion. The flapping motion is itself a product of the dynamics of the shear layer, which are determined by the dynamics of the flow on either side of the layer. Our results show that the exchange process depend on both the canyon geometry and the intensity of the external turbulence, but they are not sensitive to the external integral length scale.

6.2 Further works

As mentioned in the introduction of this thesis, this work is part of a long-term project on urban air pollution. The research project has two objectives.

The first is to carry fluid-dynamics researches in order to extend the knowledge on the mass and momentum exchange processes in complex geometries, by means of experimental and numerical methods. Two other PhD thesis started in the last two years, in order to continue the present work, concerning the extension of the this investigation to three-dimensional geometries.

The second is to describe those phenomena as simply as possible. The work done so far led to the SIRANE code, an operational tool for air pollution modelling in urban areas which adopts simple relations to describe the velocity field and the mass transfers. Moving from the knowledge acquired from the research work on those topics, the final goal will be to improve the skill and to evaluate the range of validity of these simple models.

Bibliography

- ADRIAN, R. J. 1991. Particle imaging techniques for experimental fluid mechanics. *Ann. Review of Fluid Mech.*, **23**, 261–304.
- ALBRECHT, F. 1933. Untersuchungen der vertikalen Luftzirkulation in der Grossstadt. *Met. Zt.*, **50**, 93–98.
- ANTONIA, R. A., and KROGSTAD, P. A. 2001. Turbulence structure in boundary layers over different types of surface roughness. *Fluid Dynamics Research*, **28**, 139–157.
- ANTONIA, R. A., and LUXTON, R.E. 1971. The response of a turbulent boundary layer to a step change in surface roughness Part I. Smooth to rough. *J. Fluid. Mech.*, **48 - 4**, 721–761.
- ARYA, S. P. 1999. *Air Pollution meteorology and dispersion*. Oxford University Press.
- AYOTTE, K.W., FINNIGAN, J.J., and RAUPACH, M.R. 1999. A second-order closure for neutrally stratified vegetative canopy flows. *Boundary-Layer Meteorol.*, **90 - 2**, 189–216.
- BALDAUF, M., and FIEDLER, F. 2003. A parameterisation of the effective roughness length over inhomogeneous, flat terrain. *Boundary-Layer Meteorol.*, **106**, 189–216.
- BANDYOPADHYAY, P. R., and WATSON, R. D. 1988. Structure of rough-wall turbulent boundary layers. *Phys. Fluids*, **31 - 7**, 1877–1883.
- BARLOW, J. F., and BELCHER, S. E. 2002. A wind tunnel model for quantifying fluxes in the urban boundary layer. *Boundary-Layer Meteorol.*, 131–150.
- BARLOW, J.F., HARMAN, I. N., and BELCHER, S. E. 2004. Scalar fluxes from urban street canyons. Part I: Laboratory simulation. *Boundary-Layer Meteorol.*, **113**, 369–385.
- BATCHELOR, G. K. 1967. *An introduction to fluid dynamics*. Cambridge University Press.
- BELCHER, S.E., and HUNT, J.C.R. 1998. Turbulent flow over hills and waves. *Ann. Rev. Fluid Mech.*, **30**, 507–538.
- BELCHER, S.E., XU, D. P., and HUNT, J, C.R. 1990. The response of a turbulent boundary layer to arbitrarily distributed two-dimensional roughness changes. *Q. J. R. Meteorol. Soc.*, **116**, 611–635.
- BELCHER, S.E., JERRAM, N., and HUNT, J.C.R. 2003. Adjustment of a turbulent boundary layer to a canopy of roughness elements. *J. Fluid. Mech.*, **488**, 369–398.

Bibliography

- BENTHAM, T., and BRITTER, R. 2003. Spatially averaged flow within obstacle arrays. *Atmospheric Environment*, **37**, 2037–2043.
- BÉRA, J.C., MICHARD, M., GROSJEAN, N., and COMTE-BELLOT, G. 2001. Flow analysis of two-dimensional pulsed jets by particle image velocimetry. *Experiments in fluids*, **31**, 519–532.
- BERKOWICZ, R., HERTEL, O., LARSEN, S. E., SORENSEN, N. N., and NIELSEN, M. 1997. *Modelling traffic pollution in streets*. National Environmental Research Institute.
- BEST, M.J. 2005. Representing urban areas within operational numerical weather prediction models. *Boundary-Layer Meteorol.*, **114**, 91–109.
- BLACKADAR, A. K., and TENNEKES, H. 1968. Asymptotic similarity in neutral barotropic planetary boundary. *J. Atmos. Sci.*, **25**.
- BOTT, A. 1989a. A positive definite advection scheme obtained by nonlinear renormalization of the advective fluxes. *Monthly Weather Review*, 1006–1015.
- BOTT, A. 1989b. Reply. *Monthly Weather Review*, **117**, 2633–2636.
- BOTTEMA, M. 1997. Urban roughness modelling in relation to pollutant dispersion. *Atmos. Env.*, **31** - **18**, 3059–3075.
- BOUSSINESQ, J. 1897. *Théorie de l'écoulement tourbillonnant et tumultueux des liquides*. Gauthier-Villars, Paris.
- BRITTER, R.E., and HANNA, S.R. 2003. Flow and dispersion in urban areas. *Ann. Rev. fluid Mech.*, **35**, 469–96.
- BRITTER, R.E., HANNA, S.R., BRIGGS, G.A., and ROBINS, A. 2003. Short-range vertical dispersion from a ground level source in a turbulent boundary layer. *Atmospheric Environment*, **37**, 3885–3894.
- BUILTJES, P. J. H. 1984. *Determination of the flow- and concentration-field in a street canyon by means of wind tunnel experiments*. TNO 84-02616. TNO, Apeldoorn, The Netherlands.
- BURGGRAF, O.R. 1966. Analytical and numerical studies of the structure of steady separated flows. *J. Fluid. Mech.*, **24**, 113–151.
- BUSINGER, J.A., WYNGAARD, J.C., IZUMI, Y., and BRADLEY, E. F. 1971. Flux-profile relationship in the atmospheric surface layer. *Journal of the Atmospheric Sciences*, **28**, 181–189.
- CALDER, K. L. 1952. Some recent British work on the problems of diffusion in the lower atmosphere. *Proceedings of the US Technique conference Air pollution*, vol. 787. New York: McGraw Hill.
- CARRUTHERS, D.J., and DYSTER, S.J. 2003 (November). *Boundary layer structure specification*. Report. CERC.
- CARRUTHERS, D.J., HOLROYD, R.J., HUNT, J.C.R., WENG, W.S., ROBINS, A.G., APSLEY, D.D., THOMSON, D.J., and SMITH, F.B. 1994. UK-ADMS: A new approach to modelling dispersion in the earth's atmospheric boundary layer. *J. Wind Eng. Ind. Aerodyn.*, **52**, 139–153.

Bibliography

- CASTRO, I. P., and HAQUE, A. 1987. The structure of a turbulent shear layer bounding a separation region. *J. Fluid Mech.*, **179**, 439–468.
- CASTRO, I.P., and DIANAT, M. 1990. Pulsed wire velocity anemometry near walls. *Experiments in Fluids*, **8**, 343–352.
- CASTRO, I.P., JACKSON, N.A., and ROBINS, A.G. 1975. *The structure and development of a 2m deep simulated suburban boundary layer*. R/M/N800. Central Electricity Generating board.
- CATON, F., BRITTER, R.E., and DALZIEL, S. 2003. Dispersion mechanism in a street canyon. *Atmospheric Environment*, **37**, 693–702.
- CAUGHEY, S. 1984. Observed characteristics of the atmospheric boundary layer. *Atmospheric turbulence and air pollution modelling*. Dordrecht: D. Reidel Publishing.
- CHENG, H., and CASTRO, I. P. 2002a. Near-wall flow development after a step change in surface roughness. *Boundary-layer Meteorol.*, **105 - 105**, 411–432.
- CHENG, H., and CASTRO, I. P. 2002b. Near wall flow over urban-like roughness. *Boundary Layer Meteorol.*, **104**, 229–259.
- CIONCO, R.M. 1965. A mathematical model for air flow in a vegetative canopy. *J. Applied Meteor.*, **4**, 517–522.
- CLARKE, J.F., S., CHING J. K., and BINKOSKI, F. S. Godowitch, J. M. 1978. Turbulent structure of the urban boundary layer. *Proc. Int. Tech. Meet. Air Pollut. Model. Its appl. NATO/CCMS*. New York/London: Plenum.
- CLARKE, R. H. 1970. Observational studies in the atmospheric boundary layer. *Quart. J. R. Met. Soc.*, **96**, 91–114.
- CLAUSER, F. H. 1956. The turbulent boundary layer. *Adv. Appl. Mech.*, **4**, 1–51.
- COOK, N. J. 1973. On simulating the lower third of the urban adiabatic boundary layer in a wind tunnel. *Atmos. Env.*, **7**, 691–705.
- COOK, N. J. 1977. Wind-tunnel simulation of the adiabatic atmospheric boundary layer by roughness, barrier and mixing-device methods. *J. Ind. Aerodyn.*, **3157-176**.
- COPPIN, P.A., RAUPACH, M.R., and LEGG, B.J. 1986. Experiments on scalar dispersion within a model plant canopy Part II: an elevated plane source. *Boundary-Layer Meteorol.*, **35**, 167–191.
- CORRSIN, S. 1963. Turbulence: Experimental Methods. *Pages 524–590 of: S. FLUGGE, Freiburg (ed), Handbuch der Physik, Encyclopedia of Physics*, vol. VIII/2.
- COUNIHAN, J. 1969. An improved method of simulating an atmospheric boundary layer in a wind tunnel. *Atmos. Env.*, **3**, 197–214.
- COUNIHAN, J., HUNT, J.C.R., and JACKSON, P.S. 1974. Wakes behind two-dimensional surface obstacles in turbulent boundary layer. *J. Fluid Mech.*, **64 - 3**, 529–563.

Bibliography

- DABBERDT, W. F., and DAVIS, P. A. 1978. Determination of energetic characteristics of urban-rural surfaces in the Greater St. Louis area. *Boundary-Layer Meteorol.*, **14**, 105.
- DAVIDSON, M. J., SNYDER, W. H., LAWSON, R. E., and HUNT, J. C. R. Wind tunnel simulations of plume dispersion through groups of obstacles. *Atmos. Env.*, **30 - 22**, 3715–3731.
- DE BORTOLI, M.E., NATALINI, B., PALUCH, M.J., and NATALINI, M.B. 2002. Part-depth wind tunnel simulations of the atmospheric boundary layer. *J. Wind. Eng. Ind. Aerodyn.*, **90**, 281–291.
- DE BRUIN, H. A. R. 1985. Zero-plane displacement and roughness length for tall vegetation, derived from simple mass conservation hypothesis. *Boundary-Layer Meteorol.*, **31**, 39–49.
- DE HAAN, P., ROTACH, M.W., and WERFELI, M. 2001. Modification of an operational dispersion model for urban applications. *Journal of Applied Meteorology*, **40**, 864–879.
- DEARDOFF, J. S. 1972. Numerical investigation of neutral and unstable planetary boundary layer. *J. Atmos. Sci.*, **29**, 1252–1261.
- DEPAUL, F. T., SHEIH, C. M., and NOLL, K. E. 1985. A tracer study of dispersion in an urban street canyon. *Atmos. Env.*, **19 - 4**, 455–459.
- DEZSO-WEIDINGER, G., STITOU, A., van BEECK, J., and RIETHMULLER, M. L. 2003. Measurement of the turbulent mass flux with PTV in a street canyon. *Journal of Wind Engineering*, **91**, 1117 – 1131.
- DORAN, J. C., HORST, T. W., and NICKOLA, P. W. 1978. Variations in measured values of lateral diffusion parameters. *J. Appl. Met.*, **17 - 6**, 825–831.
- DRAXLER, R. R. 1976. Determination of atmospheric diffusion parameters. *Atmos. Env.*, **10**, 99–105.
- DYER, A. J. 1974. A review of flux-profile relationships. *Boundary-Layer Meteorol.*, **7**, 363–372.
- FACKRELL, J. E., and ROBINS, A. G. 1982. Concentration fluctuations and fluxes in plumes from point sources in a turbulent boundary layer. *J. Fluid Mech.*, **117**, 1–26.
- FIEDLER, F., and PANOFSKY, H. A. 1972. The geostrophic drag coefficient and the ‘effective’ roughness length. *Quart. Jour. of Roy. Met. Soc.*, **98**, 213–220.
- FINNIGAN, J. J. 1979. Turbulence in waving wheat. I. Mean statistics and Honami. *Boundary-Layer Meteorol.*, **16**, 181–211.
- FINNIGAN, J. J. 1985. Turbulent transport in flexible plant canopies. *Pages 443–480 of: HUTCHINSON, B.A., and HICKS, B.B. (eds), The Forest-Atmosphere Interaction.* Dordrecht: D.Reidel Publishing Co.
- GARRATT, J. R. 1978. Flux profile relations above tall vegetation. *Quart. Jour. of Roy. Met. Soc.*, **104**, 199–211.
- GIFFORD, F. A. 1970. Atmospheric Diffusion in an Urban area. *2nd IRPA Conf.*
- GOODE, K., and BELCHER, S. E. 1999. On the parameterisation of the effective roughness length for momentum transfer over heterogeneous terrain. *Boundary-Layer Meteorol.*, **93**, 133–154.

Bibliography

- GRACE, S. M., G., Dewar W., and WROBLEWSKI, D. E. 2004. Experimental investigation of the flow characteristics within a shallow wall cavity for both laminar and turbulent upstream boundary layers. *Experiments in Fluids*, **36**, 791–804.
- GRANVILLE, P. S. 1976. A modified law of the wake for turbulent boundary layers. *J. Fluid Eng.*, **98**, 578–580.
- GRIMMOND, C. S. B., and OKE, T. R. 1999. Aerodynamic properties of urban areas derived from analysis of surface form. *J. Appl. Met.*, **38**, 1262–1292.
- HAMA, F. R. 1954. Boundary layer characteristics for smooth and rough surfaces. *Trans. Soc. Naval Archit. Marine Engrs.*, **62**, 333.
- HANNA, S. R., TEHRANIAN, S., CARISSIMO, B., MACDONALD, R. W., and LOHNER, R. 2002. Comparisons of model simulations with observations of mean flow and turbulence within simple obstacle arrays. *Atmos. env.*, **36**, 5067–5079.
- HARMAN, I. N., BARLOW, J.F., and BELCHER, S. E. 2004. Scalar fluxes from urban street canyons. Part II: Model. *Boundary-Layer Meteorol.*, **113**, 387–409.
- HASSAN, A. A., and CROWTHER, J. M. 1998. A simple model of pollutant concentrations in a street canyon. *Environmental Monitoring and Assessment*, **52 - 1–2**, 269–280.
- HERTEL, O., and BERKOWICZ, R. 1989. *Modelling pollution from traffic in a street canyon. Evaluation of data and model development.* DMU Luft A-129, NERI.
- HINZE, J. O. 1959. *Turbulence.* McGraw-Hill, New York.
- HÖGSTRÖM, U., BREGSTRÖM, H., and ALEXANDERSSON, H. 1982. Turbulence characteristics in a near neutrally stratified urban atmosphere. *Boundary-Layer Meteorol.*, **23**, 449–472.
- HOTCHKISS, R. S., and HARLOW, F. H. 1973. Air pollution transport in street canyons. *Environmental Protection Agency*, 1–128.
- HOYDYSH, W. G., and DABBERDT, W. F. 1988. Kinematics and dispersion characteristics of flows in asymmetric street canyons. *Atmos. Env.*, **22 - 12**, 2677–2689.
- HUNT, A., and CASTRO, I. P. 1984. Scalar dispersion in model building wakes. *Jour. of Wind Eng. and Indust. Aerod.*, **17**, 89–115.
- HUNT, J. C. R. 1985. Turbulent diffusion from sources in complex flows. *Ann. Rev. fluid. Mech.*, **17**, 447–485.
- HUNT, J. C. R., STRETCH, D. D., and BRITTER, R.B. 1988. Length scales in stably stratified turbulent flows and their use in turbulent models in stably stratified flow and dense gas dispersion. *Page 430 of: Proceedings IMA Conference.* Oxford University Press.
- HUSSAIN, M., and LEE, B. E. 1980. *An investigation of wind forces on three dimensional roughness elements in a simulated atmospheric boundary layer flow. Part II : flow over large arrays of identical roughness elements and the effect of frontal and side aspect ratio variations.* Dept. of Build. Sce, Univ. of Sheffield.

Bibliography

- IRWIN, H. P. A. H. 1981. The design of spires for wind simulation. *Jour. of Wind Eng. and Indust. Aerod.*, **7**, 361–366.
- IRWIN, J. S. 1979. Estimating plume dispersion – A recommended generalized scheme. *Pages 62–69 of: Fourth Symposium on Turbulence, Diffusion, and Air Pollution, Reno, Nev.*
- ISNARD, O. 1999. *Dispersion atmosphérique en présence de groupes d'obstacles*. PhD Thesis, École Centrale de Lyon.
- JACKSON, P. S. 1981. On the displacement height in the logarithmic velocity profile. *J. Fluid Mech.*, **111**, 15–25.
- JACKSON, P. S., and HUNT, J. C. R. 1975. Turbulent wind flow over a low hill. *J. Fluid Mech.*, **101**, 929–955.
- JIMÈNEZ, J. 2004. Turbulent flows over rough wall. *Ann. Rev. Fluid Mech.*, **36**, 173–96.
- JOHNSON, G. T., HUNTER, L. J., and ARNFELD, A. J. 1990. Preliminary field test of an urban canyon wind flow model. *Energy and Buildings*, **15 - 3**, 325–332.
- JOHNSON, W. B., LUDWIG, F. L., DABBERDT, W. F., and ALLEN, R. J. 1973. An urban diffusion simulation model for carbon monoxide. *Journal of Air Pollution Control Association*, **23**, 490–498.
- KAIMAL, J.C., and FINNIGAN, J.J. 1994. *Atmospheric boundary layer flow*. New York Oxford: Oxford University Press.
- KASTNER-KLEIN, P., and FEDOROVICH, E. 2002. Diffusion from a line source deployed in a homogeneous roughness layer: interpretation of wind-tunnel measurements by means of simple mathematical models. *Atmos. Env.*, **36**, 3709–3718.
- KASTNER-KLEIN, P., FEDOROVICH, E., and ROTACH, M.W. 2001. A wind study of organised and turbulent air motions in urban street canyons. *J. Wind Eng. Ind. Aerodyn.*, **89**, 849–861.
- KASTNER-KLEIN, P., FEDOROVICH, E., and ROTACH, M.W. 2004. Mean flow and turbulence characteristics in an urban roughness sublayer. *Boundary-Layer Meteorol.*, **111**, 55–84.
- KIM, J.J., and BAIK, J.J. 2003. Effects of inflow intensity on flow and pollutant dispersion in an urban street canyon. *J. Wind Eng. Ind. Aerodyn.*, **91**, 309–329.
- KITABAYASHI, K., SUGAWARA, K., and ISOMURA, S. 1976. A wind tunnel study of automobile exhaust gas diffusion in an urban district. *Pages 192–195 of: Fourth Int. Clean Air Congr.*, vol. II-15.
- KOLOSEUS, H. J., and DAVIDIAN, J. 1966. Free-surface instability correlations, and roughness-concentration effects on flow over hydrodynamically-rough surfaces. *USGS Water Supply Paper*, **C**, 1592.
- KROGSTAD, P. A., and ANTONIA, R. A. 1995. Structure of turbulent boundary layers on smooth and rough walls. *J. Fluid Mech.*, **277**, 1–21.
- KROGSTAD, P. A., and ANTONIA, R. A. 1999. Surface roughness effects in turbulent boundary layers. *Expts. Fluids*, **27**.

Bibliography

- KROGSTAD, P. A., ANTONIA, R. A., and BROWNE, L. W. B. 1992. Comparaison between rough- and smooth-wall turbulent boundary layers. *J. Fluid. Mech.*, **245**, 599–617.
- LANDSBERG, H. E. 1981. The urban climate. *Int. Geophys. Series*, **28**, 275 pp.
- LEE, I. Y., and PARK, H. M. 1994. Parameterization of the pollutant transport and dispersion in urban street canyons. *Atmos. Env.*, **28 - 14**, 2343–2349.
- LOUKA, P., BELCHER, S. E., and HARRISON, R. G. 1998. Modified street canyon flow. *Jour. of Wind Eng. and Indust. Aerod.*, **74–76**, 485–493.
- LOUKA, P., BELCHER, S. E., and HARRISON, R. G. 2000. Coupling between air flow in streets and the well-developed boundary-layer aloft. *Atmos. Env.*, **34 - 16**, 2613–2622.
- LUMLEY, J. L., and PANOFKY, H. A. 1964. *The structure of atmospheric turbulence*. Wiley - Interscience, NEW YORK.
- MACDONALD, R. W. 2000. Modelling the mean velocity profile in the urban canopy layer. *Boundary-Layer Meteorol.*, **97**, 25–45.
- MACDONALD, R. W., CARTER, S., and SLAWSON, P. R. 2000. *Measurements of mean velocity and turbulence statistics in simple obstacle arrays at 1:200 scale*. University of Waterloo, Department of Mechanical Engineering.
- MAHÉ, F., MAURY, F., CORFA, E., and ALBERGEL, A. 2004. Numerical evaluation of diesel locomotives contribution in the surrounding area of the railway station 'Gare de l'est'. *Pages 90–94 of: SUPPAN, Peter (ed), Harmonisation within atmospheric dispersion modelling for regulatory purposes*. Karlsruhe: Forschungszentrum Karlsruhe GmbH.
- MARTILLI, A., CLAPPIER, A., and ROTACH, M. W. 2002. An urban exchange parameterisation for mesoscale models. *Boundary-Layer Meteorol.*, **104**, 261–304.
- MC HUGH, C. A., CARRUTHERS, D. J., and EDMUNDS, H. A. 1997. ADMS-urban: an air quality management system for traffic, domestic and industrial pollution. *International Journal of Environment and Pollution*, **8**, 666–674.
- MCNEILL, J. R. 2001. *Something New Under the Sun: An Environmental History of the Twentieth-Century World*. Paperback.
- MEHTA, U. B., and LAVAN, Z. 1969. Flow in a two dimensional channel with a rectangular cavity. *Journal of Applied Mechanics*, **36**, 897–901.
- MERONEY, R. N., PAVAGEAU, M., RAFAILIDIS, S., and SCHATZMANN, M. 1996. Study of line source characteristics for 2-D physical modelling of pollutant dispersion in street canyons. *Jour. of Wind Eng. and Indust. Aerod.*, **62 - 1**, 37–56.
- MILLIKAN, C.B. 1939. A critical discussion of turbulent flows in channels and circular tubes. *Proc. 5th Internat. Cong. Appl. Mech.* 386-392. New York: Wiley.
- MILLS, R. D. 1965. On the closed motion of fluid in a square cavity. *J. Roy. Aeronaut. Soc.*, **69**, 116–120.

Bibliography

- MONIN, A. S., and OBUKHOV, A. M. 1954. Basic laws of turbulent mixing in the ground layer of the atmosphere. *Trans. Geophys. Inst. Akad. Nauk, USSR*, **151**, 163–187.
- MULHEARN, P. J. 1978. Turbulent flow over a periodic rough surface. *Phys. Fluids*, **21 - 7**, 1113–1115.
- MULHEARN, P. J., and FINNIGAN, J. J. 1978. Turbulent flow over a very rough random surface. *Boundary-Layer Meteorol.*, **15**, 109–132.
- NIKURADSE, J. 1933. Strömungsgesetze in rauhen Rohren. *Forsch. Arb. Ing.-Wes.*, **361**.
- OIKAWA, S., and MENG, Y. 1995. Turbulence characteristics and organized motion in a suburban roughness sublayer. *Boundary-Layer Meteorol.*, **74**, 289–312.
- OKE, T. R. 1979. *Review of urban climatology. 1973 – 1976*. 169. WMO T.N.
- OKE, T. R. 1987. *Boundary layer climates*. 2nd. London: Methuen.
- OKE, T. R. 1988a. Boundary layer climates. *The Meteorological Magazine*, **117 - 1394**, 89–.
- OKE, T. R. 1988b. Street design and urban canopy layer climate. *Energy and Buildings*, **11**, 103–113.
- PAN, F., and ACRIVOS, A. 1967. Steady flows in rectangular cavities. *J. Fluid Mech.*, **28 - 4**, 643–655.
- PANOFSKY, H. A., and DUTTON, J.H. 1984. *Atmospheric turbulence*. John Wiley and Sons , New York.
- PASQUILL, F. 1976. *Atmospheric dispersion parameters in gaussian plume modeling: Part II. Possible requirements for change in the Turner workbook values*. EPA-600/4-760306. US EPA.
- PASQUILL, F., and SMITH, F. B. 1983. *Atmospheric diffusion*. third. John Wiley & sons.
- PAVAGEAU, M., and SCHATZMANN, M. 1999. Wind tunnel measurements of concentration fluctuations in an urban street canyon. *Atmos. Env.*, **33 - 24–25**, 3961–3971.
- PERKINS, R. J., and BELCHER, S. E. (eds). 1997. *Flow and dispersion through groups of obstacles*. Oxford: Clarendon Press.
- PERRY, A.E., SHOFIELD, W. H., and JOUBERT, P. N. 1968. Rough wall turbulent boundary layers. *J. Fluid Mech.*, **37**, 383–413.
- PERRY, A.E., LIM, K.L., and HENBEST, S.M. 1986. An experimental study of the turbulence structure in smooth- and rough- wall boundary layers. *J. Fluid Mech.*, **177**, 437–466.
- PHILLIPS, P., and PANOFSKY, H. A. 1982. A re-examination of lateral dispersion from continuous sources. *Atmos. Env.*, **16**, 1851–1859.
- PICCOLO, C., ARINA, R., and CANCELLI, C. 2001. Fluid exchange between a recirculating region and the perturbed external flow. *Phys. Chem. Earth*, **26 - 4**, 269–273.
- PLATE, E. J. 1995. Urban climates and urban climate modelling: an introduction. *Pages 22–39 of: CERMAK, J.E., DAVENPORT, E.G., PLATE, E.J., and VIEGAS, D. X. (eds), Wind Climates in Cities*, vol. 277. NATO ASI Series E.

Bibliography

- POGGI, D., POROPRATO, A., and RIDOLFI, I. 2003. Analysis of the small scale structure of turbulence on smooth and rough walls. *Physics of Fluids*, **15** - **1**, 35–46.
- RAFAILIDIS, S. 1997. Influence of building areal density and roof shape on the wind characteristics above a town. *Boundary-Layer Meteorol.*, **85**, 255–271.
- RAFAILIDIS, S., and SCHATZMANN, M. 1995. Physical modelling of car exhaust dispersion in urban street canyons - the effects of slanted roofs. *21st Int. Meeting on Air Pollution Modelling and its Applications*.
- RAJARATNAM, N. 1976. *Turbulent jets*. Elsevier.
- RAUPACH, M. R. 1981. Conditional statistics of Reynolds stress in rough-wall and smooth wall turbulent boundary layers. *J. Fluid Mech.*, **108**, 363–382.
- RAUPACH, M. R. 1992. Drag and drag partition on rough surfaces. *Boundary-Layer Meteorol.*, **60**, 375–395.
- RAUPACH, M. R., and SHAW, R. H. 1982. Averaging procedures for flow within vegetation canopies. *Boundary-Layer Meteorol.*, **22**, 79–90.
- RAUPACH, M. R., THOM, A. S., and EDWARDS, I. 1980. A wind-tunnel study of turbulent flow close to regularly arrayed rough surfaces. *Boundary-Layer Meteorol.*, **18**, 373–397.
- RAUPACH, M. R., COPPIN, P. A., and LEGG, B. J. 1986. Experiments on scalar dispersion within a model plant canopy. Part I : The turbulence structure. *Boundary-Layer Meteorol.*, **35**, 21–52.
- RAUPACH, M. R., ANTONIA, R.A., and RAJOPLAN, S. 1991. Rough-wall turbulent boundary layers. *Appl. Mech. Rev.*, **44** - **1**, 1–25.
- RAUPACH, M.R., and COPPIN, P.A. 1983. Turbulent dispersion from an elevated line source: measurements of wind concentration moments and budgets. *J. Fluid Mech.*, **136**, 111–137.
- ROTACH, M. W. 1993a. Turbulence Close to a Rough Urban Surface. Part I: Reynolds Stress. *Boundary-Layer Meteorol.*, **65**, 1–28.
- ROTACH, M. W. 1993b. Turbulence Close to a Rough Urban Surface. Part II: Variances and Gradients. *Boundary-Layer Meteorol.*, **66**, 75–92.
- ROTACH, M. W. 1994. Determination of the zero plane displacement in an urban environment. *Boundary-Layer Meteorol.*, **67**, 187–193.
- ROTACH, M. W. 1995. Profiles of turbulence statistics in and above an urban street canyon. *Atmos. Env.*, **29** - **13**, 1473–1486.
- ROTH, M. 2000. Review of atmospheric turbulence over cities. *Quart. Jour. of Roy. Met. Soc.*, **126**, 941–990.
- ROTTA, J. C. 1962. Turbulent boundary layers in incompressible flow. *Pages 1–220 of: FERI, A., KUCHEMAN, D., and STONE, L. G. H. (eds), Progress in Aeronautical Science*, vol. 2. Pergamon.

- SCHLICHTING, H. 1968. *Boundary layer theory*. 6th. New York: McGraw-Hill.
- SCORER, R. S. 1968. *Air Pollution*. Elsevier Science Ltd.
- SINI, J-F., ANQUENTIN, S., and MESTAYER, P.G. 1996. Pollutant dispersion and thermal effects in urban street canyons. *Atmos. Env.*, **30** - **15**, 2659–2677.
- SOULHAC, L. 2000. *Modélisation de la dispersion atmosphérique à l'intérieur de la canopée urbaine*. PhD Thesis, Ecole Centrale de Lyon.
- SOULHAC, L. 2001. *Prise en compte simplifiée du bâti dans les modélisation 3D*. LMFA- Ecole Centrale de Lyon.
- SOULHAC, L. 2002. *Notice d'utilisation du modèle Sirane*. LMFA - Ecole Centrale de Lyon. Rapport d'étude EDF.
- SOULHAC, L., PUEL, C., DUCLAUX, o., and PERKINS, R.J. 2003. Simulations of atmospheric pollution in Greater Lyon an example of the use of nested models. *Atmos. Env.*, **37**, 5147–5156.
- SUTTON, O. G. 1953. *Micrometeorology*. London: McGraw Hill.
- SVENSSON, U., and HÄGGKVIST, K. 1990. A two-equation turbulence model for canopy flows. *J. Wind Eng. Ind. Aerodyn.*, **35**, 201–211.
- TAYLOR, G. I. 1935. Statistical theory of turbulence, Part I. *Proc. Roy. Soc. London, Ser. A*, **105**, 421–444.
- TAYLOR, G.I. 1921. Diffusion by continuous movements. *Proc. Roy. Soc. London, Ser. A*.
- TENNEKES, H., and LUMLEY, J. L. 1972. *A first course in turbulence*. The MIT Press.
- THOM, A. S. 1971. Momentum absorption by vegetation. *Quart. J. R. Met Soc.*, **97**, 414–428.
- THUBURN, J. 1997. TVD schemes, positive schemes, and the universal limiter. *Monthly Weather Review*, **125**, 1990–1993.
- TOWNSEND, A. A. 1976. *The structure of turbulent shear flows*. Cambridge University Press.
- TRITTON, D. J. 1988. *Physical Fluid Dynamics*. Oxford Science Publications.
- VARDOULAKIS, S., FISHER, B.E.A., PERICLEOUS, K., and GONZALES-FLESCA, N. 2003. Modelling air quality in street canyons: a review. *Atmos. env.*, **37**, 155–182.
- WALSH, M. J. 1990. Ribbllets. *Pages 203–261 of*: BUSHNELL, D.M., and HENFER, J.N. (eds), *Viscous drag reduction in boundary Layers*. New York: AIAA.
- WIERINGA, J. 1986. Roughness-dependent geographical interpolation of surface wind speed averages. *Quart. J. Roy. Meteorol. Soc.*, **112**, 867–889.
- WIERINGA, J. 1993. Representative roughness parameters for homogeneous terrain. *Boundary-Layer Meteorol.*, **63**, 323–363.

-
- WILLIS, G. E., and DEARDOFF, J. S. 1976. A laboratory model of diffusion into the convective planetary boundary layer. *Quart. J. R. Met. Soc.*, **102** - **432**, 427–445.
- WILSON, J.D. 1988. A second-order closure model for flow through vegetation. *Boundary-Layer Meteor.*, **42**, 371–392.
- WILSON, N.R., and SHAW, R.H. 1977. A higher order closure model for canopy flow. *J. Appl. Meteor.*, **16**, 1197–1205.
- WOSNIK, M., CASTILLO, L., and GEORGE, W.K. 2000. A theory for turbulent pipe and channels flows. *J. Fluid Mech.*, **421**.
- YAMADA, T. 1982. A numerical model study of turbulent airflows in and above a forest canopy. *J. Meteorol. Soc. Jpn.*, **60** - **1**, 439–453.
- YAMARTINO, R. J., and WIEGAND, G. 1987. Development and evaluation of simple models for the flow, turbulence and pollutant concentration fields within an urban street canyon. *Atmospheric Environment*, **20** - **11**, 2137–2156.

Contents

Abstract	3
Introduction	4
1. Essentials on boundary layer dynamics and atmospheric dispersion	9
1.1 Introduction	10
1.2 Similarity theory of a neutral boundary layer	10
1.2.1 The log-law region as the ‘constant stress’ layer	11
1.2.2 The log-law region as a ‘buffer’ layer	12
1.2.3 The log-law region as the ‘local equilibrium’ layer	15
1.3 Extension of the similarity theory	16
1.4 Short-comings of the similarity theory	19
1.5 Lineaments of turbulent dispersion	20
2. Flow and dispersion in urban areas	25
2.1 Introduction	26
2.2 Urban climatology	26
2.3 Spatial Scales	27
2.3.1 The regional scale	28
2.3.2 The city and the district scales	29
2.3.3 The local scale: the street canyon	39
2.4 Numerical modelling of urban pollutant dispersion	40
2.4.1 ADMS-Urban	41
2.4.2 SIRANE	42
3. Experimental methods and facilities	45
3.1 Experimental set-up	46
3.1.1 Similarity conditions	46
3.1.2 On simulating the atmospheric boundary layer	47
3.2 Measurement technique	48
3.2.1 Hot-wire anemometry	48
3.2.2 Flame Ionisation Detector - FID	48
3.2.3 Particle Image velocimetry - PIV	51
3.2.4 Flow visualizations	53

4. Influence of a two-scale surface roughness on a turbulent boundary layer	55
4.1 Introduction	56
4.2 Experimental conditions	58
4.3 Hot wire anemometry velocity measurements	60
4.3.1 Characteristics boundary layer parameters	61
4.3.2 Wall similarity in the outer and in inertial regions	65
4.3.3 Skimming flow regime	67
4.3.4 Wake-interference flow	75
4.4 Particle image velocimetry measurements	79
4.4.1 Horizontal inhomogeneities in the lower part of flow field	79
4.4.2 Spatial correlations	84
4.5 Passive scalar dispersion	90
4.5.1 Mathematical model and numerical methods	91
4.5.2 Experimental and numerical results	94
4.6 Conclusions	116
5. Mass and momentum exchange between a street canyon and the external flow	119
5.1 Introduction	120
5.2 Varying the boundary conditions within the canyon	120
5.2.1 On the influence of canyon geometry	120
5.2.2 Influence of roughness on canyon walls	128
5.3 On the influence of varying conditions of the external flow	131
5.3.1 Problem setting	131
5.3.2 Square cavity	133
5.3.3 Large cavity	146
5.4 Discussion of velocity measurements results	152
5.5 Evaluation of the wash-out time of the cavity	153
5.5.1 State of the art: the existing box models	153
5.5.2 A simple analytical model with two degrees of freedom	156
5.5.3 Experimental Results	161
5.6 Conclusions	171
6. Conclusions and further works	173
6.1 Conclusions	174
6.2 Further works	175
Bibliography	177

Annexe 1: DVD - flow visualizations.